Beam Diagnostics and Spectroscopy at X-ray Free Electron Lasers

zur Erlangung des

DOKTORGRADES DER NATURWISSENSCHAFTEN (Dr. rer. nat.)

im Fachbereich Physik

der Freien Universität Berlin

genehmigte Dissertation

vorgelegt von

Jens Konstantin Rehanek, M. Sc.

aus Berlin,

im Jahre 2014

Einreichung der Dissertation:	12. März 2014
Datum der Disputation:	28. Mai 2014
Vorsitzender der Promotionskommission:	Professor Dr. Martin Weinelt
Erstgutachter der Promotion:	Professor Dr. Alexei Erko
Zweitgutachter der Promotion:	Professor Dr. Holger Dau
Promoviertes Mitglied der Kommission:	Dr. Markus Miettinen
Promovierendes Mitglied der Kommission:	Fr. Heike Löchel

“The important thing in science is not so much to obtain new facts as to discover new ways of thinking about them.”

Sir William Henry Bragg, Nobel Prize for Physics, 1915

Mým rodičům Vladimir a Renate

pro mou rodinu

láska mého života

(To my parents, family and love of my life)

Abstract

In this work, optical systems such as special monochromators and spectroscopy elements for the beam diagnostics and spectroscopy with free-electron laser (FEL) radiation are presented. Various methods and optics for commissioning and measurement of the actually produced laser beam are shown; finally the application of FEL-radiation at experiments is demonstrated.

The demands to the FEL X-ray optics are extremely high. They must be able to preserve the properties of the new sources as good as possible; speaking not only of the enormous photon density per time, but also of coherence and extremely low divergence, generated by the FELs. This occurs at pulse repetition rates in the range of up to several kHz. Such high-energy pulses in the GW range pose the question of whether the used optics is able to withstand these conditions (for a longer time). Possible applications and limitations of modern optics such as reflection zone plates are investigated and demonstrated here.

The present work involves both simulation and experimental tests. It is divided into four sub-projects. Each one describes the different states of the FEL. The first sub-project with the European XFEL GmbH in Hamburg includes the commissioning of the FEL. Here, two different methods for the precise adjustment of the undulator segments of the long FEL undulators (200 m) are presented, by measuring the so-called K-parameter, magnet field strength in the undulator, the product of magnet field and period length of a magnetic structure. For that, a 2- or 4-crystal monochromator is used, which is able to determine the K-parameters with an accuracy of 10^{-4} to 10^{-6}. The proposed methods were successfully demonstrated using undulator radiation at the PETRA III facility.

The second sub-project with European XFEL is dedicated to the measurement of the spectral parameters of the actual resulting FEL radiation from pulse to pulse, single-shot spectroscopy. For this purpose, various methods have been investigated that can register the spectral response with sufficiently high precision. It was thereby demonstrated that resolutions down to 3.2 meV at the pulse energy of 10 keV are feasible.

In a third project, with LBNL in Berkeley and at LCLS in Stanford, a new spectroscopic setup was implemented, which is able to detect the fluorescence spectra from highly diluted elements under interaction of FEL X-ray pulses with a liquid jet in vacuum. The signals, previously not measurable due to low intensity in the complex context of photosynthesis spectroscopy were observed. The system development and a successful improvement are presented.

The fourth project describes an X-ray transport line coupled with a spectrometer for conducting cross-dispersive resonant inelastic X-ray spectroscopy (RIXS) experiments. This is theoretically examined as a case-study. With this apparatus it is possible to achieve an energy resolution of $E/\Delta E \approx$ 30,000 in the soft X-ray regime (776 eV as an example) at simultaneous recording of the absorbed and emitted radiation, which will enable a new class of fundamental research using RIXS experimental studies.

Kurzzusammenfassung

In dieser Arbeit werden optische Systeme wie spezielle Monochromatoren und spektroskopische optische Elemente für Strahlendiagnostik sowie Spektroskopie mit Freie-Elektronen-Laserstrahlung (FEL) dargestellt. Verschiedene Methoden und Optiken für die Inbetriebnahme und Messung der produzierten Laserstrahlung werden gezeigt; schließlich werden auch Experimente mit FEL-Strahlung vorgestellt.

Die Anforderungen an die FEL Röntgen-Optiken sind extrem hoch. So müssen sie in der Lage sein, die Eigenschaften der neuen Quellen bestmöglich zu erhalten. Dabei sprechen wir nicht nur von den enormen Photonendichten pro Zeit, sondern ebenso von Kohärenz und extrem geringer Divergenz, die FELs erzeugen. Eigenschaften der neuesten Quellen wie Pulswiederholungsraten im Bereich mehrerer kHz und hochenergetische Pulse im Gigawatt-Bereich werfen ebenso die Frage auf, ob die verwendeten Optiken im Stande sind, diesen Bedingungen unbeschadet für längere Zeit Stand zu halten. Mögliche Anwendungen, sowie Grenzen der modernen Optiken, mit besonderem Augenmerk auf Reflektionszonenplatten, werden hier untersucht und aufgezeigt.

Die vorliegende Arbeit beinhaltet sowohl Simulations- als auch experimentelle Ergebnisse. Sie ist in 4 Teilprojekte untergliedert. Ein jedes beschreibt Anwendungen in verschieden Status des FEL. Das erste Teilprojekt mit der European XFEL GmbH in Hamburg beinhaltet die Inbetriebnahme des FEL. Dabei werden 2 verschiedene Methoden zur präzisen Justage der Segmente der langen FEL-Undulatoren (ca. 200 m) durch Messung des sogenannten K-Parameters vorgestellt. Dafür wird ein 2- bzw. 4-Kristall-Monochromator eingesetzt, der in der Lage ist, den K-Parameter mit einer Genauigkeit von 10^{-4} bis 10^{-6} zu bestimmen, um die spontane Strahlung zu untersuchen. Die vorgeschlagenen Methoden zeigten sich bei Experimenten an PETRA III als erfolgreich durchführbar.

Das zweite XFEL-Teilprojekt widmet sich der Spektroskopischen Messung der FEL-Strahlung von Puls zu Puls, der sogenannten Einzelschuß-Spektroskopie. Hierfür wurden verschiedene Methoden vorgestellt, die die vorhandenen Änderungen des Spektrums jedes einzelnen Schusses mit genügend hoher Präzision registrieren können. Es konnte dabei gezeigt werden, dass Energieauflösungen bis zu 3,2 meV bei 10 keV Photonenenergie möglich sind.

In einem dritten Projekt mit LBNL in Berkeley am LCLS in Stanford wurde ein neuartiges Spektroskop realisiert, das in der Lage ist, das Fluoreszenzspektrum von Elementen in höchstverdünnten Lösungen, unter Nutzung von Wechselwirkung von FEL-Pulsen mit einem Flüssigkeitsstrahl, im Vakuum zu detektieren. Aufgrund zu geringer Intensität bisher unmessbare Signale im komplexen Zusammenhang der Photosynthese konnten spektroskopisch erfasst werden. Die umfassende Systementwicklung und eine erfolgreiche Verbesserung werden vorgestellt.

Im letzten Projekt wird ein Röntgenstrahlrohr, direkt verbunden mit Spektrometer zur Messung resonanter, unelastischer Röntgenstrahlung (RIXS) theoretisch als Fallstudie untersucht. Mit dieser Vorrichtung ist es möglich, eine Energieauflösung von $E/\Delta E \approx 30000$ im weichen Röntgenbereich (bei 776 eV als Beispiel), bei gleichzeitiger Aufnahme der absorbierten und der emittierten Strahlung, zu erlangen, was eine neue Klasse von Experimenten im Bereich der Grundlagenforschung mit RIXS-Studien ermöglichen wird.

Table of contents

1. Introduction/Motivation

The history of free electron light sources started in 1930, when Ernest Lawrence first proposed the concept of a cyclotron. It was realized two years later together with Milton S. Livingston; they accelerated protons to 1.2 MeV [1].

The first idea of a pulsed magnet ring appeared in a proposal in 1943 [2]. This was the foundation of a synchrotron. Julian Schwinger published his development [3] and then in a revised form in 1949 the theory for synchrotron radiation [4]. Consecutively, it was developed further by [5], [6] and [7] until the first observation of synchrotron radiation happened accidentally in the year 1947 (24th of April) at the General Electric Research Laboratory in Schenectady, New York [8]. In this case "observation" is meant literally, as they observed visible light. Actually, the radiation appeared parasitically on accelerators for high-energy particle physics built to conduct primary experiments for the production of X-rays via particle collisions. At this time, some of the old storage rings from particle physics were altered for the production of X-rays [9]. Due to promising results using these X-ray radiation sources, a second generation of sources was built in the 1980s. With these sources, generation of synchrotron radiation was primarily based upon bending magnets.

A decade later third generation sources were developed: storage rings which were exclusively designed and built for the purpose of producing synchrotron radiation, containing many undulators and wigglers as primary light source.

The latest revolution in the development of free electron sources was the 4th generation, the Free Electron Lasers (FELs), invented and first built by John Madey [10] in 1970. The development took another 31 years, until in 2001 [11] the first self-amplified stimulated emission (SASE) FEL went into operation with FLASH at DESY in Hamburg [12] [13], working in the EUV/soft X-ray regime. Its conceptual design report was already published in 1995 [14], User-operation started in 2005 [15]. Then, the development went further on, until "a milestone of paramount importance" [16] was achieved with the first lasing (in the hard X-ray regime) of LCLS in 2009 [17] [18] and SALCA in 2011 [19].

The constant enhancement of free electron light sources gives rise to new exciting possibilities for experiments which were never feasible before, maybe not even conceivable. This constantly leads to new challenges, new demands on the optical elements, which were so far developed for synchrotron sources. The newly developed sources offer extremely high peak brilliances (10 orders of magnitude more than 3rd generation synchrotrons), very short pulses (down to the fs-regime) but varying spectra from shot to shot (if generated e.g. via SASE-principle). This requires a new level of X-ray optics; especially for those dedicated to diagnostics and spectroscopy of the FEL beams and corresponding experiments.

Simultaneously with the development of free electron sources, the development of X-ray optics made a tremendous progress. X-ray Optics is the link between the source and cutting-edge experiments to probe materials in spatial, electronic and temporal scales of nanometers and femtoseconds. It is required to preserve the source's brightness best possibly. The developments in X-ray optics stays well behind the progress in source technology, by the ability to monochromatize, focus and control the high-intensity beams in the required length- and time-scale. The optics

technology needs to meet the required precision in the range of sub-nanometer height deviation and nano-radian slope errors, which needs to be preserved under high heat load, at length scales of the optical element on the order of 1 m. This is quite challenging for the production process as well as for their metrology. Modeling and simulation is the theoretical basis for the design of a diversity of optical elements. So, as well simulation and characterization methods are necessary to approach the complexity of modern beamline design, covering a large energy range from UV to hard X-rays; as it is stated in the "Report of the DOE Workshop on the Basic Energy Sciences on X-ray Optics for BES Light Source Facilities", March 27 – 29, 2013, Washington DC, USA.

The development of new spectroscopic techniques using X-rays has engaged scientists since the discovery of the unique properties of X-rays for investigation of matter. High-resolution spectrometric systems based on diffraction gratings are extremely expensive and inefficient because of their small angular acceptance, low diffraction efficiency and the high density of lines on the used gratings. Even though, they are extensively used in VUV and soft X-ray optics in combination with total external reflection mirrors. The reflectivity of applied coatings in this photon energy range is also far from 100% and leads to a drastic reduction of the photon flux, if the beamline consists of several optical elements. Recently, with the development of nano-technological methods, variable line spacing (VLS) gratings have been implemented, which are able to focus dispersed X-rays one-dimensionally onto the detector. That way, one reflection element (focusing mirror) is eliminated and the sensitivity and accuracy of spectroscopic methods [20] is increased considerably.

In [21] and [22], for the first time a new optical element was described: the reflection zone plate (RZP), which combines reflection, dispersion and focusing properties in one optical element and can be used in the energy range from 0.1 eV to 100 keV. Later, this optical element, the RZP, was successfully implemented into high resolution spectroscopy-setups for monochromatization [21] [22] [23] [24] [25]. Recently – using nanotechnology methods like e-beam patterning, reactive ion etching and metal coating – the production of optical elements with minimum structure periods down to 50 nm became realizable.

The RZP gratings do not have only two-dimensional groove spacing in the plane of diffraction, but also an optimized groove depth along the direction of dispersion axis is currently under development, which increases the efficiency. The RZP gratings were used for the construction of an extremely high-efficient monochromator for the femto-second spectroscopy beamline at BESSY II, which has up to 20 times higher efficiency than other optical beamline systems [25][26][27].

Moreover, a new generation of wavelength-dispersive parallel spectrometers with up to 5 times higher angular acceptance compared with traditional spectrometers was developed [28][29]. All this became possible due to rejection of multiple mirror reflections in the optical system. The new developments in X-ray optics, described in this work, are of very high importance within the development of X-ray free electron laser facilities. The unique time and spectral properties of these modern sources, in fact, do not require the abandonment of traditional optical designs, but rather an orientation towards new developments in optical elements, in order to avoid multi-element optical schemes which suffer from low output efficiency.

A comprehensive analysis of options in the alignment process, preservation of the laser's properties and the transmission onto the experiment is obligatory. Following this intention, new ideas for instrumentation and methods for XFELs are presented in this work. It is divided into 4 main chapters:

Chapter 1 is the introduction and motivation behind the design and development of new optical elements for devices meeting the demands rising from the challenging properties of state-of-the-art free-electron light sources.

Chapter 2 provides the fundamentals of X-ray optical elements. The basics of generating X-ray radiation and their properties are shown. The specific properties of modern X-ray free-electron sources are summarized as development from Synchrotron sources to FELs. A short survey over possible interaction of X-rays with matter is presented, to serve as a basis for possible experiments using these sources. Based on this, X-ray optical elements and their properties are introduced.

Chapter 3 presents X-ray optical systems for diagnostics and analysis of SASE FEL sources. Two crucial challenges on running this source are described. First, a spectrometer for commissioning of an undulator and then the alignment of a chain of undulator segments is presented. This alignment is essential to get an FEL (based on SASE-principle) into lasing-action. Secondly, as the FEL starts lasing, the determination of the entire shot-to-shot spectrum comes into play. Regarding this, different approaches in terms of commissioning as well as single-shot spectrometers have been proposed and simulated and partially compared with experimental results.

Chapter 4 consists of the presentation of two experiments using X-FEL radiation. The first project deals with spectrometry on a highly dilute solution in FEL radiation applying X-ray absorption spectroscopy (XAS). Hence, a highly transmissive RZP spectrometer is used to meet the experimental demands. It shows the development of a spectrometer for fluorescence detection at the Mn edge from the first ideas to an extensive simulation and the first experiments with this spectrometer. Furthermore, from the first experiment in 2012 ideas accrued on how to improve the efficiency of the entire setup. The upgraded setup has already been tested in a follow-up experiment at LCLS at the end of 2013. The second project is basically a case study on how to apply the gathered knowledge to a resonant inelastic X-ray spectroscopy (RIXS) experiment. An entire beamline, dedicated to highly efficient, high resolution RIXS experiments is proposed. It is capable not only of providing information about energy-loss at a very precise level, but also about momentum-transfer during the process. Considerations and simulations regarding these challenges are presented.

Within these two chapters, the characterization and diagnostics of an SASE-FEL is presented. Hereupon, an actual experiment, using an FEL source is presented and finally a prospective experimental setup as a case study is simulated and discussed.

Chapter 5 gives a résumé of the presented self-contained process from commissioning to analysis and application to actual experiments of an XFEL. It summarizes the (experimental and) simulated results and states the potential within the different projects presented as an outlook.

All the ray-tracing simulations from the single optical elements up to entire beamlines below are conducted using the in-house developed software RAY [30].

This work was done in a collaboration project of the “Helmholtz-Zentrum Berlin” with the “European X-ray Free Electron Laser GmbH” in Hamburg, Germany.

2. Fundamentals

In this chapter, the theoretical background is presented which serves as basis for the different experimental demands that should be met and will be described more in detail in chapters 3 and 4 (by simulations and experimentally).

As shown in Figure 1, visible light represents just a small fraction of the entire spectrum of electromagnetic radiation. Within this work, the spectral range of X-rays from its generation to application to cutting-edge challenging experimental setups is examined and dedicated optics is investigated.

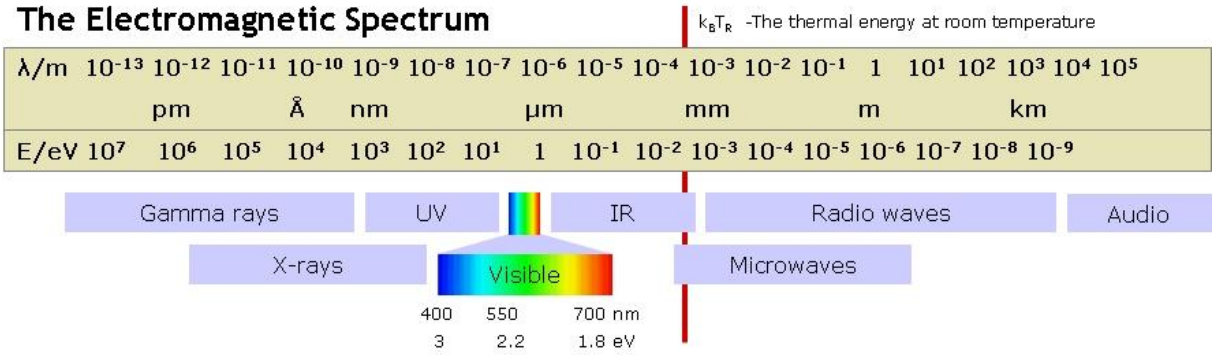

Figure 1: ***overview of the electromagnetic spectrum. (Taken from http://en.wikibooks.org)***

Radiation of lower energy up to the infrared range is mostly absorbed by matter via excitation of molecular or atomic oscillations, which then produces heat. When applying visible light (VIS), shell-electrons of molecules can be lifted to higher energy levels. The energy "stored" in this way, can be released by fluorescence radiation, chemical reactions or other non-radiative decay channels. Furthermore, ultraviolet light can even cause ionization (see photo-electric effect). Important interactions of X-rays with matter will be described more in detail within the next chapter 2.2.1.

Electromagnetic radiation has both wave and particle properties. On one hand, it shows classical wave behavior in Huygens' and Young's experiments involving diffraction and interference. On the other hand, it shows the behavior of particles for example at Crookes radiometer, also known as light mill, but also at experiments using double-slits (at which actually both properties could be shown). Mathematically, electromagnetic radiation is described by **Maxwell's equations** [31]:

1st: Gauss's Law, which means, electrical field lines diverge in presence of electrical charge. The charge is the source of the electrical field.

$$\nabla \cdot \vec{E} = \frac{\rho}{\varepsilon_0} \quad \text{with E – electrical field, } \rho \text{ – charge density.} \quad (2.1.)$$

2nd: Gauss's Law for magnetism, magnetic field lines do not diverge, the field of magnetic flux density is free of sources, and magnetic monopoles do not exist.

$$\nabla \cdot B = 0 \quad \text{with B – magnetic field.} \quad (2.2.)$$

3rd: Faraday's Law of induction: changes in the magnetic flux density lead to an electric vortex.

$$\nabla \times E = -\frac{\partial B}{\partial t}. \qquad (2.3.)$$

4th: Ampere's circuital law: electrical current leads to a magnetic vortex.

$$\nabla \times B = \mu_0\left(J + \varepsilon_0 \frac{\partial E}{\partial t} \right) \text{ with J – electric current density;} \qquad (2.4.)$$

with the universal constants ε_0 – *permittivity of free space*, and μ_0 – *permeability of free space*.

No matter if natural or artificial, electromagnetic radiation is always created by movement of charged particles or magnetic dipoles.

The quantum mechanical properties of particles will be described more detailed within sub-chapter 2.2.1 (interaction with matter), but, in general, electromagnetic radiation consists of quantums called photons. A photon has the energy E = hν (e.g. see photoelectric effect) and no mass (m_0 = 0), propagates at the speed of light c and is carrying the momentum p = hν/c = h/λ (e.g. see Compton Effect) and the angular momentum h/2π.

In the year 1895 Wilhelm Conrad Röntgen conducted several experiments using the newly discovered cathode rays. For this work he received the Nobel-prize "in recognition of the extraordinary services he has rendered by the discovery of the remarkable rays subsequently named after him" in 1901. With the idea of the X-ray tube Röntgen laid the foundation for the most common type of X-ray sources in even today's laboratories. Nowadays though, there are much larger, up to 22 orders of magnitude more brilliant X-ray sources available; without which modern research in many fields would be impossible. The evolution of these sources will be described within the subsequent chapter 2.1.

Generally, photon energies between 100 eV up to a few keV are considered as "soft" X-rays. Photon energies up to a few 100 keV are called "hard" X-rays. Since most X-ray sources are based on the acceleration of charged particles, the commonly used unit for the photon energies is electron Volt [eV]; where $1eV = e_0 \cdot 1V = 1.626176 \cdot 10^{-19} J$. The relation between the photon energy in eV and its wavelength in nm is defined by $E = \frac{hc}{\lambda}$; a conversion can easily be done by the approximation $E_{eV} = \frac{1239.85}{\lambda_{nm}}$.

2.1. Free electron X-ray sources

This section presents the development of modern large-scale X-ray sources in general – from synchrotrons to the state-of-the-art generation, the Free Electron Lasers (FELs). The common principle of these X-ray sources is the acceleration of unbound ("free") electrons to nearly the speed of light. The intensity (brilliance) of the emitted X-rays depends on the trajectory of these electrons and the adjustment of the insertion devices (see following subchapters). The properties of FELs will be described in detail within the subchapter 2.1.2. The principles described below are described more in detail in [32], [33], [34], [35], [36], [37], [38], [39] and [40].

2.1.1. Synchrotron radiation sources

In principle, at a synchrotron radiation source, relativistic electrons (or positrons) are circulating on a closed orbit. As mentioned above, accelerated charged particles emit energy in form of electromagnetic radiation. The electrons are travelling at relativistic velocity and are kept on an almost circular, polygonal track while producing synchrotron radiation – using electron optics like bending magnets, dipoles for deflecting, quadrupoles for positioning and sixtupoles for focusing the beam of electrons. In between the bending magnets, the electrons pass through wigglers or undulators, which guide them on sinusoidal curves with high concavities (small radii), causing synchrotron radiation of different energies (see below, further description of synchrotron light production). Due to the flexibility of the undulators and wigglers, this type of radiation can cover the entire range from infrared up to gamma radiation, depending on the machine parameters.

Typical electron energies of modern synchrotrons lie in the range of a few GeV, for instance BESSY II (HZB) operates at 1.7 GeV. Considering the relation between the speed of an electron and its relativistic energy given by

$$E_e = \gamma m_e c_0^2 \text{ with} \qquad (2.8.)$$

$$\gamma = \left(1-\beta^2\right)^{-\frac{1}{2}}, \qquad (2.9.)$$

$$\beta = \frac{v}{c_0} \approx 1 - \frac{1}{2\gamma^2} \qquad (2.10.)$$

and the rest mass of the electron m_e, we see that the speed of the electrons at BESSY II differs from the speed of light by only about 13.5 m/s (they travel at 99.99999995% of c).

In the classical manner, the radiation originating from an electron moving in a magnetic field is shaped in a dipole pattern (see Figure 2). Due to the Lorentz transformation, though, at a speed closer to the speed of light this pattern changes to a conical form with the emission strongly beamed along the direction of motion for an observer in rest. Its opening angle Θ_0 can be calculated according to the relativistic aberration:

$$\cos\Theta_0 = \frac{\cos\Theta_s - \frac{v}{c}}{1 - \frac{v}{c}\cos\Theta_s}, \qquad (2.11.)$$

with v – the source velocity relative to the observer and an emission angle Θ_s relative to the vector from observer to source at the time when the light is emitted.

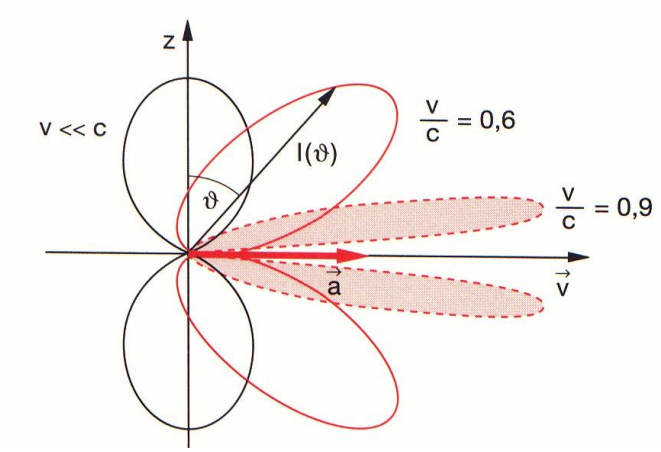

Figure 2: ***radiation pattern from a charged particle travelling at different velocities (from speed far away from speed of light – black curve – up to velocity very close to the speed of light – red curve, respectively, dashed curve around reddish area) (picture taken from: RWTH Aachen).***

Looking at this in three dimensions, Figure 3 shows the radiation pattern with respect to the orbit of movement of the charged particle:

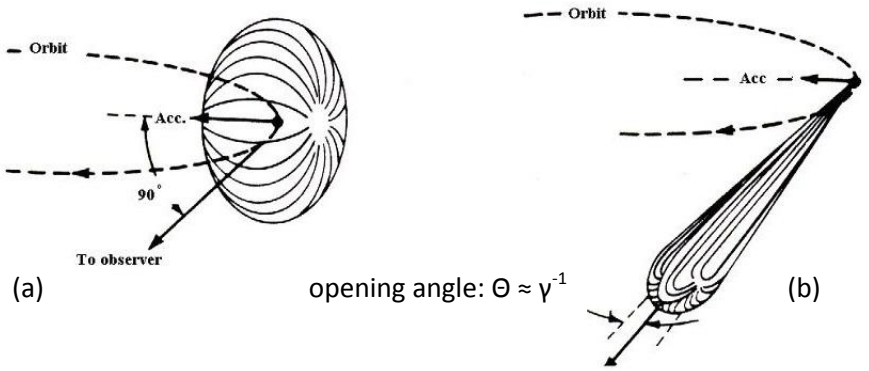

Figure 3: ***radiation pattern from a charged particle on an orbit: (a) as seen from an observer at rest in the laboratory at non-relativistic and (b) at relativistic velocity of the circulating electron (picture taken from wikipedia.org).***

Figure 4 shows schematically how the opening angle is transformed by changing the laboratory frame.

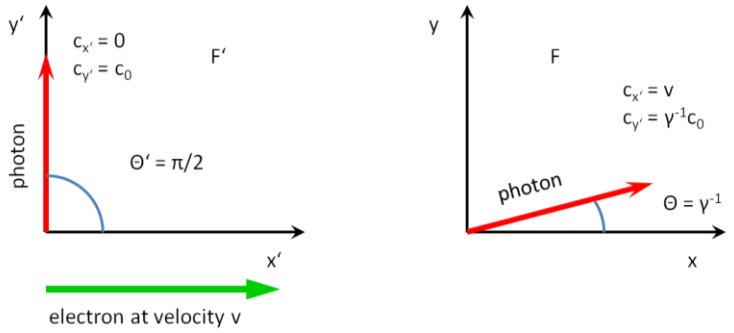

Figure 4: ***scheme of relativistic aberration: Lorentz transformation of the opening angle Θ in the frame of the electron in motion (a) and the frame of reference in rest of the observer (b), respectively. $c_{x,y}$ – speed of light, ratio in each direction.***

From that, the Lorentz transformation for the frames F' and F reads:

$$x = \gamma\left(x' + vt'\right) \qquad (2.12.)$$

$$y = y' \qquad (2.14.)$$

$$t = \gamma\left(t' + \frac{v}{c_0^2}x'\right). \qquad (2.15.)$$

Assuming x' = const. it follows that cx' = dx'/dt' = 0 and dt/dt' = γ. Hence:

$$c_x = \frac{dx}{dt} = v \qquad (2.16.)$$

$$c_y = \frac{dy}{dt} = \frac{c_{y'}}{\gamma} = \frac{c_0}{\gamma} \text{ and} \qquad (2.17.)$$

$$\tan\Theta = \frac{c_y}{c_x} = \frac{c_0}{\gamma v} = \frac{1}{\gamma\beta}. \qquad (2.18.)$$

With the BESSY II parameters γ = 3332 and β ≈ 1 from the last equation the emission angle can be approximated:

$$\tan\Theta \approx \Theta \approx \frac{1}{\gamma}. \qquad (2.19.)$$

The concentration of the emitted photons into such a small cone, caused by the relativistic aberration, is the reason for synchrotron radiation being such a powerful X-ray source. For very high relativistic electrons the radiation is concentrated in a narrow beam with high photon density.

As mentioned above, storage rings are shaped polygonal. So they consist of straight sections and bending magnets. The straight sections contain insertion devices, electron optical components and radio frequency devices/cavities. Multi-pole electron lenses are used for focusing the electron beam. The energy loss due to emission of radiation is compensated by radio frequency cavities.

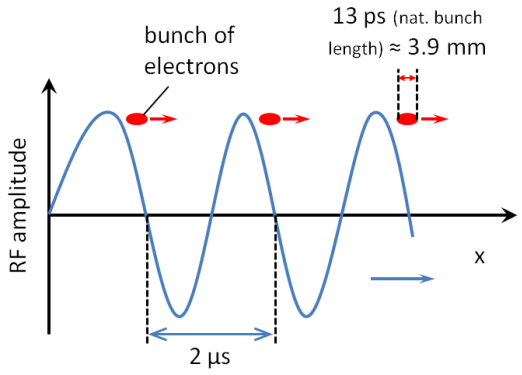

Figure 5: ***acceleration of electron bunches by a radio-frequency wave. The electron bunches with the right phase can "surf" on a wave and be thereby accelerated (parameters for BESSY II).***

Figure 5 gives an idea of how a radio wave is used to re-accelerate the electrons. “To prepare an RF cavity to accelerate particles, an RF power generator supplies an electromagnetic field. The RF cavity is molded to a specific size and shape so that electromagnetic waves become resonant and build up inside the cavity. Charged particles passing through the cavity feel the overall force and direction of the resulting electromagnetic field, which transfers energy to push them forwards along the accelerator. …the ideally timed particle, with exactly the right energy, will see zero accelerating voltage when the storage ring is at full energy. Particles with slightly different energies arriving earlier or later will be accelerated or decelerated so that they stay close to the energy of the ideal particle. In this way, the particle beam is sorted into discrete packets called “bunches”” (taken from: [41]).

The electrons at the right phase can gain energy from the radio wave just like a surfer using water waves. So to fulfill the phase condition, the electron beam consists of bunches, rather than being continuous. The maximum number of bunches storable in a ring is defined by the ratio between the circumference of the ring and the wavelength of the radio wave; the so formed bunches shape the time structure on the resulting synchrotron radiation.

The experimental demands determine the mode of running the storage ring. So it could be varied over the range from single bunch mode, providing low synchrotron flux only, but long time intervals (for example to study dynamical processes), to a permanent filling up with high photon flux (topping-up-mode).

As mentioned at the beginning of this chapter, X-ray radiation can be gained from the storage ring by three main applications: bending magnets, wigglers and undulators.

2.1.1.1. Bending magnets

Between two straight sections of the ring the electrons are kept on their track by the application of a constant, homogeneous magnetic field $\vec{\mathbf{B}}$. The radius of curvature of the trajectory of an electron within a bending magnet is smaller than the radius of the storage ring. It can be calculated considering the balance of the magnetic and the centrifugal force

$$\frac{\gamma m_e v^2}{r_{bend}} = e_0 \left| \vec{v} \times \vec{B} \right|; \qquad (2.20.)$$

with the radius of the bending curve r_{bend}, and the velocity v of the electron. So the radiation which is emitted by a bending magnet is “collimated” to an angle of emission γ^{-1} in the vertical direction (due to the aforementioned relativistic aberration), but spreads over the full angle of deviation in the horizontal plane (as shown in Figure 6).

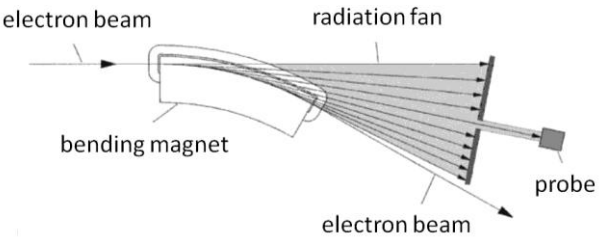

Figure 6: ***emission angle of a bending magnet, γ^{-1} due to relativistic aberration (here perpendicular to the image plane), α – opening angle "radiation fan" due to the deviation of the electron beam (picture from [42]).***

This spread of emitted radiation within the plane of the storage ring originates from the fact that the electrons travel through the entire bending magnet and release radiation from the point of entrance until the point of exit. As the electron emits radiation randomly, a broad continuous spectrum is obtained. As depicted in Figure 6, there are always huge losses of intensity, due to the inevitable slits, necessary for cutting out the part of the spectrum that is delivered to the experiment. The total duration of a flash of synchrotron radiation originating from a bending magnet can be approximated with the relation between the bending radius and the angle of emission $\Theta = \gamma^{-1}$, respectively.

$$T_{flash} \approx \frac{2r_{bend}}{3c_0\gamma^3}. \qquad (2.21.)$$

The light flashes emitted in the single bunch mode are periodic with the repetition rate, depending on the circumference of the storage ring and the speed of the electrons.

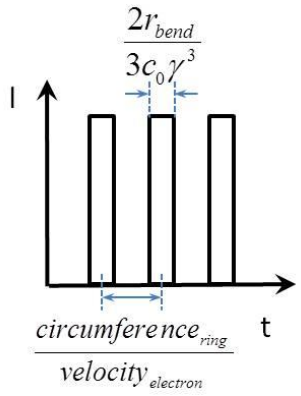

Figure 7: ***sketch of total duration of a flash originating from a bending magnet in a synchrotron ring.***

The duration of one flash of light T_{flash} equals the time of emission for a single photon; due to the fact that the probability to emit a photon stays the same over the entire trajectory from entrance to exit of the bending magnet. Hence, the frequency spectrum of a bending magnet can be obtained as the Fourier-transformation of the time structure; so, that this spectrum frames about γ^3 harmonics of a base frequency ω_0, up to a characteristic frequency ω_c:

$$\omega_0 = \frac{c_0}{r_{bend}},\ \omega_c = T_{flash}^{-1} = \frac{3c_0}{2r_{bend}}\gamma^3. \qquad (2.22.), (2.23.)$$

For an experimental purpose, radiation generated by a bending magnet is much more intense than that of any X-ray tube, of course. However, it is typically 2 orders of magnitude less brilliant than that

of a wiggler, and 5 orders of magnitude less brilliant than radiation produced by an undulator, which will be outlined in the following.

2.1.1.2. Undulators

In nowadays synchrotrons the so called insertion devices are the main application used as radiation source. This name stems from the fact that they should not affect the optics of the electron accelerator. They could be "inserted afterwards", without changing the properties of the electron beam. As seen in Figure 8, the field integral over the entire range is zero, as averaged over the duration of passing the entire device there is no action of force on the electrons. So overall, this does not influence the accelerator. These devices induce many bends of the electron paths to increase the radiation flux compared to the single bend of a bending magnet. The flux is defined as the number of photons per second at 0.1% bandwidth [1/s/0.1%BW]. They are called wigglers or undulators – depending on their purpose and construction. Both of them steer the electrons onto oscillation courses (sinusoidal). They consist of periodically arranged magnets, as shown in Figure 8.

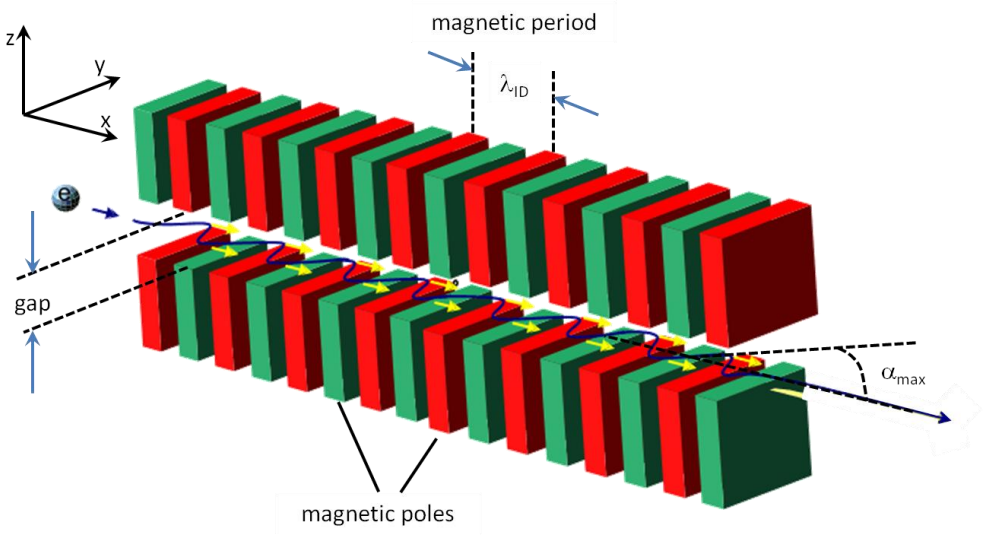

Figure 8: ***schematic chart of an insertion device and the trajectory of electrons within the device (picture adapted from wikipedia.org).***

The oscillating magnetic field $\vec{B}$ along the path of the electrons can be written as:

$$\vec{B} = \left(0,0,B_0 \sin\left(\frac{2\pi x}{\lambda_{ID}}\right)\right). \qquad (2.24.)$$

While the magnetic period (λ_{ID}) and the number of magnetic periods (N_{ID}) are fixed parameters, the maximum magnetic field B_0 as seen by the electrons can be slightly varied by changing the gap between the two rows of magnets. So the motion of the electrons within the x-y-plane is then given by

$$\begin{pmatrix} m_e\gamma\dfrac{d^2x}{dt^2} \\ m_e\gamma\dfrac{d^2y}{dt^2} \end{pmatrix} = \begin{pmatrix} +e_0\dfrac{dy}{dt}B_0\sin\left(\dfrac{2\pi x}{\lambda_{ID}}\right) \\ -e_0\dfrac{dx}{dt}B_0\sin\left(\dfrac{2\pi x}{\lambda_{ID}}\right) \end{pmatrix}. \quad (2.25.)$$

The trajectory of the electrons is modulated in both x- and y-direction, respectively. So an observer travelling at the speed of the electrons would see a movement of the electrons in the x-y-plane which looks more like "8-shaped". This would change for the same observer within a very weak magnetic field, as it would become purely sinusoidal; but, with increasing magnetic field the sinusoid gets more and more distorted, which gives rise then to higher harmonics.

Thus, for weak magnetic fields, corresponding to small transversal movements, the coupling of the movements in both directions could be neglected. So we assume that the electron velocity along the x-direction is given by $v = \beta c_0$. Using

$$\frac{dy}{dt} = \frac{dy}{dx}\frac{dx}{dt} = \beta c_0\frac{dy}{dx} \quad (2.26.)$$

$$\Rightarrow \frac{d^2y}{dt^2} = (\beta c_0)^2\frac{d^2y}{dx^2} \quad (2.27.)$$

and $\beta\gamma \approx \gamma$ (2.28.)

the motion in y-direction can then be integrated as:

$$\frac{dy}{dx} = \frac{K}{\gamma}\cos\left(\frac{2\pi x}{\lambda_{ID}}\right) = \tan\alpha \approx \alpha \quad (2.29.)$$

$$y(x) = \frac{K}{\gamma}\frac{\lambda_{ID}}{2\pi m_e}\sin\left(\frac{2\pi x}{\lambda_{ID}}\right) \text{ with} \quad (2.30.)$$

$$K = \frac{e_0 B_0 \lambda_{ID}}{2\pi m_e c_0} = 0.934 \cdot B_0[T] \cdot \lambda_{ID}[cm]. \quad (2.31.)$$

Depending on the amplitude of the magnetic field and period length, the maximum possible deflection of the electron beam is $\alpha_{max} = K/\gamma$. The K-parameter describes the optical properties of the insertion device, it has no dimension. The undulator regime is characterized by a maximum angle of deviation (α_{max}) of the same order or smaller than the angle of the emission cone (γ^{-1}). So for an undulator in general the relation [43]:

$$\alpha_{\max} \le \frac{1}{\gamma} \Leftrightarrow K \le 1 \text{ applies.} \quad (2.32.)$$

Assuming this relation, the cones of the emitted radiation overlap and it is impossible to determine at which magnet inside the undulator a specific X-ray photon is generated. So the quantum-mechanical probability for the emission of a photon in the undulator is given by the modulus square of all probability amplitudes to emit a photon at each magnet. This sum contains interferences, so

that the intensity of the emitted radiation is proportional to N_{ID}^2 and the emitted spectrum can be described by

$$\lambda_j = \frac{\lambda_{ID}}{2\gamma^2 j}\left(1+\frac{K^2}{2}+\gamma^2\Theta^2\right)$$ with j = 1, 2, 3,…, and Θ = vertical angle of observation.

From that can be derived that

$$E_j[keV] = \frac{0.95E_e^2[GeV]}{\lambda_{ID}[cm]}\, j\left(1+\frac{K^2}{2}+\gamma^2\Theta^2\right)^{-1}. \quad (2.33.)$$

(Formulae and deduction as well as a more precise description can be found in section 2, Kwang-Je Kim in [44] and at [43]). The highest possible energies are always observed on the x-axis, where Θ = 0. $\gamma^2\Theta^2$ provides a sharp edge at high energy and a continuous foothill at lower energies; for that reason, as first optical element behind an undulator mostly pinholes or slits are installed.

Even and odd harmonics appear due to the acceleration of the electrons along the x-axis and y-axis, respectively. So the even harmonics (at j = 2, 4, 6 …) are radially emitted from the electron beam and produce only weak radiation intensities. Odd harmonics on the other hand are emitted along the electron beam; they produce high radiation intensities. Due to interference the angular divergence σ_Θ of the odd harmonics is smaller than the cone γ^{-1} of a single emission:

$$\sigma_\Theta = \frac{1}{\gamma}\sqrt{\frac{3}{4\pi}\left(\frac{1+\frac{K^2}{2}}{jN_{ID}}\right)}. \quad (2.34.)$$

The width of a single odd harmonic in the energy spectrum along the emission axis is given by:

$$\frac{\Delta E_j}{E_j} = \frac{\Delta\lambda_j}{\lambda_j} = \frac{1}{jN_{ID}} \approx 10^{-2}. \quad (2.35.)$$

A **wiggler** now on the other hand, is an insertion device similar to the undulator, but with a stronger magnetic field, and the angle of maximum deviation α_{max} is much larger than the emission cone:

$$\alpha_{max} >> \frac{1}{\gamma} \Leftrightarrow K >> 1. \quad (2.36.)$$

From this property it follows that it is even possible (in principle) to determine exactly at which magnet within the wiggler the emission of a specific X-ray photon occurs. Therefore, the quantum-mechanical probability of the emission of a photon in the wiggler is given by the sum over the squared probability amplitudes to emit a photon at each magnet. This sum does not contain interference terms; the intensities of each magnetic pole have to be summarized to obtain the total emission intensity of the wiggler. Hence, a wiggler emits a spectrum very similar to that of a bending magnet, with an intensity of the emitted radiation proportional to $2N_{ID}$. The emission cone has a vertical opening angle of γ^{-1}, similar to a bending magnet, and a horizontal opening angle of $2K/\gamma$.

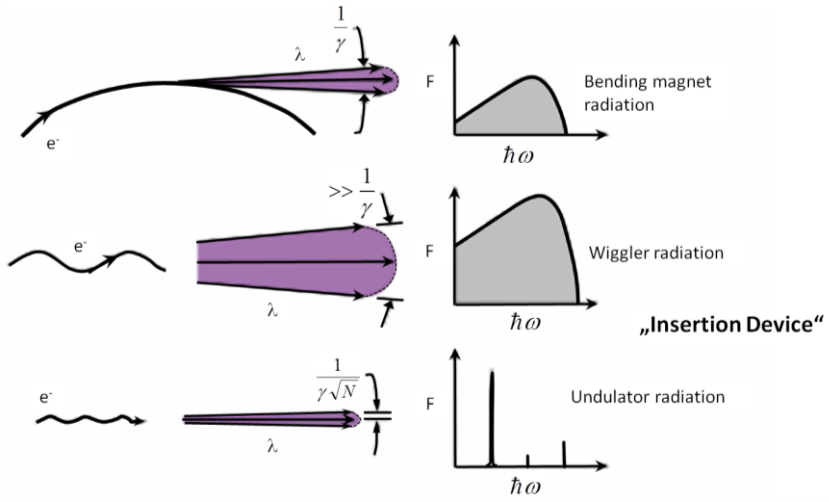

Figure 9: ***radiation emitted by different "decoupling devices"; top: bending magnet, center: wiggler, bottom: undulator (picture taken from [45]).***

The brilliance of X-ray sources – which is a parameter that reveals the number of photons per second, per mrad^2 of the solid angle and per mm^2 of the area within 0.1% of the bandwidth, $\frac{photons}{s \cdot mrad^2 \cdot mm^2 \cdot 0.1\%BW}$ – has dramatically increased over the last 50 years. Its unit is called "Schwinger" (Sch).

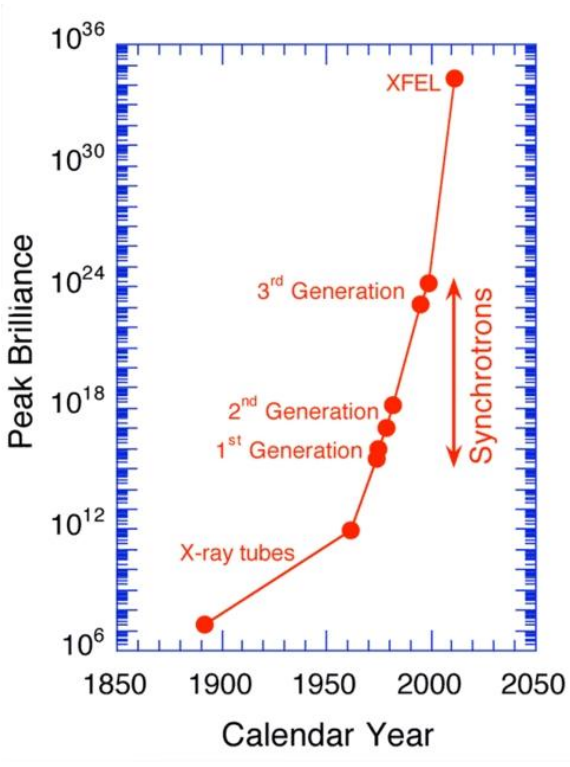

Figure 10: ***brilliances survey; left: peak brilliance evolution over years (picture taken from [46] and [47]).***

Whereas the brilliance of X-ray tubes barely exceeds 10^8 Sch, 1st and 2nd generation synchrotron sources reach around 10^{17} to 10^{20} Sch. X-ray FELs have increased or will increase further by a few orders of magnitude, resulting in 10^{22}-10^{26} Sch in average. Even up to 10^{34} Sch are expected in the peak brilliances of the newest machines. These high brilliances and closely related very high

intensities pose problems for the first optical elements and for some of the samples. So, great caution has to be taken while designing experiments and beamlines for such outstanding photon densities. As this work is strongly related to XFELs specifically, this kind of source will be presented within the next subchapter.

2.1.1.3. polarization

Another key feature of synchrotron radiation is its polarization. By manipulating the magnetic field of undulators and wigglers, any polarization could be generated, linear, elliptical or circular. This is another big advantage over other X-ray sources. The polarization of electromagnetic waves can be described by several different formalisms; in most of the synchrotron radiation literature the "Stokes parameters" developed 1852 by George Gabriel Stokes (1819 – 1903) are used. They are derived from the polarization expressed via the relationship between the two orthogonal components of the electric field:

$$E_x = E_{x0}\cos(\omega t) \qquad (2.37.)$$

$$E_y = E_{y0}\cos(\omega t + \delta). \qquad (2.38.)$$

These two equations contain three independent parameters, the two field amplitudes E_{x0} and E_{y0} as well as the phase difference δ, ω - frequency. If there is 0 phase difference, then the light is linearly polarized (the angle is then given by the relative field amplitudes). In case of a phase difference of $\pi/2$ and if E_{x0} equals E_{y0}, the light is circularly polarized. However, as these quantities are not directly measureable, Stokes created a formalism, which is based upon real observables, the Stokes parameters. The intensity can be measured for different directions of polarization; linear perpendicular is represented by intensities in x- and y-direction, I_x and I_y, respectively, linear skew parts by $I_{45°}$ and $I_{135°}$, circular by I_R (clockwise) and I_L (counter-clockwise). They are defined as:

$$S_0 = I_x + I_y = I_{45°} + I_{135°} = I_R + I_L = \left\langle E_x^2 + E_y^2 \right\rangle \qquad (2.39.)$$

$$S_1 = I_x - I_y = \left\langle E_x^2 - E_y^2 \right\rangle \qquad (2.40.)$$

$$S_2 = I_{45°} - I_{135°} = \left\langle 2E_xE_y\cos\delta \right\rangle \qquad (2.41.)$$

$$S_3 = I_R - I_L = \left\langle 2E_xE_y\sin\delta \right\rangle. \qquad (2.42.)$$

So these intensities are the measured after the light has passed an ideal polarizer for horizontally (0°), vertically (90°), 45° and 135° oriented as well as circularly (right and left) polarized light. Generally, the Stokes parameters are normalized on the incoming intensity by the division by S_0; used as vector components they are called the normalized Stokes-vector:

$$\overrightarrow{S_N} = \frac{1}{S_0}\begin{pmatrix} S_0 \\ S_1 \\ S_2 \\ S_3 \end{pmatrix}.$$

The basic polarization (boundary) states of light emitted from any source are shown in Figure 11:

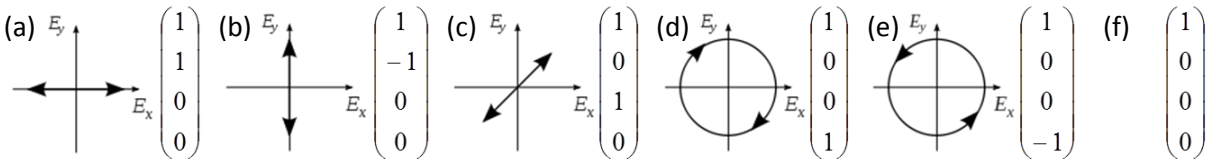

Figure 11: ***possible polarization states with respective Stokes-vectors; (a): linear-horizontally, (b): linear-vertically, (c): linear 45°, (d): circularly-clockwise, (e): circularly-counter-clockwise, (f): unpolarized.***

The polarization rates P1, P2 and P3 are given by:

$$P_1 = S_1/S_0 \;,\; P_2 = S_2/S_0 \;,\; P_3 = S_3/S_0$$

They are dimensionless and lie between -1 and 1, with the total polarization rate $\sqrt{P_1^2 + P_2^2 + P_3^2}$, or, for linearly polarized light, $\sqrt{P_1^2 + P_2^2}$, respectively.

Totally polarized light means that $S_0^2 = S_1^2 + S_2^2 + S_3^2$; totally unpolarized means that $S_1 = S_2 = S_3 = 0$, but $S_0 \neq 0$.

However, in an undulator the permanent magnets are used to induce different periodic electron trajectories through the entire device. Oscillations confined to a plane lead to linear polarization of the radiation; so if the trajectory is helical, the radiation will be circularly polarized (the right- or left-handedness will then be determined by this helix).

Regarding all considerations above, the properties of synchrotron radiation can be summarized as follows:

- It provides a very broad continuous range of electromagnetic radiation, from terahertz over infrared (IR), visible light (VIS), ultraviolet (UV), up to the hard X-ray range.
- It has a very high Intensity, compared to other radiation sources.
- It is emitted tangentially to the direction of motion of the particles.
- Depending on the electron beam quality, it provides high Brilliance.
- It is pulsed; the frequency and duration are selectable (within certain ranges).
- It is polarized; possible is both linearly and circularly as extreme cases of all intermediate elliptical polarizations.

2.1.2. European X-ray Free Electron Laser

Free Electron Lasers are the 4th generation of X-ray radiation sources. They are the logical evolution of synchrotrons, as they provide advanced radiation properties, exceeding that of synchrotrons by orders of magnitude, in terms of intensity/flux, brilliance, coherence and pulse length. There are 23 Free Electron Lasers currently operating worldwide; another 11 are under construction with an additional 7 proposed (all numbers from [48]). In Hamburg, Germany a very powerful X-ray free electron Laser is under construction, the European XFEL. It is planned to generate X-ray flashes at 27

kHz with a peak brilliance of 5 x 10^{33} Schwinger (the average brilliance will be in the range of 10^{25}) at pulse durations of less than 100 femtoseconds. The total length of the machine will have a very impressive value of 3.4 kilometers. Its working principle, properties and requirements on X-ray optics applied will be described within the next subchapters.

The electrons which produce the light within this laser, are free, not bound to atoms, as in conventional lasers (solid-, gas-, liquid-based), hence the name. The idea of an FEL was proposed the first time in 1971 by John M. J. Madey. The idea of the SASE-principle was discussed for the first time in 1984 by Anatoli M. Kondratenko and Evgeni L. Saldin and elaborated in detail by Rodolfo Bonifacio, Claudio Pellegrini and their coworkers.

2.1.2.1. The SASE principle

The working principle of an undulator was described within the precedent subchapter concerning synchrotron/X-ray radiation produced from different kinds of sources. So in principle the highly intense X-ray laser flashes are produced within a long undulator as well. In an FEL though, the electrons are accompanied by a beam or flash of light. If this light matches the undulator radiation wavelength, the electrons emit radiation in phase, which results in much more intense light (by several orders of magnitude) than at a synchrotron source. The electrons actually interact with the light.

At the frontend of the undulator all electrons possess the same (kinetic) energy. As mentioned before, this changes, if they interact with the waves of light accompanying them. For any charge, this light wave is “simply” an electromagnetic field, from which they can gain or release energy. Generally, within an undulator at a constant magnetic field, each single electron energy results in a certain trajectory; the higher the energy, the “flatter” the radii of curvature (the smaller the amplitude, see Figure 12).

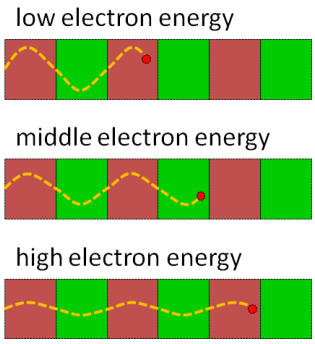

Figure 12: ***accelerated electrons of different energies travel on different trajectories within a certain magnetic field (note, the electrons of each energy, depicted by red “balls”, started at the same time) (picture adapted from www.desy.de).***

The exchange of energy with the field actually changes the trajectory of the electrons. This effects that some particles are decelerated, others get accelerated. The effect of the so called **Microbunching** appears. Assuming the same energy for the incoming electrons, the electrons are travelling at a certain trajectory at appropriate corresponding velocity. The electrons are slightly slower than the speed of light. The velocity of the electrons and the magnetic field now are set up and aligned such that the particles are back at the same situation after two changes of direction. They drop back by exactly the amount of one wavelength of the undulator radiation (with respect to

the faster propagating light wave). Due to the periodicity of waves, the particles are in the same situation as before in the sense that electrons which gained energy before, gain again even more. Electrons which have lost energy before continue losing at that point. This effect happens until all electrons are "shifted" into regions (relatively), where there is no energy exchange anymore. The light arranges the moving electrons into little groups. The distance between these groups is exactly corresponding to the wavelength of the undulator radiation. As groups, the electrons emit undulator radiation like before, no more or less; but within the described microbunches they emit almost exactly at the same time. The emitted light waves are perfectly superposed. Moreover, the distance between the microbunches causes perfect addition of the radiation along the undulator. This is what leads to coherent superposition, leading to very high intensities.

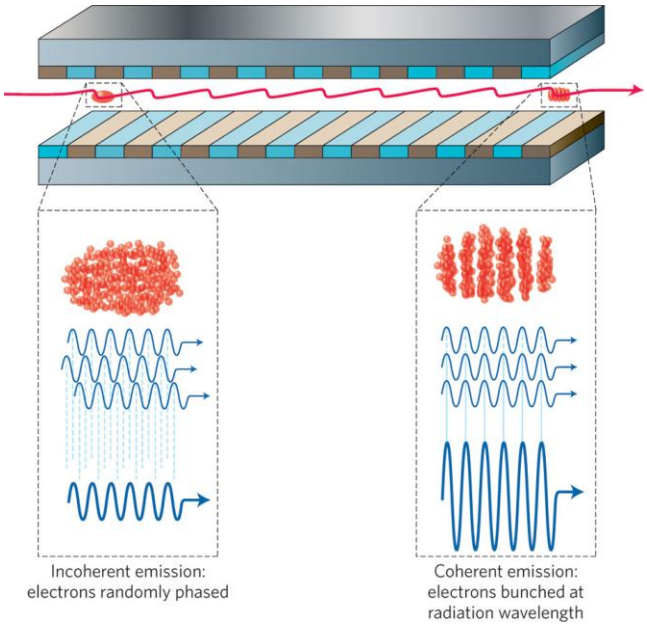

Figure 13: ***microbunching: electrons enter the undulator initially at random phases. Mostly incoherent radiation is emitted at the resonant radiation wavelength. Due to interaction with the undulator radiation sorting into bunches takes part. This collective process continues until the electrons are strongly bunched towards the end of the undulator (on the right), where the process saturates and the electrons begin to de-bunch (picture taken from [49]).***

To initiate this whole process, the FEL needs at least a flash of light at the right wavelength, capable of arranging the electrons. There are two options to produce this flash: one is to use an external light source (so called "seeded FEL"); the other one is to use the light, which is produced spontaneously (from the undulating electrons themselves). This effect is called **Self Amplified Spontaneous Emission (SASE)** (see Figure 13 as well). Hence, the initial light pulse has to be produced at the frontend of the undulator. It cannot be reflected back like in conventional VIS optical resonators or lasers and in this way pass through the FEL several times (as a cavity containing the laser-medium at VIS) – simply because there are no mirrors for such a high energetic X-ray radiation. So the entire amplification needs to happen sufficiently within one single pass through the undulator. This requires very long undulator lengths – the European XFEL will have an undulator length of about 200 m in total at "SASE 1" and "SASE 2" (which are the branches planned for generation of hard X-ray radiation), and about 136 m at "SASE 3" (branch planned for the soft X-ray radiation).

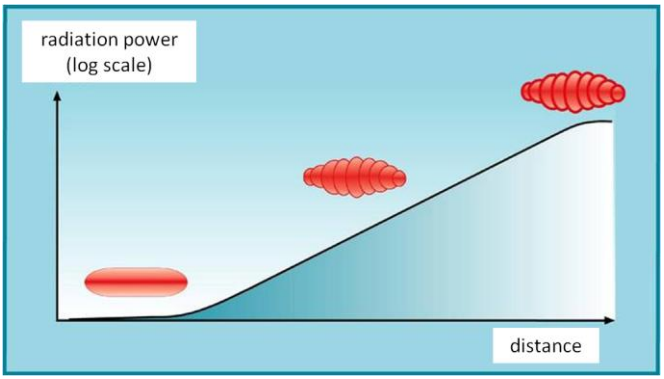

Figure 14: ***microbunching at SASE effect. The more the electrons are perfectly arranged within the micro bunches, the higher the emitted radiation power (picture taken from [50]).***

The undulator needs to have the ideal length; otherwise, if it is too long, a saturation of the microbunching effect happens. This then leads to less radiation power than possible at the perfect length. In summary, the electrons carry initially energy slightly higher than resonance with the undulator field; by energy transfer to the radiation field, the electrons finally get off resonance condition, which is at the point of saturation.

2.1.2.2. Particular properties of FEL radiation

The properties of an undulator, which were described within the previous chapter 2.1.2, apply of course for the undulator of an FEL. As described above, the process of microbunching arises after a certain distance of undulator. The undulator of the European XFEL, of SASE 1 (and SASE 2), will have a total length of about 200 m (33 undulator segments of 5 m length, each followed up by an intersection of 1.1 m length for reshaping and refocusing of the electron beam – total magnetic length of 165 m); SASE 3 will be 136 m long (containing 21 undulator segments and additional intersections). From this length and the process of creating the lasing results the **very small divergence** of the emitted X-ray radiation. Most of the radiation emitted by the electrons is not directed along the undulator and gets either wasted within the walls or will not be amplified by the microbunching effect. Of course, the strictest demand on the photons to contribute to this process is that they need to stay within the electron beam, otherwise that simply cannot interact with the electrons. This is a similarity to "conventional" laser systems (consisting of two reflective surfaces and an active medium); here the amplification happens mostly in the ideal direction of motion perpendicular to the mirrors at each end of the laser active medium.

The low divergence implies that $\Theta \approx \frac{1}{\gamma}$ tends to zero; this means γ tends to very high values. The aforementioned relation

$$T_{flash} \approx \frac{2r_{bend}}{3c_0\gamma^3} \qquad \text{(see 2.21.)}$$

now results that, if γ tends towards infinity, the time of the emitted flash T_{flash} tends to very small values, meaning **pulse durations in the range of picoseconds to femtoseconds at the European XFEL**.

Almost all the energy of the electrons is transferred into the "desired" energy by the microbunching effect (until their energy drops down below resonance). In the ideal case, the electrons are perfectly arranged within the bunches, which leads to the **very high power (around 100GW/pulse) and brilliance (10^{34} peak brilliance)** of the FELs.

The microbunching leads to highly coherent radiation. During this process the electrons ideally emit at exactly the same time (at a spatial distance matching exactly the wavelength of the undulator radiation), resulting in **high spatial or transversal coherence** of the flashes of light. The most intense radiation arises at the point of perfect microbunching, ideally right at the end of the undulator.

Unfortunately, these properties only apply for the ideal case. There are different factors reducing the beam quality (or properties of the emitted radiation) from SASE generated FEL-radiation.

First of all, the use of spontaneous radiation at the beginning of the undulator is a source of imprecision. As the term "spontaneous" implies, the source point for this initiating flash is not definite and influences the location of the ideal microbunching as well. Hence, the saturation point can be at different positions, each for a different starting point of the initial flash. This means, the source point of the entire device is not stable, which could then become an issue for the experimental demands. Another consequence of the spontaneous emission is temporal spiking (see below, Figure 16). Within those spikes the light is of very high longitudinal coherence, but in general, SASE-generated FEL-light is not very highly longitudinal coherent.

Secondly, the emitted energies spread a little around the center energy from pulse to pulse. Shot noise from random fluctuations within the electric current and within the photons emitted by the electrons lead to fluctuations within the spectrum of the resulting light pulses.

A third source of instability and non-uniformity within the spectrum and actual point of impact of the generated beam is the fact that the large undulator length is only "artificial" or rather "simulated", just an approximation of the real case. The real machine consists of several undulator segments divided by intersections. In these intersections, the electron beam has to be reshaped, as the electrons start to spread while losing energy.

2.1.2.3. Specific requirements on FEL optics

The above mentioned particular properties of FEL radiation lead to certain requirements concerning the spectrometers for different purposes of using FEL radiation. The high coherence, high intensity, high brilliance and the small divergence should be preserved as good as possible. Having such an exceptional X-ray source inevitably gives rise to very high demands on the optics used, concerning the conservation of these properties.

The quality of these properties could suffer from multiple scattering on many surfaces of numerous optical elements. So, in general, it makes sense to minimize the number of optical elements within a beamline as well as in an experimental setup. Additionally, every optical element absorbs a very high

percentage of the photons passing it, with only a fractional amount reaching the actual experiment. However, most experiments require high power at certain energies; hence, the optical element must meet these demands. An example of such an optical element will be shown below at an actual experimental setup which was designed, conducted and afterwards improved for a subsequent experiment (PS-II experiment, conducted at LCLS).

The energy and power distribution during a single shot within the SASE-resulting spectrum could vary from shot to shot – typical SASE-FEL single shot spectra are shown in Figure 15:

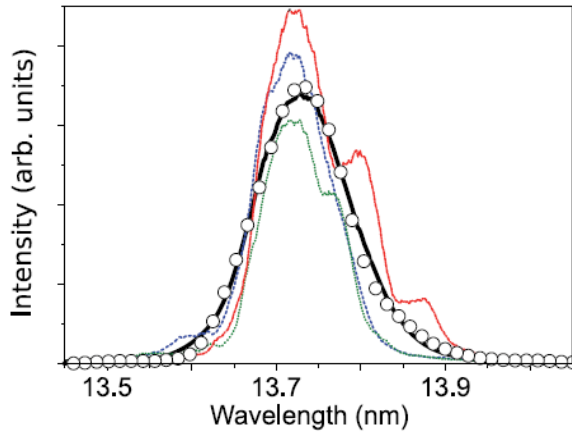

Figure 15: ***typical SASE spectral distribution of a few shots (taken from [51])***

Yet, in order to conduct experiments, one needs to know the exact spectral distribution of the delivered radiation. Without sufficient knowledge about the actual energy transferred into an experimental setup, the results could be falsified. This means, the information about the spectral distribution has to be provided in situ, during the experiments. An appropriate project will be presented below (high-resolution single-shot spectrometer proposed for the European XFEL). Only this way the data coming out of measurements can be interpreted properly. Some experiments demand in particular a very clear energy peak at a certain value, as they are performed in order to detect weak spectral changes of vibrational state levels (regarding that demand, later in this work a proposed beamline for RIXS is shown).

Furthermore, the applied optics must preserve the time structure of the X-ray pulses, or at least not influence it more than to an absolutely minimal level.

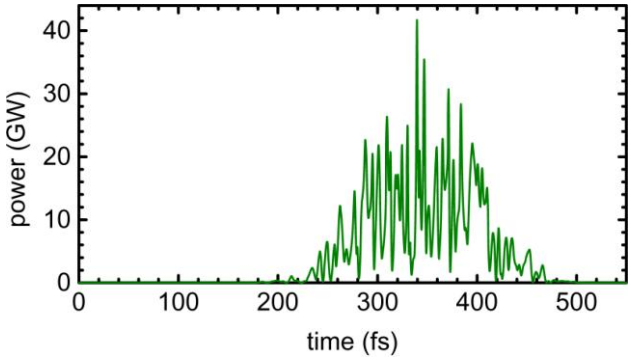

Figure 16: ***time distribution of a single shot – spiking appears (taken from: [52]).***

Figure 16 shows what the power distribution within a single shot of around 300 fs could look like. Here, the above mentioned spiking appears. Additionally, the high repetition rate (so far planned to be in the order of 27 kHz) should not be destroyed by coalescence of the single shots. Moreover, there are always time delays within a light pulse passing one of the X-ray optical elements, meaning that the part of the light wave hitting the front part of the optics is of course temporally shifted with respect to the part hitting the rear part – increased by the fact that these optical elements are mostly used under grazing angles of incidence (see chapter 2.2). This could considerably influence the property of temporal coherence. The time structure (single bunch, multiple bunches…) can be worsened as well.

In addition, as described in another proposed scheme below (K-Monochromator, applied at the European XFEL), the optics could meet the demand of conserving the spatial structure or rather the distribution of the light emitted from the X-ray source.

Eventually, one needs to consider preserving the optical elements themselves as well. The very high intensities mentioned above, especially the peak intensities in very short pulses, could destroy the surfaces of the optical elements. So one needs to reflect about this carefully, if the optical elements should be applied for example only for certain ranges of energy, or where (literally locally) they should be placed; or if they should be covered with any kind of coatings or even shielding. Everything means constantly finding a compromise between the actual optical demands and technically contrivable opportunities.

Conclusion:

A new generation of free electron sources with improved properties demands new optical elements for light handling. These optical elements must be capable of providing a high energy resolution as well as of allowing ultra-high time resolved measurements. They also need to survive the ultra-high power of the FEL radiation up to 100 GW per pulse. Furthermore, the optical elements have to be able to preserve as much as possible of the unique characteristics of the FEL. In particular their high brilliance and coherence should be transmitted loss-free to the samples. For the alignment of the FEL as well as for experimental applications in spectrometers or other analytical tools, such new and powerful optical elements are highly required.

2.2. X-ray Optics for Free-Electron Sources – basic principles

This chapter summarizes different interactions of X-rays with matter. This is not only intended for experimental purposes, but as well the working principle of optics applied to influence X-rays is based on these interactions. Hence, optical elements and its basic principles are presented here. The principles described below can be found more in detail at [53], [54], [55], [56].

2.2.1. Interaction of X-rays with matter

Photons can interact with the core or an atomic shell of an absorber. As they do not possess an electrical charge, they are not subject to Coulomb's force, but rather transfer energy by direct collisions mostly with electrons. The energy of a photon which does not collide remains constant. X-rays, as well as γ-rays, are among indirect ionizing radiation. As the interaction of photons with

matter has a very low probability, compared to charged particles, this type of radiation is very pervading with an exponential attenuation within the absorbing matter.

Rayleigh scattering – the effect, which is well known for causing the sky's blue color appearance – occurs when the X-ray photon interacts with the whole atom so that the photon is scattered without any energy transfer.

To provide evidence of ionizing radiation, there are mainly 3 effects which play a role: the Compton scattering, the photoelectric effect and pair production.

The first possible main interaction is elastic collision of the photon with an electron, the **Compton effect** (or incoherent scattering). At photons of higher energies (between 100 keV up to around 10 MeV) only a part of their energy is used for the excavation of an electron. On the contrary to the photoelectric effect (shown below), the photon remains, but changes its direction of motion and releases a certain amount of energy to the separated electron. This effect mostly happens at the outermost, weakly bound electrons from the shell of the absorber. The wavelength λ_C is called Compton wavelength and is characteristic for a massive particles (as electrons). It is the value of increase of the perpendicularly scattered photon. The Compton wavelength of an electron for example is approximately 2.43×10^{-12}m (picometers). The probability of appearance of Compton scattering is simply reciprocally proportional to the photon energy.

Photoelectric absorption of X-rays occurs when the X-ray photon is absorbed resulting in the ejection of electrons from the atom – resulting in the ionization of the atom. Subsequently, the ionized atom returns to the neutral state by emission of an X-ray characteristic for the atom. Its energy is then split into three parts: the energy needed to overcome the electronic binding energy as well as the potential difference between the solid and the vacuum outside and the kinetic energy of the ejected electron. Hence, there is a threshold energy (work function plus binding energy) – depending on the properties of the solid – below which this effect cannot take place. This effect is the so-called **photoelectric effect**.

The **electron pair production** describes the conversion of electromagnetic radiation into matter. At even higher X-ray photon energies (sometimes already defined as gamma radiation) this effect dominates. Here a photon interacts with the electrical field of the atomic core and decays into an electron-positron pair. The threshold for this effect is set by the sum of masses of the two particles (1.022 MeV). Energies higher than that are distributed into the kinetic energies of the electron and positron. The core stays unchanged during this process. It serves only as buffer for the law of conservation of energy (and momentum) during the creation of matter-antimatter.

If the hole left behind from a photo electron is filled by an electron from a higher shell, the energy difference between the two shells is either transferred into characteristic photon radiation or to another electron from the same atom. This process is called **Auger-effect**. The emittance of characteristic photons competes with the Auger effect; for lighter elements, the Auger effect is predominant.

Moreover, photons can interact with the electromagnetic fields of nucleons. The energy of the incident photon is absorbed from the core and hence the core is lifted to a level of excitation. If the excitation energy exceeds the threshold for the release of a nucleon (the bonding energy of it), the

emission of a neutron or proton is possible. This threshold for the most elements lies between 6 and 20 MeV. Analogically this is called **photonuclear reaction**.

Probability of occurrence

The probability of all types of possible interactions depends on the photon energy of the irradiating photon and the atomic number of the absorber in a complex manner. The different areas, where interaction processes each are predominant, are sketched in Figure 17.

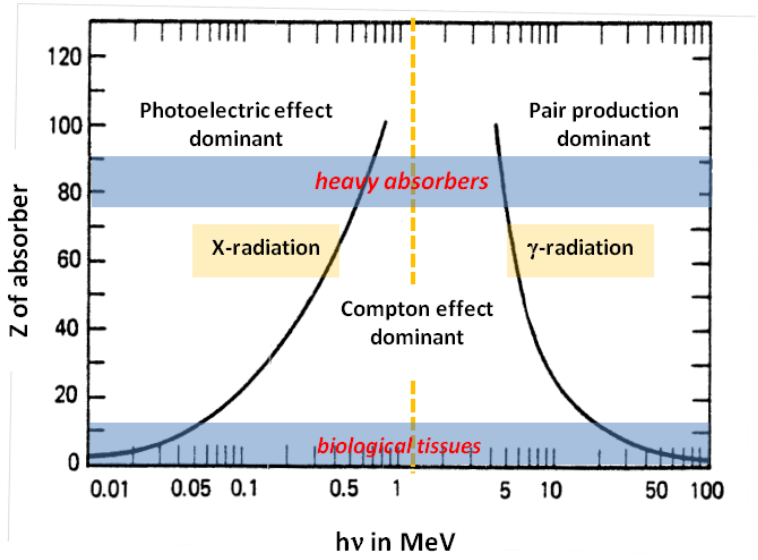

Figure 17: ***Area diagram of the probability of interaction of photons (dashed line at 1.24 MeV marks the approximate border between X-rays and γ–radiation).***

Absorbers are used for technical (e.g. shielding) or experimental applications as Tungsten (atomic number 74), Plumb (82) or Uranium (92); for example absorbers of medical interest are of very low atomic numbers (e.g. Nitrogen, 7; Oxygen, 8). For heavy absorbers at photon energies up to around 500-700 keV the photoelectric effect is dominating. So the most important materials for shielding operate mostly due to photo absorption, which is advantageous in terms of the nonexistent photon scattering. But it produces still characteristic X-ray radiation. The Compton Effect is predominant for a wide range of elements of low atomic numbers below 10. As mentioned before, the pair production takes not place up to photon energies close to 1.022 MeV. Above photon energies around 25 Mev and atomic numbers larger than 20 it is the predominating process.

2.2.1.1. Attenuation

As photons are neither charge-carrying nor massive, their general interaction with matter is very low. The amount of ion pairs, which are produced in a certain way, is just a few percent of the amount produced by β-radiation for example. During the passage of a photon of 1 MeV just around 1 ion pair is produced per cm in air. Resulting from that very low specific ionization, the total ionization is rather of secondary rank. On the contrary to heavier particles for example, which lose their energy

usually via several collisions, photons are mostly stopped by just one (or very few). If we have a short quantitative look at the attenuation, the particle rate can be written as

$$N = \frac{particlenumber}{time} = \frac{\Delta n}{\Delta t} \qquad (2.50.)$$

and the intensity

$$I = \frac{energy}{area \cdot time} = \frac{E}{\Delta A \cdot \Delta t}, \text{ respectively.} \qquad (2.51.)$$

At mono-energetic radiation E = Δn x E_{photon}, we obtain

$$I = \frac{E_{photon} \cdot \Delta n}{\Delta A \cdot \Delta t} = \frac{E_{photon}}{\Delta A} \cdot N, \qquad (2.52.)$$

which gives us a direct proportional relation between the intensity and the particle rate $I \propto N$.

Hence, for the intensity of a narrow mono-energetic ray of photons we obtain (after passing a homogeneous absorber of thickness dx) the Beer-Lambert law of absorption (assuming $dN = -\mu \cdot N \cdot dx$):

$$\begin{aligned} &\Rightarrow N(x) = N_0 \cdot e^{-\mu \cdot x}, \\ &\Rightarrow I(x) = I_0 \cdot e^{-\mu \cdot x} \end{aligned} \qquad (2.53.)$$

With the linear coefficient of attenuation (dimension cm^{-1}) μ, which is the sum of all the partial coefficients of attenuation $\mu_{total} = \tau_{photo} + \sigma_{coherent} + \sigma_{Compton} + \chi_{pair\text{-}core} + \chi_{pair\text{-}electron} + \kappa_{photonuclear}$.

At a fixed energy we can generally assume (Z – probability of appearance of process):

$$\begin{aligned} &dN = -\mu(x, y, E_{photon}, \rho, Z) \cdot N \cdot dx \\ &\Leftrightarrow \frac{dN}{N} = -\mu \cdot dx \\ &\Leftrightarrow \int_{N_0}^{N} \frac{1}{N} dN = -\int_0^x \mu \cdot dx \\ &\Leftrightarrow \ln\left(\frac{N}{N_0}\right) = -\int_0^x \mu \cdot dx \\ &\Leftrightarrow N = N_0 \cdot \exp\left(-\int_0^x \mu \cdot dx\right) \end{aligned}$$

From which the intensity can be derived as:

$$\Rightarrow I(x) = I_0 \cdot e^{\left(-\int_0^x \mu \cdot dx\right)}. \qquad (2.54.)$$

In general, the coefficients for photonuclear effects and pair production are negligible. A factor, which describes the depth of photons travelling within a material, is the so called mean free path λ:

$$\lambda = \frac{\int_0^\infty x e^{-\mu x} dx}{\int_0^\infty e^{-\mu x} dx} = \frac{1}{\mu}. \qquad (2.55.)$$

(After passing through the length of x, the original intensity is decreased by a factor of 1/e.) To account for the fact that different materials have different densities, very often instead of the linear coefficient of absorption its division by the density ρ of the absorber is used, the so called **mass attenuation coefficient μ' = μ/ρ** [cm^2/g]. It can be derived from the mass attenuation coefficients of the different elements of an absorber and the respective percentage contained within a material. The following Figure 18 shows the mass attenuation coefficient as a survey for lead (atomic no.82):

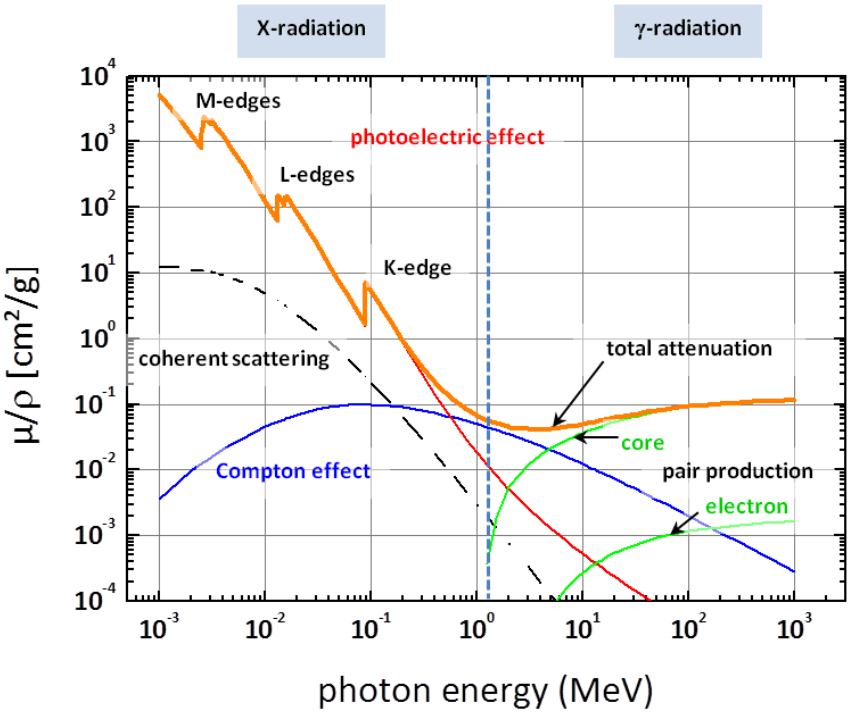

Figure 18: ***mass attenuation coefficient of Pb as an example. Orange curve shows its total value; other colors show partial attenuation coefficients (dashed line at 1.24 MeV marks the approximate border between X-rays and γ-radiation) (data generated using [57]).***

The number of absorbed or rather scattered photons is proportional to the density of the absorber itself. For compounds it is the sum of all elementary mass absorption coefficients (p_i = mass fraction of the i^{th} element):

$$\mu' = \sum_i \left(\frac{\mu}{\rho}\right)_i \cdot p_i$$
$$\sum_i p_i = 1.$$

To sum up in short, one can state that the attenuation of radiation is a combination of different parameters and its influences. The attenuation increases proportionally cubic to the wavelength of the photon and cubic to the atomic number of the absorber itself. It increases exponentially with the density and thickness of the absorber. So, X-rays in general are attenuated by the density of electrons. Regarding the cross-section one can state that not every invading quant of light (photon)

has an effect, but direct collision is essential. The cross-section itself can be described roughly by $\sigma_{interaction} = \mu_{interaction}$/particle density.

2.2.1.2. Secondary processes

If an X-ray quantum is absorbed in a solid by one of the former mentioned processes where electrons are ejected, such an electron could release its energy via secondary processes to the atoms within the atomic lattice. During this process, weakly 007-electrons are lifted from the valence band into the conduction band. This leaves a hole within the valence band. Together with an electron it forms an electron-hole pair. Since a part of the energy of the electron (created by X-ray interaction) is used for excitation of phonons, the energy needed for the creation of such an electron-hole pair is higher than the valence-conduction band gap. The number N of created electron-hole pairs could be calculated by $N = E/E_i$, where E is the absorbed energy and E_i the mean energy necessary to create this pair.

2.2.1.3. X-ray fluorescence

X-ray fluorescence, simply put, is the emission of characteristic fluorescent (secondary) X-ray radiation from an atom that has been excited via X-ray radiation. It is very similar to (or is in principle the same as) the process of characteristic X-ray radiation (appearing in X-ray tubes); in the sense that the X-ray photon directly hits an electron in the inner shell, so this electron is lifted to a higher state or even liberated. By relaxing into the hole, another electron from an outer shell emits energy in form of electromagnetic radiation. The amount of energy is equal to the energy difference of the two shells involved. The term "fluorescence" is basically used for any phenomena, in which absorption of radiation of certain energy comes down to re-emission of radiation of a different, generally lower, energy. For incoming X-rays, this process is shown in Figure 19; a typical plot of radiation originating from fluorescence (in this case, the K_α- and K_β-lines) is shown in Figure 20.

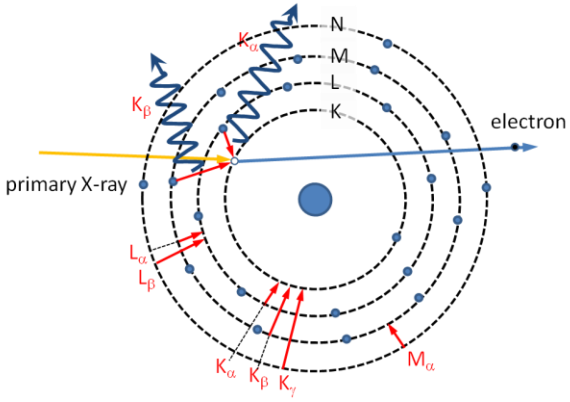

Figure 19: ***principle of X-ray fluorescence; the possible case of K-lines is shown. An incoming X-ray liberates an electron, which leads to "filling up" of the left over hole. This leads to element-specific, characteristic X-ray radiation, which can be used to characterize any material applying this experimental technique. Additionally, origins of different possible characteristic lines of X-ray radiation are indicated by small red arrows.***

If electrons are emitted from the inner shell (K-shell), all characteristic lines can appear. Concerning the nomenclature of the lines, (K, L, M, and N) is the name of the shell to be filled. The index (α, β, γ,…) means filling up from the 1st next, 2nd next, etc. higher level (indicated by small red arrows within Figure 19).

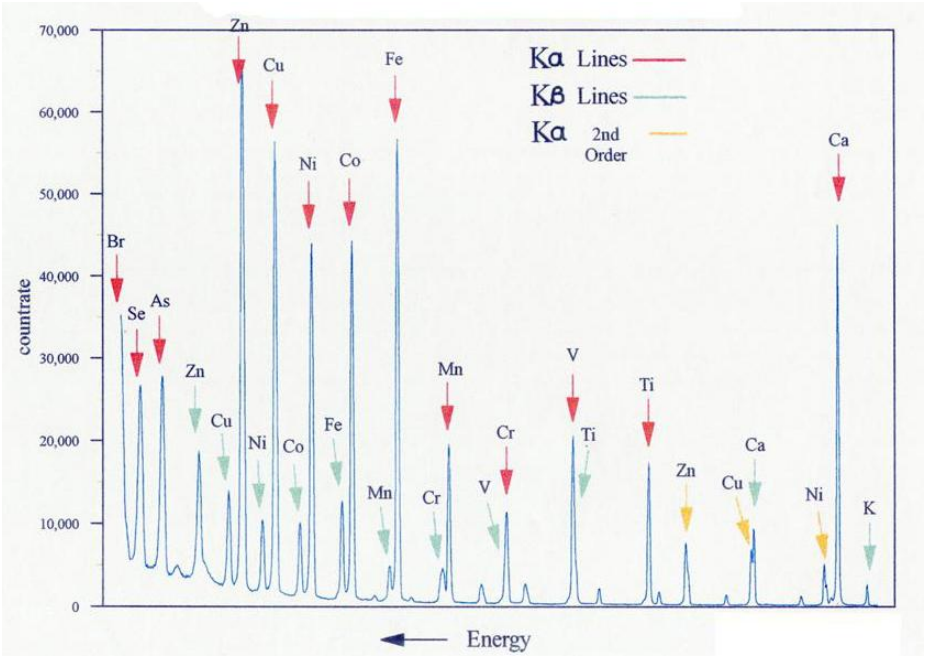

Figure 20: ***possible element-specific, characteristic lines of X-ray radiation. The more intense peaks (marked with red arrows) are mostly the K_α-lines, the other peaks (marked with green arrows) are the K_β-lines and even some higher order K_α-lines (marked with yellow arrows) could appear.***

2.2.1.4. Refraction and reflection

At large, as X-ray optical components suffer from the weak refraction of X-rays in matter and from relatively strong absorption (as in comparison to that of VIS in combination with glass), the index of refraction (IOR) for X-rays in matter can be written as $n = 1-\delta$, and is close to 1. Here, δ is the so called decrement, which is only in the order of 10^{-4} to 10^{-6} [58], four to six orders of magnitude smaller than the decrement of 0.5 for VIS light in glass. The small decrements lead to an IOR (only slightly) smaller than the IOR for vacuum, which is defined as 1. This is caused by the fact that the oscillation frequency of X-ray radiation is larger than the resonant frequency of the outer electrons of atoms. Remarkably enough this even results in group velocities higher than the speed of light in vacuum.

The IOR smaller than 1 has geometric consequences as well: If an X-ray coming from air or vacuum permeates a liquid or a solid sample (where always n<1), it is refracted away from the surface normal (see Figure 21, left), $\alpha_2 > \alpha_1$, whereas VIS is refracted nearer to the normal, we get that incoming light gets refracted closer to the normal (Figure 21, right), $\alpha_2 > \alpha_1$, according to Snell's law of diffraction:

$$\frac{\sin\alpha_1}{\sin\alpha_2} = \frac{v_1}{v_2} = \frac{n_2}{n_1}, \qquad (2.56.)$$

with α_1 and α_2 – angles of entrance and exit, v_1 and v_2 – speed of travel within the area of index of refraction n_1 or n_2; $n_i = c_0/v_i$.

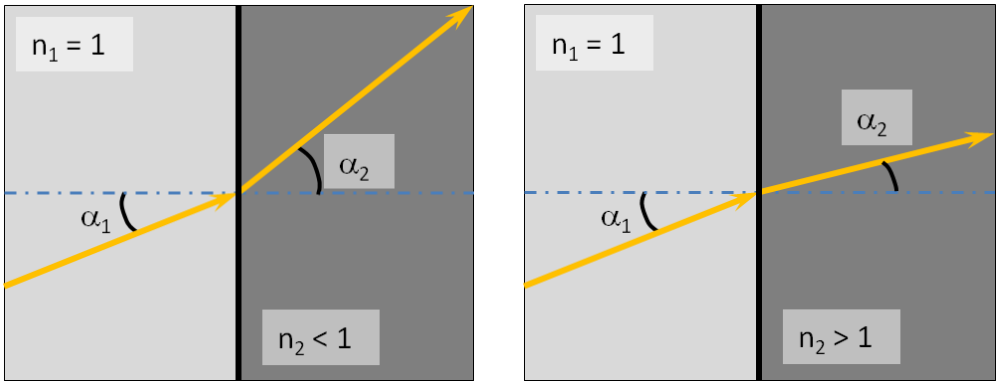

Figure 21: ***refraction at a boundary surface. Left: at X-rays ($\alpha_2 > \alpha_1$). Right: in VIS-region ($\alpha_2 < \alpha_1$).***

For refractive X-ray optics this means that converging lenses must be shaped like diverging lenses for the VIS. For every kind of electromagnetic waves there is a critical angle α_1, above which the incoming beam is not refracted anymore but completely reflected (total external reflection). At the border angle ($\sin \alpha_2 = 1$, at 90°), the refracted beam propagates on the surface. As the decrement δ is very small, this angle α_2 is very large. Hence, reflective X-ray optical elements like mirrors or reflection zone plates are very often used at grazing incidence.

2.2.1.5. Diffraction

Huygens-Fresnel principle

One of most important concepts of the wave theory of light is the Huygens-Fresnel principle. In general, it states that every point of any wave front can be seen each as origin of a new hemispherical wave – a so called elementary wave. The phase and the direction of propagation of the newly generated wave front result from superposition of all the wavelets. Huygens principle offers an explanation for many optical phenomena like diffraction and refraction (principles shown in Figure 22) or any other occurrence involving the interference of electromagnetic waves (e.g. gratings and zone plates).

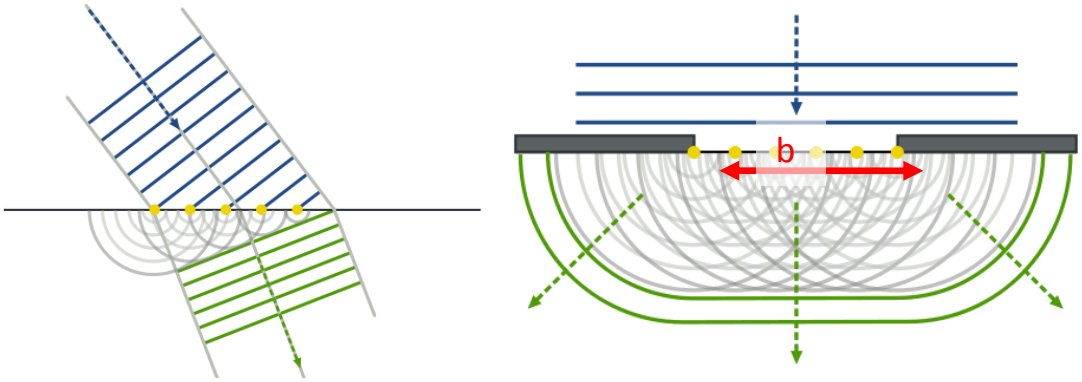

Figure 22: left: ***refraction at a surface after Huygens-Fresnel. An incoming plane wave gets refracted at the boundary surface of two media, in which it propagates. The direction of the refracted beam depends on the***

(difference of) refractive indices. Right: diffraction at a slit according to Huygens-Fresnel principle. The incoming wave leads to generation of wavelets at each point within the hole. The near-field interference (Fresnel diffraction) close to the slit appears different than the far-field interference (Fraunhofer diffraction). Focusing diffractive elements such as VLS gratings and Fresnel zone plates make use of near-field diffraction (see chapter 2.2.2.4) (pictures taken from [59]).

Bragg- and Laue-case, respectively

Any periodic structure on nano scales – no matter if artificially made gratings or in single crystal lattices – can be used to create far field X-ray diffraction patterns. In case of crystal lattices or multilayer structures, the geometrical conditions for positive interference of the outgoing rays are given by Bragg's law of diffraction (as shown in Figure 23). Here, the distance d between the lattice layers (or artificial nano-layers) is an important parameter. The angle Θ of positive interference is given by

$$n\,\lambda = 2\,d\,\sin\Theta, \qquad (2.57.)$$

with the photon wavelength λ and the integer n that defines the order of diffraction.

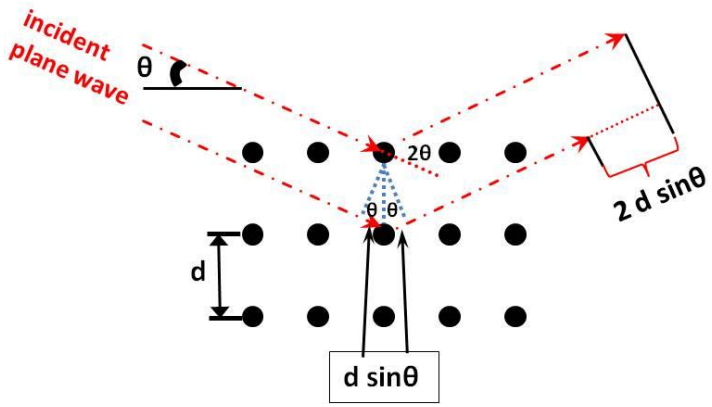

Figure 23: ***Principle of Bragg-diffraction in a crystal. Constructive interference occurs if: nλ=2dsinΘ ("Bragg's Law")***

A monocrystalline solid or multilayer structure can be used as a transmissive or reflective optical element. In Figure 24 the diffraction processes in both cases (Bragg-geometry (left) and Laue-geometry (right)) are illustrated by the k-vectors of the X-rays involved (k_0 – incident and transmitted light paths, k_G – diffracted beam, n – normal of crystal surface, γ_0, γ_G – angles between normal and course of beam after "interaction" with the crystal):

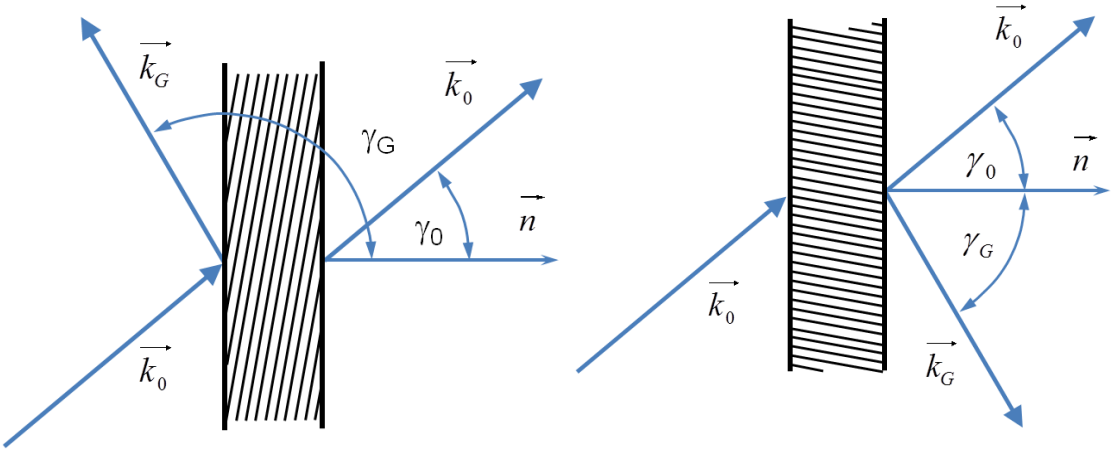

Figure 24: ***scheme of optical paths using crystals in Bragg-geometry (left) and Laue-geometry (right).***

The considerations of Bragg-diffraction in reflection will be described in detail for crystals within the following subchapter, as it will be needed to make considerations about the spectrometry of the spontaneous undulator radiation (as to be seen and used for the K-monochromator – see below).

2.2.2. Optical elements

One of the first things as a basis for my work in the field of Synchrotron and X-ray radiation I learned was: "the best optics for application with X-rays is no optics at all". In general, this implies that many of the produced photons are depleted within the experiments or even before, within the optical paths of the beamlines at X-ray sources. In the following subchapters, the set-up and properties of different X-ray optical devices typically used in beamlines are described. The principles of these devices provide an important background for the ray-tracing considerations that will be presented in chapter 3 and chapter 4.

2.2.2.1. Crystals

As described above, crystals can be arranged in reflection (Bragg-geometry) or transmission (Laue-geometry), depending on the particular application. Due to the high transmission and absorption of X-rays in matter, X-ray crystals in Bragg-geometry only make sense at grazing incidence, if one is interested in having the highest possible throughput of the beamline, which means as many photons reflected as possible. X-rays in general only interact efficiently with any optical element, if illuminated at grazing incident angles; which is a major constriction in design of beamlines with high efficiency.

Properties of a single crystal

The detailed shape of a peak of positive interference of a Bragg crystal is given by its so called "rocking curve" (see Figure 25). As a visualisation of Bragg's Law ($n\lambda = 2\,d\,\sin\Theta$, where: n – order of reflection; λ – wavelength; d – distance of crystal planes; Θ – glancing angle), the wavelength is plotted over the glancing angle (top left). The natural width of these lines for different harmonics (diffraction orders), the Darwin-width, is represented by the rocking curve around this glancing angle (at a certain energy, looking at a certain plane of reflection within the crystal):

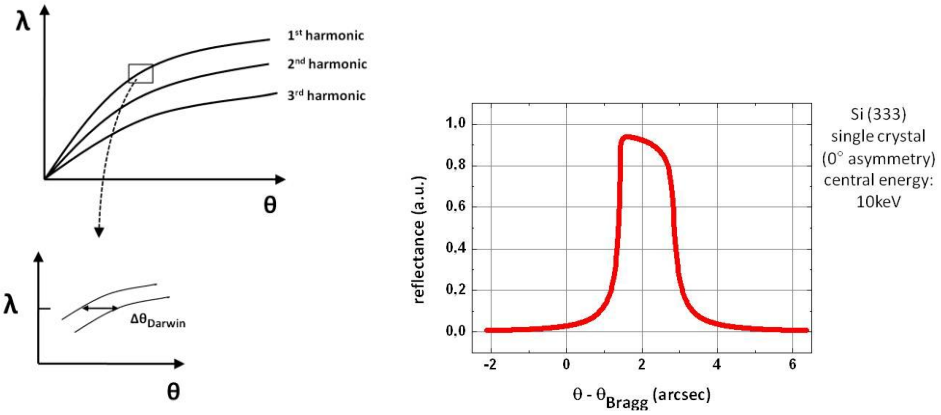

Figure 25: ***Top left: plot of Bragg's law for different harmonics (diffraction orders). Bottom left: a zoom into a harmonic shows a certain natural width, the Darwin width. Right: Rocking curve around the Bragg angle at a particular energy using the (333)-reflex of a single silicon crystal as an example.***

The extraction of a rocking-curve is usually done as follows: assume a diffractometer with a fixed source, a tiltable sample/crystal and a tiltable detector; fix a detector at a position of 2Θ (double of Bragg angle of reflection, glancing angle) with respect to the lattice plane within a crystal under examination. Then tilt the crystal by an amount of ΔΘ, starting from Bragg-angle Θ. The resulting curve of reflectance is the rocking curve. This recording technique is depicted in Figure 26, as an example a sample containing 3 crystallites is shown.

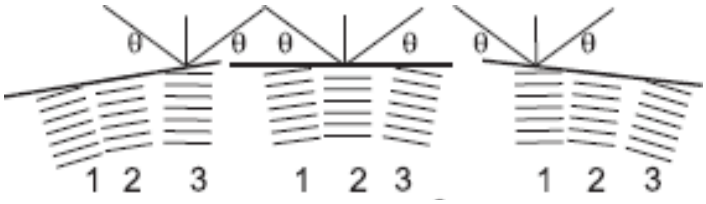

Figure 26: ***a sample containing 3 crystallites within a crystal. The source and detector are at fixed positions at angle Θ, the sample is tilted (depicted by the tilted surface line). The resulting curve delivers information about uniformity of the crystalline sample.***

If the detector is fixed at the Bragg angle Θ and the sample is tilted relative to the incoming ray of light, then crystallite 3 fulfills the Bragg-condition. With further tilting consecutively crystallite 2 and 1 are in Bragg-condition. The selectivity of this tilt strongly depends on the size of the incoming radiation. For precise measurements one tries to keep the width of the incident ray as small as possible at the smallest possible divergence at the same time. Intensity and full width at the half maximum (FWHM) of the resulting curve is a quantity of the uniformity of the lattice plane with respect to the surface of the sample. With the help of the rocking curve and its FWHM the crystalline quality can be described or quantified. The basic principles were taken from [60], [61] and [62].

Representation with DuMond diagram

A zoom into the plot of Bragg's Law leads to the so called DuMond diagram, which is shown in the left part of Figure 27. The DuMond diagram provides a relation between the accepted angular width and the respective energy resolution/acceptance range.

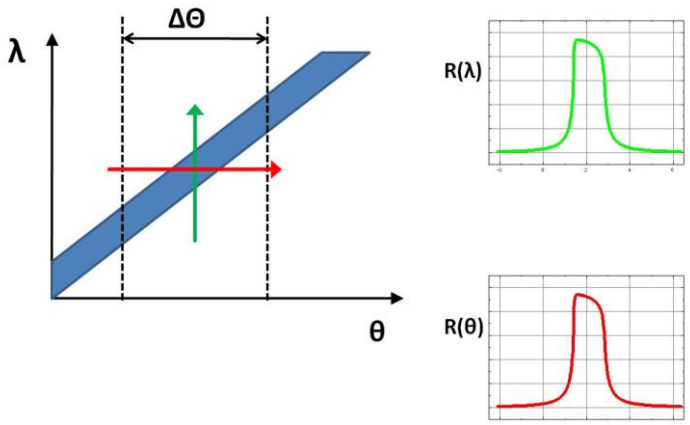

Figure 27: ***DuMond diagram and the Rocking-curve of the reflectance (showing the Darwin-width) for both depending on the wavelength/energy (top right) and the rocking angle (bottom right) around the Bragg angle, respectively.***

2-crystals-combinations

It is possible to combine two crystals into two general configurations and any combinations of these – dispersive and non-dispersive. Figure 28 shows a sketch of optical paths through these two dispersive and non-dispersive arrangements of two crystals, at different wavelengths:

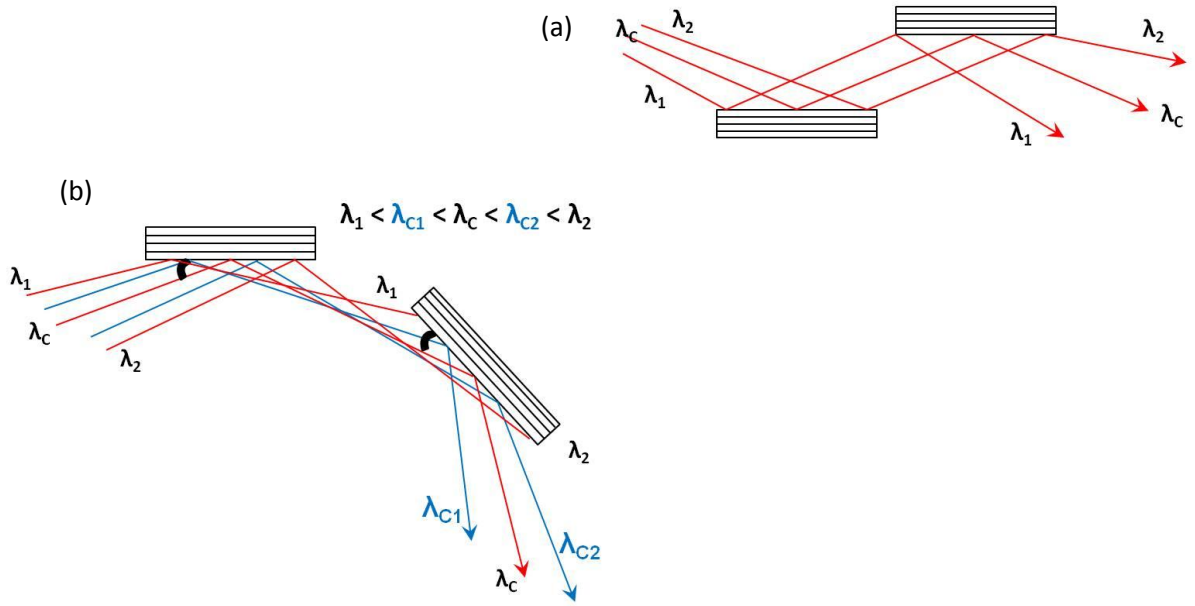

Figure 28: ***(a): Two identical crystals used at the same reflection layers (e.g. Si (111/333/...) in dispersive arrangement. All the wavelengths and the divergence of the beam, which are accepted (and then further delivered), are accepted from the 1st as well as from the 2nd crystal due to the parallel arrangement and hence the same Bragg-condition and rocking curves or the crystals, respectively. The angle of emergence from the 1st crystal equals the angle of incidence at the 2nd crystal. (b): Two identical crystals in non-dispersive arrangement. The band of energies around the center energy fulfilling the Bragg-condition at the 2nd crystal is smaller than the energy acceptance of the 1st one.***

The Bragg-condition and the corresponding DuMond representations (for the 2 crystals) are shown in Figure 29 and Figure 30, respectively:

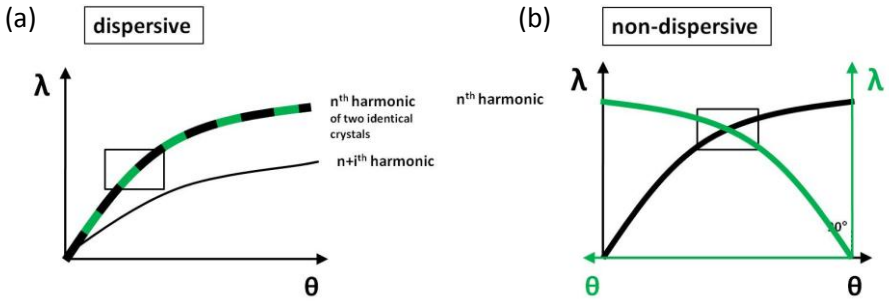

Figure 29: ***(a): Bragg-condition of two identical crystals in dispersive arrangement is depicted by an overlapped black and green line. (b): Bragg-relation of two identical crystals in non-dispersive arrangement. It is conventional to flip the resulting curve around the ordinate and shift it to the right (or left respectively) to the extent of the angle between the surface normals of the crystals.***

The resulting DuMond-diagams (zoomed into the region of interest – as displayed in Figure 29 in the form of a rectangle) are given in Figure 30:

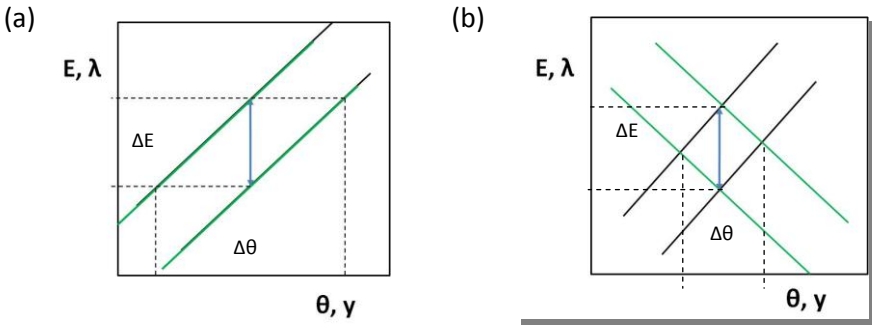

Figure 30: ***DuMond diagrams of two identical crystals. The blue double-headed arrow depicts ΔE, a certain energy resolution. (a): arrangement in dispersive configuration. The curves of the 1st and 2nd crystal overlap perfectly, indicated by overlapped black and green curve of the two crystals. (b): arrangement in non-dispersive configuration; the curves intersect at a certain angle according to the angle between the normals of the crystals.***

Here we see that at an equal energy resolution of both arrangements the $\Delta\theta$ or $\Delta\psi$ of the accepted angles is smaller in the non-dispersive arrangement.

Due to the dispersive properties of single crystals and the optional filtering feature of arrangements of multiple crystals, these devices are often used as beamline monochromators. The angle of acceptance can be modified for the desired beamline purposes by using asymmetrically cut crystals, with an angle between the surface and the reflecting lattice layers. Using DuMond diagrams as a representation of the crystal monochromator properties the change of the angular acceptance using these angles of asymmetry can be demonstrated as in Figure 31:

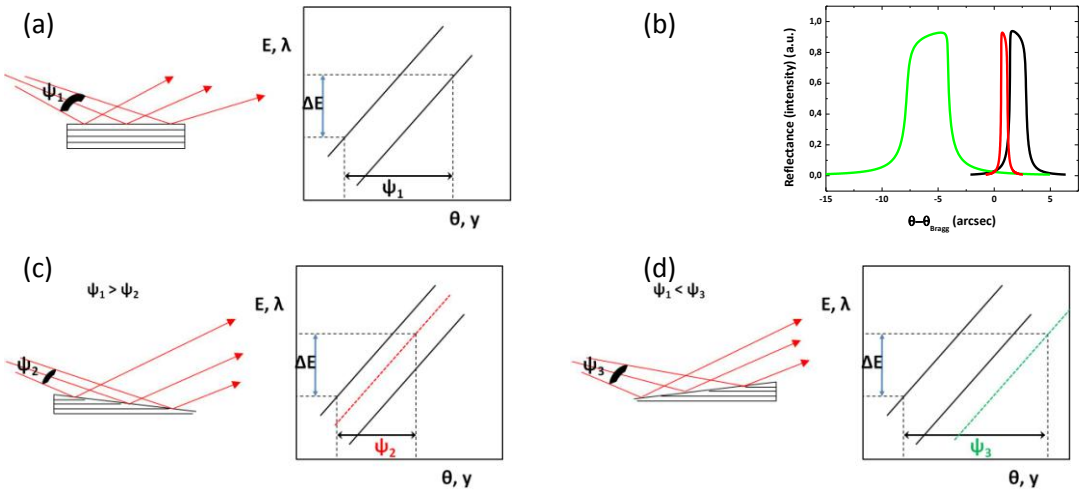

Figure 31: ***(a): as reference both the incoming and outgoing rays as well as the associated DuMond diagram are shown. Here the angles of incidence and emergence are the same. (b): the rocking curves of a Si (333) single crystal (at 10 keV) and the influence of the angle of asymmetry on its width (simulation done using REFLEC [30]) black: reference (without angle of asymmetry), green: asymmetry angle = +45°, red: asymmetry angle = -45°. Bottom: influence of angle of asymmetry between crystal surface and reflecting lattice planes; (c): negative angle of asymmetry leads to narrowing of the angle of accepted rays. (d): positive angle of asymmetry leads to broadening of the angle of accepted rays.***

As an intermediate conclusion it is clear that the angle of acceptance can be increased using asymmetrically cut crystals, but at the same time we have a dramatic decrease of transmission, which will be shown in chapter 3.

2.2.2.2. One- and two-dimensional gratings

Besides the natural periodicity of crystals, an artificial periodical structuring of a surface is a very efficient method to cause diffraction patterns. For X-rays, one-dimensional gratings are commonly used as dispersive optical elements. Together with focusing mirrors they can be used as monochromators. However, these two functions – dispersion and focusing – can be combined in VLS-gratings (focusing in one dimension) or Fresnel zone plates (focusing in two dimensions). This chapter presents the principles of all types of these diffractive optical elements. As the name says, the physical principle is diffraction. Particular attention is paid to reflective elements.

2.2.2.3. Gratings

An optical grating, so called diffraction grating, is simply said a sequence of slits of same width and a constant distance to each another. Hence, it could be called multiple-slit. As every grating slit diffracts the incoming light like a single slit, the interference pattern on a screen behind the grating can be calculated as superposition of the interference patterns of all the slit elements. At high numbers of slits, the sinusoidal pattern of a few slits merges into sharp diffraction peaks in the far field. White light, containing different wavelengths or energies, is fanned out like at a prism; every single energy is transmitted to another angle.

According to the principle of Huygens (see chapter 2.2.1), one can observe regions of bright and dark fringes (maxima and minima) at positions y, respectively, on a screen at a certain distance z away from a single slit (the principle condition for minima is shown in Figure 32):

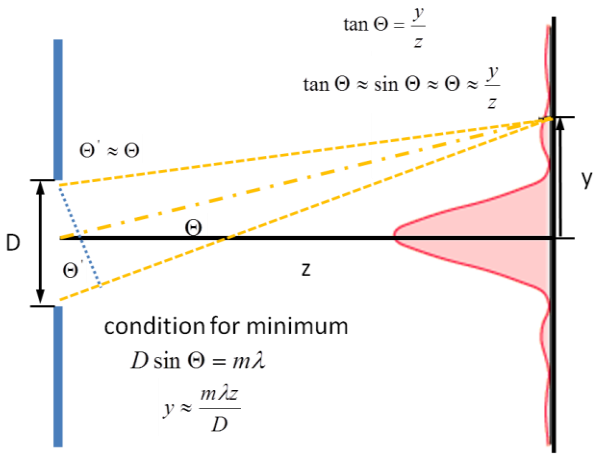

Figure 32: principle of obtaining the position y of the minima (correlated to the angle of deflection Θ), depending of the wavelength λ and slit size D (picture adapted from www.hyperphysics.phy-astr.gru.edu).

The positions of minima and hence the positions of maxima is obtainable for the case of a single slit as shown in Figure 33; for the next higher number, double slit, it is shown below in Figure 34.

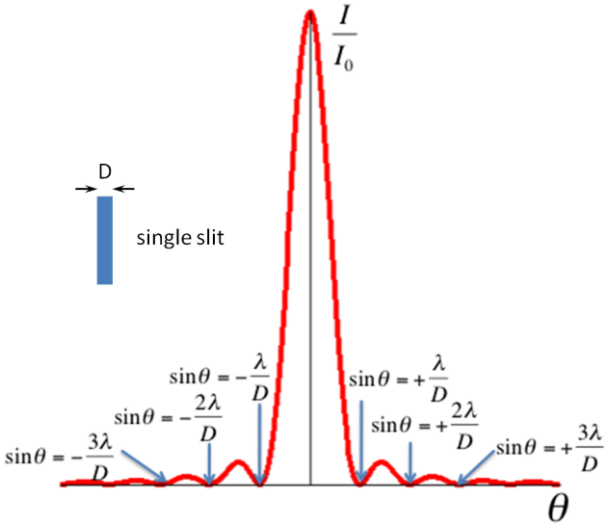

Figure 33: positions of the local minima and maxima of intensity in case of passing through a single slit (picture adapted from www.colorado.edu).

The width of the central maximum is 2 Θ_{min}, with

$$\Theta_{min} = 1.22\frac{\lambda}{D}. \qquad (2.58.)$$

Note here that the width corresponds to the FWHM of the peak in the middle (not the distance between the first minimum and the according maximum).

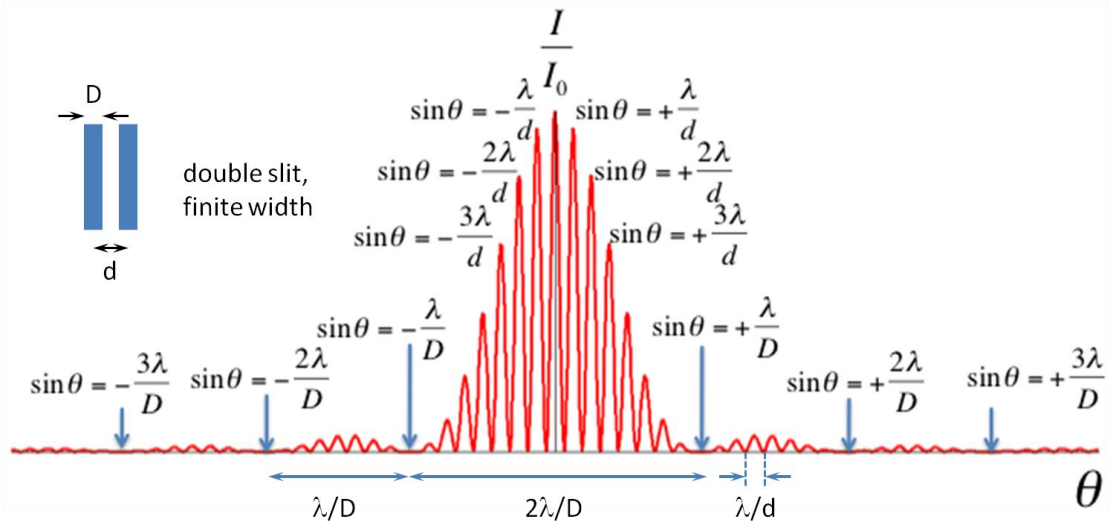

Figure 34: positions of the local minima and maxima of intensity in case of passing through a double slit (picture adapted from www.colorado.edu).

Comparing the positions of the minima in the single and double slit patterns, one can see that the intensity pattern for a single slit is an envelope for the next higher number of slits. This property scales up with increasing number of slits (see Figure 35). The center peaks become higher and sharper and the adjacent peaks lower up to very high intensities at the center positions and wider regions of no or low intensity between them is formed. The peak positions are called diffraction orders (0, ±1, ±2, ±…), whereas the zero signifies the direct light (or, in case of reflective gratings as explained below, direct or specular reflection) as labeled in Figure 35.

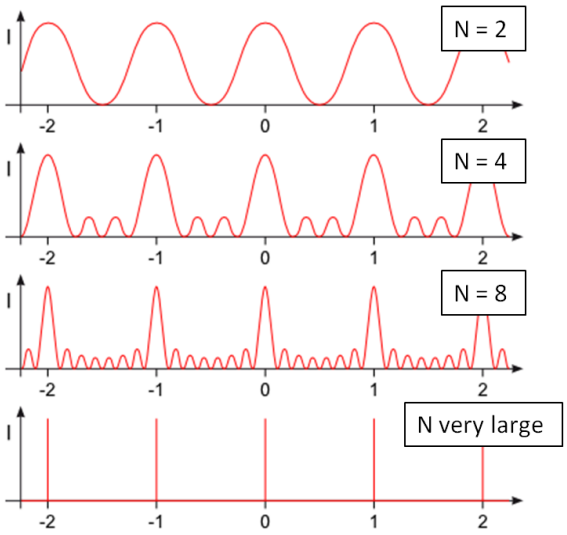

Figure 35: ***survey of the intensity pattern (1-dimensional) after passing through multiple-slits. From top to bottom the number of slits N is noted in boxes on the right (from double-slit to grating). The integer numbers (0, ±1, ±2) depict the location of the respective diffraction orders (picture taken from [63]).***

The interference patterns described so far for transmission of light through a slit or grating equal those of light being reflected by a periodically structured surface. Figure 36 shows the equivalence of diffraction induced by light passing through a slit and light being reflected by a mirror of the same size.

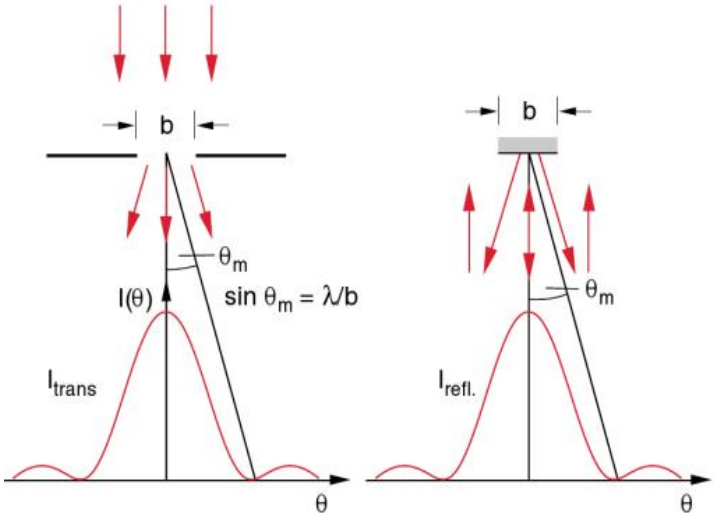

Figure 36: equivalence of the intensity pattern using the example of light in transmission (left) through a single slit of size "b" and reflection (right) at a surface of the same size "b". In case of transmission the slit is illuminated by parallel light, so as the case of reflection. (courtesy of H. Loechel)

In other words, the grating in transmission with a certain line density shows equal optical properties as a grating used in reflection with the same parameters (see Figure 37 and Figure 38).

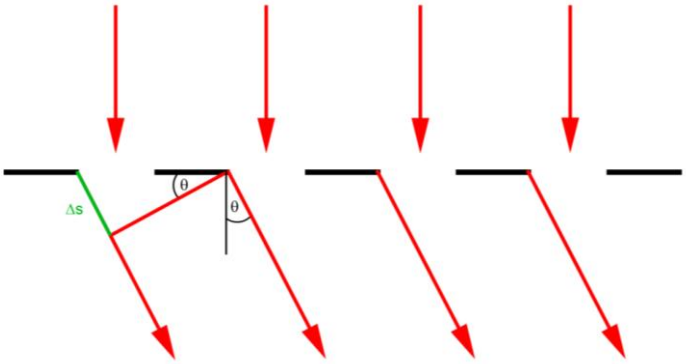

Figure 37: ***grating used in transmission with normal incidence. The path length difference Δs (depicted in green color) needs to be an integer multiple of the wavelength for constructive interference at the screen behind the transmission grating. (courtesy of H. Loechel)***

In both cases, for normal incidence (used mostly on transmission gratings, see Figure 37), the grating equation, which is the main relationship between the grating spacing d, the angle of incidence and the angles of positive interference, can be written as (Δs is the path length difference, which needs to be considered in order to obtain constructive interference of a certain wavelength λ):

$$\Delta s = d \cdot \sin \Theta = m \cdot \lambda \,, \qquad (2.59.)$$

with outgoing angle Θ and the diffraction order m.

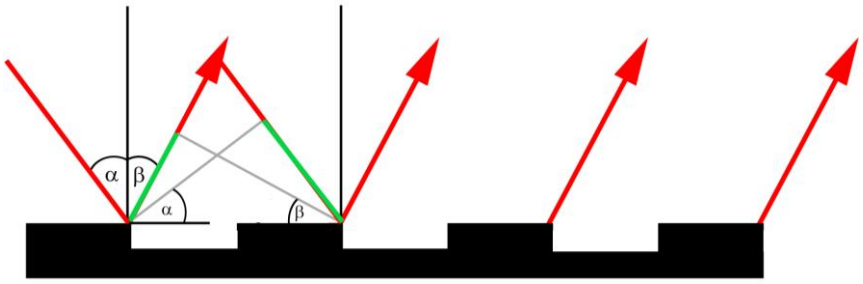

Figure 38: ***laminar grating used in reflection. (courtesy of H. Loechel)***

For other angles of incidence than normal (mostly used in case of reflection), the grating equation is extended by another term (α is the angle of incidence; β is the exit angle of the diffracted beam):

$$\Delta s = d \cdot (\sin\alpha + \sin\beta) = m \cdot \lambda . \qquad (2.60.)$$

An important parameter for the characterization of a diffraction grating is its energy resolution. The formal Rayleigh criterion, which is heuristically found, enables to make a statement about the minimal distance of two sources of light, at which they can still be regarded as separated. It states that this minimal distance is equal to the distance of the first minimum to the center of the diffraction pattern by the simple relation:

$$\frac{\lambda}{\Delta\lambda} = mN , \qquad (2.61)$$

with m as order of maximum and N the total number of illuminated lines at the grating.

A general property of diffraction of light is the fact that different wavelengths are diffracted to different positions, which we call “dispersion”. As an example Figure 39 shows a schematic of distribution of different wavelengths (in the VIS spectral region) diffracted by the same grating. It is clearly visible that for the +1st order (to the right within the graph) the longer wavelengths (lower energies) like red or orange are diffracted farer away from the center than the shorter wavelengths like violet or blue, which are closer to the center. In the center, all the energies are diffracted into the same spot (depicted by all colors together). Within the -1st order the distribution is vice versa. Commonly, the intensity of the different orders of diffraction scales reciprocally proportional to the square of number of order m:

$$I_m = \frac{I_0}{m^2} . \qquad (2.62.)$$

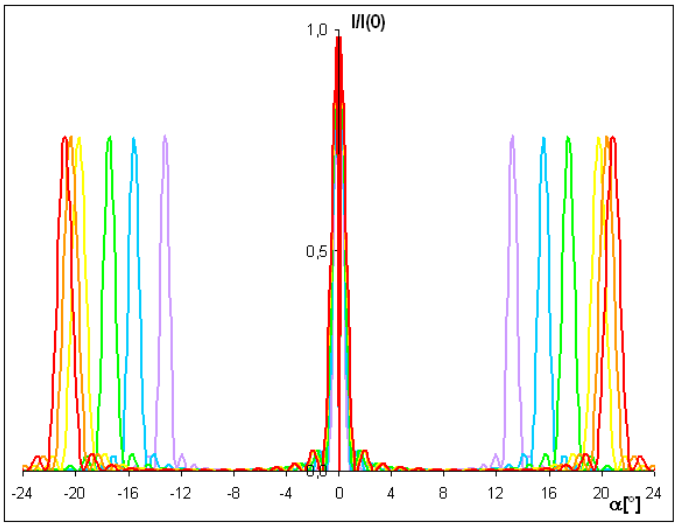

Figure 39: ***distribution of different wavelengths within the +1st and -1st order of diffraction after having passed a grating. Exemplarily it is shown with colors out of the visible spectral range (intensities are normalized to show just the principle of separation). This effect is called "dispersion" (picture taken from www.chemiephysikskripte.de).***

Another parameter, which could influence the quality of a diffraction grating, is the depth of profile. Usually on a reflection grating, just the upper part of the structure is used for forming the diffraction pattern. But, actually, this is a waste of at least half of the reflecting surface. If the bottom part of the structure would be used to contribute to the positive interference, the intensity and efficiency of this optical element could be increased significantly. For positive interference at an angle of incidence Θ the ideal profile depth t must cause a path difference of λ/2 (see Figure 40), which corresponds to a phase shift of π, which means

$$2t\sin\Theta = \frac{\lambda}{2}, \qquad (2.63.)$$

or

$$t = \frac{\lambda}{4\sin\Theta}, \text{ respectively.} \qquad (2.64.)$$

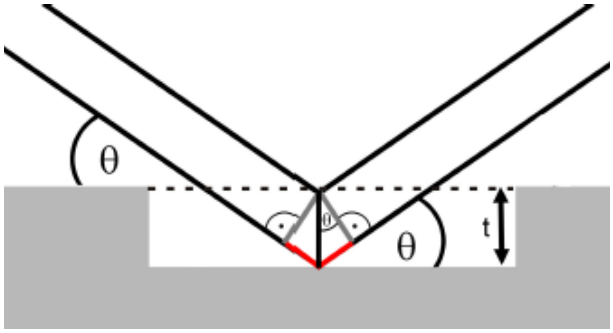

Figure 40: ***scheme of the ideal profile depth of a reflective grating. The path difference (marked in red) between two rays of light, which are reflected at the upper and lower structure level must correspond to half of the wavelength λ/2. (courtesy of H. Loechel)***

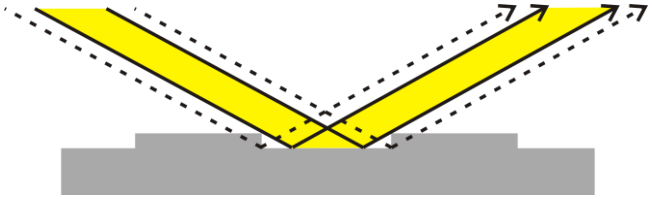

Figure 41*: shadowing effect on laminar gratings: the lower level areas contribute only partially to the interference of the incoming light (marked yellow), the other parts are lost due to shadowing (dashed arrows) (courtesy of H. Loechel).*

Obviously even with the ideal profile depth one cannot use the complete reflective surface of the diffractive element, as every angle of incidence and emergence other than normal incidence (90°) causes some parts of the lower surface to be shadowed (see Figure 41). The larger the angles (measured from the surface normal), the higher are the intensity losses due to this effect.

Summarized in a few words, a grating used in reflection, or a grating-like reflective optical element, can be optimized via the following parameters:

The angles of incidence and emergence are set by the maximum of the plain reflectivity of the surface for the energy of interest. This leads to the corresponding grating period with an ideal depth of the structure (profile depth), for which the effect of shadowing is minimized. For X-rays the angle of incidence is best around grazing incidence (as explained in chapter 2.2). This influences the energy band, which can be diffracted and reflected at all (as possible certain energies will not be reflected at angles which either are not shielded or do not lead to any constructive interference at all). How these parameters could influence the total efficiency and energy resolution, will be shown within the description of the project of a single-element spectrometer in chapter 4.1.

2.2.2.4. VLS-gratings and Zone Plates

In general, zone plates are the next logical step of diffractive optical elements for X-rays – nowadays state-of-the-art. They combine the imaging properties of a lens (leading to focusing) with the dispersive properties of a diffractive optical element as described above. Starting with a normal laminar diffraction grating, the next step towards a zone plate is the variation of the line density in one dimension, which is, as will be shown below, actually a borderline case of a zone plate structure. Basic VLS-principles are to be found in detail in [64], [65], [66], [67] and [68].

VLS-gratings

At a laminar grating with constant line spacing and slit width (applied in transmission) or grating period (reflection), parallel rays of light are diffracted at different angles of positive interference. If the line density of a grating, as described in detail in the previous chapter, is varied and if the light source has a finite distance to the grating, the far-field diffraction becomes near-field diffraction. The energies are distributed and focused at particular positions in the plane of observation. This property of a so called “varied line spacing” (VLS) grating leads to the advantage that one can use it for focusing of different orders and energies in one dimension onto an observational screen. In this way, the different lines of energy are de-magnified and thus can be separated better than using a

plain/regular laminar grating. This again results in a higher possible energy resolution. And finally, one can stint on additional focusing optical elements (which causes always additional loss of photons).

The different diffractions (distribution of different energies at different angles) at a plain laminar grating and a VLS-grating are shown schematically in Figure 42 and Figure 43:

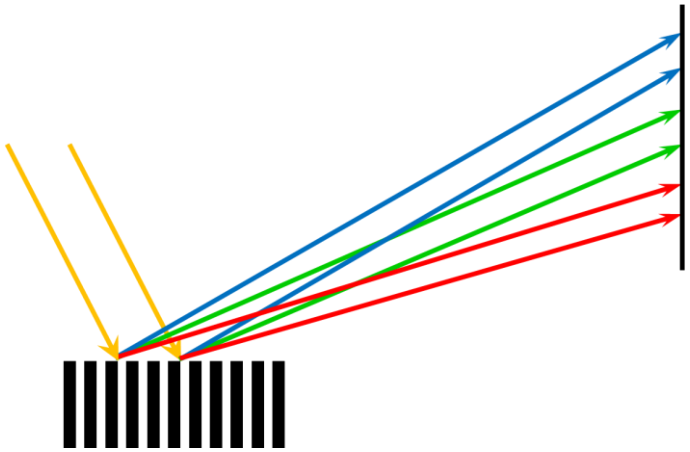

Figure 42: ***diffraction of light from a regular laminar grating; the contained different energies which are distributed to an observational screen are reflected at parallel rays of light (note, -1st order is depicted).***

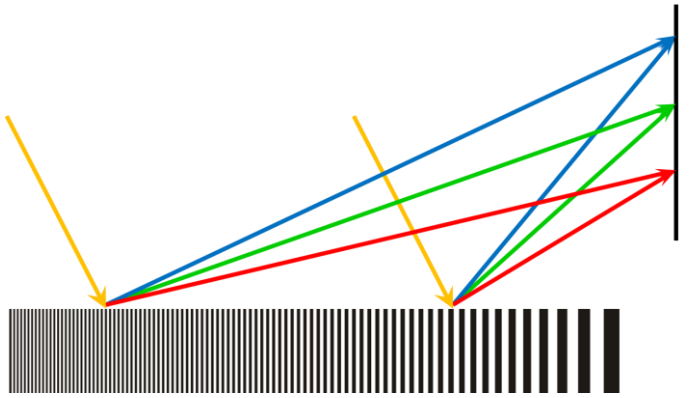

Figure 43: ***diffraction of light from a VLS-grating; the different energies which are distributed onto an observational screen, are additionally focused at fixed distances between the grating and the screen (due to different Bragg-condition at the different positions at the grating) (note, -1st order is depicted).***

Fresnel Zone Plates

This principle of line width variation is applied in two dimensions at so called Fresnel Zone Plates. In this case, the focusing of the different energies (and diffraction orders) happens in both directions in the observational plane. In order to understand the mode of operation of such an optical device, shortly the fundamental construction principle of Fresnel zones should be mentioned.

By analogy with the technique of drawing an ellipse on a piece of paper (using only two pins, a thread and a pencil), it is assured that the sum of the distances to the two foci has the same value on each point of the generated ellipse. This way, one can generate the 3-dimensional version, the ellipsoids around two focal points A_1 and A_2 (see Figure 44). The sum of the distances R_1 and R_2 to the foci is constant as in the 2-dimensional case.

In an analogous manner, the two foci can be taken as a light source (e.g. A_1) and a detector point (A_2). Then, the surfaces of the 3-dimanesional ellipsoids correspond to a particular path length which the light travels from A_1 to A_2.Diffraction takes place at the point at which the light touches the ellipsoid's surface. The actual Fresnel zones arise, if only a certain set of ellipsoids is assumed. This set correspond to wavelengths that differ from the direct connection between A_1 and A_2 (the optical axis) by integer multiples of $\lambda/2$. The areas between those discrete ellipsoids are the so called Fresnel zones. In this way, a phase shift of π is generated; hence, negative interference is induced between two contiguous zones. Obstructing the light in every second zone produces only positive interference in the detector point A_2.

Fresnel zone plates can be recognized as cuts through these ellipsoids; both cuts through the optical axis (transmission zone plates, TZP) and cuts outside the optical axis (reflection zone plates, RZP) can be realized technically:

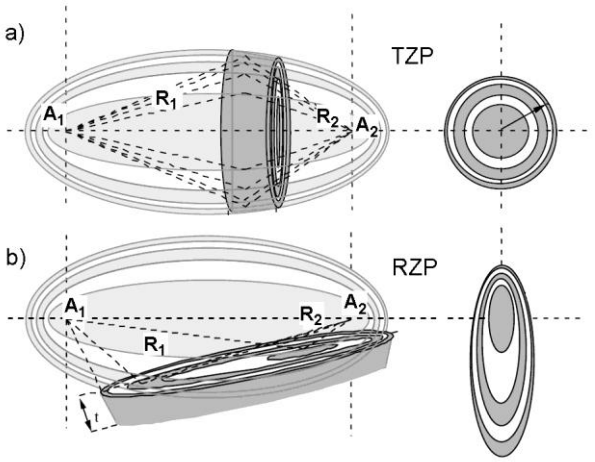

Figure 44: ***schematic view of Fresnel zones around two focal points A_1 and A_2, respectively. Fresnel zone plates can be seen as cuts through the ellipsoids, as depicted each on the right. a) represents a cut through the optical axis between A_1 and A_2 (used for transmission zone plates); b) represents a cut offside the optical axis (used for reflection zone plates) (picture taken from [69]).***

Zone plates are designed for perfect focusing of a fixed energy only as the sizes of Fresnel zones, and thus the radii of the ellipsoids, are given by the path difference of $n\lambda/2$ (n – integer) between the edges of the zones. Consequently their design depends on the wavelength of the light that is emitted from the source. This property causes the very useful dispersion, similar to VLS-gratings described above, but in this case resulting in a two-dimensional focal spot.

In realistic cases no 0-dimensional point in A_2 as focal spot, but a real image of the source. The image size depends i.a. on the distances R_1 and R_2 (between the center and A_1 and A_2, respectively). Let us consider a transmission zone plate with a source at infinite distance, which is according to a concave refractive lens that focuses parallel light into its focal distance. Parallel incoming light (diffracted by a

zone plate) produces a series of foci, corresponding to different diffraction orders, which are located on the optical axis at distances f_m to its center. For m > 1, foci are closer to the zone plate:

$$f_m = \frac{f}{m}. \qquad (2.65.)$$

The position of the first order focus corresponds to the focal position of the above mentioned refractive lens and has the highest intensity. The intensity of all foci is reciprocally proportional to the square of the number of the order m:

$$I_m = \frac{I_1}{m^2}. \qquad (2.66.)$$

The focal length of a zone plate is determined by the wavelength of the incoming light and by the radius of the innermost zone (the ellipsoid around the two foci with $(R_1 + R_2)$ differing just by $1\lambda/2$ from the direct connection):

$$f = \frac{r_1^2}{\lambda}. \qquad (2.67.)$$

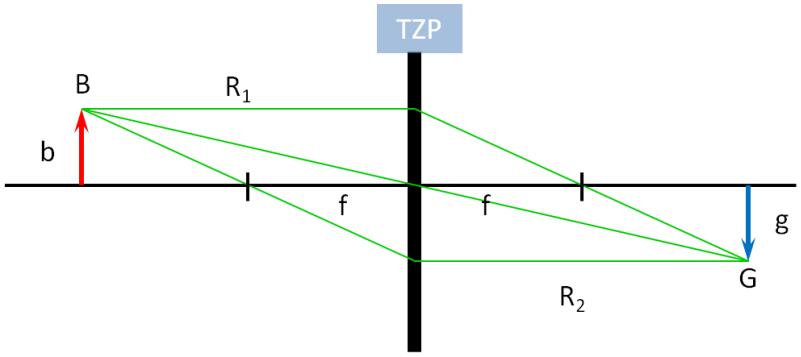

Figure 45: ***scheme of the imaging property of a TZP with a finite source at B of the size b. The paths of 3 rays are charted; all three meet in point G, which sets the image size g (courtesy of H. Loechel).***

Despite the fact that zone plates work only using diffraction and interference, they have the same optical properties as refractive lenses. As shown in Figure 45, the imaging equation can be deduced as:

$$\frac{1}{f} = \frac{1}{R_1} + \frac{1}{R_2}. \qquad (2.68.)$$

The magnification (or diminution) factor is:

$$M = \frac{b}{g} = \frac{R_1}{R_2}. \qquad (2.69.)$$

The resolution of zone plates is defined by the width of the outermost zone; connected with that, the minimum size of the image of a light source. This is caused by the Rayleigh-criterion, which states: the angular resolution $\Delta\Theta_a$ of an optical element is given by

$$\sin \Delta\Theta_a = 1.22 \cdot \frac{\lambda}{A}, \qquad (2.70.)$$

where A is the aperture of that element. In the case of a TZP a spatial resolution of

$$\Delta l = 1.22 \cdot \frac{f\lambda}{A}, \qquad (2.71.)$$

results, because of $\sin\Delta\Theta_a \approx \Delta l/f$ (see Figure 46).

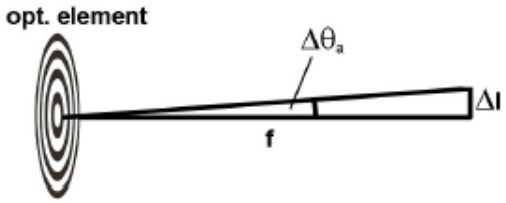

Figure 46: ***the angular resolution of an optical element can be transformed via $\sin\Delta\Theta_a \approx \Delta l/f$ into its spatial resolution on a detector (courtesy of H. Loechel).***

The aperture of a TZP can be conceived as its diameter (twice the radius of the outermost zone).

The spatial resolution of a TZP can finally be written as:

$$\Delta l = 1.22 \cdot \delta r_{n,\max}, \qquad (2.72.)$$

with the zone width of the outermost zone $\delta r_{n,\,max}$. Due to technical limitations, zone plates can thus only be fabricated up to a certain diameter (minimum zone width), which of course results in a certain minimum spatial resolution. RZPs are used at grazing angles of incidence, which leads to a great advantage of zone plates designed and used in reflection in comparison to the ones used in transmission. The angular cut through the ellipsoids leads to a huge stretching of the zones. The outermost zone for the same energy and zone number is much larger at an RZP than at a TZP (in direction of the beam).

Technically, TZPs consist of zones with different materials – transmissive and non-transmissive for the corresponding design wavelength (in this way the non-constructive interfering parts of the radiation get suppressed). RZPs are, like other reflective gratings, two-height-level-structures; in principle laminar gratings with a curved structure. Their structure is comparable to a superposition of two VLS-gratings perpendicular to each other. Applying this assumption, the two dimensional focusing is possible.

Conclusion:

An overview of interaction of X-rays with matter was given. Main effects like Rayleigh and Compton scattering, Photo and Auger effects, pair production, and high energy interaction were described and explained in detail and their probability of occurrence were given. The attenuation of light by interaction with matter was explained. Secondary processes like X-ray fluorescence, and further, refraction, and reflection were introduced and described. The Huygens-Fresnel principle as a fundamental of the wave theory was used to explain diffraction. Based on this, optical elements are described, as they are of central interest for guiding X-rays. Bragg crystals, gratings, VLS-gratings, and zone plates were presented. Their construction, physical effectiveness, and their impact on X-rays through the guiding process were presented.

3. X-Ray Optical systems for diagnostics and spectroscopy of Free Electron Laser radiation

Within this chapter two types of spectrometers for XFEL beam diagnostics are described, which were developed and simulated in this work.

In the first part, the spectrometer for spontaneous undulator emission diagnostics which will be used during commissioning of the undulator sections of the European XFEL is described. This is of particular interest, as the alignment is essential for the lasing-process to be initialized; geometrically and, not less important, radiation parameter wise.

The second part presents different options for spectroscopic inspection of the entire XFEL spectrum. The process of lasing, especially using the SASE principle, leads to completely different radiation spectra from shot to shot. In order to cover this problem, a spectrometer is required, which extracts the full spectral information for each single shot coming from the European XFEL. Different designs are analytically compared.

3.1. Inspection of spontaneous radiation of undulator segments to align the SASE undulators of the European XFEL (K-monochromator)

General considerations

This chapter is focussed on considerations and ray tracing simulations which were done within the scope of this project. Different proposed solutions how to determine the K-parameter (definition see in chapter 2.1.1.2) of the undulator segments are examined – in order to get them aligned not only geometrically but also to match the K-parameters (of the single undulator segments) sufficiently to start the lasing process.

Taking the considerations of the previous paragraph (2.3.1) into account, we started with simulation of the energy resolution and transmission of double-crystal-monochromators (DCM) and four-crystal-monochromators (FCM); first using a simplified source, then using source-files as output of the program WAVE [70]. These source files, designed especially from the undulator parameters provided in the CDR of the European XFEL X-ray Optics and Transport [72], were used as input for our simulation. The programs RAY and REFLEC, developed at BESSY, have been used for the simulations.

K-monochromator layout

The optical layout of the beamline is shown in Figure 47, a simple sketch of the beamline at SASE1 and 2, respectively, using the DCM/FCM or so called K-Monochromator. The monochromator consists of two channel-cut crystals mounted on two independent goniometers. The crystals were fabricated by Dr. Horst Schulte-Schrepping at the DESY workshop. Their topography and quality were tested at the BESSY II KMC-2 beamline and BAM-beamline, respectively.

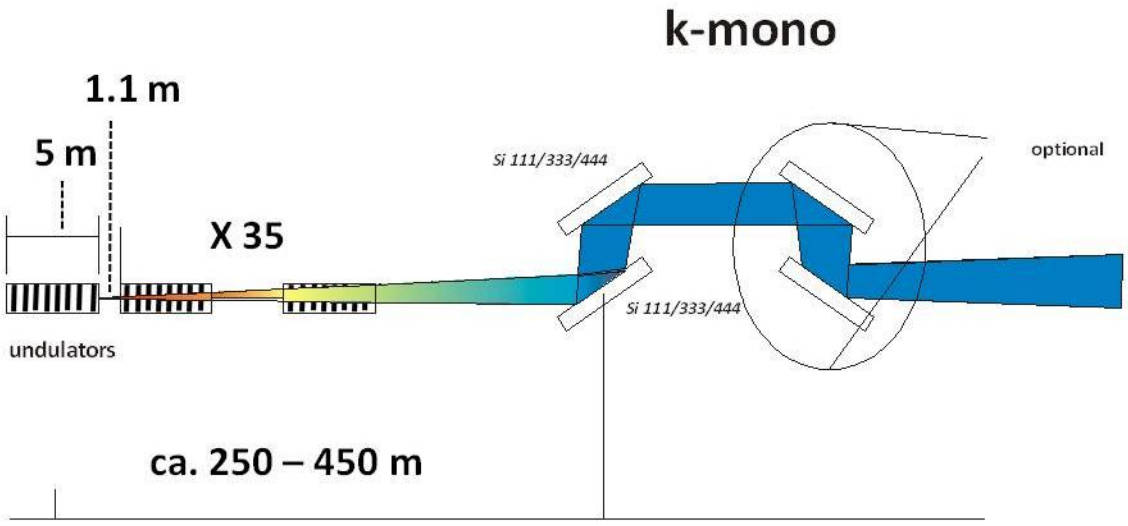

Figure 47: ***simplified sketch of the K-Mono beamline. The SASE1 and 2 undulators are shown as 35 segments. Depending on the undulator which is switched on, the source point is assumed to be located each at the end of one of the single undulator segments; to cover the full range of possibilities, the parameters for distances used for the following simulations are 450m from the very first undulator segment, 250m from the very last segment, respectively – as assumed in the year 2011.***

Firstly, the case of the simplified source parameters of a source size of (16x16) µm² (σ) and divergence of (2x2) µrad² (σ) are used. The first crystal stands at 500 m behind the supposed source point. The following simulations were done for the case of SASE 1 and SASE 2 respectively.

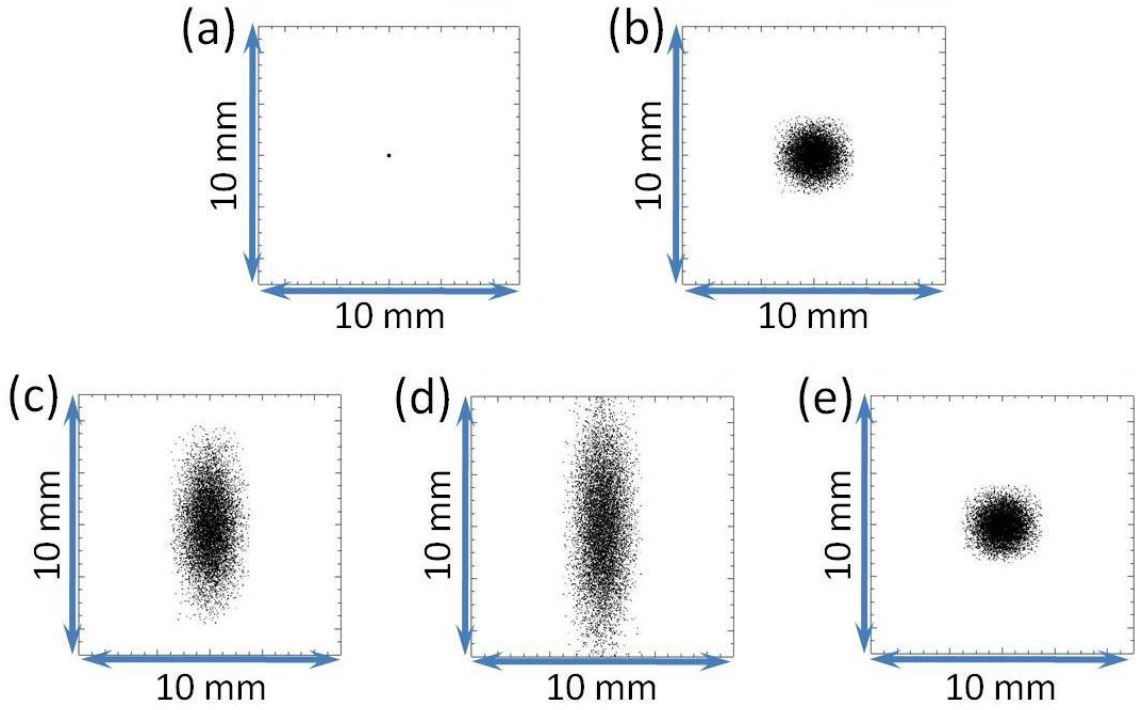

Figure 48: ***footprint of the ray tracing through a DCM (output from the RAY [30]) (a): source point ((16x16) µm² (σ); (37x37) µm² (FWHM)). (b): cross section of the photon beam 100 m after source – (44x44) µm² (FWHM). (c): footprint at the crystal surface (Si (111) @ 5keV) – (2.9x1.16) mm². (d): footprint at the crystal surface (Si (444) @ 30keV) – (4.43x1.16) mm². (e): cross section of the photon beam 1 m after having passed the DCM – (1.17x1.16) mm².***

The goniometers are mounted in a vacuum chamber to avoid X-ray beam scattering in the atmosphere.

Crystal optical scheme analysis

As general information, a first survey of the intrinsic energy resolution of the different reflection planes of two silicon crystals in dispersive arrangement (DCM) is shown in Figure 49.

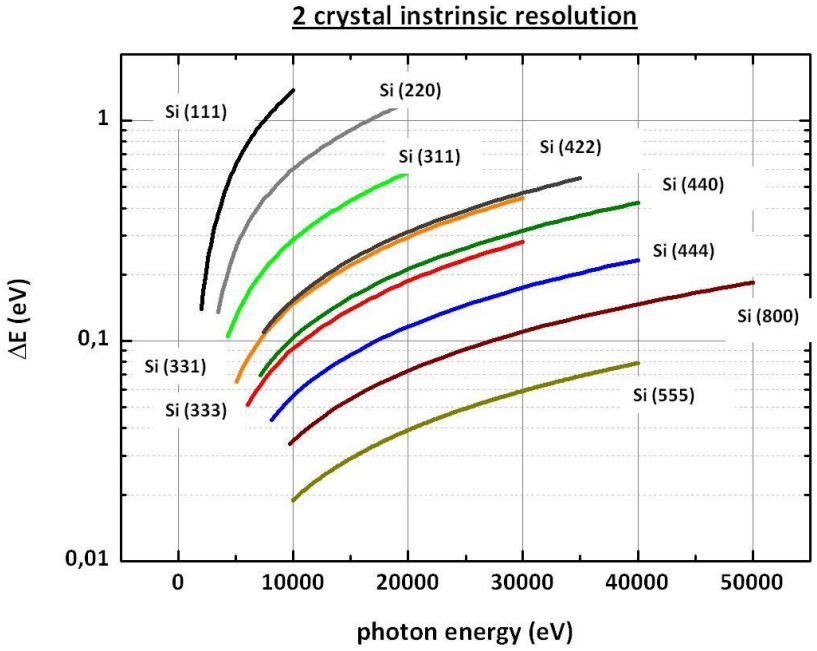

Figure 49: ***survey of the intrinsic energy resolution depending on the incident photon energy of different reflection planes in a silicon crystal (DCM). The curves are generated using REFLEC [30].***

From Figure 49 it is evident that use of higher indexed reflection planes of a silicon crystal result in better energy resolution; but, of course, for lower energies (below 7 to 10 keV) only lower indexed planes lead to any reflection at all. As general information about the required precision of the used goniometer, the Rocking-curves as a comparison for three reflection planes, at the minimum (best possible), medium and maximum (worst) intrinsic energy resolutions are displayed in Figure 50. (The corresponding parameters can be found in Table 1):

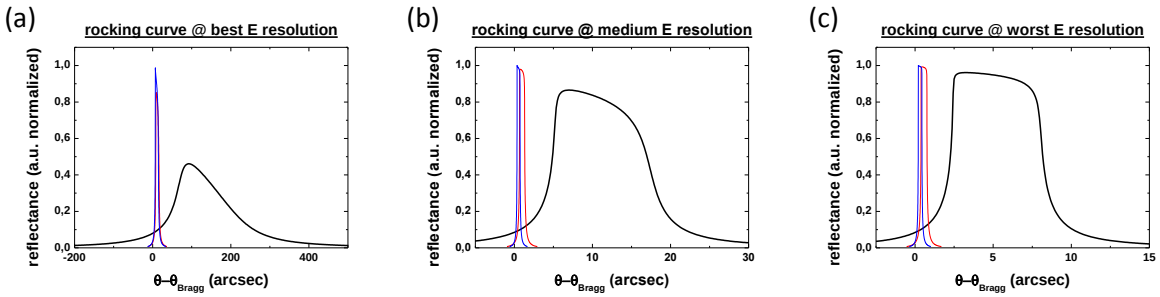

Figure 50: ***Rocking-curves of three reflection planes of a single silicon crystal (generated using [30]). In each case, the black curve corresponds to the Si (111) reflex, red curve to Si (333), blue curve to Si (444) reflex. (a): around the best energy resolution. (b): around the medium energy resolution. (c): around the worst energy resolution.***

The resulting FWHMs of these different rocking curves (Figure 50) around the Bragg reflexes each are summarized in Table 1:

Table 1: ***survey of the FWHM of the rocking curves of different silicon crystal reflexes at three different remarkable points of the intrinsic energy resolution. In the table at each cell the following parameters are given: photon energy (and the corresponding Bragg angle), FWHM of the rocking curve around this angle, relative energy resolution.***

used reflex	best energy resolution	medium energy resolution	worst energy solution
Si (111)	1.978 keV (90°)	5 keV (23.295°)	10 keV (11.404°)
	125 arcsec (FWHM)	10.2 arcsec (FWHM)	4.8 arcsec (FWHM)
	$1x10^{-4}$ ($\Delta E/E$)	$1.2x10^{-4}$ ($\Delta E/E$)	$1.4x10^{-4}$ ($\Delta E/E$)
Si (333)	5.931 keV (90°)	18 keV (19.239°)	30 keV (11.403°)
	7 arcsec (FWHM)	0.6 arcsec (FWHM)	0.3 arcsec (FWHM)
	$8.8x10^{-6}$ ($\Delta E/E$)	$9.4x10^{-6}$ ($\Delta E/E$)	$9.3x10^{-6}$ ($\Delta E/E$)
Si (444)	7.908 keV (90°)	25 keV (18.441°)	40 keV (11.146°)
	4 arcsec (FWHM)	0.3 arcsec (FWHM)	0.2 arcsec (FWHM)
	$5.1x10^{-6}$ ($\Delta E/E$)	$5.6x10^{-6}$ ($\Delta E/E$)	$5.8x10^{-6}$ ($\Delta E/E$)

From Figure 50 and Table 1 can be derived that of course the energy resolution is much better for the higher indexed reflection planes. The widths of the Rocking-curves are quantities for the required goniometer precision which will be applied in the chamber at the K-mono crystal.

A next idea to improve the energy resolution even more, was to make use of an asymmetrically cut crystal. So, in the following we take a look at the energy resolution and transmission of a DCM and a FCM with respect to different angles of asymmetry:

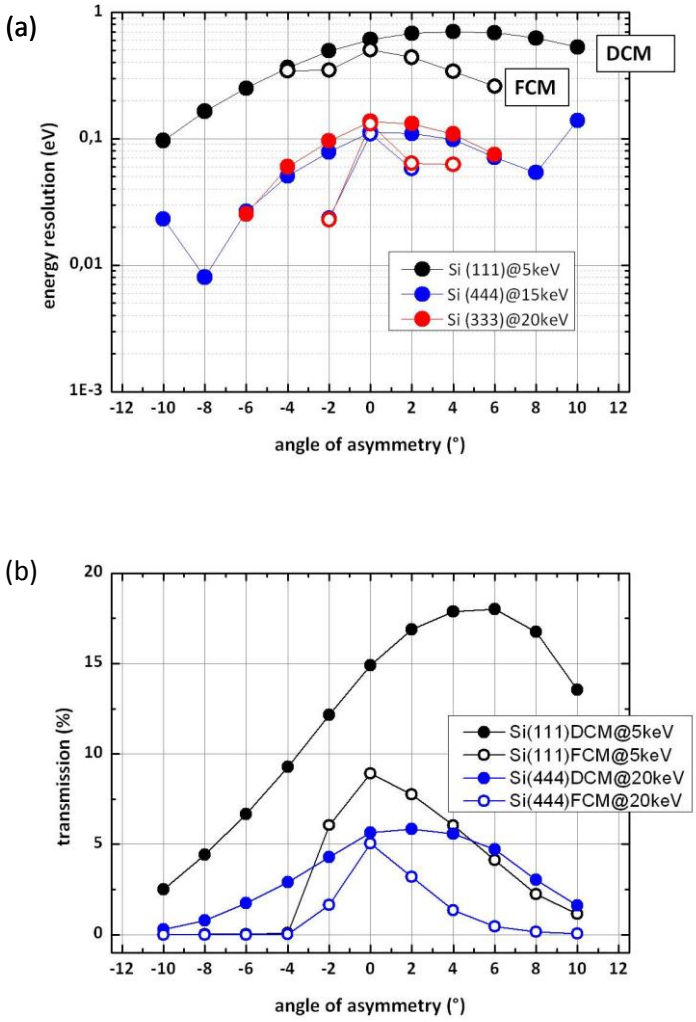

Figure 51: ***(a): absolute energy resolution of DCM and FCM arrangements at different energies inspected using 3 different reflection planes. (b): transmission of DCM and FCM at different energies inspected using 2 reflection planes.***

From Figure 51 we obtain that the use of an angle of asymmetry leads to a fast decrease of transmission. Furthermore, the energy resolution does not increase significantly. Therefore, an asymmetrical cut crystal is not recommended to improve the energy resolution in this case.

In the next step, the energy resolutions using a collimated beam, and a simplified source (*slightly divergent* – (2x2) µrad²), respectively are compared (using RAY, solid and dashed lines, and REFLEC, open and full bullets):

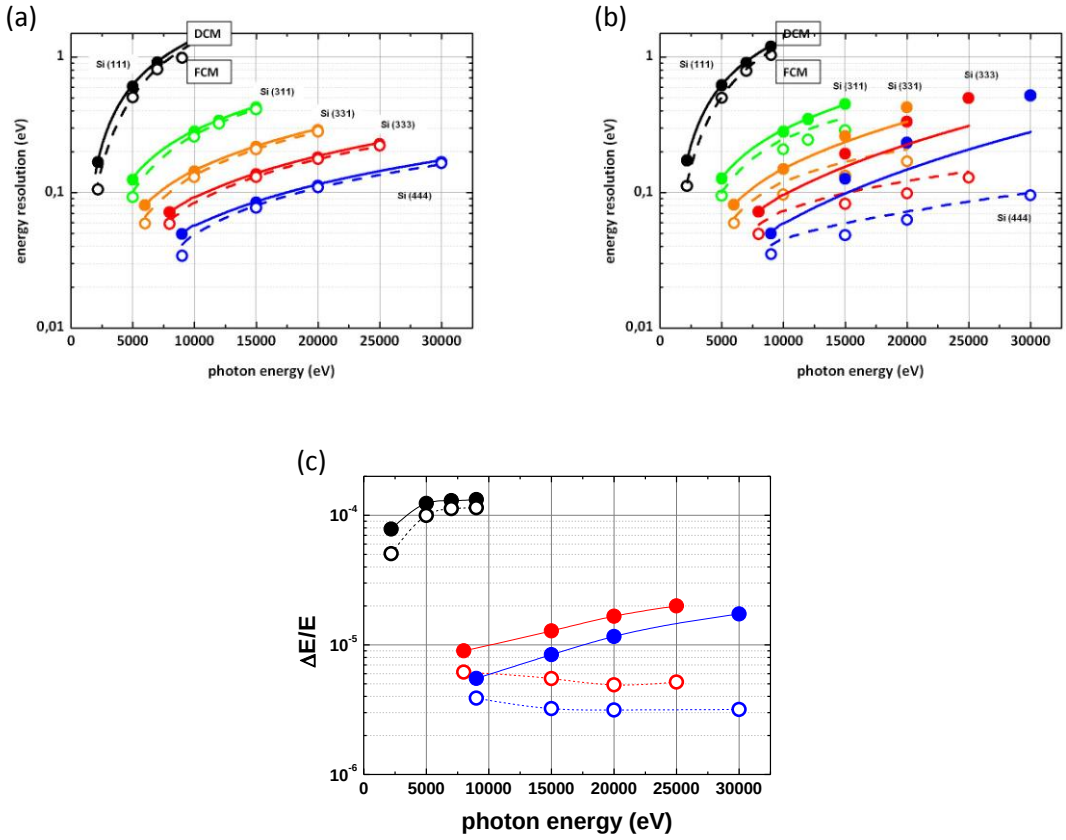

Figure 52: ***survey of the energy resolution of DCM and FCM arrangements as function of the irradiated photon energy. Filled bullets (calculated using RAY) and solid lines (calculated using REFLEC) respectively correspond always to DCM; open/empty bullets (RAY) and dashed lines (REFLEC) correspond accordingly to FCM arrangement. (a): using a collimated beam. (b): using a "divergent" beam (of being (2x2) µrad²). (c): the respective relative energy resolution at three different Si-crystal reflexes (black: Si (111), red: Si (333), blue: Si (444)).***

From these figures one can see that the energy resolution of the device seems to be independently the same for each a DCM and FCM arrangement in case of a perfectly collimated source. But, if a very slight divergence is applied (as certainly will be the case at the European XFEL), the energy resolutions improve remarkably at higher indexed reflection planes in the hard X-ray regime above 10 to 15 keV. For Si (111) reflex in the regime between 2.4 keV up to roughly 10 keV there is no apparent difference. The results of the simulations using the simplified source can be summarized as follows:

- The best obtainable energy resolution for the DCM case is 50 meV at 8 keV using a Si (444) reflection plane; the best for the FCM case is 35 meV at 8 keV ($(\Delta E/E)_{DCM/best} = 6.25 \times 10^{-6}$; $(\Delta E/E)_{FCM/best} = 4.38 \times 10^{-6}$).
- The worst energy resolution for the DCM case is 600 meV at 5 keV using the Si (111) reflection; the worst for the FCM case is 500 meV at 5 keV ($(\Delta E/E)_{DCM/worst} = 1.2 \times 10^{-4}$; $(\Delta E/E)_{FCM/worst} = 1 \times 10^{-4}$).

- The transmission using Si (444) at 9 keV is 4.3% at DCM, and 2.4% at FCM; it is, using Si (111) at 5 keV, 44% at DCM, and 26% at FCM. (these values are obtained using RAY with the parameters listed in the annex (table: Si investigation in Annex))

- It is not recommended in this case to use asymmetrically cut crystals. It causes more complicated alignments. The manufacturing of the crystals is too hard in terms of precision and very time consuming to be worthwhile. Separate crystals for different energy-sets would be required. Moreover, there must be a certain inclination of the second crystal, which causes an even more complicated alignment process. By use of an angle of asymmetry the transmission of the monochromator is reduced dramatically and there is no significant gain in terms of resolution. The only Pro-criterion seems to be that it increases the angle of accepted incoming rays.

- Regarding the use of a DCM in comparison with a FCM it was discovered that the transmission of a DCM arrangement is roughly twice as much as at FCM. At the same time the energy resolution (ΔE/E) of the device is e.g. (using Si (333)-reflex at 20 keV) $5x10^{-6}$ in case of FCM or $2x10^{-5}$ in case of DCM, respectively. As the energy resolution even at the "worst point" is in the range of 10^{-4} using DCM arrangement, this should be already sufficient, if the proposed method (see below, within the part about obtaining the K-parameter theoretically) would be applied.

In the following an output file from the program WAVE [70] is used as source file for our simulations.

Source and Beamline Parameters

For this purpose considerations were made on what should be expected if the spontaneous radiation from just one single undulator segment is inspected. For the simulation the following parameters (electron beam parameters for SASE 1 and SASE 2, see table 2) are used:

Table 2: ***electron beam parameters for SASE 1/2 as taken from the open announcement of simulation code benchmark [71] and personal communication with Michael Scheer.***

Electron energy	14 GeV
Emittance	0.97 mm mrad
Betafunction	32 m
Period length	40 mm
No. of periods	125
Gap-range	10-28 mm

And as electron source parameters:

$\sigma_x = \sigma_y = 34$ µm

$\sigma'_x = \sigma'_y = 1$ µrad (use of σ always corresponds to rms-values)

Using the formulae for the photon source size $= \sqrt{\left(\sigma_{x,y}^2 + \sigma_U^2\right)}$ (each in x- and y-direction), for the

source divergence $= \sqrt{\left(\sigma_{x,y}^{'2} + \sigma_U^{'2}\right)}$ (v.s.) and for the undulator radiation

$$\sigma_U = \frac{\sqrt{2\lambda L}}{2\pi}, \quad \sigma_U^{'} = \sqrt{\frac{\lambda}{2L}}.$$

With the length L = 5 m of one single undulator segment, one obtains the following properties:

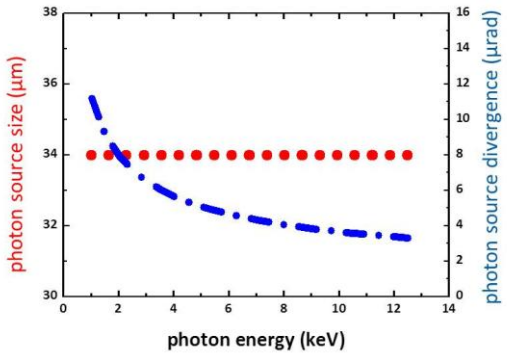

Figure 53: ***the photon source size (red dotted curve) and divergence (blue broken curve) of the calculated undulator, using the parameters mentioned above.***

Figure 53 shows that the source size stays stable over the range of 1 to 13 keV, whereas the source divergence decreases exponentially.

Determination of the K-parameter

This part presents the proposed procedures to obtain the K-parameter by using the channel-cut crystal monochromator. This will be followed by experimental results from beam time at PETRA III at DESY in Hamburg.

Photon-based commissioning of the European XFEL undulators will require a precise adjustment of the K-parameters of all undulator segments and the phasing between these segments. The LCLS approach with a double channel-cut monochromator was found to be a good starting point. In the case of the European XFEL, the large gap setting range and wavelength ranges have to be taken into account. The undulator commissioning spectrometer – the K-monochromator - will analyze spontaneous radiation from single segments up to the full undulator length.

The K-monochromator will be used to select a narrow bandwidth of the X-ray photon beam in order to tune individual undulator segments. This process is called photon beam-based alignment and will minimize the difference in the K-parameters of the undulator segments and optimize the phases between segments. The photon source can be a single segment, two adjacent segments, two distant segments, and up to all undulator segments at once. In case lasing cannot be immediately established, the only way to measure and tune the undulator K-parameters in-situ will be with the K-monochromator [72].

The process in theory

Inspection mode I: fixed K, varied E

A general property of the spontaneous radiation of an undulator is that the flux and the on-axis flux density vary over a certain energy range around the resonance of the undulator; a change of the undulator gap results in changes of the distribution and intensity of the white beam and monochromatic cone, respectively. For linearly polarized X-ray radiation, the undulator radiation intensity distribution (white beam) is a Gaussian. Changing the gap strongly affects the x-ray distribution in the polarized direction. The distribution of monochromatic power is generally a Gaussian (at the first harmonic energy), but narrower than the total power. The central cone width decreases with increasing undulator gap, but not as rapidly as the total power width decreases. Hence, the central cone width takes up an increasing percentage of the total power width as the gap is increased. In case of linear polarization, the width in polarization direction changes, meaning, it gets broader and the peak intensity decreases at the same time. In case of circularly polarized light, the Gaussian broadens in both directions, until one obtains a Donut-kind structure (see figure 62). So, the generated monochromatic energy changes its shape and intensity significantly with change of the undulator gap [73]. This was observed in two ways. First, keep the K-parameter constant (by fixing the undulator gap) and vary the photon energy (by scanning with the monochromator) (Figure 54), second, the other way around (Figure 55):

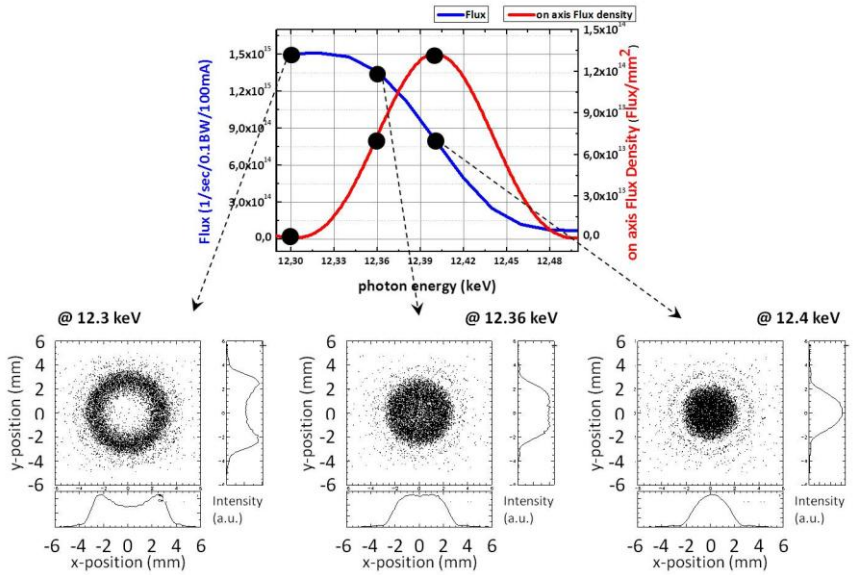

Figure 54: ***Flux and on-axis Flux density depending of the inspecting energy with fixed K-parameter and the respective shape of the footprint at three different energies as an example.***

From this we see, that, if the K-parameter is kept fixed and we inspect the Flux by varying the monochromator (the energy), the Flux decreases exponentially and the on-axis Flux density does not have its maximum at the maximum Flux position. The "on-axis Flux" here means the flux through a pinhole of certain width located at the centre of the X-ray beam. Obviously the on-axis flux changes remarkably during this scan – until we obtain a donut-kind of structure inspecting off-resonance of the undulator.

Inspection Mode II: fixed E, varied K

The same beam shapes appear, if we keep the inspecting energy fixed with the monochromator and vary K.

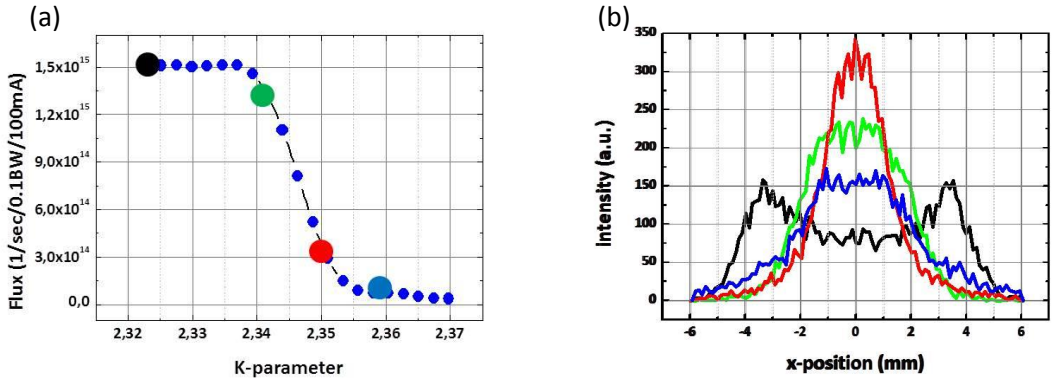

Figure 55: ***(a): Flux depending on varying K-parameter at a fixed energy. (b): the respective horizontal/cross-sectional beam profile at distinguished points at the Flux curve.***

In Figure 55 (right) the different shapes of the horizontal/cross-sectional beam profile at different points at the Flux curve are shown – changing from Gaussian to the donut shape as within the other inspection mode.

In the following we will use this information and propose three different methods of determination of the K-parameter using this mode of inspection (fix monochromator at certain inspection energy, vary the K-parameter).

Method (a): Insertion of a Pinhole

The first idea is to apply a very "direct method" inserting a pinhole of a certain width (in our case we decided to use a pinhole of (1x1) mm²) mounted on axis into the beam in front of the K-Mono. From our simulations we get the result that even at 80% of the maximum the width of the resulting curve is in the range of $\Delta K/K \approx 2.7 \times 10^{-3}$, which is not sufficient (regarding the required precision of $\Delta K/K$ being in the range of 10^{-4}). The resulting flux curve is shown in Figure 56:

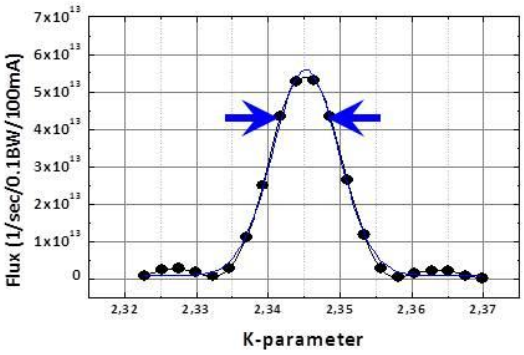

Figure 56: ***Flux curve, into an undefined but sufficiently large detector, straight through a pinhole of size (1x1) mm². The arrows mark the position of around 80% of the maximum – from that method we obtain only $\Delta K/K \approx 2.7 \times 10^{-3}$.***

Method (b): "Donut" method

The next idea is to use a more "geometric" method, applied already at SACLA in Japan. The idea is to kick the electron beam right between the two undulator segments under inspection. In this way the light, which will be produced from the two consecutive or adjacent undulators, will be appearing at two different points. The light will then be analyzed; the K-Mono will be set slightly below resonance in order to use the aforementioned property of the donut structure for each of the two/X sources. So the transferred light through the K-monochromator should result in two structures close to each other (see Figure 57). This method has the advantage of being capable to inspect two segments at the same time and compare them directly.

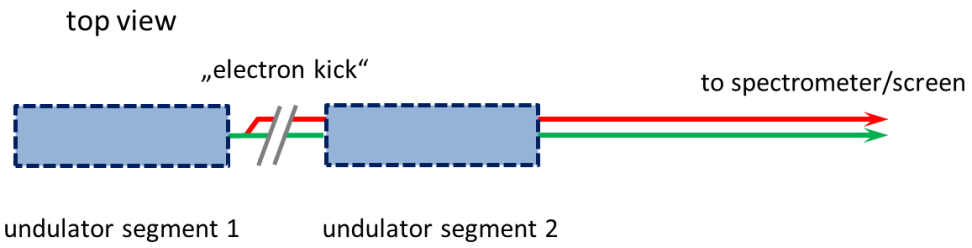

Figure 57: ***„electron-kick"-method in principle. The electron beam is slightly displaced between two subsequent undulator segments, but as much as is needed to separate the resulting spot on and after having passed the K-Mono.***

Here, two undulator segments will be inspected and compared at the same time (the diameter of the donut-structure will be compared and tuned, whereas no information about the electron beam is needed during the measurement):

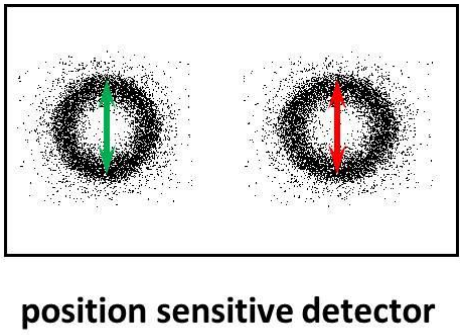

Figure 58: ***picture on a detector after the "electron-kick" or "geometric method": the K-parameter of two inspected undulators should be matched only by detection and analysis of the diameter and shape of the "donut"-structure coming through the monochromator.***

For this method no precise estimations exist, yet. In recent publications the following statements are found:

Tanaka [19] states: "...we roughly have criteria on the tolerance...$\Delta K<10^{-3}$..."

Freund [72] states: "...it is sufficient to measure and compare the K parameter between the segments. ... As we are mainly interested in the measurement of ΔK, the ...quadrupole kick method...will be not sensitive to the absolute electron energy... Following table gives maximal ΔK/K for FEL operation...: ΔK/K = 2.4 (at 1Å).

Method (c): Post-processing

As a last method we propose the use of a "mathematical/post-processing" method which will be sketched shortly in the following. The maximum position of the flux-curve of an undulator is most likely not easy to be determined, as it could be a broader plateau, rather than a sharp peak. On the other hand, the flux curve itself and its slope is certain for each fixed setting of the undulator parameters (as K-parameter fixed or energy fixed with the monochromator).

The procedure in short is: Fix the energy (set the monochromator at a certain energy) and vary K. Then the Flux curve will be inspected using the K-Mono. Derive the Flux curve and then fit the resulting curve with a Gaussian (Figure 59). As the derivative of the Flux curve has a Gaussian-like shape, it is fit with a Gaussian and its minimum value gives the point of the steepest slope in the flux curve – which then can be compared with the one of the next curve at a different energy. For the second curve (red in Figure 59) we have inspected the same method with all the very same parameters except using a second, different photon energy – in order to see if these two flux curves and the respective post processing parameters are sufficiently distinguishable.

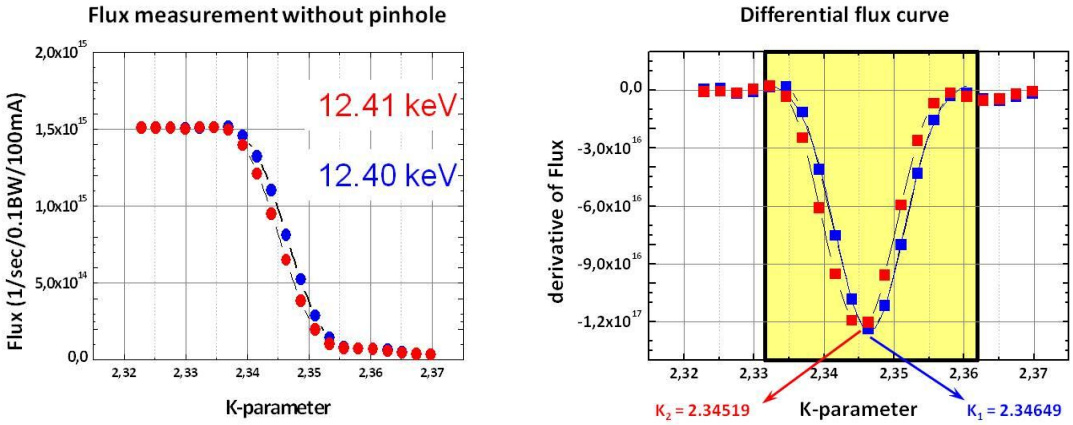

Figure 59: ***"mathematical/post-processing method": (a): use the measured flux curve of the undulator. (b): derive it, and then fit the resulting curve with a Gaussian. From this fit the centroid is obtained, which corresponds to the point of the steepest slope of the flux curve.***

Table 3: ***the resulting ΔK/K resolution and the corresponding energy resolution (ΔE/E) (in order to obtain the desired resolution for ΔK/K an energy resolution of 8x10^{-4} is needed – intrinsically the energy resolution of the crystal (Si (111)) is even better (1.2x10^{-4}), which means, from simulation this method should result in determination of ΔK/K with the desired/demanded precision):***

E_{ph1} = 12400 eV	Center @ K = 2.34649
E_{ph2} = 12410 eV	Center @ K = 2.34519
$\Delta E/E = 8x10^{-4}$	$\Delta K/K = 5x10^{-4}$

With this method and the energy resolution of the monochromator being better than 8 x 10^{-4} (it is around 1.2 x 10^{-4}), which is necessary to get a $\Delta K/K \approx 5 \times 10^{-4}$, we derive that the K-monochromator using the Si (111) reflex is capable to measure or determine the K-parameter in the range of $\Delta K/K \approx 10^{-4}$ and possibly better.

Intermediate result:

Based on the considerations and the simulations which were carried out in the scope of this project, one can conclude that a device consisting of a Si (111) double crystal monochromator arranged in dispersive configuration results in a sufficient energy resolution to determine the K-parameter to a precision of $\Delta K/K \approx 10^{-4}$ and better. This comes from the property of the crystals' intrinsic energy resolution, combined with the beamline parameters and using a realistic (including emittance effects) source file, based on the SASE 1 undulator parameters. So the post-processing method results in a determination of the K-parameter to the aforementioned precision. Hence, this could be the recommended method to determine the K-parameter for each of the undulator segments separately.

The other method, the "donut" method, is proposed, because in this way it is not necessary to have information about the electron beam properties during the measurement (determination of the K-parameter of the undulator segments under inspection), as it would be necessary within the post-processing method. Simulations show that the spatial distribution of the emitted radiation is preserved throughout the monochromator.

Experimentally

In order to check the different proposed procedures to obtain the K-parameter to a sufficient precision, we checked the principles and feasibility at the P01 beamline at PETRA III in Hamburg, Germany. PETRA III (in operation since 2009) is the most brilliant storage-ring-based X-ray radiation source at Germany´s research centre DESY. This facility operates in top-up mode, the storage ring current is kept constant to within 1% or less via frequent injections of particles. The beamline offers high energy resolution in the range from 1 meV to about 1 eV and high spatial resolution in the (sub-) micron regime. The unique possibility that it is equipped with two adjacent undulators, individually tuneable, gives rise to the ideal capability for us to check exactly the proposed schemes mentioned above. In the following, the experiments which were conducted to obtain at least some evidence are described.

The beamline after the two undulator segments and beam-shaping slits is shown in Figure 60. From the left (entrance of the beam) there is a high-heatload (crystal) monochromator (HHM), which is capable to resist the high intensity of the entire X-ray radiation. After that another pair of beam-shaping slits is situated, followed by an Ion chamber, which basically serves for the analysis of the incoming beam. Then there is a High-resolution monochromator (HRM), which consists of crystals as well, but operating at very high Bragg-reflexes. In the end the K-monochromator (chamber containing a channel-cut Silicon crystal) is installed.

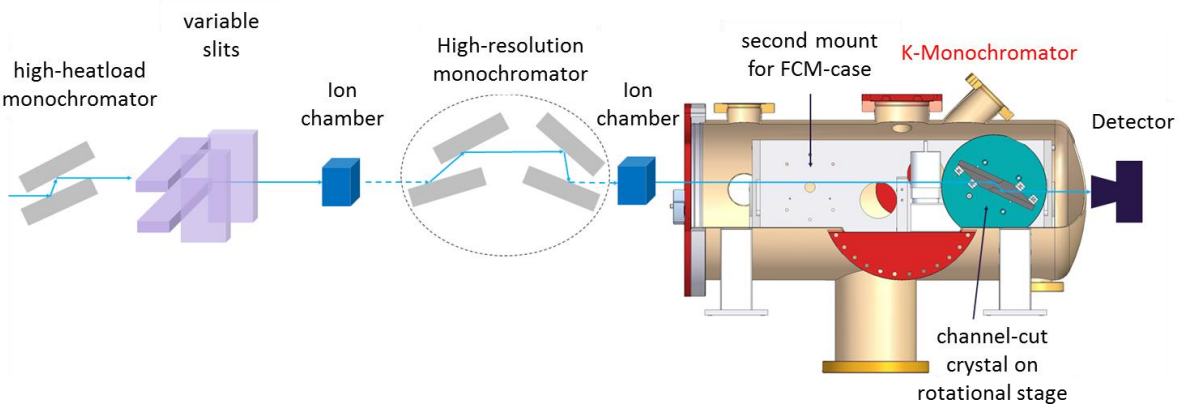

Figure 60: ***beamline testing setup at P01 (courtesy of [74], C. Ozkan and W. Freund, European XFEL).***

As first experiment, the HHM was used, together with the HRM, in order to check, if the Flux-curve could be recorded and distinguished from each other. In general, this very rare opportunity of having two individually tuneable undulator segments should serve as testbed for the electron beam-kick method for inspecting and direct comparison of both at the very same time. Additionally, the procedure to obtain the point of steepest slope from the experimental data should be tested. In principle the setup as shown in Figure 61 is used for this purpose.

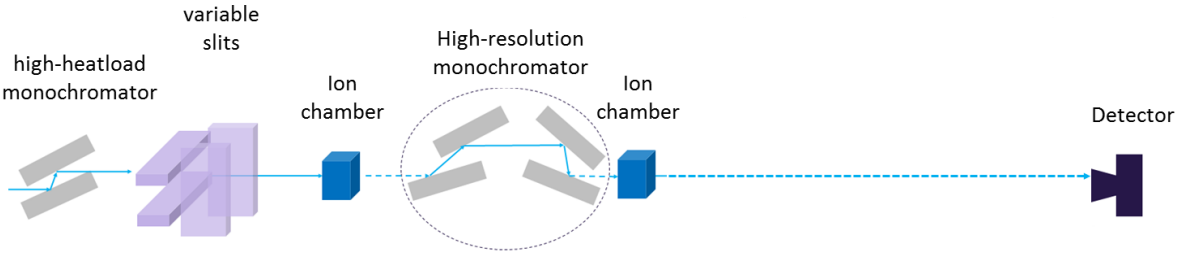

Figure 61: ***setup as for the first proof of principle if the flux curves of the undulators are recordable to a sufficient precision (picture adapted from [74]).***

As outcome of these first measurements we obtained the flux curves of the two different undulators, which are presented in Figure 62.

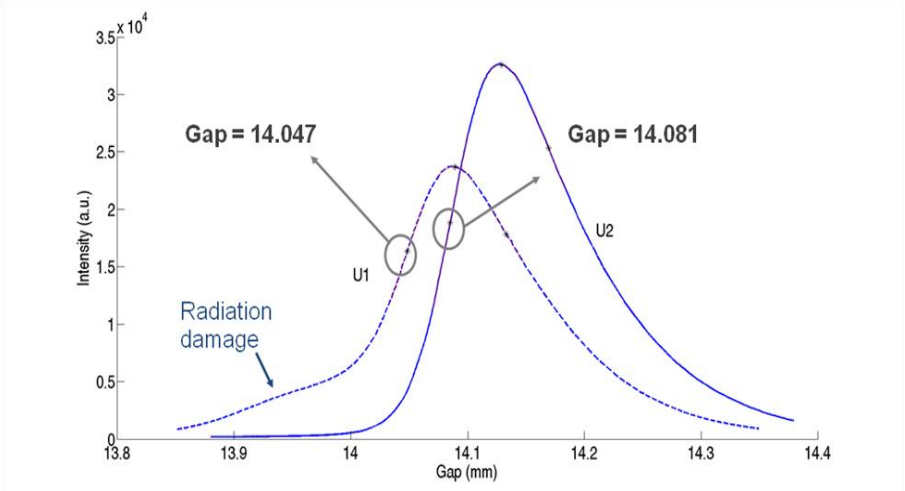

Figure 62: ***resulting curves of gap scanning of the two adjacent undulators (for simulation of two undulator segments as needed for proof of principle of the proposed procedures for obtaining the K-parameter). At these curves, the point of steepest slope is calculated, too – see circles and numbers within the graph (courtesy of [74]).***

As a result from this first test we obtain that the two undulators are obviously not in the same condition. The first undulator (U1) shows already radiation damage, as it is the first insertion device in the 14 PETRA III beamlines. Thus, it is most exposed and most likely to suffer from radiation damage to its magnetic structures. Therefore, for the following undulator scans, only the undulator U2 is used. Unfortunately, because of this difference, the case of having two undulator segments tuned to the same parameters could not be tested at P01.

In the following, the two principles mentioned above should be tested. In order to simulate the 4-bounce-case of the K-monochromator, the HHM and the channel-cut crystal are used (see Figure 63).

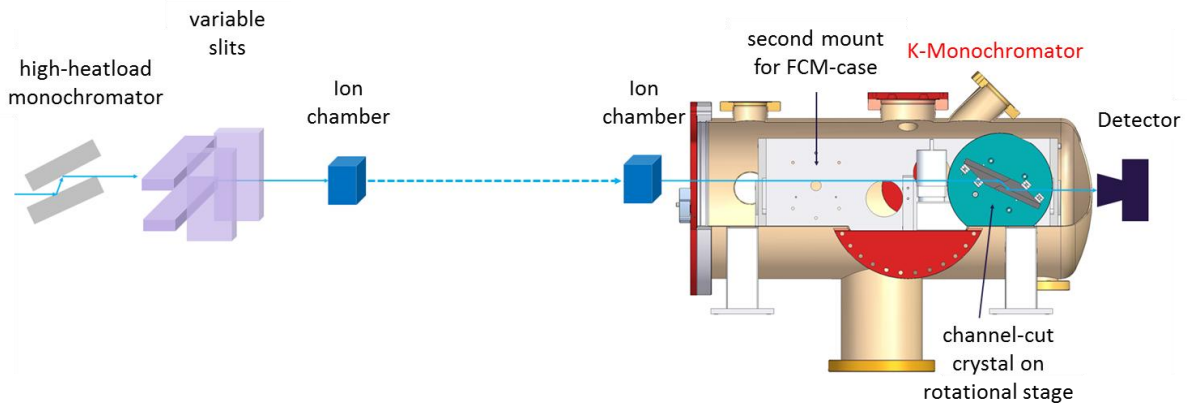

Figure 63: ***setup as for simulation the 4-bounce-case (FCM) – only HHM in combination with the channel-cut crystal of the K-monochromator is used. This setup is the same for the "post-processing" method as well as for the imaging method (picture adapted from [74]).***

At first, the post-processing method was examined. In this case, the monochromators were set to a specific energy and the gap was scanned. The resulting flux signal is shown for 4 settings as to be seen in Figure 64. Here, one can see four different curves. Then the point of steepest slope is

obtained (see inlay in Figure 64, left. The different energy-settings and the corresponding values for the k-parameters (obtained from a table of gap-distance correlated to the k-parameter) are listed in the table on the right.

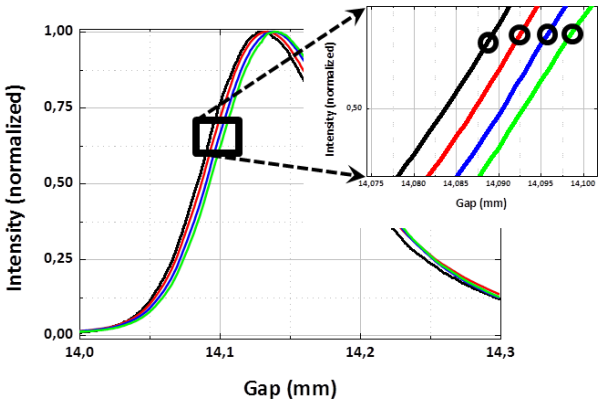

E1 = 14,338.4 eV	k=1.6111
E2 = 14,339.8 eV	k=1.6103
E3 = 14,341.7 eV	k=1.6098
E4 = 14,346.6 eV	k=1.6094

Figure 64: ***Gap-scans at fixed monochromators (HHM + K-Mono). The inlay represents a zoom into the region of points of steepest slope of each individual Flux-curve (marked each with a circle). On the right side the energies at which the monochromator is set and the corresponding k-value is depicted.***

From these curves and the corresponding k-parameters we obtain that the energy difference ΔE/E in the range of 10^{-4} relates to a ΔK/K between 2.5 x 10^{-4} to 5 x 10^{-4}. This correlates well to the simulations described above, as the crystal is capable to resolve ΔE/E within this range at least.

As second approach it was tested if the shape of the beam could be transmitted sufficiently, so that imaging the beam could be used for the alignment procedure proposed for the inspection of two (or even more) undulator segments simultaneously, without knowing the electron beam parameters (which must be considered for any serial examination). So the setup simply contains the HHM in the beam, the undulator is slightly detuned away from the maximum flux by up to 2%. The resulting image is shown on the right in Figure 65. It shows the circular shapes with local maxima in the horizontal when observing the second harmonic at 10keV, as expectable from simulation using SPECTRA [SPE]. (When we observed the fundamental at 10keV, we obtain the local maxima in the vertical; unfortunately we did not record a good image from that.)

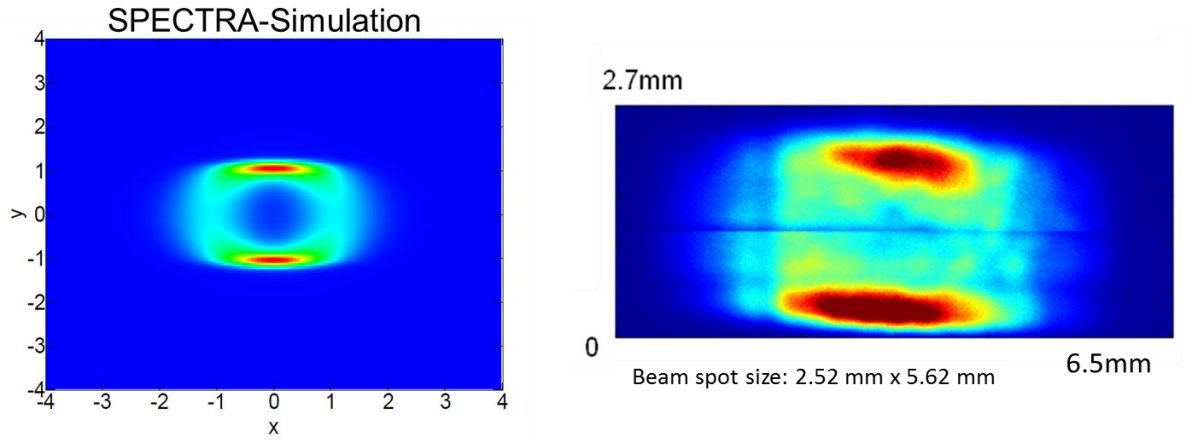

Figure 65: ***picture on the imager. On the left side the shape of the P01 undulator radiation is simulated using SPECTRA [SPE], on the right side the image at the scintillator is shown (the line in the middle is a result of the fact that the first slits before the HHM (in the left before HHM, not shown in figures 68, 69, 71) are set to 1mm. Thus, the slit needed to be scanned over in order to obtain the full image. The resulting two images are clipped together.) (courtesy of [74]).***

With this result it can be stated, that the shape of the beam can be transferred via the crystal monochromator. Hence, the crystal does not influence the shape significantly, the electron-kick-method, described above could be applied to tune the gaps, thus the K-parameter, of the undulator segments sufficiently to get the lasing process started.

Finally, the particle beam could not be changed at this beamline, of course, as it would have influenced all the subsequent beamlines. So it could not be evaluated experimentally the influence on any of the above proposed methods. More simulations about the influence of this parameter will be done in the future. Furthermore, it should be mentioned that the crystal monochromator will be stable enough for the entire purpose. It will surely survive as only spontaneous radiation of a single or two adjacent undulator segments are inspected. Possibly, the radiation of more than two segments should be investigated, but for sure, crystals are the best choice for this purpose anyway.

Conclusion:

The undulator segments of a long FEL undulator can be aligned by matching their K-factor. In order to obtain this matching, the K-factor has to be matched to a precision of ΔK/K in the range of 10^{-4}. Only optimally aligned undulators guarantee a maximum photon flow in the FEL. An advanced method for the optimizing procedure using a 2- or a 4-crystal monochromator is proposed. Both methods were analyzed by ray tracing simulations and by measurements at the P01 beamline at the PETRA III ring at DESY in Hamburg. Simulations as well as measurements at PETRA III showed the applicability of the proposed methods for the optimization of the K-factors at FELs. It could be shown that the application of Si (111)-crystals in the K-monochromator fulfils the demands and the K-factor was determined to a precision 5 x 10^{-4}. The photon energy range, which could be covered, reaches from 2.4 keV up to 40 keV – depending on the reflection plane or higher-order reflexes of the Si (111) used. Si (333)- or (444)-crystals as monochromator crystals improve the situation and deliver K-factors to a precision in the range of 10^{-6}.

Another possibility of taking measurements of the K-parameter is using the "donut"-method, as applied at SACLA at Spring-8 near Osaka for a precise adjustment of FEL undulators. Using this method the K-monochromator was set slightly below the resonance of the undulator, kept constant, and the gap of the undulator was varied. At photon energies below the resonance the lateral intensity distribution of light forms a "donut" like ring-shape. In the simulation, using two undulator segments and applying an electron kick to the beam after the first undulator to form two adjacent beams; two different donut rings were produced. Experimentally, at PETRA III only one undulator was used by modifying the undulator gap until the donut ring shows. This proves that the K-monochromator does not destroy the expected shape of the light.

Parts of the project results are published in:

[Rehanek_SPIE]: J. Rehanek, F. Schäfers, A. Erko, M. Scheer, W. Freund, J. Grünert, C. Ozkan, S. Molodtsov, *"Simulations of diagnostic spectrometers for the European XFEL using the ray-trace tool RAY"*, Proceedings of the SPIE, Vol. 8141, 814109, pages 1-15 (2011)

[Rehanek_pDR]: J. Rehanek, F. Schäfers, A. Erko, *"preliminary design report: Design considerations and simulation on the K-Monochromator"*, technical reports XFEL (2012)

[Ozkan_SPIE]: C. Ozkan, W. Freund, J. Rehanek, J. Buck, I. Zizak, J. Grünert, F. Schäfers, A. Erko, S. Molodtsov, *"Initial evaluation of the European XFEL undulator commissioning spectrometer with a single channel-cut crystal"*, Proceedings of the SPIE, Volume 85040, pages 1-7 (2012)

(poster XFEL-User's meeting 2012)

3.2. Entire spectrum European XFEL (Single Shot Spectrometer)

Once the FEL undulator segments could be matched in this way as described in the previous project chapter, the actual lasing-process starts, the generated radiation needs to be inspected. As described above, the resulting spectrum could vary from shot to shot. In order to cover these variations, X-ray optical elements are required that are capable to deliver/result a spectrum which contains the information with a sufficient energy resolution. At the same time the entire spectrometric system needs to work at very high temporal resolution, meaning that it should result the spectral information from each single shot. Best case, one could obtain this information right during performing experiments, in the sense of an online-device, able to deliver most of the XFEL-generated radiation towards the experiment while getting spectral information instantaneously. This chapter will present the results of considerations and simulation of different approaches to meet the demand of obtaining an image of the entire European XFEL spectrum in a single shot.

3.2.1. Mirror-crystal Design (Yabashi, Spring-8)

The first design, which is described, is a combination of a curved focusing mirror and a crystal. It is a setup proposed by M. Yabashi et al. [75], tested at Spring-8 FEL and now applied at the SACLA XFEL (see Figure 66). The proposed scheme consists in total of two optical elements: the XFEL-beam is delivered directly onto a plane elliptical mirror, which focusses the beam. From the focal point it travels directly to an analyzer crystal; the (555) – Bragg reflex of a silicon crystal is used to have the highest possible energy resolution, expectable as well for the hard X-ray region (see survey in Figure 49, chapter 3.1). By this big divergence delivered into the silicon crystal, ideally all different energies should be dispersed, which results the entire spectrum of the single shot. This scheme was simulated using RAY [30].

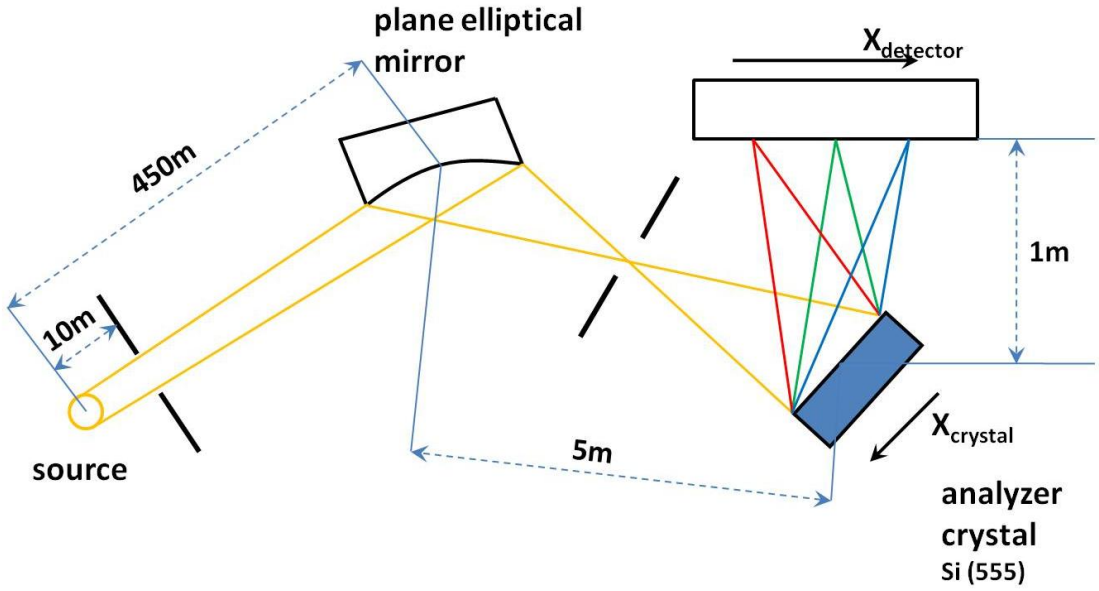

Figure 66: ***schematic sketch of the top view of the design as proposed by Yabashi et al. [75], using the approximate distance between the source and the device at the European XFEL. The slits are just put during simulation for inspecting the cross-section of the X-ray beams; they are of no importance for the entire device itself.***

The parameters of the setup which were used for the simulations are given in Table 4:

Table 4: ***Parameters for simulation of the design proposed by M. Yabashi***

Source		**Plane elliptical mirror**		**Crystal**	
$\sigma_{x,y}$	17 µm	size (X x Y)	(500 x 60) mm^2	material	Silicon (555)
		grazing incidence angle	0.4°		
$\sigma'_{x,y}$	1.1 µrad	entrance arm length	450 m	size (X x Y)	(30 x 5) mm^2
		exit arm length	0.5 m		
photon energy	10 keV	coating	platinum 30 nm	Bragg angle	81.3°
		roughness	0.3 nm (rms)		

There different ways of declaring or rather determining the achievable energy resolution: on very limiting factor is always the detecting or imaging device. More precisely, the detector pixel size is mostly a crucial factor of an entire spectrometric device. So one way of simulating the "real" energy resolution of a system is to "feed" into the simulation a so called "white band", a broad band of continuous energies, and put a slit of the size of a single detector pixel at the detector position. After ray-tracing this setup, a certain bandwidth is delivered through the entire setup and finally through the slit. This, or rather then for example it's FWHM, could determine the value of energy resolution. If the detector pixel size is no question, as for example the image is far beyond being at the limit of the pixel size itself, one could trace more than one discrete energies through the setup and have a look at the image. As long as they are well distinguishable on the imager, the energy spacing between these could be a value of possible energy resolution.

In this case, the idea is: as soon as the dispersed energy spots are not anymore clearly distinguishable, this should mark the ultimate energy resolution of the spectrometer. A common approach is to decide for "separability" is the FWHM of a single broadened energy peak at the imager. From all previous simulation we obtain some scaling, how many millimeters or even micrometers correspond to how many electronvolts or millielectronvolts and by simple combination of this knowledge with the obtained FWHM of the traced single energy, a value for possible energy resolution is finally determined (see Figure 68 (b)).

Hence, the simulation to determine the ultimate energy resolution of this proposed setup was strated, using RAY [30], at energies of 10 keV ± 50 meV, then slightly scaling down the differences of the discrete energies, to compare directly with the results of Yabashi's results (see Figure 67).

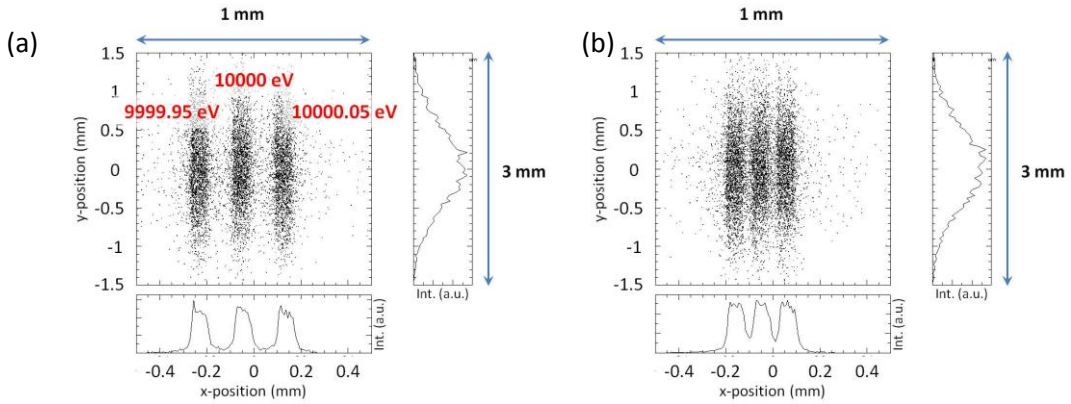

Figure 67: ***Beam image at the detector located at a distance of 1 m after the analyzer crystal. (a): the energies inspected are 10 keV ± 50 meV – marked by the red numbers of 10,000 eV in the center, ± 0.05 eV right and left. (b): the minimal energy difference of ΔE = 30 meV, where energies are still clearly distinguishable – this number is a totally subjective perceived value as it comes simply from "looking at the resulting ray tracing image".***

Additionally the influence of slope errors (during manufacturing of the mirror) on the resolution was investigated, as this is often a possible source of degradation of the best possible energy resolution (see Figure 68 (a)):

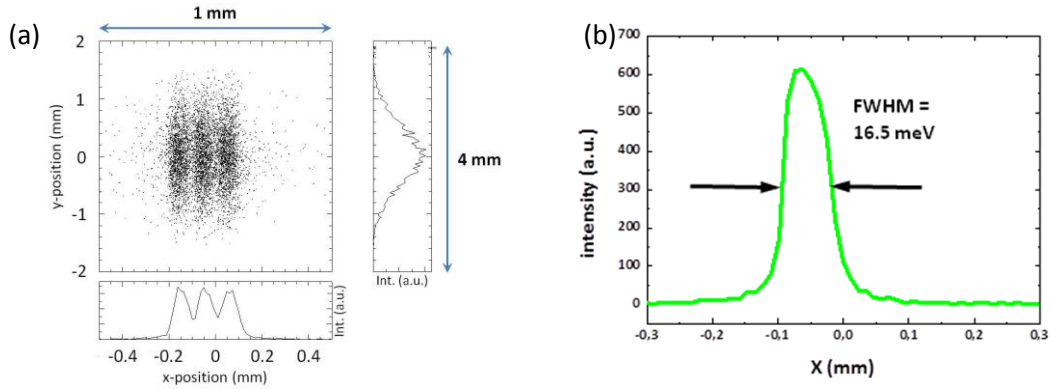

Figure 68: ***(a): beam footprint at the detector for E_{photon} = 10 keV ± 30 meV. Applied slope errors (@mirror): 0.5'' x 1.5'' (saggital x meridional), which are reasonable slope errors, taken from personal communication with Frank Siewert at BESSY II in 2011. (b): intensity distribution of the single "dispersed" energy of 10 keV as function of x-position at the detector. The FWHM yields the minimum possible energy spacing which should be distinguishable, hence, it results the energy resolution of the entire system.***

In order to compare these results with the ones from Yabashi's paper, one simply has a look at his experimentally found results (see Figure 69):

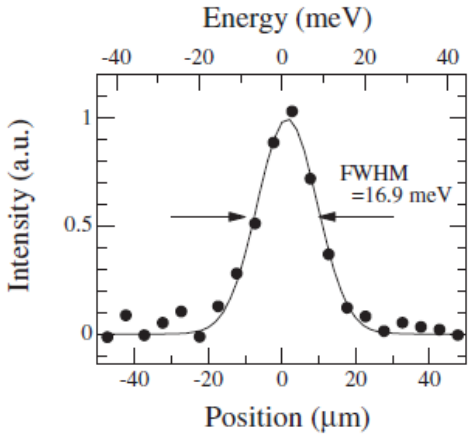

FIG. 3. Spatial profile of dispersed beam (lower axis). The corresponding energy scale is shown on the upper axis.

Figure 69: for comparison of the simulation with the actual data, obtained experimentally. (picture taken from [75])

From these simulations a limiting energy spacing of 30 meV was obtained (for the distance of 1 m after the analyzer crystal). The FWHM of the intensity distribution at 10 keV was measured to be 16.5 meV, which is comparable with the FWHM = 16.9 meV obtained experimentally by Yabashi et al. [75] (see Figure 69).

This apparent discrepancy (between the statement of limiting energy spacing of 30 meV and resulting possible energy resolution of 16.5 meV) comes from the fact that at the ray tracing resulted image simply the “points of impact” of a photon are shown, without giving a weighting intensity wise, yet. In the graphs below and at the side of the simple distribution a simple addition of the channels (vertically for the graph below, horizontally for the graph on the side) is represented, which could in lead to misunderstanding in some cases. One needs take care clearly how to determine the ultimate energy resolution; best, always the procedure of how to obtain any value should be stated and communicated with all them it may concern for any project.

From further variation of the influence of slope errors, one can state that the slope errors of the used mirror should be smaller than 1.0 arc seconds, so these errors would have no significant influence on the resolution. The current state of the art is around 0.3 arc seconds [76].

3.2.2. RZP-Design (Erko, HZB)

The second design considered for the single shot spectrometer applies a reflection zone plate (RZP), which combines focusing and reflection in one element. Additionally its application results dispersion as it can be considered as VLS-grating, focusing in two dimensions (see chapter 2.3.2.2).

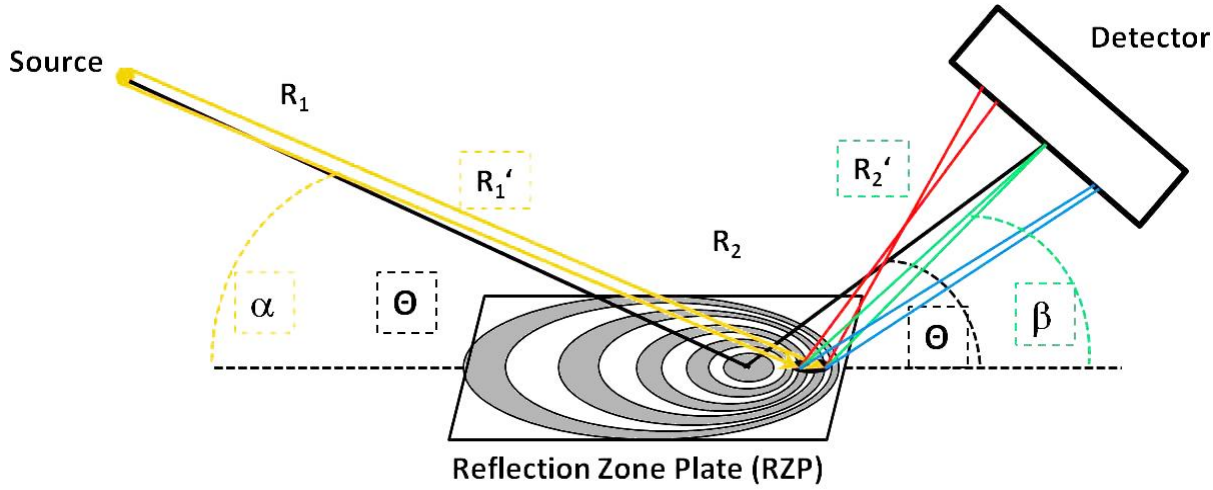

Figure 70: ***Simplified sketch of the working principle of a reflection zone plate. Illumination of an off-axis part of the zone plate suppresses the 0th order and helps obtain the spectrum (indicated by 3 different beams) at the detector. This is done simply by delivering the light of the specular reflection to another point in the detector plane than this of any higher reflected order of diffraction.***

The working principle of a RZP is shown in Figure 70. An off-axis part of the zone plate is illuminated in order to suppress the influence of the 0th order reflection in the detector plane. Its contribution is suppressed simply in that way that the light originating from the specular reflection of the surface (0th order) is delivered to a different position in the detector plane than that of any reflected diffraction order of the structure on the surface itself. (The detector plane is assumed to be perpendicular to the incident ray of the design energy.) The term "off-axis" means in this context the use of a part of the entire RZP-structure, which does not include the center of the design structure (see Figure 70, here it is depicted by the black area illuminated). In this case, the +1st order of the RZP is used. This method allows obtaining the spectrum of the incident beam at an imaging-detector. The zone plate is optimally designed for one certain energy, which is then focused at the desired point (green lines from the illuminated area to the detector). It focuses the differing energies around this "center energy" at different points in space (red and blue lines, red gets focused before, blue behind the detector plane; note, the differences are dramatized). The design of the reflection zone plate can be described by the following formulae (coming from geometry):

Input angle: $$\alpha = \tan^{-1}\left(\frac{R_1.\sin\Theta}{R_1.\cos\Theta + x}\right)$$

Exit angle: $$\beta = \tan^{-1}\left(\frac{R_2.\sin\Theta}{R_2.\cos\Theta - x}\right) = \cos^{-1}\left(\cos\alpha - \frac{\lambda}{d}\right)$$

Average grating period: $$d = \frac{\lambda}{(\cos\alpha - \cos\beta)}$$

For the ray tracing simulations a symmetrically designed zone plate ($R_1 = R_2$) was considered. Figure 71 shows a detailed sketch of geometrical parameters of the RZP as it is necessary to simulate an RZP used as dispersing element, not simply as focusing element reasonably.

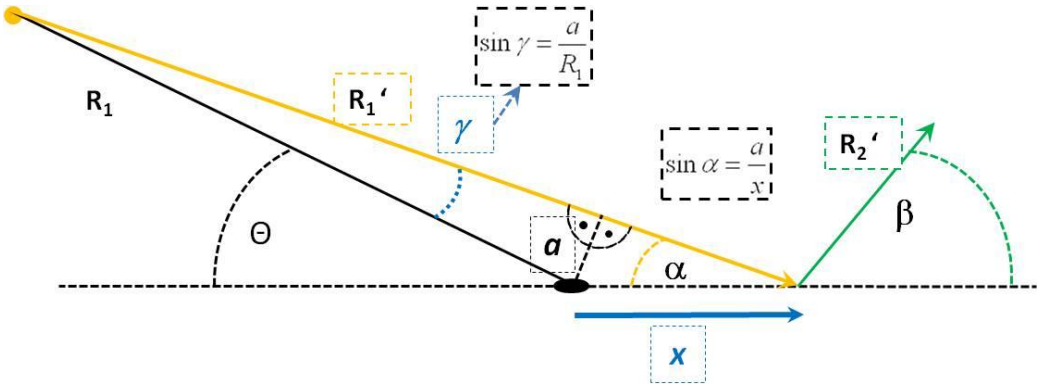

Figure 71: ***side view; in order to illuminate the off-axis part, the source is turned by an angle of γ (here only the center wavelength is depicted): the determination of the parameters for simulation.***

The displacement of the incident X-rays for simulation with RAY needs to be figured out, previously to any simulation made. The mentioned displacement needs to be applied to the simulation by displacement or rather "angular misalignment" of the source. There were different methods tried out to "illuminate" an off-axis part of the structure during simulation. One possible option is to leave the source stable but shift the RZP. But this means a more complicated movement of the entire setup: as the simulation code RAY assumes always the center of the designed RZP as "used", everything (all distances and angles) relates to it geometrically. So then the distance to the detector could be slightly shifted, the incoming angles at the actually illuminated part of the structure can be changed. Another method would be to increase the entire angle of emitted rays from the source by increasing the source divergence and then placing a slit of the right dimensions and at the appropriate position to "cut out" the desired divergence and position at the RZP-structure as wanted. But this gave rise to other problems: as RAY is designed to simulate X-ray optical beamlines as realistic as possible, the optional slit has as well diffractive properties included. So the incoming light gets diffracted at the edges of the slit, which then led to images at the detector which required interpretation in a more complex manner than necessary. Another disadvantage of this method is that a lot of rays are lost as cut out by the slit. This leads to a very high number of rays in order to get any reasonable results from the simulation (otherwise it would result bad statistics, the result could be questionable as not enough rays could be traced…).

Hence, in this specific case, one starts with the following parameters, which were used to define the setup:

α (actual angle of incidence at the zone plate part) = 0.2°

E (photon beam energy) = 10 keV

d_{av} (average grating period) = 100 nm

results in:

$$d = \frac{\lambda}{(\cos\alpha - \cos\beta)}. \Rightarrow .\beta = 2.861°$$

$$\Theta = \arctan\left(\frac{1}{\left[0.5\left(\frac{1}{\tan\alpha} + \frac{1}{\tan\beta}\right)\right]}\right). \Rightarrow .\Theta = 0.3739°$$

β - actual exit angle

Θ - angle of incidence at the center of the zone plate for the design

For the design of the reflection zone plate for our simulations (of the displacement or turning angle of the source γ) we obtain the geometrically derived parameters (from Figure 5) simply by following these steps:

$$x = \frac{R_1 \sin\Theta}{\tan\alpha} - R_1 \cos\Theta$$

$$a = x \sin\alpha$$

$$\sin\gamma = \frac{a}{R_1}$$

And the actual distances R_1' and R_2' respectively:

$$R_1^{'} = \frac{R_1 \sin\Theta}{\sin\alpha}$$

$$R_2^{'} = \frac{R_2 \sin\Theta}{\sin\beta}$$

γ (angle of turning the source for simulations) ≈ 0.1739° ≈ 3.039 mrad

$R_1' \approx 280$ m

$R_2' \approx 20$ m.

As source, the aforementioned parameters used for simulating the Yabashi design were applied here as well ($\sigma_{x,y}$ = 17µm; $\sigma_{x,y}'$ = 1.1 µrad) – for the sake of comparability. These values are given as rms, as RAY calculates mostly with them. Ray tracing delivers the 2D scatter (distribution) of the beam at the imaging detector. The results for E_{photon} = 10 keV ± 10 meV are shown in Figure 72 as footprint at the detector plane and the respective intensity distribution:

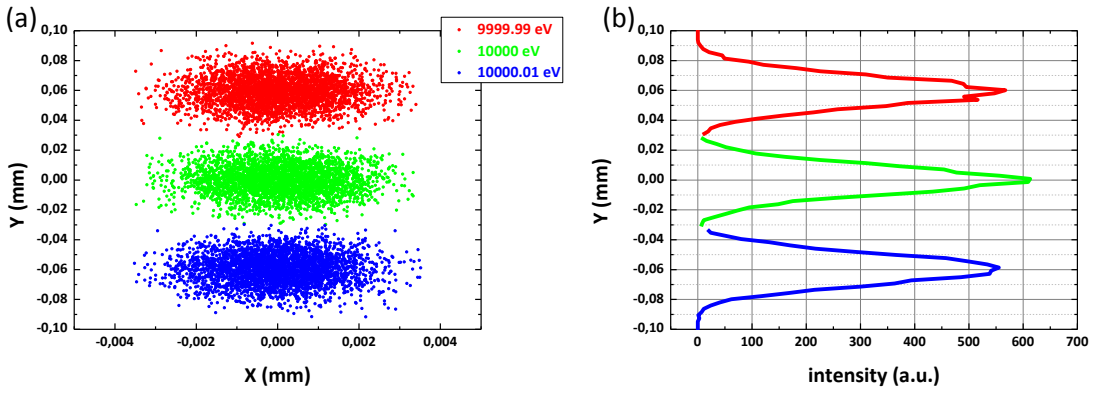

Figure 72: ***(a): Footprint at the detector for the photon energies of E = 10 keV ± 10 meV. (b): intensity distributions along Y-position (of the corresponding energies).***

Assuming an average grating period at the zone plate of 0.1 µm, a minimal energy spacing of 10 meV / 60µm (which is clearly distinguishable at a distance of 20 m after the zoneplate) and a FWHM of 3.2 meV, were obtained.

The same simulations for the lower energy of 1 keV and a zone plate with an average grating period of 1 µm delivered a minimal energy spacing of 1 meV / 60µm (clearly distinguishable at distance of 20 m after the zoneplate) and a FWHM of 0.327 meV.

This shows that the zoneplate for the lower energies could be designed with the very same parameters (as these two are exemplarily chosen by construction to be applied for two ranges of energies of just an order of magnitude difference). The only difference in this case is, in fact, the assumed average grating period for simulations; which however certainly needs to be adapted for the real fabrication. Zone plates for both (lower and higher energies) can be placed at the identical position after the beam, while the detector position remains the same. These shall be realized in different ways. The reflection zone plate for the high-energy range could be manufactured using (diamond or probably DLC- coated) multilayers. The low-energy reflection zone plate can use a total external reflection silicon substrate with probably another appropriate coating. The matter of coating of X-ray optical elements will be described in detail within the next sub-chapter about an RZP spectrometer with certain requirements. First successful tests for hard X-ray RZPs were conducted at synchrotron radiation (BESSY II) in 2011 [77].

A short comparison of these two designs of the single shot spectrometer is given in the Figure 73 (for the sample energy of 10 keV):

	Crystal design	**RZP design**
resolution ΔE	30 meV / 100 µm	10 meV / 60 µm
dispersion	300 meV / mm (1 m after Crystal)	167 meV / mm (20 m after RZP)
FWHM	16.5 meV (55µm)	3.2 meV (20µm)
slope errors	< 1.0 arcsec (state of the art: 0.3 arcsec)	0.1 - 0.2 arcsec (estimated)

Figure 73: comparison of the different designs for the single shot spectrometer (@10 keV)

The ray tracing tool RAY was successfully used to perform simulations of the possible diagnostic spectrometers for the European XFEL. For the single shot spectrometer two setup designs were simulated so far. The calculations of the crystal design in a highly convergent beam resulted in a resolution of FWHM = 16.5 meV (at a photon energy of 10 keV), which is in accordance with the experimental results obtained by Yabashi et al [75]. A set of reflection zone plates could cover the full energy range of the SASE 1, 2 (E_{photon} = 3 - 25 keV) and SASE 3 (E_{photon} = 0.28 - 3 keV). Their performance is shown in principle at photon energies of 10 keV and 1 keV respectively. The energy resolutions (FWHM) are 3.2 meV at the photon energy of 10 keV and 0.327 meV at the photon energy of 1 keV.

Actually, there is another possible option for application of this device. The principle is shown for the case of soft X-ray radiation (see Figure 74). Basically, the idea is to make use of a RZP for online diagnostics of the FEL pulses at the European XFEL in Hamburg. The SASE 3 undulator delivers soft x-ray radiation in the energy range between 0.26 keV and 3 keV. A double (plane) mirror arrangement

at a variable grazing incidence angle creates a vertical offset from the direct FEL-pulse. It leads the beam to the monochromator as well as the user experiment.

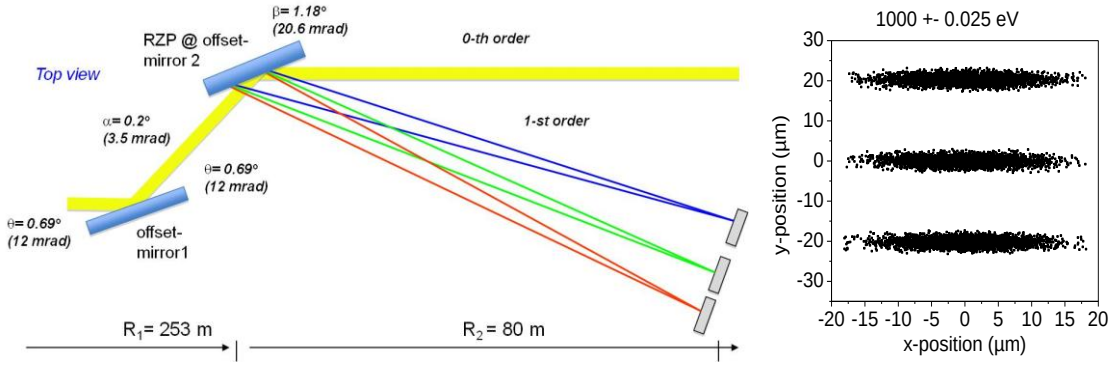

Figure 74: ***(Left): schematic setup of the RZP spectrometer for single shot diagnostic of XFEL pulses; (Right): result of ray tracing simulation. (Ray trace-parameters: point source with the size of (34µm)² (FWHM) and with divergence of 1 µrad², RZP: R_1 = 253m, R_2 = 80m, "d_{av}" = 160 lines/mm, length = 155mm) Spot pattern at the detector for three energies of 1 keV ± 25 meV). A detector with a pixel size of 20 µm is sufficient to obtain an energy resolution E/ΔE = 40 000 (picture taken from [78]).***

When the second mirror is structured with a zone plate, the zero-order beam path to the experiment is not affected. The 1st order diffracted beam will be spatially separated from the zero-order beam and the dispersed radiation hits a detector array. To prevent damage of the detector, the diagnostic spectrometer structure should have low diffraction efficiency. Therefore, the modulation profile of the mirror surface should only be on the order of 1-2 nm. Low efficiency of the RZP will not affect the primary beam too much, but is sufficient for the monitoring purpose. In this way one could obtain a very useful device for getting the entire spectral information from shot-to-shot of the XFEL, without damaging the detector.

Another emerging option of the use of an RZP-structure with higher efficiency would be conceivable in combination with a slit. This slit would be positioned in the focal plane of the RZP, which then is acting as an exit slit of a monochromator to select a certain wavelength out of the dispersion plane. In this case, most likely the energy resolution must not be that high.

In Figure 74, right side, the calculated energy resolution of such a device is plotted. This result was obtained by raytracing [30] the proposed optical setup. Three closely spaced energies of 1000 eV ± 25 meV are spatially separated at the detector by 20 µm. Hence, a moderate detector pixel size of 20 µm in dispersion direction is sufficient to obtain an energy resolution of E/ΔE = 40,000. Nevertheless, to provide necessary time resolution, the energy resolution of the spectrometer must be optimized to the FEL pulse duration.

3.2.3. Bent crystal (Zhu, LCLS)

A third option is currently still under investigation and will be fully developed and documented within a follow-up project in collaboration with the colleagues of the European XFEL GmbH within the year 2014. In figure the setup in principle is shown as proposed by [79]:

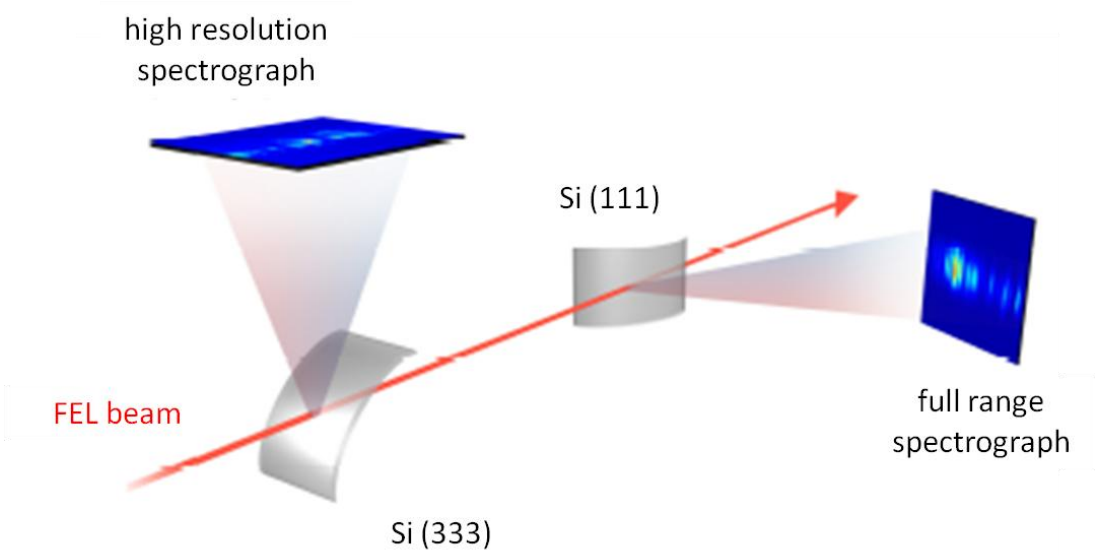

Figure 75: ***bent crystal setup as proposed by D. Zhu for an online single shot spectrometer at the European XFEL (picture taken from [79]).***

This setup would allow for a possible full spectral range by diffraction from the second Si (111) crystal at lower energy resolution and at the same time spectral information of very high resolution by turning the Si (333) crystal into the beam. So far this is proposed for the hard X-ray range, but this will be further investigated within the mentioned collaboration project within the next year (2014).

Conclusion:

Lasing FELs produce pulsed radiation with ultra-high intensity in a broad spectral composition. The spectrum varies from shot to shot. In order to monitor the spectrum simultaneously, special optical devices are necessary. Three different optical approaches of such a High-Resolution Single-Shot Spectrometer (HR-SSS) were tested by simulation to operate as analyzing tool for XFEL radiation. Within the conducted simulations, the RAY software was tested extensively.

A curved mirror-crystal based installation was used at the SPring-8-FEL SACLA in Japan. The simulation was performed using the BESSY raytracing program “RAY” and delivers a limiting energy spacing of 30 meV and an energy resolution of 16.5 meV for the SACLA spectrometer. Experimental measurements result in a possible energy resolution of 16.9 meV. Hence, a good agreement of simulation and experimental results could be shown.

A Reflection zone plate (RZP) spectrometer designed and produced at the HZB in Berlin is much more compact and easier to handle. It is proposed for the first time as a spectrometer for Free Electron Laser sources. It is characterized by a limiting energy spacing of 10 meV and delivers an energy resolution of 3.2 meV.

A bent crystal spectrometer proposed at the LCLS in Stanford is under development. Extensive simulations will be carried out in the near future. A resolving power of 42000 is reported at a photon energy of 8.3 keV [79].

Further testing of an RZP-structure brought directly into the FEL beam is inevitable; to preserve the structure from damage, coating of DLC (diamond-like carbon) or direct writing into a diamond crystal are potential approaches.

Parts of the project results are published in:

[Rehanek_SPIE]: J. Rehanek, F. Schäfers, A. Erko, M. Scheer, W. Freund, J. Grünert, C. Ozkan, S. Molodtsov, *"Simulations of diagnostic spectrometers for the European XFEL using the ray-trace tool RAY"*, Proceedings of the SPIE, Vol. 8141, 814109, pages 1-15 (2011)

[Rehanek_SRI]: J. Rehanek, F. Schäfers, H. Löchel, A. Firsov, J. Grünert, W. Freund, C. Ozkan, S. Molodtsov, A. Erko, *"A case study of novel X-ray Optics for FEL sources"*, Journal of Physics: Conference Series, Volume 425, 052013, pages 1-4 (2013)

Poster: Rehanek, J; Schäfers, F; Firsov, A; Grünert, J; Freund, W; Ozkan, C; Molodtsov, S; Erko, A: *"A case study of novel X-ray Optics for RIXS experiments at the European XFEL"*, DESY/XFEL Users' meeting Hamburg, Germany, 25.01.2012 - 27.01.2012 (2012)

4. X-ray Optics for spectroscopy with Free Electron Laser radiation

This chapter concentrates on experimental challenges during developments and experiments using FELs. It presents two applications of RZPs for totally different purposes.

The first part presents the application of a Reflection Zone Plate as the core of a spectrometer, which is designed to address a single element (energy) or dedicated parts of the spectrum of an experiment, which is conducted at the Linac Coherent Light Source (LCLS) in Stanford. The challenge of that described spectrometer is to obtain a spectrum out of a low quantum yield fluorescence experiment.

The second project deals with the application of RZPs as sole elements forming an entire beamline, which allows for obtaining the spectrum of Resonant Inelastic X-ray Scattering (RIXS) experiments. The demands to be met in this specific case are obtaining a broad range of energy at a very high resolution at the same time. The advantages and disadvantages of "classical optics" on the one hand and the RZP-solution on the other hand are presented. Additionally, the limits which are generally possible to reach with these optical elements are discussed.

4.1. Spectrometer for highly dilute materials using FEL radiation

This chapter describes the development of a high transmission RZP spectrometer for fluorescence detection at the Mn edge from first ideas to extensive simulation to first experiments with this spectrometer; furthermore, from the first experiment in 2012 accrued ideas on how to improve the entire setup efficiency wise. This was then further developed and already in a follow-up experiment at LCLS tested and applied in the end of 2013. Hence, this chapter presents an actual experiment and the demands/requirements which should have been met with the shown device.

"Although the global demand for energy is steadily increasing, most of the current sources of energy are either nonrenewable, nonsustainable, or contribute toward greenhouse gases in the environment. In addition to wind power and biofuels, solar energy is a renewable and clean alternative energy source, but current methods used to convert it into transportable fuels are costly and inefficient. However, solar energy is used efficiently in Nature via the process of photosynthesis in plants, cyanobacteria, and algae." [80] – This is the motivation for the next project which will be described here.

The evolution and detection of O_2 within the process of photosynthesis is under investigation for several decades already. Research results regarding this process can already be found in publications of P. Joliot and A. Joliot in 1968 [81] and 1969 [82]. Their colleague B. Kok finally proposed in his publication of 1970 [83] the steps of development until the release of Oxygen from photosynthesis as a series of electronic states S_i^{i+}.

To summarize, the overall process of photosynthesis can be shown by the simple equation:

$$6CO_2 + 12H_2O + light \longrightarrow C_6H_{12}O_6 + 6H_2O + 6O_2$$

carbon dioxide — water — glucose — water — oxygen

Even if all life on earth is depending on this process, only a small part of the incoming energy is actually used for photosynthesis. Roughly 50% of the energy coming from the sun is lost for evaporation of water, 15% is reflected and approximately 32% passes through the leaves just untouched. Hence, only 2% to 3% of the incoming energy can be trapped and finally used for photosynthesis. But still, "the photosynthetic splitting of water (i.e. oxygen evolution) is the source of nearly all of the O_2 in the atmosphere, and takes place in the **o**xygen **e**volving **c**omplex (OEC), which is located in the multisubunit membrane protein complex Photosystem II (PSII). The OEC is a cluster of four Mn atoms and one Ca atom (Mn_4CaO_5) …The critical questions that remain to be answered involve how the Mn_4CaO_5 cluster changes structurally and electronically as the OEC proceeds through the *S*-state Kok cycle (see Figure 76)" [80]

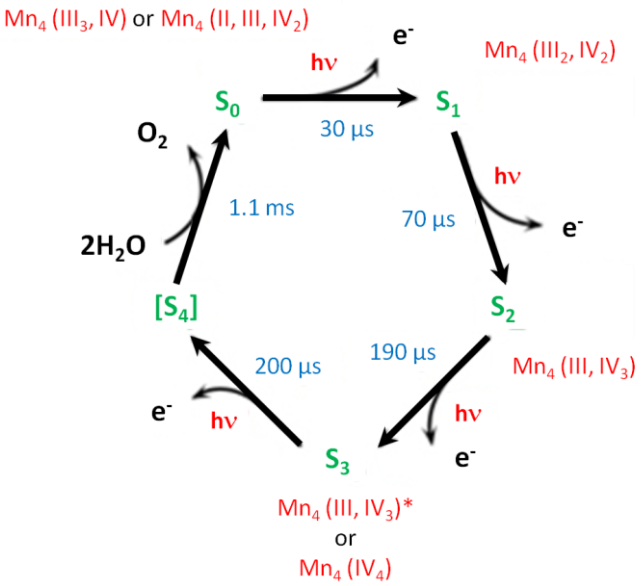

Figure 76: ***Kok-cycle of the S-states (green) of the Mn_4CaO_5 cluster, leading to release of Oxygen; explicitly containing questionable Manganese electronic states (in red) and each the respective lifetime (in blue) of the states of Mn during this process (picture adapted from [80]).***

These states of the Manganese cluster can each be investigated by examination of the Mn L_3 edge which is at 638 eV [84]. We apply X-ray absorption spectroscopy (XAS) by detection of fluorescence at the Mn-edge. This is done within a solvent in order to keep it in its most realistic environment, and, convolved with that, not to destroy it. Other methods are not yielding results; as for example measurement in transmission is simply not feasible due to the very low concentration or Auger electron spectroscopy would be only examining the surface of the sample. "It is clear that Mn complexes play crucial roles in the metabolism of O_2 in many biological systems. In the Kok cycle, O_2 is not released until the transition from S_4 to S_0, whereas the release of protons occurs along the cycle starting from S_0. There is no doubt that this process is critical for keeping the oxidation potential of the OEC low enough so that subsequent oxidation events can occur. Although the formation of the O-O bond during photosynthesis has been extensively investigated via a number of methods, the mechanism of this process is still under debate." [80]

From previous experiments, the group of Vittal Yachandra and Yunko Jano could form the following demands on a spectrometer capable to investigate the different states of Manganese, which are addressed in the setup:

- The experiment will be basically a liquid-jet setup running both at room temperature and cooled down.
- The energy of interest is the L_3-edge of Manganese (> 638 eV)
- Both energies will be present; as oxygen in the solution is present in the solvent and in the protein complex, as well, so the signal of O will be at least of two or three orders of magnitude higher than that of Mn. Both signals should be well distinguishable, Mn needs to be made clearly visible above the level of noise.
- As the number of photons in general decreases exponentially with the distance and the fluorescence process itself is of very low efficiency (quantum yield of ca. 0.01), the optical element should be brought as close as possible to the source of X-ray radiation in order to "catch" as many photons of the energy of interest as possible. The solution is of very low concentration (10^{-3} molar).

These requirements led to the following considerations: the demand of separating the two existing energies is basically addressed by using a reflection zone plate. In this case, an off-axis part shall be used to first, separate the specular reflection (0^{th} order of the RZP surface structure) from the signals of interest and second, sufficiently separate the two signals spatially from each other. The RZP structure is be designed to focus the energy of the Manganese L-edge (640 eV) well, whereas the energy of the Oxygen K-edge (525 eV) will be focused just worse or just distributed apart from Mn due to the achromaticity of RZPs. As well the use of a single RZP has the advantage that the solid angle and the transmission of the spectrometers can be maximized in comparison with for example XES, which is typically further away from the source and very likely contents more optical elements (which then would deplete precious photons). Additionally, by applying simply one single optical element, the throughput of photons is expected to be the highest possible.

Optimization of the diffraction spectrometer

Spectrometer design

A simplified setup is shown in Figure 77:

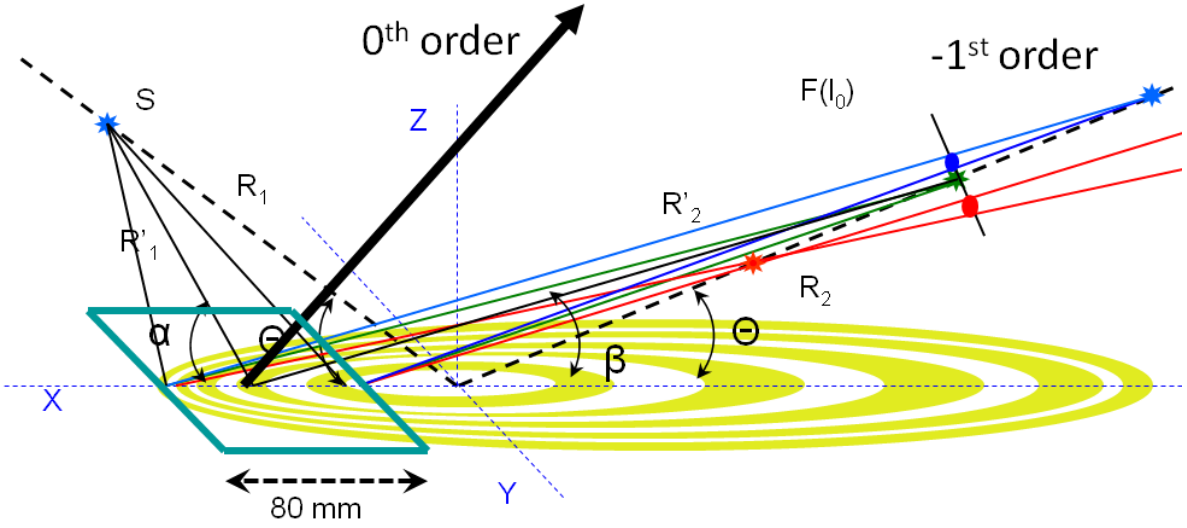

Figure 77: optical layout of the spectrometric element, ***the reflection zone plate. The green frame represents schematically the used area (off-axis – away from the center of the "entire" RZP) for suppressing the zeroth order by separating it (in this case) from the minus first order spatially.***

The main dispersive element of the spectrometer is a reflection zone plate (RZP), a projection of a transmission Fresnel zone plate on the plane surface. To provide the necessary value of dispersion in the focal plane of the RZP, a periphery part of the RZP structure is used, as shown in Figure 77. In this case, the radiation reflected and diffracted on the surface of the RZP, will be focused on the optical axis of the element. The focal distance will be linear dependent on the radiation wavelength as:

$$F(\lambda) = F(\lambda_0)\frac{\lambda_0}{\lambda} \qquad (4.1.)$$

Where $F(\lambda_0)$, the focal distance, corresponds to the design wavelength λ_0. The input beam emitted by the source S will be dispersed along the optical axis. This phenomenon can be used for recording of a spectrum by use of a spatially resolving detector placed in the focal plane of the RZP. The same phenomenon is used in VLS gratings in one dimension to provide spectral dispersion of the input radiation.

The center of the working area of the RZP is located outside of the optical axis. This offers two main advantages of the optical element: (1) the zeroth diffraction order is directed out of the optical axis and does not add background noise on the detector; (2) spectral selection could be done using a slit, placed in the focal plane perpendicular to the optical axis. All the other energies will be dispersed in the focal plane and will not be transmitted through the slit.

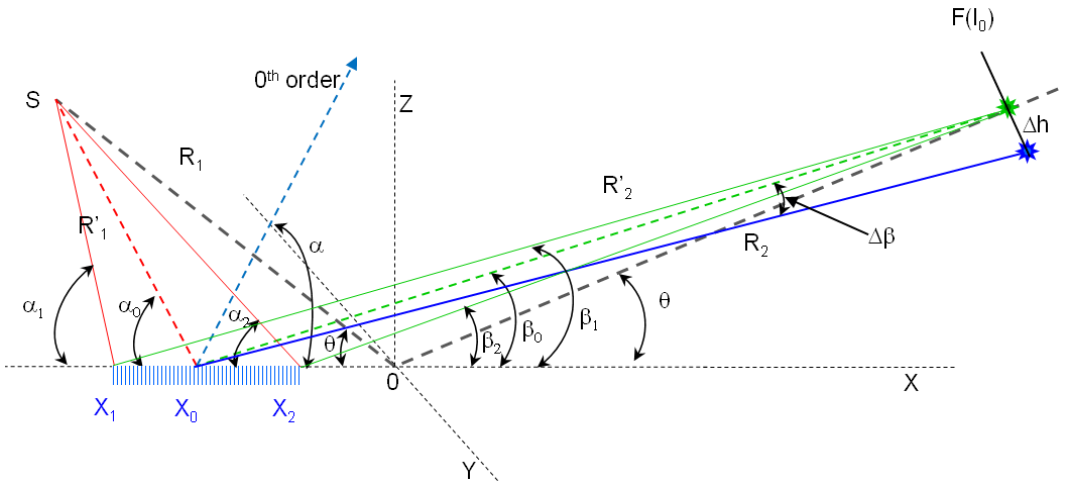

Figure 78: ***working principle of the RZP spectrometer (side view).***

The spatial linear dispersion in the plane perpendicular to the optical axis can be calculated using the so called grating formula

$$d(\cos\alpha - \cos\beta) = n\lambda \qquad (4.2)$$

where d is the grating period, α is the input angle on the RZP area and β is the diffraction angle (see Figure 78). The boundaries of the working area are indicated as the coordinates X_1 and X_2. The corresponding diffraction angles (β_1, β, β_2) and input angles (α_1, α, α_2) as well as the grating periods can be obtained using the mentioned grating equation. Using a simple transformation, we can derivate the angular dispersion of the grating in the middle of the working area (X_0):

$$\Delta\beta = \frac{\Delta\lambda}{d\sin\beta} \qquad (4.3)$$

with $\Delta\lambda$ – wavelength bandwidth.

Using this equation, one can calculate the energy resolution, which corresponds to a defined slit size Δh, or pixel size on the detector in the focal plane:

$$\frac{\lambda}{\Delta\lambda} = \frac{R'_2\,\lambda}{\Delta h d\sin\beta}, \text{ if } \Delta h \geq \Delta S\frac{R'_2}{R'_1} \qquad (4.4)$$

where Δh is the slit width, R_1' and R_2' the corresponding source-grating and grating-focus distances, ΔS is the source size. The last equation indicates the role of the geometrical magnification factor, which is the limit of the minimum size of the slit width. Therefore, the resolution can be varied by the value of the diffraction angle β, the period of the structure and the slit (focal) size.

$$d\sin\beta = \frac{R'_2\,\lambda}{\Delta h}\left(\frac{\Delta\lambda}{\lambda}\right) \qquad (4.5)$$

Equation (4.5.) indicates that the product of the local grating period and the sinus of the diffraction angle is constant for the defined geometrical parameters and energy resolution of the experiment. By combination of equations (4.2) and (4.5) one can calculate the local grating period on the optical element:

$$d = \frac{\lambda}{\sin^2 \alpha}\left[\sqrt{1+\sin^2\alpha\left(\frac{R'_2}{\Delta h}\frac{\Delta\lambda}{\lambda}\right)^2} - \cos\alpha\right] \qquad (4.6)$$

Using this equation, the design parameters of the RZP can be calculated; the angle between the optical axis and the RZP surface (θ) and the distances R_1 and R_2 centre of the RZP - source and center – image, respectively (Figure 78).

$$\theta = a\tan\left[\frac{R'_1 \sin\alpha + R'_2 \sin\beta}{R'_1 \cos\alpha + R'_2 \cos\beta}\right] \qquad (4.7)$$

$$R_1 = a\sin\left(\frac{R'_1 \sin\alpha}{\sin\theta}\right),\ R_2 = a\sin\left(\frac{R'_2 \sin\beta}{\sin\theta}\right) \qquad (4.8)$$

RZP spectrometer for 638 eV (Mn L-edge)

As an example of the spectrometric structure one can calculate a spectrometer, designed for the energy 638 eV with the maximal possible angular acceptance of the diffraction grating with defined aperture: length L and width H. The reflectance of the grating coating to be chosen depends on the grazing incidence angle α and the grating's length as:

$$R = L\sin\alpha\sqrt{R(\alpha)R(\beta)} \qquad (4.9)$$

where R(α) and R(β) are the reflectance at a grazing incidence and diffraction angle, respectively. the corresponding optimization curve for Si surface, Au and Ni coating at 640 eV is shown in Figure 79.

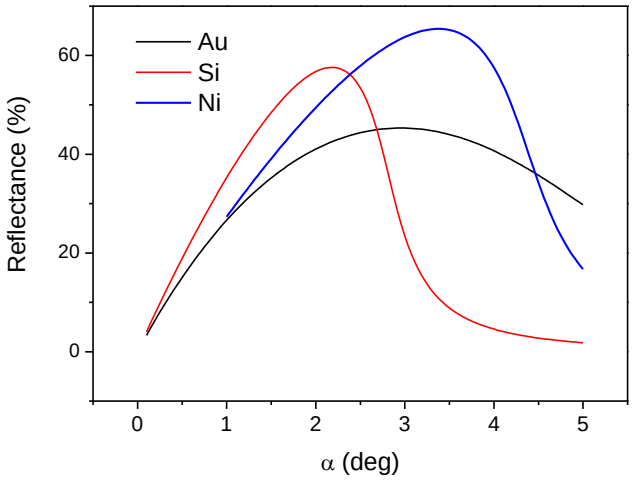

Figure 79: reflectance of the incident angle range for 3 coating materials (on a plane mirror surface): gold, silicon and nickel at 640 eV – needed for the process of optimization of the optical device's parameters.

According to the graph shown in Figure 79, the maximum efficiency can be obtained at the grazing incidence angle α_0 = 2.18° (if only pure silicon substrate is used), which corresponds to the optimal use of the RZP area at the photon energy of 640 eV. The angle α_0 corresponds to the beam which hits the middle of the diffractive optical element (see Figure 78). The limiting incidence angle on the structure α_1 and α_2 are calculated from geometrical considerations as:

$$\alpha_{1,2} = a\tan\left(\frac{R'_1 \sin\alpha_0}{R'_1 \cos\alpha_0 \pm L/2}\right). \qquad (4.10)$$

The corresponding diffraction angles at a fixed β_0 are calculated using a similar equation:

$$\beta_{1,2} = a\tan\left(\frac{R'_2 \sin\beta_0}{R'_2 \cos\beta_0 \pm L/2}\right). \qquad (4.11)$$

Finally, the design parameters for the spectrometer structure are shown in Table 5. Here is assumed that the working length of the diffraction structure (X_2-X_1) is equal to 80 mm. In Table 5 $\lambda/\Delta\lambda$ is the energy resolution, α_0 and β_0 the input and corresponding diffraction angles and d_0 is the local grating period in the center of the spectrometer area; R'_1 and R'_2 are the respective entrance and exit arm lengths to the center. The geometrical parameters of the off-axis spectrometer part:

Table 5: ***spectrometer design parameters***

$\lambda/\Delta\Lambda$	α_0 (deg)	β_0 (deg)	R'_1 (mm)	R'_2 (mm)	E (eV)	d_0 (µm)	L (mm)
100	2.2	1	90	400	640	3.5	80

The spectrometer area is only an (off-axis) part of the entire zone plate as it is shown in Figure 77. The design parameters for the initial RZP are calculated using equations (4.7) and (4.8). The distance between the RZP center "0" and the spectrometer area X_0 is derived from the geometrical parameters of the zone plate and position of the spectrometer area as:

$$X_0 = R'_1 \cos\alpha - R_1 \cos\theta. \qquad (4.12)$$

Table 6: ***corresponding design parameters of the actual RZP-structure***

θ (deg)	R_1 (mm)	R_2 (mm)	X_1 (mm)	X_0 (mm)	X_2 (mm)
1.22	161.12	328.9	31.2	71.2	111.2

Table 7: ***the limiting angular ranges and corresponding local grating frequencies***

	α_1 (deg)	β_1 (deg)	α_0 (deg)	β_0 (deg)	α_2 (deg)	β_2 (deg)
	3.92	0.9	2.2	1	1.5	1.1
density (l/mm)	79		285		1156	

Order of diffraction

The design parameters are chosen in this way that an optimum is found between a large solid angle and high diffraction efficiency (which is strongly dependent on the surface reflectivity of the Si-substrate at the desired energy of interest). The energy resolution was set to only $E/\Delta E = 100$, which does not allow to resolve the sub structure of the Manganese fluorescence. But, it has the advantages that the grating has in general not those high line densities, which means intrinsically a bigger solid angle and higher efficiency. Furthermore, it is sufficient to discriminate spatially the fluorescence signal at the L-edge of the Manganese from the overwhelming Oxygen K-edge fluorescence. Figure 80 shows a comparison of the diffraction efficiency of the +1st and the -1st order, respectively. Applying the geometric parameters and taking the different considerations into

account, the curves are produced using the code REFLEC [30]. In this case, the grating parameters are fed into the simulation as grating period at specific positions on the optical element, angle of incidence, material and roughness. This leads to a certain value of reflectivity and efficiency which is then plotted versus the position at the optical element (RZP). The overall efficiency is then obtained by integrating the resulting curve.

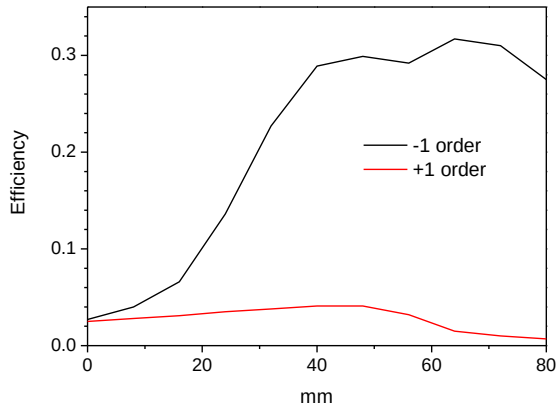

Figure 80: simulated diffraction efficiency at 640 eV along the middle of the RZP for the first negative (black curve) and first positive (red curve) order of diffraction. For this simulation the REFLEC code was used, in combination with the looping-code LOOPER [85]; this results that the -1st order yields higher diffraction efficiency than the +1st order (picture taken from [86]).

Within the experimental conditions, the highest integral diffraction efficiency can be achieved for the -1st order. This results from the fact that for the +1st order the exit angle increases drastically compared to the use of the -1st order; hence, in the end the integral efficiency is about 7 to 8 times higher in the -1st order (ca. 16%) than at the +1st order (ca. 2%).

Another advantage of the application of this RZP-structure for this experiment appears as follows: the efficiency comparison of the minus first order for the simple Silicon surface of both present energies results the following feature:

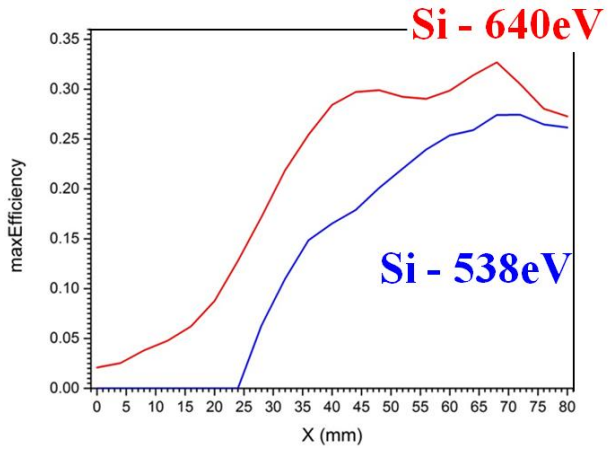

Figure 81: ***comparison of the efficiency of simply the structure on Silicon resulted that the efficiency of the structure for the energy of 538 eV (Oxygen edge) is zero for almost the first third of the RZP. This means that the higher intensity present of Oxygen is even suppressed a bit during the experiment. This comes simply from the fact that the geometrical conditions fit perfectly for transferring the energy of Mn and a little bit of suppression of the energy of O at the same time, meaning that there is no reflection of 538 eV at these angles and line densities.***

Figure 81 one can compare even with the very first ray tracing simulations (see Figure 82 (b)) and see that in fact the structure does not reflect the energy of Oxygen during the beginning – visible at the little jump of the intensity at the projection in dispersive direction of the incoming rays at the RZP. This way, at the beginning of the RZP structure closer to the radiation source, the signal of the Oxygen fluorescence is suppressed. In due consideration of the fact that the number of photons decreases reciprocally with the increasing distance from the source, this yields higher relative efficiency for 638 eV than for the energy of the Oxygen K-edge.

In the following, simulation of all possible misalignments of the RZP-structure using the software Ray [30] is presented. This is necessary to design and construct the entire setup (vacuum-chamber, detector, RZP-mount and utilized motors) around the RZP. Thus, information about the positioning accuracy, necessary for obtaining best possible images at the CCD detector as well as best possible spectral information from the measurements will be gained. Additionally the results of ray tracing should help to interpret and understand the obtained images during the alignment process and possibly later from the actual experiment.

Raytracing simulation for the reflection zone plate as imaging optics for the LCLS-experiment L632

Actually, the parameters which are needed for simulation are the parameters with respect to the RZP structure as the center position of the entire zone plate. So in order to have the right structure simulated, the “real” simulation parameters are shown in Table 7, the illumination of the desired region of the RZP is done by misaligning of the source (as described in chapter 3.2.2).

One begins simply with the ray tracing of the three energies, extracted from an experimental fluorescence spectrum of a PSII solution (640 eV – center of Mn flourescence, 570 eV and 520 eV – center of O), being of the same amount of intensity. The source size is of 10 µm x 10 µm (FWHM). From that we see that the design energy (640 eV, meaning, for which the zoneplate is designed to focus it) is focused best by the reflection zone plate (RZP). The footprint/distribution of rays at the source, the distribution on the zone plate and finally the distribution at the detector are displayed in Figure 82 – as it is in the perfectly aligned case:

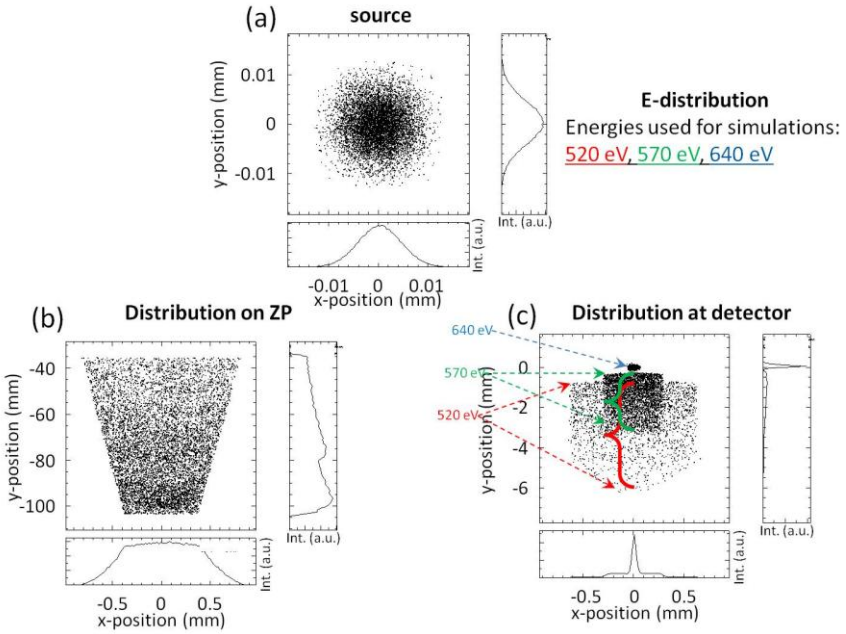

Figure 82: ***results of ray tracing simulations. (a): footprint of the source. (b): footprint on the zone plate (c): distribution at the detector; the three energies which are of interest (indicated by curly brackets) are differently highly focused.***

In the next step, the simulations are modified according to the aforementioned assumptions, as the intensity distribution (in matters of proportions) of the different energies under investigation is anticipated.

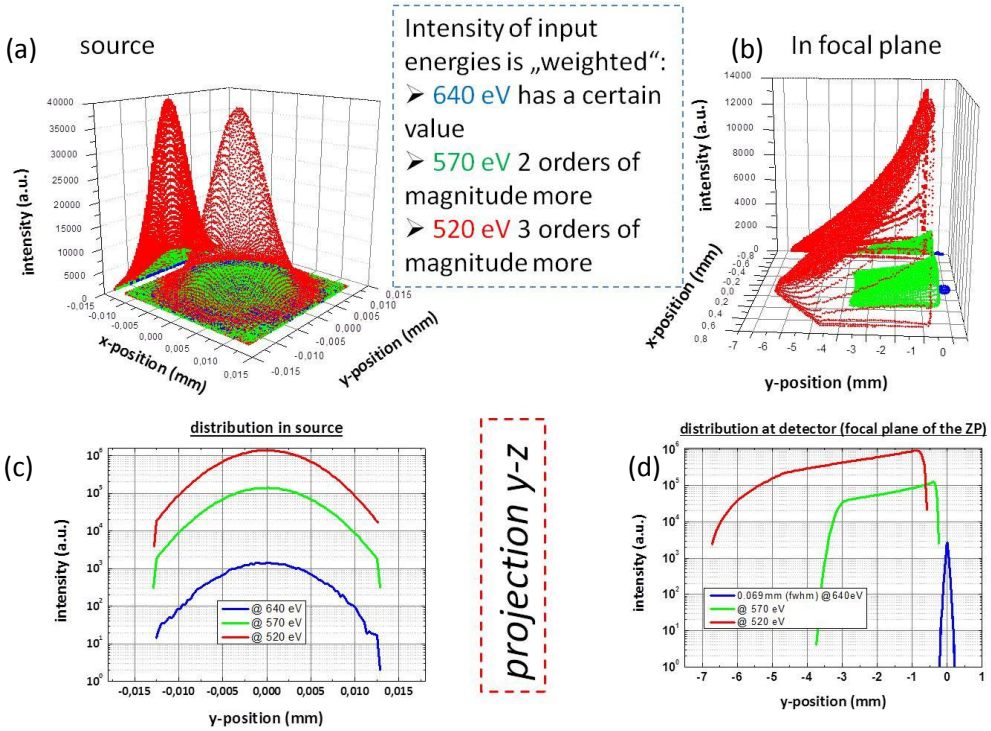

Figure 83: ***Intensity distribution. (a): 3D distribution in the source and (c): respective intensity distribution, projection dependent of the y-position. (b): 3D distribution in the focal plane and (d): respective intensity distribution, projection with respect to the y-position.***

From Figure 83 we learn that even if the intensities, after having passed the zone plate, are still much higher for the lower energies, the Mn fluorescence at 640 eV is well separated from lower energies. For the next simulations, except as an example again for a single misalignment, the results are presented only quantitatively (without weighting the intensities) in order to show simply the (optical) effects. As a result of the simulations (and the experimental confirmed experience as well) both the tilt around x- and y-axis (the normal of the zone plate) turned out to be the most critical, because most sensitive. Exemplarily these two tilts will be shown in the next Figure 84 and Figure 85.

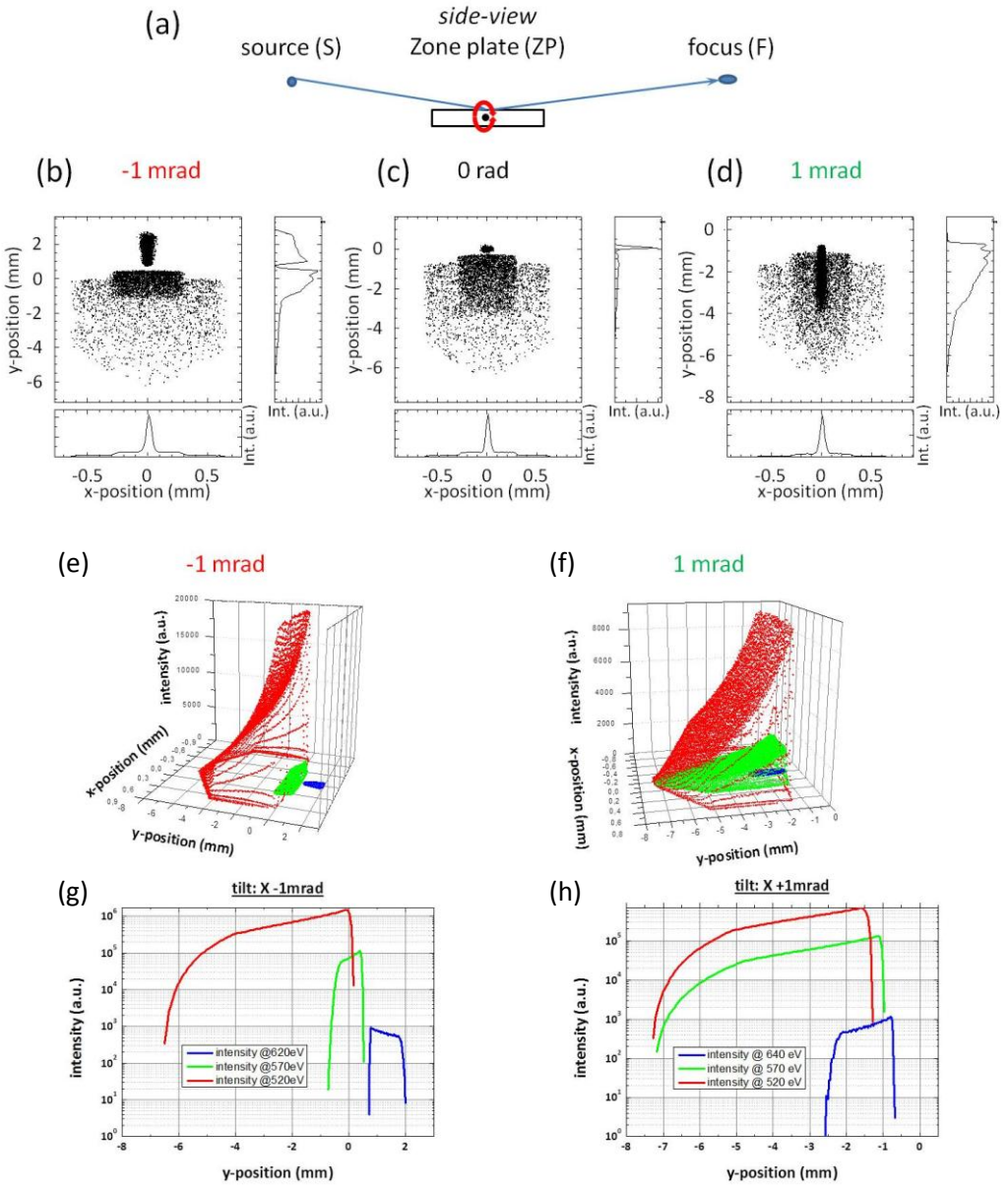

Figure 84: ***Top: footprint at the detector after tilting the zone plate around x-axis (as depicted in the simplified sketch of the "entire setup" (a)): (b): tilt of -1 mrad. (d): tilt of +1 mrad with respect to the perfect aligned (c). Bottom: the respective 3D representation of the weighted intensity distribution. (e): tilt of -1 mrad and the respective projection of the intensity distribution with respect to the y-position (g). (f): tilt of +1 mrad and respective projection (h).***

From Figure 84 we learn that one could possibly almost "gain" in resolution – by separation of the intensity peak of the main energy of interest, see (b) and (g) – but only in one direction, because if

we tilt it the other way around the energies will be mixed up, see (d), (f) and (h). Unfortunately, the total intensity of the peak of 640 eV would decrease, though, as it broadens; this could give rise to the problem that it could dissolve itself within the background noise.

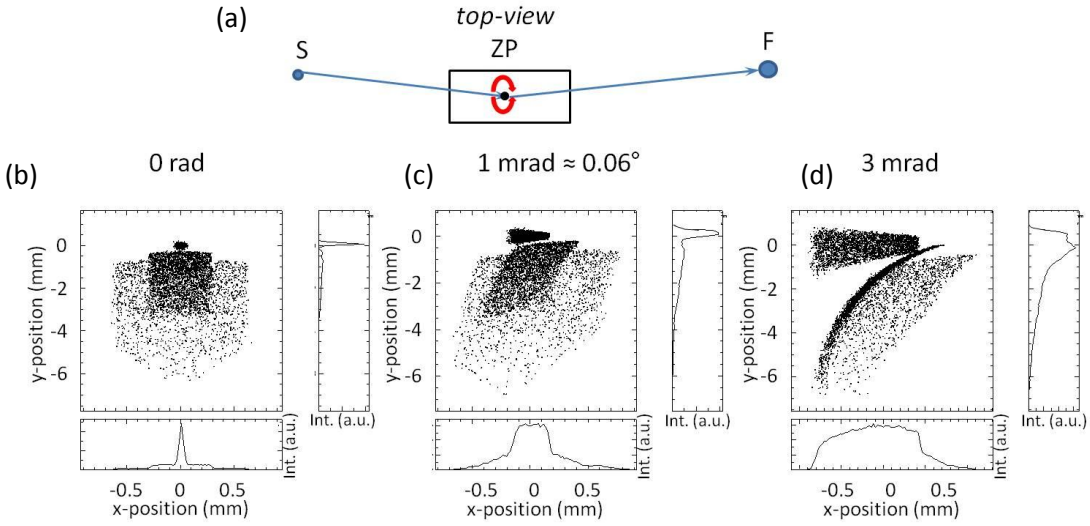

Figure 85: ***footprint at the detector after tilting the zone plate around the y-axis (as depicted in the simplified sketch of the "entire setup" (a)). Tilt around the y-axis is symmetrical in the sense of that the image looks exactly mirrored, if tilted the other direction than depicted here; so only one direction is shown. (b): perfectly aligned (for comparison). (c): tilt of +1 mrad. (d): tilt of +3 mrad; this leads to a complete mess up of the image at the detector.***

As the fluorescent scattered light coming from the jet-source is in principle equally distributed, one can assume that a tilt around the z-axis (which is parallel to the propagation direction of the light) does not influence the focusing property of the zone plate at all – of course apart from a rotation of the entire image around this axis, which will be clearly apparent at the detector. Next, the influence of horizontal, vertical and longitudinal misalignment of the RZP is simulated.

The results are shown in Figure 86, Figure 87 and Figure 88 respectively:

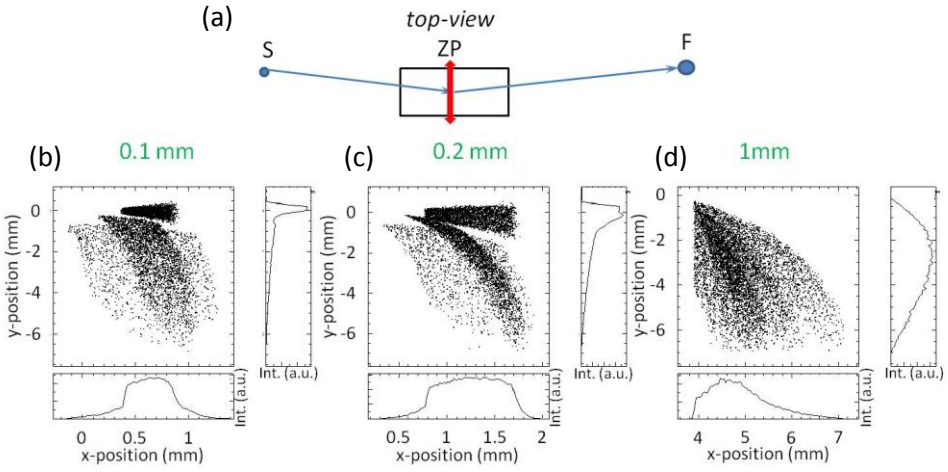

Figure 86: ***horizontal misalignment (along the x-axis) of the zone plate; as the effect on the imaging/focusing property is highly symmetrical, just the displacement in one direction is shown: (a): simplified sketch of the "entire setup". (b): displacement of 100 µm. (c): displacement of 200 µm. (d): displacement of 1000 µm.***

From Figure 86 we learn that at a shift of 200 µm horizontally, the different energies merge and cannot be easily discriminated anymore. It appears as well to be at least a very similar change of the optical image as with a tilt around the y-axis (compared with Figure 85).

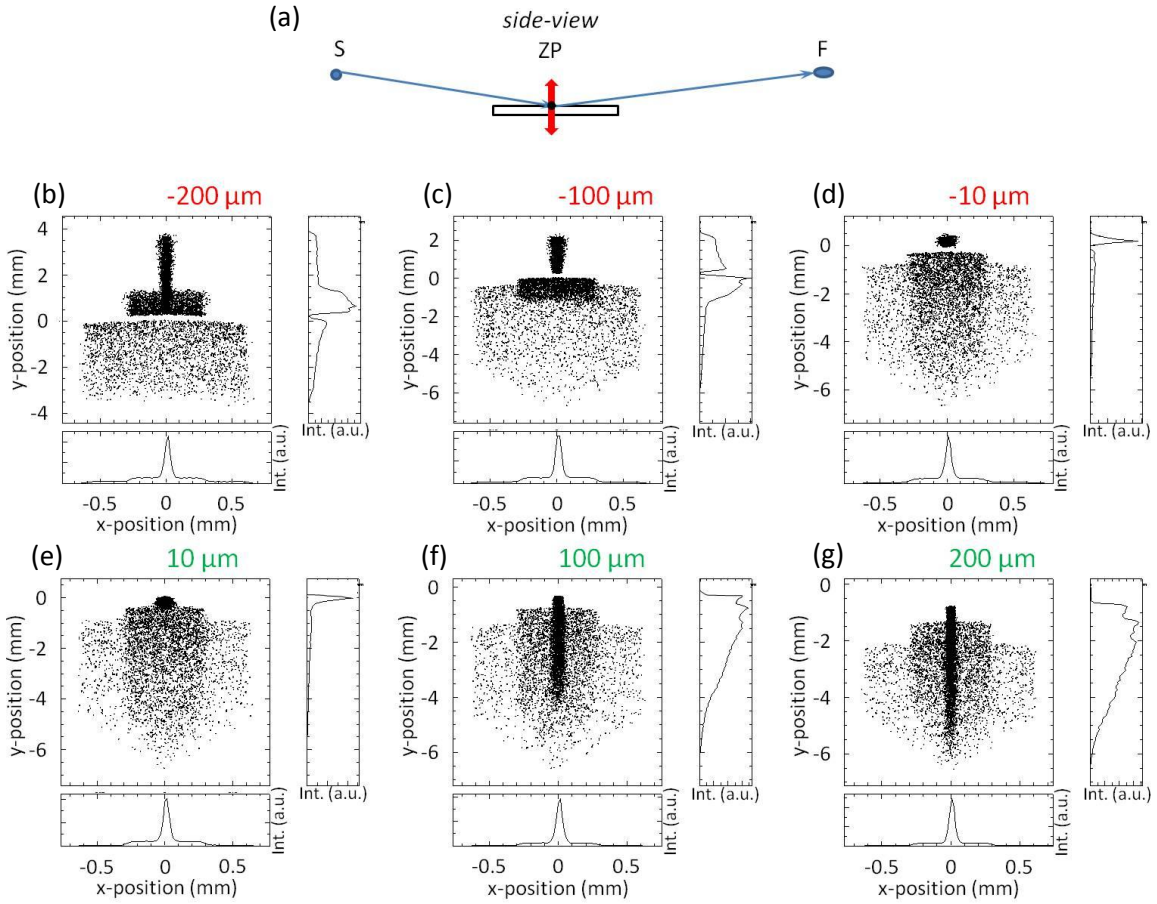

Figure 87: ***vertical misalignment (along the y-axis) of the zone plate. (a): simplified sketch of the "entire setup". (b): displacement of -200 µm. (c): displacement of -100 µm. (d): displacement of -10 µm. (e): displacement of +10 µm. (f): displacement of +100 µm. (g): displacement of +200 µm.***

In Figure 87 it is obvious that a shift of 100 µm vertically leads to the shade of the design energy into the other present energies. On the other hand, a vertical shift of -100 µm shows very similar behavior as with a tilt around x-axis of the RZP (compare Figure 84).

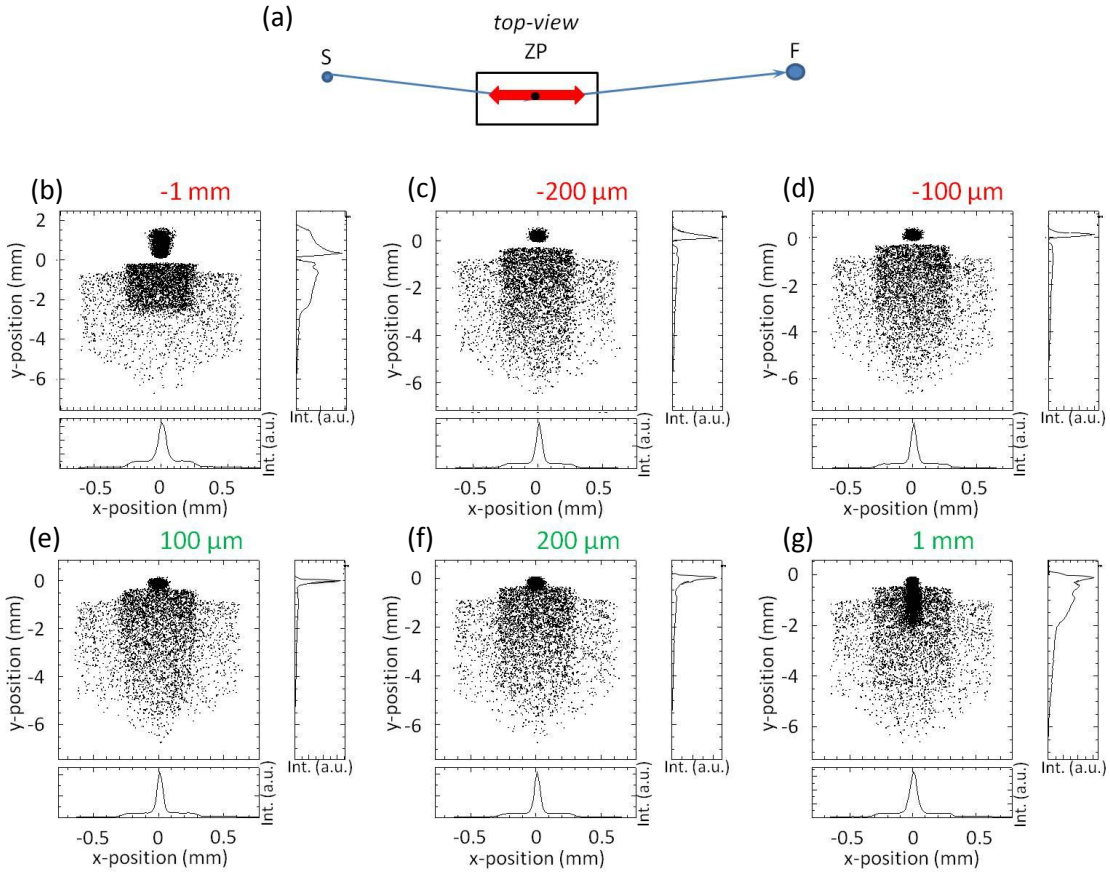

Figure 88: ***longitudinal misalignment (along the z-axis) of the zone plate. (a): simplified sketch of the "entire setup". (b): displacement of -1000 µm. (c): displacement of -200 µm. (d): displacement of -100 µm. (e): displacement of +100 µm. (f): displacement of +200 µm. (g): displacement of +1000 µm.***

As a result of Figure 88 we obtain that even at a shift of 200 µm along the z-axis (parallel to the propagation direction of the light) we can still clearly resolve the focal spot of the design energy and it could be separated from the other energies.

As a result of these simulations we get that the critical tilts can get compensated using combinations of x-, y- and z-translations of the zone plate – as the optical effects are similar and we need to save space inside the experimental chamber. Related with that, the number of stages could be kept at the minimum number of three; no rotational stages will be necessary for alignment.

In the end, simulation of a misaligned detector is done and the results are presented in the following Figure 89 and Figure 90.

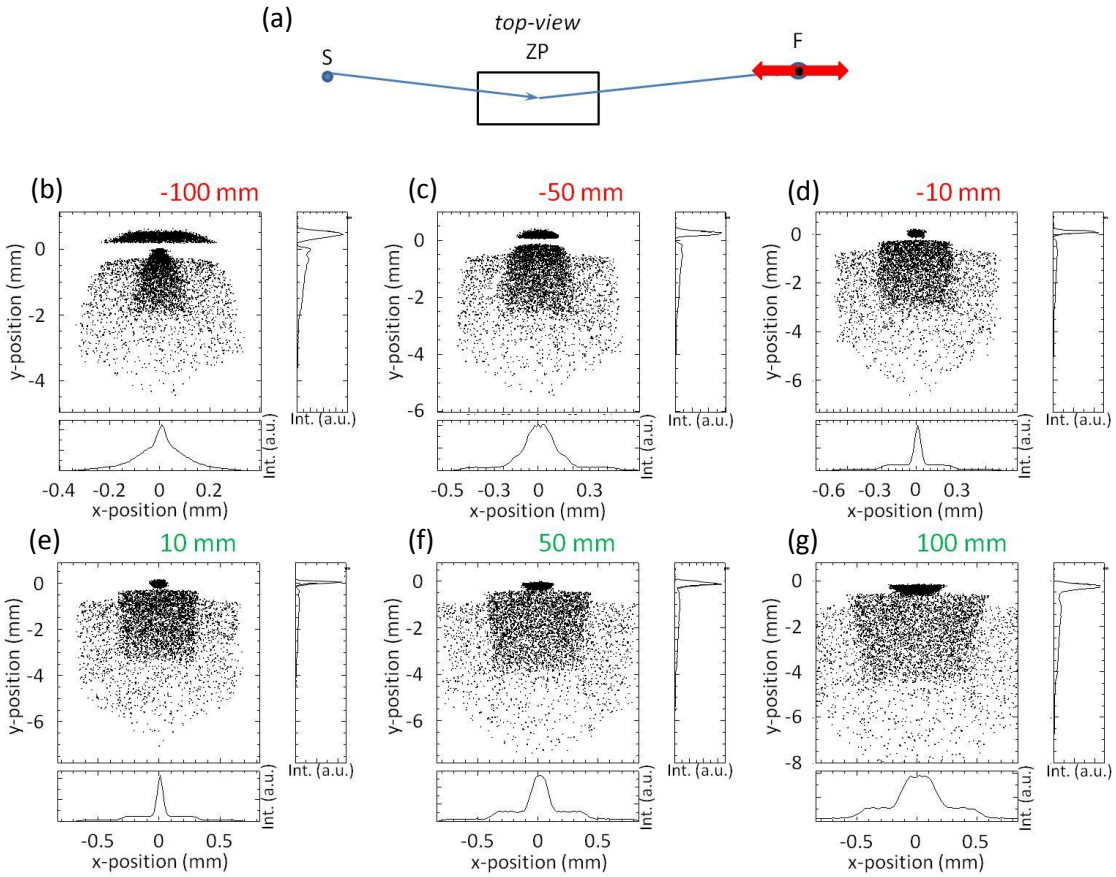

Figure 89: ***detector longitudinally misaligned (along the z-axis). (a): simplified sketch of the "entire setup". (b): displacement of -100 mm. (c): displacement of -50 mm. (d): displacement of -10 mm. (e): displacement of +10 mm. (f): displacement of +50 mm. (g): displacement of +100 mm.***

In total one can state that a longitudinal displacement of the detector does not influence the quality of the image remarkably, if the misalignment stays in the range of a few millimeters. As expected, the focal spot of the design energy of 640 eV broadens as soon as it is displaced from the optimum position to both sides. The other energies are narrowed in the one and broadened in the other direction; this is as well in good agreement with expectations because the focal position for these other energies is at another position than that of the design energy (see Figure 77). As the misalignment of the detector in the direction of both x and y does not result in any change of the distribution (will only change location of the spots but in the very same plane), the other directions of misalignment do not affect the image.

A tilt of the detector around the z-axis will also simply cause displacement in the very same place and the tilt around the x-axis will simply broaden the spots (possibly lower energies could be "focused" better, but not of a remarkable amount), the results are not shown here. But there is one important tilt left, the one around the y-axis, which has at least a measurable effect on the image at the detector. The result is shown in Figure 90:

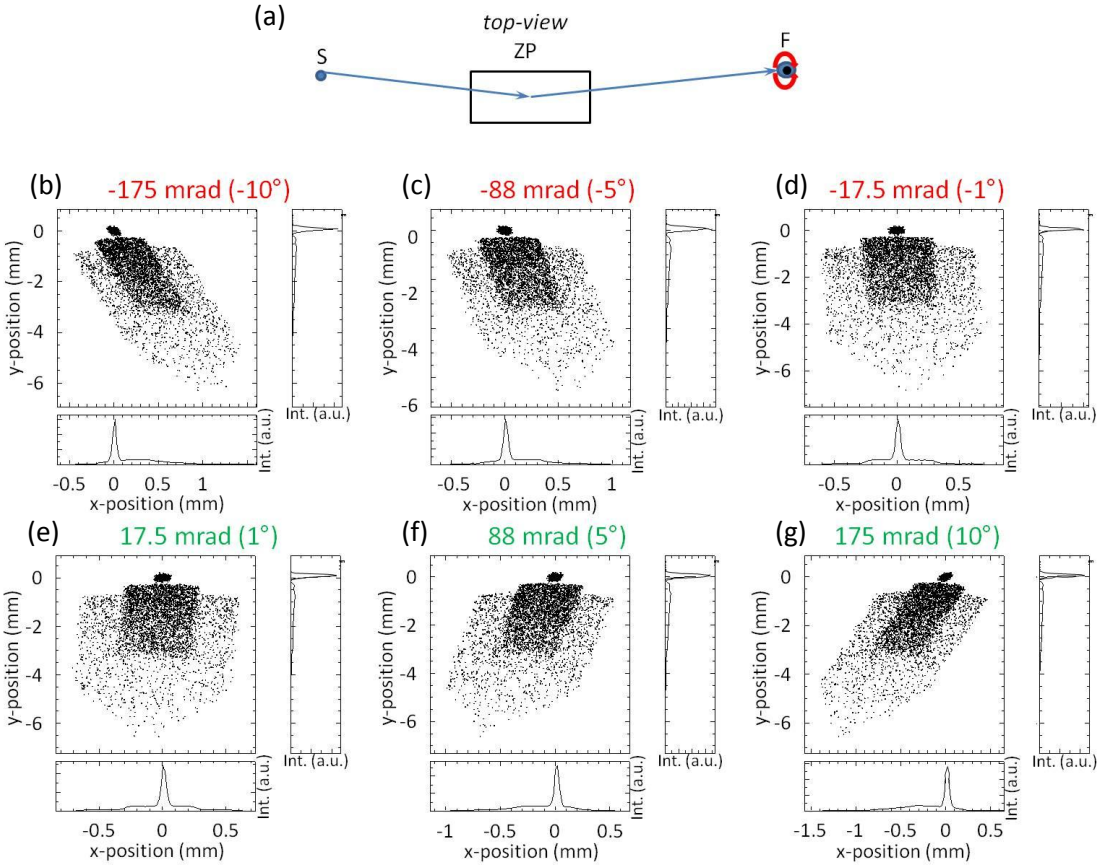

Figure 90: ***detector tilted (around the y-axis). (a): simplified sketch of the "entire setup". (b): tilt of -10°. (c): tilt of -5°. (d): tilt of -1°. (e): tilt of +1°. (f): tilt of +5°. (g): tilt of +10°.***

In Figure 90 we see that rotating the detector leads to tilt of the resulting image of the focused energies, as a simple geometric projection is expectable.

The deduced requirements on precision of positioning of the RZP are summarized shortly: horizontally: some 10µm-step-wise, pre-positioning at least few mm; vertically: a few µm-step-wise, pre-positioning at least within 1 mm; longitudinally: 10µm or even 100µm-step-wise, pre-positioning in mm-range. All these values are RZP vs. source. As from simulation of detector misalignment obvious, it should be placed at the right distance within very few mm, tilts around the x- and z-axes do not affect remarkably, and around y-axis it should be well aligned around very few degrees. Hence, the RZP-structure could be fixed/rigidly coupled with the detector after pre-alignment with respect to each other using an auto-collimator. The axes are depicted in Figure 100.

Efficiency optimization

The overall maximum efficiency can be achieved by adjusting the appropriate profile depth. But, as the RZP is a grating of variable line spacing or local grating frequencies (here just the line densities in the middle of each of the structures is considered), and the angle of incidence varies over a certain range (see Table 8), it is obvious that the efficiency cannot be the same over the entire structure of 80 mm length (see chapter about gratings, 2.3.2.1).

The general idea is to vary the depth of profile in this way that it is perfect for each case of line density and angle of incidence to result the best possible efficiency of the RZP (see Figure 91):

Figure 91: ***general idea of adaption of the profile depth according to the line density. In principle, the higher line density should give higher efficiency at lower profile depths than the lower line density (see red line on the right).***

Table 8: ***variation of the structure parameters, which leads to different possible efficiencies over the entire optical element***

angle of incidence α_i	exit angle β_i	local grating frequency
1.5°	1.1°	79 lines/mm
2.2°	1.0°	285 lines/mm
3.9°	0.9°	1156 lines/mm

The optimal profile depth for the entire variation of the line widths and the corresponding angles of incidence to achieve everywhere the highest possible efficiency locally was simulated (see Figure 92). This led to a variation of the profile depth each at the different positions of the RZP structure (see Figure 93 and Table 9). The simulation was carried out in this way that each a specific grating of a certain line density is chosen. Then the depth of profile is varied and the respective efficiency value at the design energy of 640 eV is obtained. This is done for the entire range each every four millimeters over the entire length of the structure. This way, curves are obtained (plotted in Figure 92) with the respective first maximum of efficiency at certain depths of profile. Resulting from that, the local optimum depth of profile over the entire structure is obtained for the device to result highest possible integral efficiency.

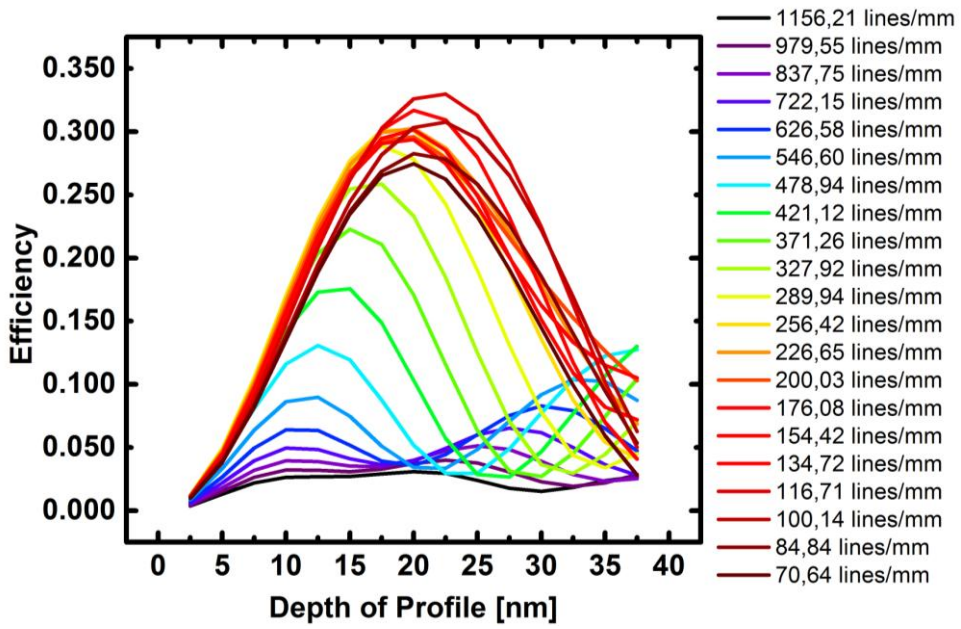

Figure 92: ***simulation of variation of the depth of profile each for the different line densities and the corresponding angles of incidence to obtain the optimal profile depth for each position of the RZP-structure. The point of first maximum at each curve represents the optimal choice which should be taken in order to get the best possible resulting integral efficiency (courtesy of [87] and [88]).***

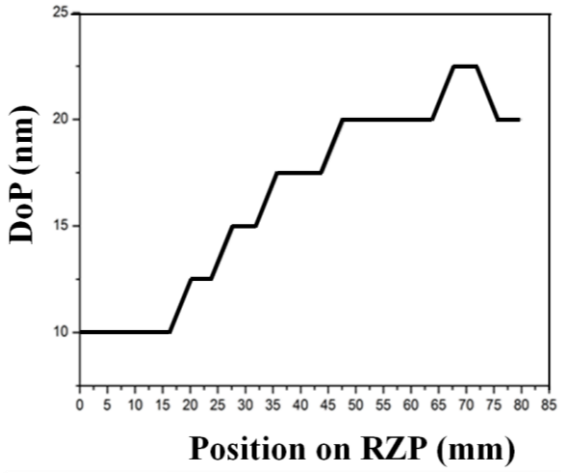

Figure 93: ***the resulting depths of profile (DoP) at the respective real position on the RZP-structure (courtesy of [87]).***

The corresponding parameters are shown in Table 9:

Table 9: ***result of simulation parameters for the optimal depth of profile (DoP) at the specific line densities (left and right row, respectively); the corresponding position at the RZP-structure is depicted in the second row, the respective efficiency in the third row (courtesy of [87]).***

lines /mm	x-position (mm)	efficiency (%)	DoP (nm)
1156.21	0	2.64	10
979.55	4	3.22	
837.75	8	3.95	
722.15	12	4.94	
626.58	16	6.39	
549.60	20	8.98	12.5
478.94	24	13.08	
421.12	28	17.56	15
371.26	32	22.29	
327.92	36	25.86	17.5
289.94	40	28.88	
256.42	44	30.11	
226.65	48	30.28	20
200.03	52	29.59	
176.08	56	29.36	
154.42	60	30.17	
134.72	64	31.70	
116.71	68	32.99	22.5
100.14	72	30.76	
84.84	76	28.25	20
70.64	80	27.46	

According to this result, the overall integral efficiency of the device with the perfect profile depth at each position could be simulated. This is done by taking the results of simulation of the efficiency of a grating each at the position of the RZP-structure with the appropriate parameters as line width, angle of incidence, depth of profile all at the design energy of 640 eV.

Coating

One parameter, which can be optimized and which influences the efficiency of an X-ray optical element remarkably, is the application or coating of different materials. The reflectivity of a surface is depending on the applied energy and strongly associated geometric parameters as angle of incidence (at specific energies) and, for example at a grating, line density. So the idea came up to apply some higher reflective material than pure silicon, of which the substrate of the RZP-structure is made. From tables and experience of colleagues inspired, typical materials for coatings were simulated: pure silicon (as comparison), then with exactly the same geometrical and structural parameters the other materials were applied. The "classical" materials like Gold and Platinum were taken into consideration as well as Nickel. In case of Nickel it is well known that it oxidates very fast when exposed to air. So the combinations NiO and Ni_2O_3 were simulated as substrates as well. In the end, the most realistic case for simulation of the case of Ni coating was, to use pure Ni as substrate and put on top a monolayer of 3nm thickness to cover the case of ongoing oxidation the best. Overall a roughness of 0.5 nm (rms) was applied in all cases. The resulting curves are displayed in Figure 94:

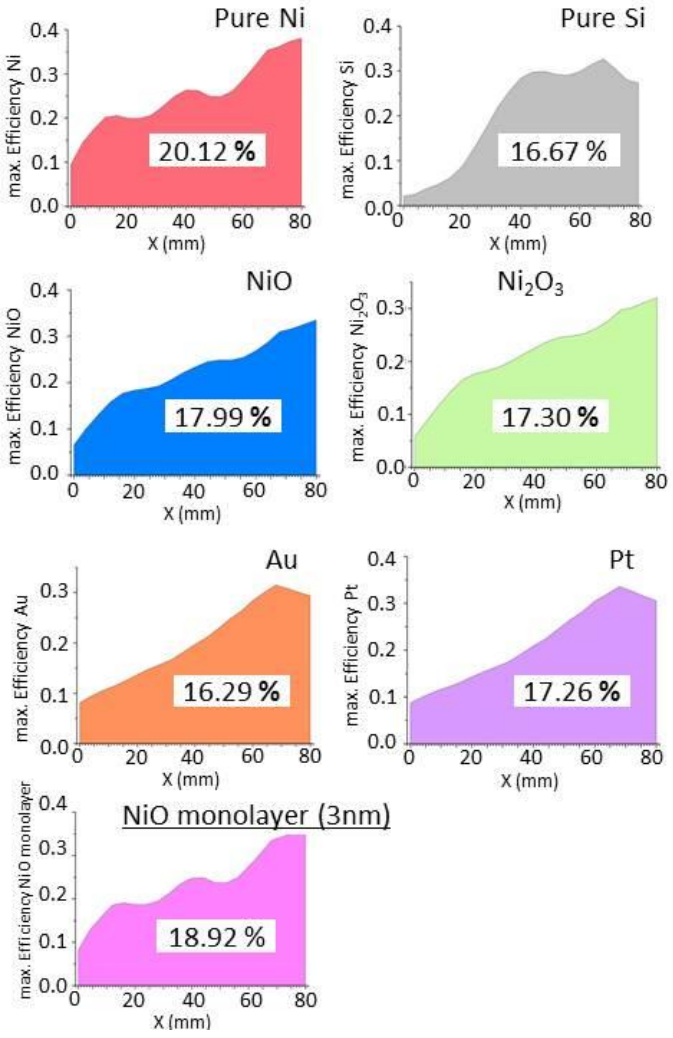

Figure 94: ***resulting curves of ray tracing simulation of the same structure with different materials applied considerable as coating for increasing the device's integral efficiency. Each, the maximum efficiency versus position on the RZP is shown. The integral efficiency is depicted as inlay in each case. As a result, NiO coating (as most realistic) yields the highest efficiency at around 19% (courtesy of [87]).***

Here one obtains as a result that a coating with oxidized Nickel gives the highest possible integral efficiency; it yields an increase of approximately 14% with respect to use of pure Silicon (non-coated substrate) – in case of pure Nickel one gets even an increase of around 21%.

Having a deeper look into the resulting curves of simulation, some noteworthy advantages of coating the substrate in this case with Nickel become evident. There are two facts which are present in this experiment: the intensity (equal to number of photons) decreases exponentially with distance, which means that unfortunately at the end of the optical element the number of photons is anyway much lower than at the beginning, which leads unfortunately to the fact that one cannot leverage the very high efficiency at the end of the structure. On the other hand is the solid angle, which is synonymic with number of photons, as well in this case is very much higher at the beginning of the structure simply by geometrical reason; the angle of accepted rays/photons is at the beginning higher with respect to the illuminated length of the surface than at the end, just because the angles here are steeper than at the end. Inspection of the curves results that the local efficiency of pure Silicon is dramatically lower at the beginning, until almost half of the device, than that of NiO. Right in the middle it seems to be of almost the same local efficiency. We keep this in mind for interpretation of the further experimental results.

Experimental measurements of the RZP efficiency

Then, the different options for coating should be further investigated. At first, thin Silicon wafers were coated with evaporation technology at the HZB (thanks to Ivo Rudolph and Adrian Polok). Technologically, fabrication of the Platinum coatings was the most difficult as it has a very high melting point (1,768 °C) compared to the others (Ni: 1,455°C, Au: 1,064°C), which led in several cases to burning of the tiny crucible, containing the evaporating material. This is the reason why the thickness of the Platinum-coatings is not as regular as in the two other material cases. In total, there were three wafers coated with Gold, three with Platinum and three with Nickel. Then at first the roughness of the surface was diagnosed using AFM (thanks to Johannes Wolf and Christoph Waberski). As a hint of quality of the coatings, the roughness of the different used Silicon wafers was diagnosed as well. The respective results are shown in Table 10:

Table 10: ***resulting roughness values from AFM measurements. These values are a quantity of the coating's quality.***

material	thickness	roughness (rms-value)
Ni	10 nm	0.2 nm
Ni	30 nm	0.2 nm
Ni	44 nm	0.3 nm
Pt	11 nm	0.2 nm
Pt	13 nm	0.2 nm
Pt	33 nm	0.3 nm
Au	10 nm	0.3 nm
Au	20 nm	0.15 nm
Au	40 nm	0.25 nm
Si (wafer)	500 nm	0.082 nm
Si (wafer)	1000 nm	0.126 nm

As Table 10 shows, the coatings were already of very high quality concerning their surface roughness. Then, the reflectivity of the produced coatings was investigated using the Reflectometer at BESSY II (thanks to Andrey Sokolov, Friedmar Senf and Franz Schäfers). As result of the measurements, one of the actual RZP-structures for the second experiment at BESSY II was coated with Nickel, but using sputter-technology by a collaborating company. This technique has the advantage that the material which is deposited should at least by construction be more stable than any evaporating technology as the material simply hits the surface at very higher energies than possible applying evaporation. This surface was then examined with the same procedure. The AFM measurement resulted in a roughness of about 0.2 nm to 0.3 nm (rms) at a thickness of around 30 nm, both examined at two different positions at the surface.

Technologically, nowadays a variable profile depth especially for this kind of complex (curved) surface structure cannot be fabricated, yet. First attempts and test of a machine, capable of etching different depths of profile (by varying the etching exposure time of the written structure over the entire length) are currently ongoing and conducted by Alexander and Anatoly Firsov at the HZB and could not be applied during the previous time. Other ideas as different masking and coating of the structure during development are under investigation by Max Schöngen, Jürgen Probst and Heike Löchel and will be presented in subsequent theses of my colleagues.

The prototypes of RZP were fabricated by A. Firsov and M. Brzhezinskaya according to the procedure described in Appendix 1 with a constant depth profile optimized for the overall RZP length.

Then the structure was investigated as well using the Reflectometer at BESSY II. The procedure is an angular scan basically at the center of the structure (at a line density of approximately 285 l/mm) at a fixed photon energy. The efficiency is obtained by normalization of the measured intensity I_R with the parallel recorded I_0.

As an example, the result of the efficiency measurements for Si coating is plotted in Figure 95. The optimal calculated depth of profile for the 285 l/mm and the photon energy of 640 eV was 17 nm. The measured maximum of efficiency for the minus first order of diffraction of this structure is not at 640 eV, as by design assumed, but rather at 740 eV, which corresponds to the fabricated profile depth of 12 nm.

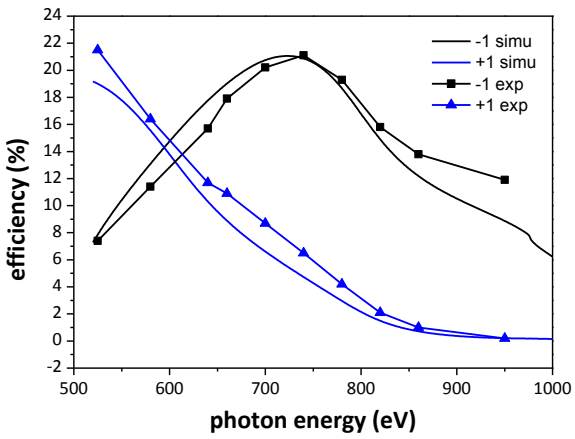

Figure 95: the resulting efficiency curves for the examined RZP-structure. The result is that the efficiency maximum of -1st order is at 740 eV, not at 640 eV – due to the depth of profile (12nm) (data as a courtesy of [89]). A surface roughness of 1 nm rms was used for theoretical simulations using [30] of the efficiency.

The fit parameters for the simulation, the depth of profile (12 nm) and the accuracy of the depth (1 nm rms), were put into the calculation with REFLEC [30]. The respective measured efficiency parameters for the different diffraction orders are shown in Table 11:

Table 11: ***the resulting values of efficiency for the different orders of diffraction (specular/0th, -1st, +1st) (courtesy of [89])***

hv (eV)	Efficiency 0th order (%)	Efficiency -1st order (%)	Efficiency +1st order (%)
525	15,1	7,4	21,5
580	10	11,4	16,4
640	6,8	15,7	11,7
660	6,1	17,9	10,9
700	4,2	20,2	8,7
740	3	21,1	6,5
780	2,9	19,3	4,2
820	3,3	15,8	2,1
860	3,6	13,8	1
950	4,4	11,9	0,2

This was further investigated and from AFM-measurement of the examined RZP-structure, the actual value of depth of profile was approximately 13 nm. This of course shifts the maximum of the efficiency towards higher energies, as expectable from simulation (see Figure 96):

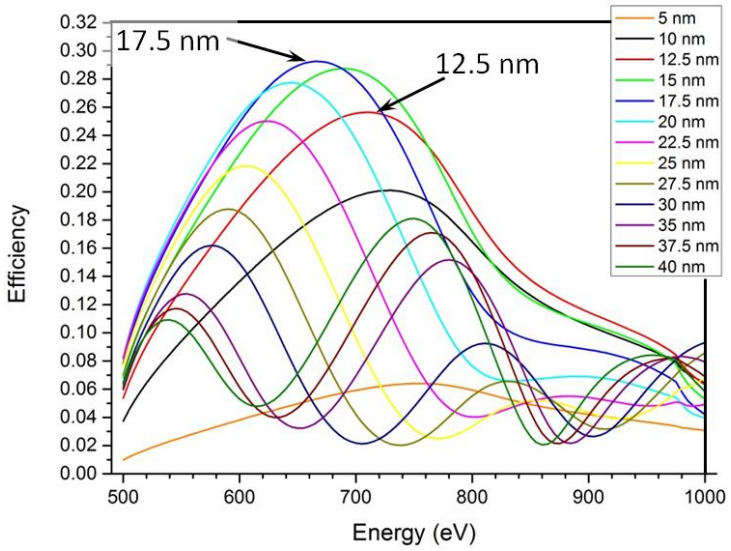

Figure 96: ***simulation of efficiency versus photon energy using different profile depths. As a result, one can see that the maximum of efficiency for a profile depth of 12.5 nm (which is close to the actually measured value) is shifted clearly to a higher energy than that of a profile depth of 17.5 nm (as originally designed) (courtesy of [87]).***

Actually, the following needs to be taken into consideration: if the maximum of efficiency of the structure is shifted towards the lower energy of 640 eV, as well the intensity for the "non-desired" energy of Oxygen at 538 eV is increased. Hence, in this way the error of fabrication at a different profile depth leads finally to the advantage that the intensity of Oxygen is relatively lower than it would be at the first considered profile depth.

In the end, the Nickel sputter-coated structure was investigated and its efficiency was compared to the value of last time's structure (the three RZP-structures as used at the experiment at LCLS in 2012) and found to be of the same value approximately.

This might astonish as the simulation of efficiency shows some remarkable increase of efficiency (as described before). But, as described already, the technique of obtaining the value of efficiency experimentally using the reflectometer has the slight disadvantage that the value of reflectivity is simply examined at a single spot around the center position of the optical device. The simulations make a statement about the integral efficiency. However, of course the value of local efficiency can be extracted from the simulation as well, which gives as result, that the efficiency for the Silicon substrate exactly in the middle of the structure has the value of approximately 28%, whereas the value for the NiO coating is approximately 25%. Hence, the overall integral efficiency should still be better in case of NiO.

Another result of the AFM-measurement was that the rising angle of the lamellar structure of the RZP was actually 7° – the simulations so far have always been done with a lamellar angle of 90°. So this was suspected to be another source of diminution of the efficiency of the RZP-structure. But, it needs be taken into consideration that very likely that this angle could be already within the limitation of accuracy of the AFM. Feeding the simulations again with the newly measured parameters (depth of profile: 13 nm; roughness: 0.3 nm (rms); lamellar angle 7°/90°) resulted the following:

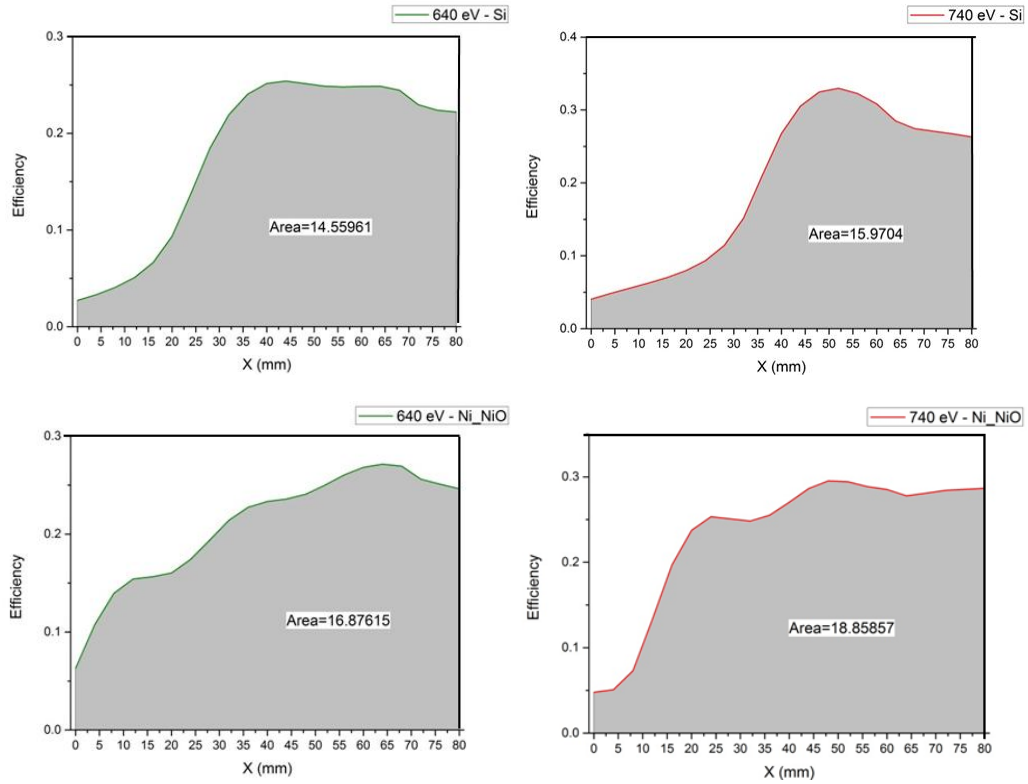

Figure 97: ***simulation of the influence of low rising slope angle of 7° at the lamellar grating on the integral efficiency. Top left: 640 eV on pure Si (integral efficiency 14.6%); top right: 740 eV on pure Si (int.eff. 16%); bottom left: 640 eV on NiO-layer (int.eff. 16.9%); bottom right: 740 eV on NiO-layer (int.eff. 18.9%) (courtesy of [87]).***

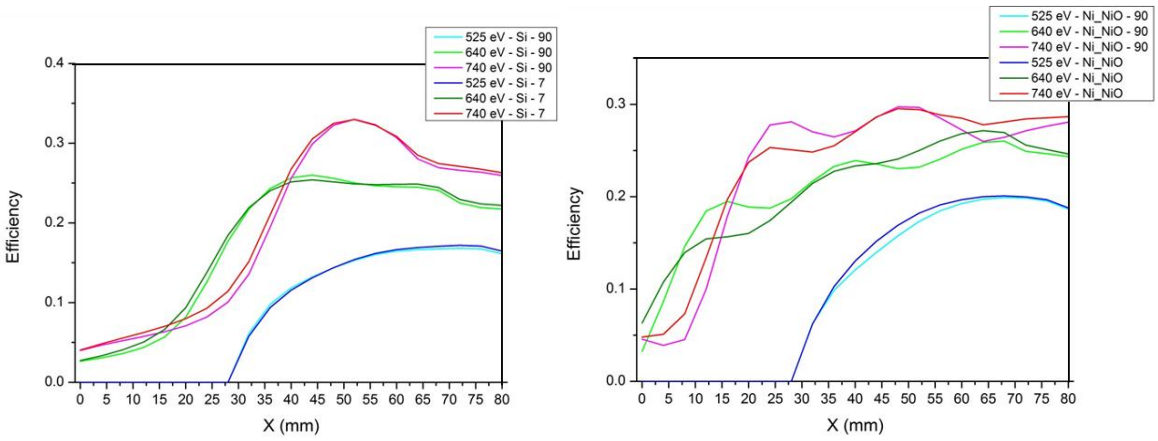

Figure 98: ***survey of the overall efficiencies at the lamellar angle of 90° and 7°, respectively. Left: on pure Silicon; right: applied on Nickel Substrate with additional layer of 3 nm of NiO (courtesy of [87]).***

As the result of this simulation, Table 12 gives the values. One can state that the rising angle at the slope of the grating structure does not influence remarkably the integral efficiency of the entire device:

Table 12: ***results of simulation of the influence of angle at the slope of the grating structure***

	integrated efficiency			
energy	**Si at 90°**	**Si at 7°**	**Ni+NiO at 90°**	**Ni+NiO at 7°**
525 eV	7.12	7.16	8.05	8.31
640 eV	14.32	14.56	16.87	16.88
740 eV	15.48	15.97	18.57	16.86

Spectrometer tests at the BESSY II facility

The structure described here was made using high-voltage electron beam lithography (VISTEC EBPG 5000plusES) and reactive ion etching techniques. A super-polished silicon substrate, with 0.2 nm rms roughness and slope error smaller than 0.6 mrad rms war used. An RZP with lateral dimensions of 80 mm x 2.4 mm, lamellar profile of 13 nm and the minimum zone width of 70 nm was produced on the surface of the substrate. Figure 99 shows an image of the RZP (actually, already the second evolved version containing 3 zone plate structures is shown, but the parameters for the first tests at BESSY II and LCLS were the same). The optics was tested using the X-ray reflectometer at the BESSY II optical test beamline. The parameters of the structure, the depth of profile (13 nm rms) and the accuracy of the depth (1.2 nm rms) were measured at the BESSY II optics beamline. The energy resolution of the spectrometer was expected to be of $\lambda/\Delta\lambda = 63$ with 150 µm slit size and 10 µm source size (see figure below; an optical image of the spectrometer element structure (Si substrate, Au coating). The size of the substrate is 100x30x10 mm^3.)

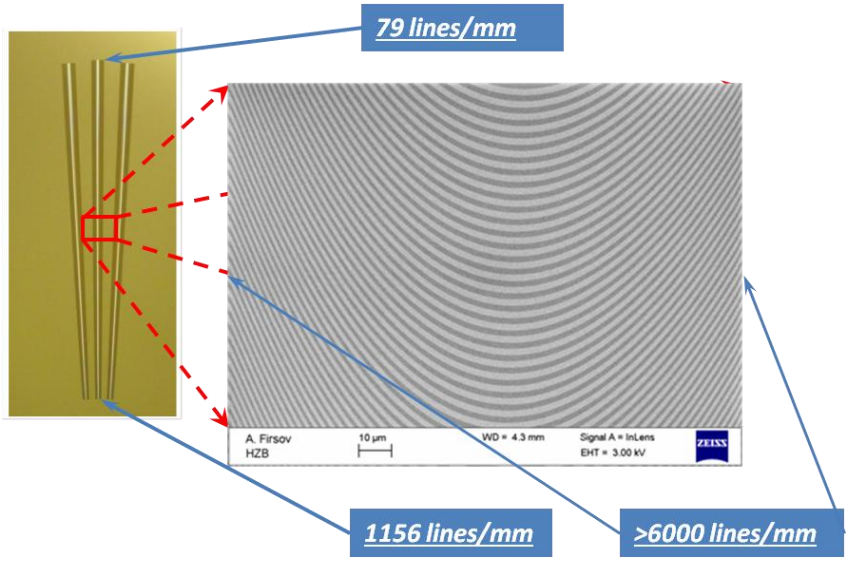

Figure 99: ***the three RZP-structures and the respective line widths at the different positions (courtesy of A. Firsov and M. Brzhezinskaya). These very high variations especially the high number of more than 6000 lines per mm at the brinks of each of the structures causes very low efficiency locally at these positions.***

All RZP structures described within this project were manufactured within our institute by Alexander Firsov, Maria Brzhezinskaya and Heike Löchel. The technological process is summarized in the Annex. The resulting image of the first experimental test at BESSY II is shown in Figure 102. The actual setup as initially planned in principle is shown in Figure 100. At **BESSY II no jet was used**, but a solid sample, as it has a high Mn concentration (compared to a jet) and thus a relatively high fluorescence signal. This allows for a quick and fast-forward adjustment.

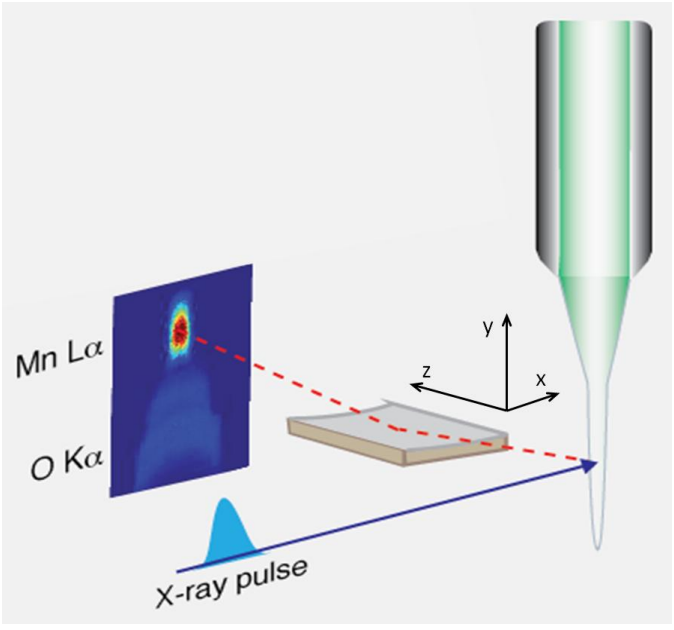

Figure 100: ***setup for the proposed partial fluorescence yield spectrometer as it is used at LCLS. On the right the jet is shown (green) – at BESSY II, no jet was used, but a solid sample at the same position – the RZP-structure is on the surface of the optical element, the image on the CCD-chip of the camera is shown in the back (picture adapted from [86]).***

Experimental testing of the different variations of structures has been done at BESSY II. The spectrometer chamber was constructed by Christian Weniger at HZB and the actual experiment was conducted; first, experimental testing at BESSY II, second, actual experiment at LCLS. The spectrometry bank is shown in Figure 101:

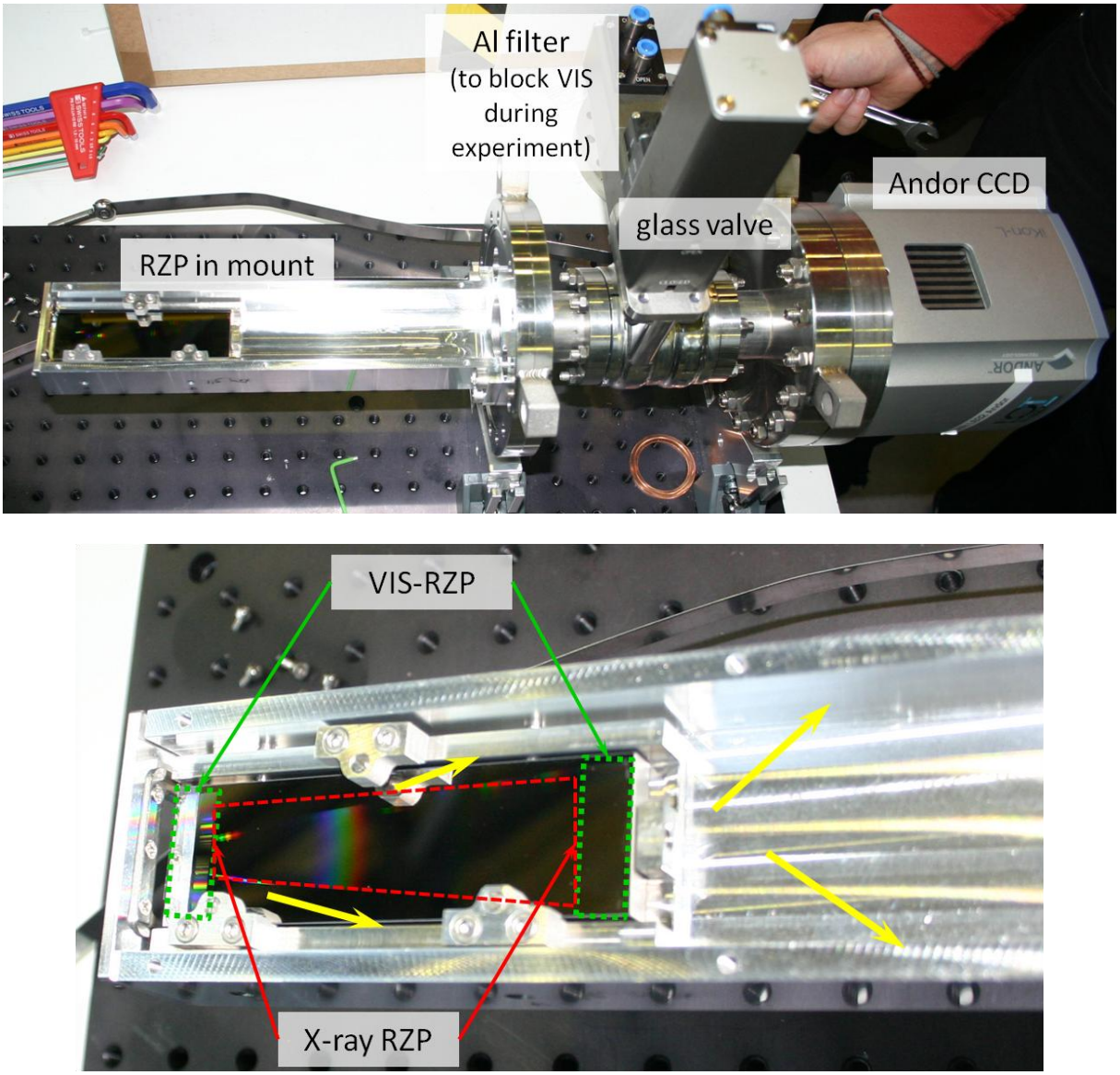

Figure 101: ***photograph of the entire spectrometer. Top: "entire setup" with the RZP-mount in front of the CCD. Bottom: The mount of the Si-substrate (the inner part of the spectrometer) is seen, the RZP-structures for the VIS-range are in the green frames, the walls of scattering reflections are depicted by the yellow arrows, the area of the X-ray RZP-structure(s) (which serves as scattering reflective surface for the visible light, too) is charted by the red frame.***

The tests were performed at the beamline PGM1-U49 using a solid sample irradiated with synchrotron radiation. The CCD back-illuminated ANDOR camera was used for the spectra detection in the focal plane of the RZP. Resulting images is shown in Figure 102.

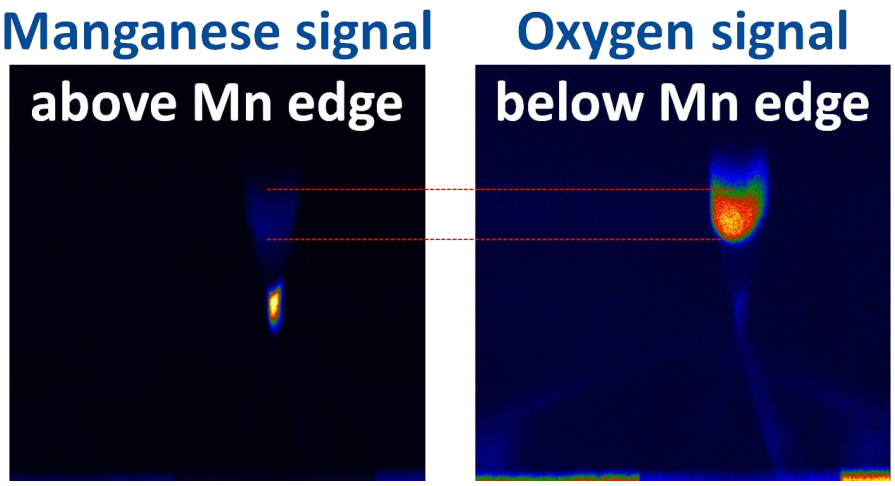

Figure 102: ***images at the CCD of the designed RZP, recorded at BESSY II using the fluorescence signal of a solid MnO sample. In the left image, the brightest spot is the focused signal of the energy of 640 eV. On the right side, the same image is recorded, but with excitation below the Manganese edge; so one can see the broader spot of Oxygen. Note that the regions of the broad Oxygen spot are actually of the same intensity in both cases; the background is almost mostly black in the left image as the scaling was adjusted. The remaining spot at Mn-position in the right image comes from higher harmonics of the beamline itself so that slight excitation at this energy still took place. At the lower edge one could identify as well the specular reflection of the RZP structured surface (brighter regions at the bottom) and the shadow of the RZP structure itself (darker region between brighter lines at the bottom).***

For illustration, Figure 103 shows a spectrum of the first test measurements at BESSY II from the solid sample using a single RZP. The positions of the peaks are as expected, but the intensities are strongly distorted by saturation effect; but this will not be discussed here.

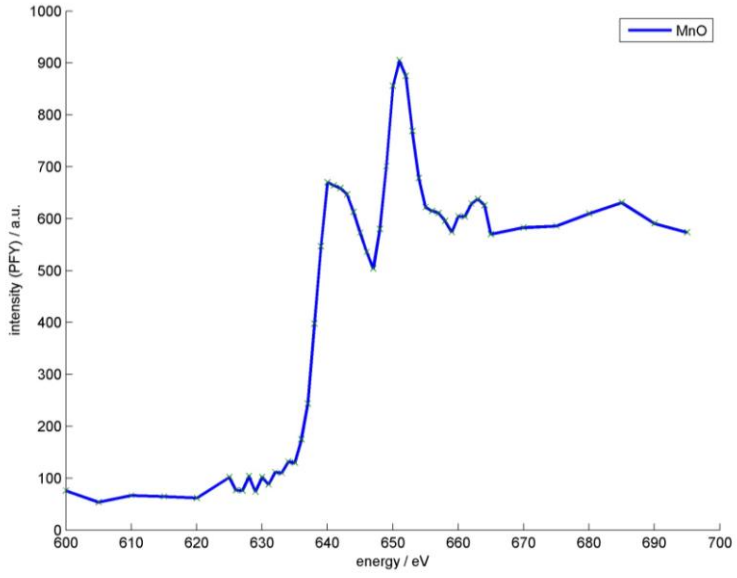

Figure 103: ***first spectrum of the test experiments at BESSY II in 2012. Clearly the Mn edge at 640 eV is recognizable (courtesy of H. Schröder and R. Mitzner).***

As written above, the more detailed description of the different used structures at different stages of the project will be presented in my colleagues' (Heike Loechel) thesis. But, in short, these different structures under examination were: two VLS kind of structures, following the idea of minimizing the

parts of lower local efficiency by using only center parts in direction of the dispersion (see Figure 108); a substrate containing 40 single RZP-structures, whereas the outer parts (containing the very high and thus, very inefficient line density) are minimized and in this way each of the single RZP-structures is brought closer to each other than in the first experiment at LCLS using three single RZP-structures; as last option, the very first single RZP-structure was examined, in order to compare directly the different structures and make conclusions about the outcome of structural and surface changes with respect to the efficiency of the devices. As the outcome of these measurements it was shown that the different structures did not differ very much in efficiency – except for the one which was coated with Nickel. It resulted in a few times higher efficiency value than all the other structures. Hence, it was decided to coat all the structures for the second actual experiment at LCLS with Nickel.

Experimental test at the X-FEL laser facility LCLS

The actual setup as initially planned in principle is shown in Figure 100.

For the first experiment at LCLS in 2012 was then decided to make use of a broader solid angle (angle of accepted rays/radiation) than possible to exploit using a single zone plate structure: simply by placing three RZP structures on the very same substrate and improve in this way the number of used photons. The actual setup at LCLS in principle is shown in Figure 104:

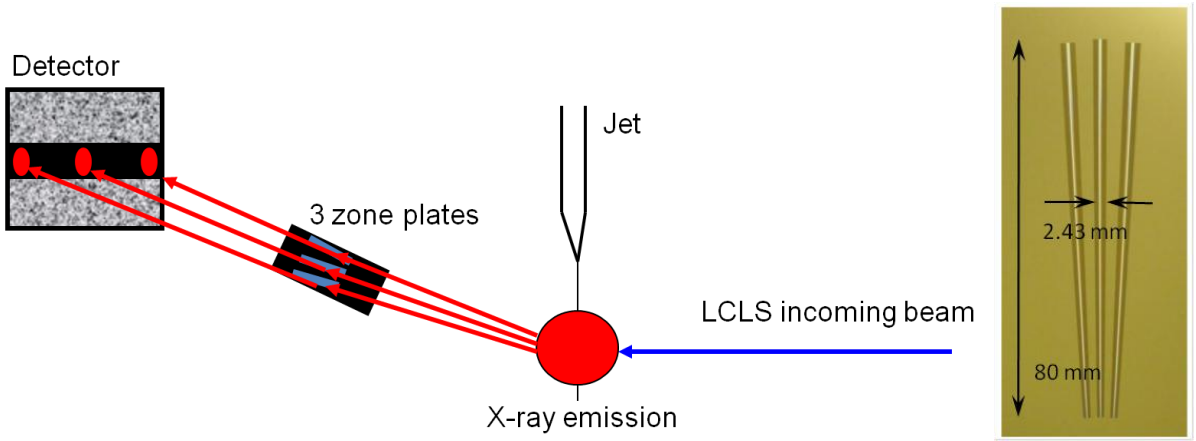

Figure 104: ***schematic setup at LCLS in the end of 2012 (courtesy of W. Quevedo). On the right side the actual structure is shown (courtesy of A. Firsov and M. Brzhezinskaya).***

With this setup the following images were recorded at LCLS in 2012:

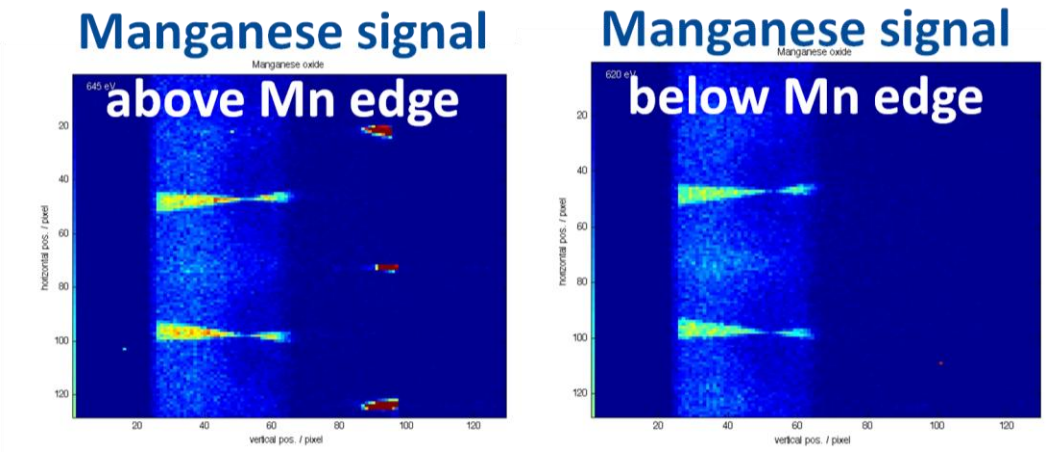

Figure 105: ***images at the CCD from the actual experiment at LCLS in 2012. On the left side clearly the three spots of the three RZP structures are visible (as red dots. Red means highest intensity); on the right side the sample was excited below the Mn edge so the spots clearly vanished as no fluorescence energy of 640 eV is present (courtesy of R. Alonso-Mori). The spots of Mn and O were that well separated that those of O are not in the image anymore. Note the images are tilted by 90°. On the left side the specular reflection of the silicon surface containing the shadows of the RZP structures is visible. (Note, the shape of the brighter regions between the shadows comes from the fact that the outer regions of the three RZP-structures themselves touch each other at a certain position – accidentally generated simply during fabrication of the structures.)***

From this experiment already some spectra could be extracted, which were then used for the follow-up project application and published within 2013, see [86]. The procedure for the measurement was: first pre-alignment of the spectrometer on a solid sample (for example as well on a Mn-coated part of the jet-fiber, then go on with more precise alignment on the actual jet running with a solution containing highly concentrated Mn, finally keep the alignment and continue running the jet with the actual low concentrated Mn containing solution. Only one resulting spectrum should be shown here as an example. Due to strong fluctuations of jet and FEL (essentially to overlap both spatially), normalization is essential. It is obtained by subtracting the intensity values of the area between the bright Mn spots from the intensity of the Mn spots themselves (as background correction) and the resulting intensity then divided by the intensity of the horizontal stripes (see Figure 105) as a kind of I_0 (as normalization). The resulting curve is shown in Figure 106:

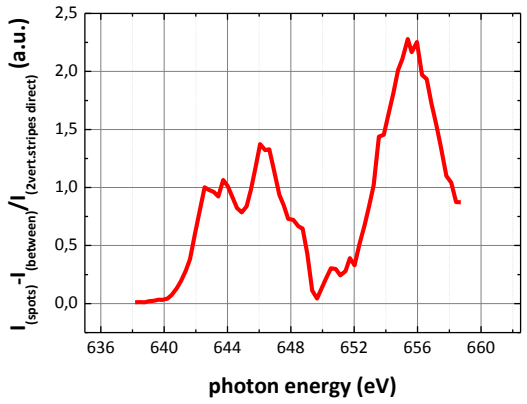

Figure 106: first/preliminary spectrum extracted from the experimental data of beamtime L632 in November 2012 at LCLS. Here, the spectrum (of L_2 and L_3 lines) of the cubane complex $Mn_2^{III}Mn_2^{IV}O_4(OAc)_3$ is shown (data as a courtesy of J. Yano and R. Mitzner).

Nevertheless, the device was not totally capable to obtain all the very low signals of Mn during the actual measurement of PSII-samples at the jet experiment. Of course, this was a combination of the fact that the jet was not stable during the entire time and additionally the overall-efficiency of the entire device was not exhausted, yet. Hence, considerations arose on how to improve the device in total for the next upcoming experiment already partly on-site at LCSL by discussing the different issues with our collaborating groups, more in detail then back at our home institutes. Considerations about coating and depth of profile optimizations were already mentioned; concerning the diffracting/dispersing structure itself will be mentioned in short in the following.

Improvement of the entire device

During the first beamtime at LCLS it was very obvious that the alignment procedure should be improved, in order to save very precious time, as the alignment procedure using the LCLS X-ray beam is time-consuming and in this way burns money every moment which is not used for the actual experiment. So a first idea in the beginning of 2013 was to bring additionally to the X-ray RZP-structure some substructures designed for a source of visible light, which then should serve as good pre-alignment before the actual beamtime. The principle of one idea is shown in Figure 107.

The practicability of the auxiliary RZP-structures for the visible light was tested during the second beamtime at BESSY II. The outcome of that testing was that the actual signal (focus of green light on the CCD) was a lot superimposed with stray light being reflected and scattered by all the inner walls of the RZP-substrate containing chamber (see Figure 101). As well, the X-ray RZP-structure itself might have caused a lot of scattering light delivered onto the detector, as it is simply a scattering reflective surface for the green light. But finally, one could find the focal spots of the VIS RZP-structures.

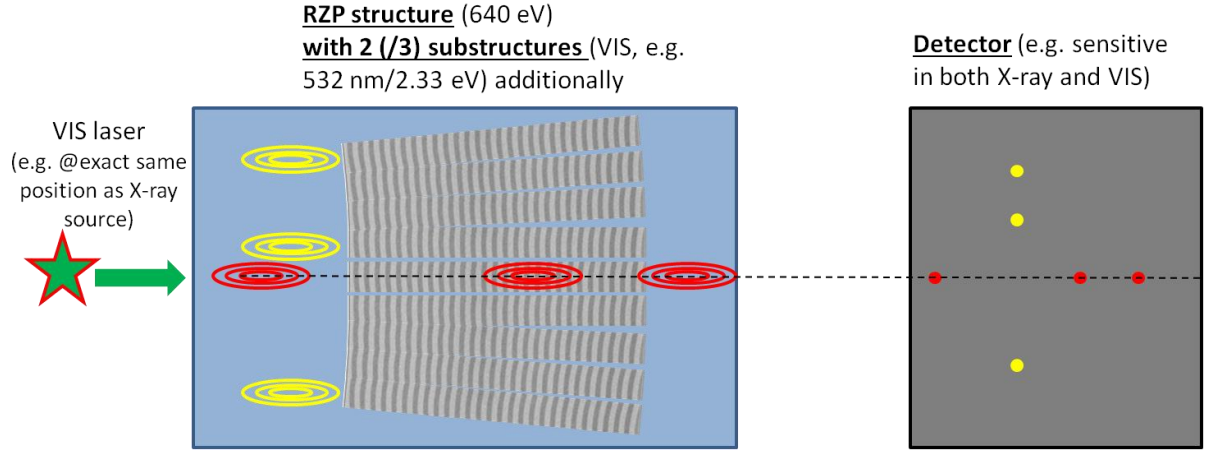

Figure 107: ***possible solution as pre-alignment sub-structures on the substrate containing the X-ray RZP-structure as well to save time during the actual experiment at LCLS.***

At LCLS there is an alignment laser anyway installed at the SXR beamline, which could possibly be used for this purpose as well in our case. The principle idea would be to bring some scattering source right in place of the actual experiment/jet, illuminate it with the alignment laser and then collect the light using additional RZP-structures on the same substrate surface. Either for example in the compilation as the three (or maybe just the two outer ones, as the X-ray structure should not be

influenced too much by diffraction on the borders between the VIS and the X-ray structures) red sub structures or as the compilation of the yellow ones. All the structures should have its focal position at the same detector. The number three and position is chosen, as this could be a hint during alignment that at least the direction of movement and positioning might be right or wrong. These ideas were not or just partially adapted as finally it was decided to use one structure in front before the X-ray structure and one in the end behind the X-ray structure. These two additional structures were made of the very same design, so they should focus into the same point at the detector.

The design of a single RZP with large solid angle has intrinsic limitations. Namely, the very high variation of line density over the entire optical element results in some problems. Figure 99 gives an overview of the different line densities contributing to the efficiency of the entire RZP-structure. One can guess that the very high number of 6000 lines per mm already results efficiency in the range of only per mill. This posed the idea to try to avoid them and to make use of the surface with an actually higher efficient structure. In principle, the outer regions should be "cut out", simply the inner core, which is as efficient as possible, should be left over and then multiplied. One could possibly cut out the outer structure to the maximum possible amount of simply keeping one point each in the middle remainder at each structure, which would lead to some VLS-kind of structure. The principle is sketched at Figure 108:

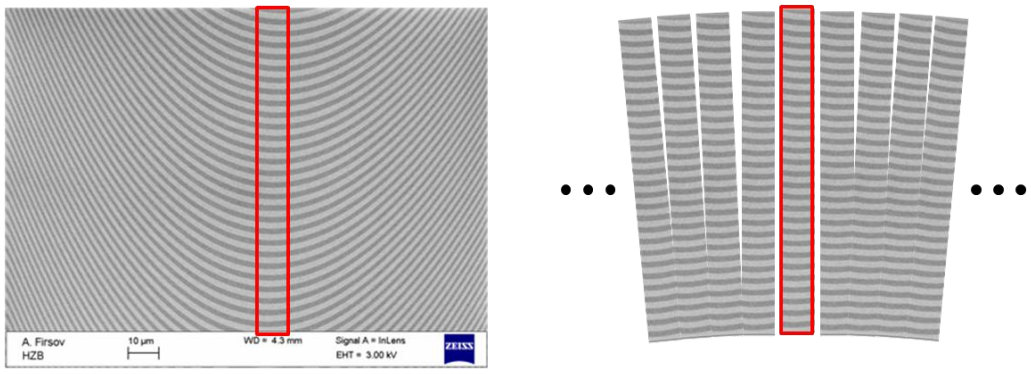

Figure 108: ***first ideas how to improve the efficiency of the RZP-structure for this specific experiment. Left: AFM picture of the actual structure (courtesy of A. Firsov and M. Brzhezinskaya). Right: the centering structure (marked with a red frame in both cases) should be multiplied; either by multiplying them simply by leaving out the outermost regions of very high line densities, or by choosing actually only small parts or a single point of each of the resulting structures and combine them reasonably.***

The above described structure should lead to a remarkable improvement of the overall efficiency of the RZP-structure, by increasing the solid angle and improve the diffraction efficiency. Further developments are presented in this work only shortly. The principle idea is to multiply either the more efficient parts of the structure and in this way to create an array of more than three RZPs, each of them of higher overall efficiency than the former ones, leading to a row of focal spots on the detector. Or, to minimize the cut out region so far that finally an almost 1D VLS-kind of structure will arise, leading to a line focus at the detector – probably of the length of the used CCD, ideally. Anyway, the entire solid angle should be used and covered with as much highly efficient structure as possible.

As result of the preliminary experiments at BESSY II, the multiple RZPs containing structure (Ni-coated) was decided to be used at the second actual experiment at LCLS in December 2013. As it was originally designed for the use of a detector of 100 mm size, at the 28 mm sized detector only 16

spots could appear. It was found to be the easiest to be aligned; as well known resulting images are expected, such as clearly focused spots of minus first order at the position of Mn, broader spots of minus first order at position of O and an overlay of zero order and shadows of the illuminated RZPs below the Mn signals (see Figure 109).

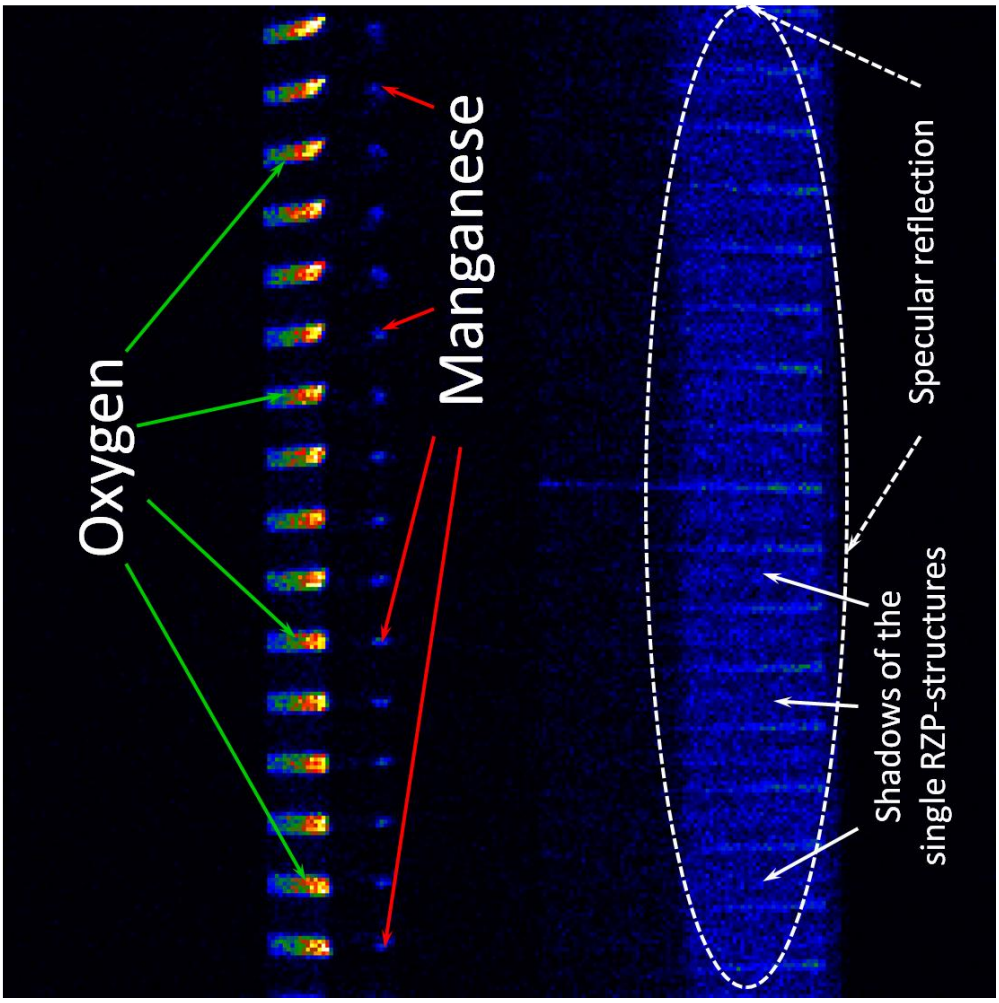

Figure 109: ***resulting image from the LCLS-beamtime in December 2013. Here a picture during alignment using a solid sample is shown. The different regions of interest are described within the image exemplarily. Using this kind of alignment the energy scans at the different model compounds were made (courtesy of J. Yano and R. Mitzner).***

At Figure 109 one can see that the alignment is not perfectly done, yet. The shadows and the focal spots are tilted a bit (the inclination angle is increasing from the center to the outer parts), which embodies that the distance to the source is either not perfect or the structure itself is not perfectly applied to the substrate. This is not totally improbable as it is extremely complicated to keep the conditions during e-beam writing of such a big, sophisticated structure totally stable; in addition, the minimal angular tilt of only very few milliradian (or transversal misalignment relating to the source point of only a few 100 µm) already leads to a tilt of the resulting image – clearly visible as well at the patches of Oxygen on top of Figure 109 (compare with simulation Figure 85 and Figure 86).

In this figure it is obvious that the resulting image at the CCD seems to be rotated by 90° compared to the original design. This is actually a real image, as it was during the improvement process decided that in this way the size of the source in dispersive direction of the RZP-structures should be

minimized (kept more stable) compared to last year's experiment. It was not mentioned so far, but the simulations were originally made for a source size of 10 µm times 10 µm (FWHM). This was assumed to be the real source size as the jet itself should have a diameter of 10 µm, the same as the LCLS-beam should have. During the first beamtime at LCLS in 2012, in order to prevent saturation effects in the sample, the beam size of the FEL was set to approximately 20 µm (10 µm jet, still) horizontally and 100 µm vertically. This led to an effective source size in dispersive direction of the RZP-structures of this order. Of course, the dispersive direction is the most important if good separation of the different energies or high energy resolution is aspired (see next project chapter 4.2). This caused broadening of the Manganese focal spot and possibly could lead to merging of the two energies as well.

One needs to understand that the alignment procedure during beamtime at LCLS is not as easy as for example at a synchrotron source. The first difference is of course the much lower peak intensity at a synchrotron, which leaves a lot of time to do proper alignment, without burning for example any alignment sample used for pre-alignment of the spectrometer itself. As the signal of Manganese in case of PSII compounds (which are of very high interest) is so small that one can barely see it at the CCD image, pre-alignment is inevitable. This specific beamtime in 2013 has furthermore suffered a lot from instabilities of the FEL itself. Several times, the X-ray itself got lost during alignment procedure; several times it has even never appeared at all. The three components, LCLS, jet and spectrometer needed to be in perfect interplay, which simply did not happen very often.

Conclusion:

Spectrometers and strategies for analyzing FEL light are of increasing interest. Especially spectroscopic approaches using time resolved methods are demanded. Reflection Zone Plates (RZP) are in the focus of present developments.

A special zone plate spectrometer built at the HZB was used at the Linac Coherent Light Source (LCLS) in Stanford. The single-element spectrometer consists of an array of single RZPs. The aim of the experiment was to receive the highest possible optical intensity in a fluorescence experiment in the energy range of the Mn L-edge. The challenge was to separate the Mn signal from the very intense O K-edge signal on a CCD camera.

Investigations concern a solar energy experiment. Only 2 – 3 % of incoming sun light is used from the leaves of plants for photosynthesis with chlorophyll. The oxygen evolving component in this reaction is a manganese cluster. Its electronic state can be analyzed by measuring the Mn L_3-edge (638 eV) in absorption mode. To improve the spectrometer efficiency, a relatively low energy resolution of $E/\Delta E \approx 100$ in minus first order was chosen. A low energy resolution decreases the number of the grooves (Lines/mm) and leads to a higher efficiency of the optical element. The properties of such an RZP were simulated extensively for the manufacturing of the entire spectrometer setup. All possible misalignments of RZP and detector were simulated. As a result, the parameters for the construction of the chamber, containing the mounts and motors were finalized. After first tests at BESSY II, the first actual experiment at LCLS was conducted in 2012. After a subsequent improvement of the optical system's efficiency, a follow-up experiment was then conducted successfully in 2013.

The photosynthesis reaction takes place in water, so that a liquid jet experiment had to be arranged, in order to stay as close to the natural process as possible. Hence, some of the measurements should be done at room temperature as well. In 2013, three model compounds could be examined. It could be proved that, since the compounds (being) yield such a low Mn signal caused by a very low molar concentration, the improved device in its current state should be absolutely capable of yielding significant results from the actual photo component system. As a result of these experiments it will be possible for the first time to understand the electronic structure of the different states of the photo component protein complex of Photosystem II (PS II) in the Kok-cycle.

Parts of the project results are published in:

[29]: A. Firsov, A. Erko, F. Senf, J. Rehanek, M. Brzhezinskaya, R. Mitzner, Ph. Wernet, A. Föhlisch, *"Novel wavelength-dispersive X-ray fluorescence spectrometer"*, Journal of Physics: Conference Series, Volume 425, 152013, pages 1-5 (2013)

[86]: R. Mitzner, J. Rehanek, J. Kern, A. Föhlisch, A. Erko, U. Bergmann, V.K. Yachandra, J. Yano et al., *"L-Edge X-ray Absorption Spectroscopy of Dilute Systems Relevant to Metalloproteins Using an X-ray Free-Electron Laser"*, Journal of Physical Chemistry Letters, Volume 4, pages 3641-3647 (2013)

[Kern]: J. Kern, J. Hattne, R. Tran, R. Alonso-Mori, H. Laksmono, S. Gul, R. Sierra, J. Rehanek, A. Erko, R. Mitzner, P. Wernet, U. Bergmann, N.K. Sauter, V. Yachandra, J. Yano, *"Methods development for diffraction and spectroscopy studies of metalloenzymes at XFELs"*, Philosophical Transactions of The Royal Society B, Vol. 369 no.1647 20130590 (2014)

[Braig]: C. Braig, H. Löchel, R. Mitzner, W. Quevedo, P. Loukas, M. Kubin, C. Weniger, A. Firsov, J. Rehanek, M. Brzhenzinskaya, P. Wernet, A. Föhlisch, A. Erko, *"Design and optimization of a parallel spectrometer for ultra-fast X-ray science"*, Optics Express, Vol. 22, Issue 10 pp. 12583-12602 (2014)

Poster: Rehanek, J; Mitzner, R; Yano, J; Kern, J; Weniger, C; Firsov, A; Senf, F; Quevedo, W; Alonso-Mori, R; Schröder, H; Schlotter, W; Wernet, P; Föhlisch, A; Bergmann, U; Brzhezinskaya, M; Yachandra, V; Erko, A: "Design of a Reflection Zone Plate Spectrometer with Ray Tracing and First Results for Fluorescence Experiments at LCLS", European XFEL Users' Meeting, Hamburg, Germany, January 23rd – 25th 2013

4.2. RZP technology for cross-dispersive RIXS measurements at synchrotron- and FEL-sources – a case study

One leading goal for researchers nowadays is the understanding of the physics of matter on fundamental dimensions. The properties of materials are closely related to the energies for the low-lying excited states of atomic, electronic and magnetic degrees of freedom, etc. Inelastic scattering techniques for spectroscopy probe these in the most direct way by using energy transfer during scattering processes. Moreover, by determining **not only the energy but also the momentum transfer** via variation of the detection angle, the dispersion of collective excitations in solids and the symmetry of low-energy excitations in molecular systems can be mapped.

Resonant inelastic X-ray scattering (RIXS) is what is called a photon-in/photon-out experimental technique, based on synchrotron radiation. It provides the user with information about charge-neutral excitations. It is called "resonant", as the energy of the incident X-ray is chosen so that it coincides with one of the X-ray absorption edges of the atoms within the system under examination; so it resonates with the system. For example at the Co 2p->3d resonance (776 eV) a Co 2p core-hole electron is excited to an empty 3d state. In the following, this core-hole can be refilled e.g. with an electron from the occupied valence band. Figure 110 shows a sketch of such a process:

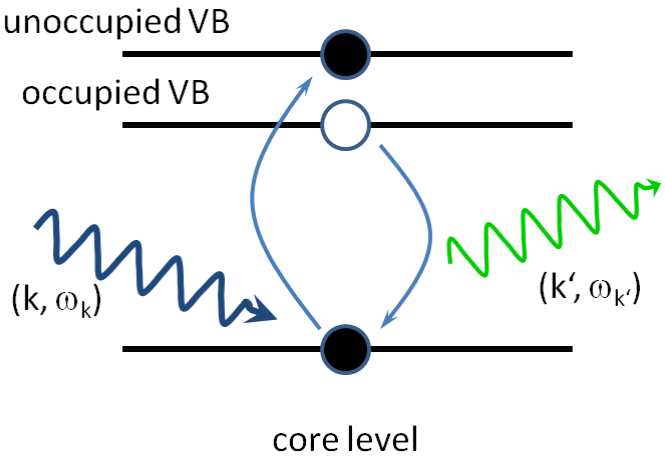

Figure 110: example for a *RIXS process: electronic interband excitation. It is a second-order optical process, in which a core electron is resonantly excited to absorption threshold by an incident X-ray. Then, an electron from an occupied valence band is de-excited (by emission of an X-ray of lower energy). The absorption process (which energy excites the electron from the core hole) reveals information about the empty electronic states of the system. The emission on the other hand results the information about the occupied states.*

Due to this energy selectivity, RIXS is sensitive to a wide range of elementary excitations in solids, liquids and gases, like inter-band and crystal-field excitations [90], but also charge-transfer excitations of electronic nature, magnetic excitations [91], phonons in solids and vibrational excitations in molecular systems [92], [93], [94]. The wealth of the physical information available from RIXS depends strongly on the resolution and detection efficiency.

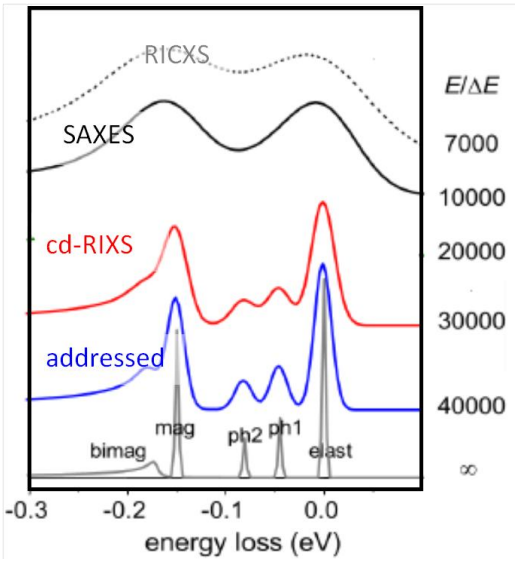

Figure 111: ***demonstration of the demand for high-resolution momentum resolved RIXS data. Survey of current state of the art instruments (SAXES in operation at PSI, RICXS commissioning at HZB). These cannot resolve fundamental energy scales in correlated-electron system solids sufficiently. This is addressed by different synchrotron facilities (e.g. €RIXS at ESRF) (and our proposed cd-RIXS; cross-dispersive RIXS). At the bottom excitations of interest and the connected energy losses are depicted (based on [95]).***

At the bottom of Figure 111 a survey is presented, which would be the possible components (elastic peak, magnon peak, multi-magnon continuum and (multi-)phonon components) of excitations for a correlated electron system, which are addressed to be resolved clearly.

For RIXS it is exceedingly important to propose approaches for an energy resolution as high as possible (see Figure 111) with the smallest possible amount of losses in photon flux. As demonstrated in the previous chapters, an RZP is well applicable as a soft X-ray monochromator and fluorescence spectrometer; though up to now for a rather low energy resolution of $E/\Delta E = 100$. It is already proposed to apply the RZP as a monochromator for the European XFEL (see chapter 3.2.2). Actually, it is already applied in the broadest sense as a monochromator in the precedent project (chapter 3.3): the both present energies of interest (640 eV and 538 eV) are clearly separated spatially and in that sense analyzable individually, and both present at the same time on the detector. So it comes to mind to use the diffraction and focusing ability property of RZPs for soft X-rays in the function of a monochromator and fluorescence spectrometer within a proposed scheme for resonant inelastic X-ray scattering (RIXS) experiments. The RZP as a monochromator in the previous project worked very well, but is presented so far at very big energy distances. The question for the following will be: is it as well capable of resolving very small energy differences (energy resolutions in the range of $E/\Delta E \approx 20{,}000 – 40{,}000$).

cd-RIXS at the proposed undulator UE30 at BESSY II

In this work, a particular case will be presented exemplarily for a synchrotron source; as well design and simulation for the European XFEL are currently ongoing. The conceptual designed RIXS beamline is proposed to be set up at a newly proposed UE 30 undulator beamline. It will be installed at the low-β section L06, which provides a small emittance and is therefore ideally suited for high-brilliance

applications. Additionally, the intended sector provides enough floor space to install a 7 meter long detector arm that can be rotated horizontally around the sample. It enables an angular detection range of at least 20 to 160 degrees for detection/measurement of momentum transfers. Furthermore, since the monochromator is supposed to be used without exit slit, it enables the horizontal dispersion of the spectrometer; this opens the option of "multi-color" RIXS by placing the sample in the position of the focal plane of the design energy of the RZP-Mono. Thus, different spots on a sample are exposed to different photon energies. A parallel detection of these spots provides simultaneous RIXS spectra for different excitation energies [96]. Figure 112 shows a sketch of the planned RIXS (METRIXS) beamline at BESSY II:

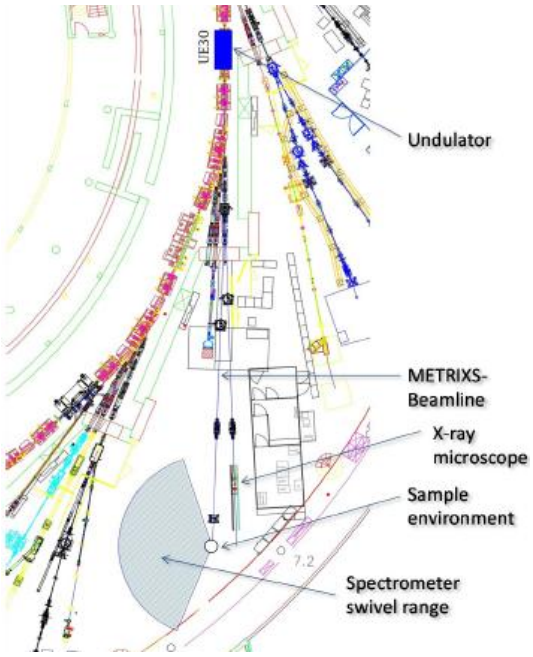

Figure 112: ***Floor plan of the L06 sector at the BESSY II storage ring with the X-ray microscope and the planned/proposed RIXS (METRIXS) station (courtesy of [97]).***

The HZB undulator department is currently developing an in-vacuum APPLE II undulator UE30. Its properties are summarized in table 1. Figure 2 shows the flux/energy characteristics of the undulator for different harmonics.

Table 13: ***BESSY II machine parameters at the low-β section***

BESSY II				**UE30**		
Ring energy	E	[GeV]	1,70	**Period length**	[mm]	30
Critical energy	ε_c	[keV]	2,50	**Periods**		50
Bending Radius Magnetic Field	R	[m] [T]	4,359 1,3	**Total length L**	[mm]	1500
Ring current (top-up)	I	[mA]	300,00			
Source size hor. (UE30)	σ_x	[µm]	71,60			
vert.	σ_y	[µm]	9,90			
Divergence hor. (UE30)	σ_x'	[µrad]	74,60			
vert.	σ_y'	[µrad]	8,10			

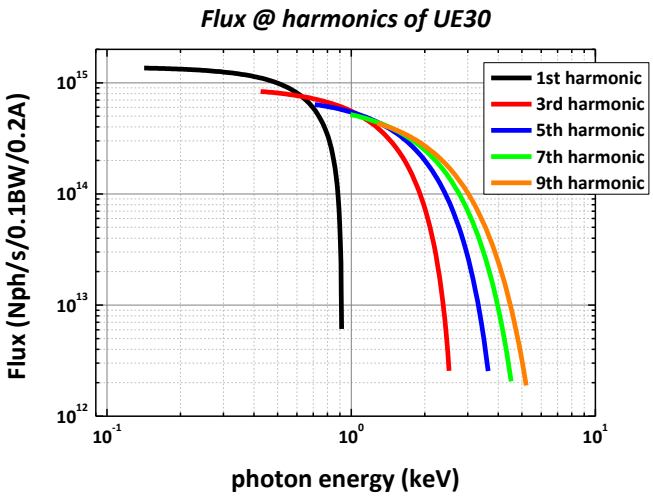

Figure 113: ***Flux curves for the in-vacuum UE30 undulator (calculated for a ring current of 200mA) (courtesy of [98]).***

Knowing these parameters, and having a look at the flux curves, as the main energy of interest for this case study is 776 eV (the CoLa-edge randomly chosen as soft X-ray), the third harmonic of this undulator is chosen and a source file for simulation with RAY is generated, using the code WAVE. Hence, simulation of the proposed beamline can be started.

"classical" – SGM approach for monochromator

The first approach, which means one step back in terms of modern optical elements (meaning RZP and its applications), is to have a look at a "classical" but state-of-the-art monochromator beamline, a spherical grating monochromator (SGM) (according to [99]). The goal of this beamline design is to have a focus (on the sample), which is horizontally approximately 2 µm (and possibly variable) and vertically images the largest possible part of the undulator harmonics into an energy dispersed line. This number arose from the simulations shown below about the actually proposed RZP-RIXS-beamline – to be specific, its RZP-spectrometer contained.

In order to avoid complications with inhomogeneous samples, the energy dispersion should be as small as possible but still compatible with the vertical detector resolution of the spectrometer. For high-resolution applications, a spherical grating monochromator is usually the best choice. The usable energy range for a single grating is smaller than for a plane-grating monochromator. However, with a combination of different gratings the whole energy range of interest can be covered with high energy resolution. The peak resolving power is of the order of 40,000. The energies for the optimum resolving power can be chosen to match relevant energies. A solution with five gratings, optimized for the C K-edge, N K-edge, O K-edge, Mn L-edge or Fe L-edge, Ni L-edge, is exemplified in Figure 114:

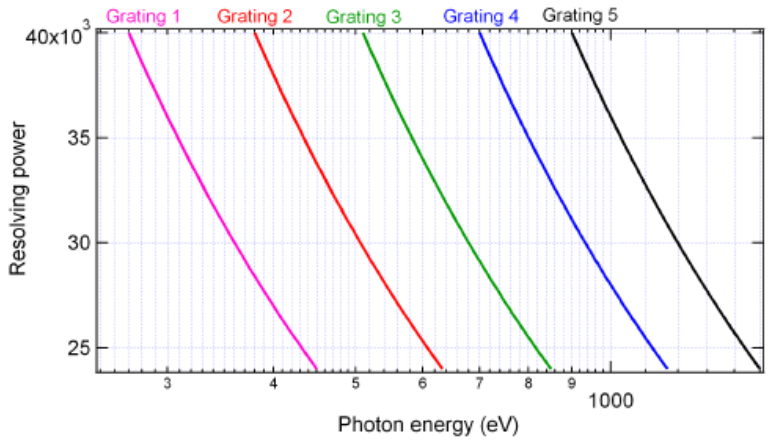

Figure 114: ***Energy dependence of the resolving power of a spherical grating monochromator in principle. It is shown to present capability of the monochromator to cover the entire energy range of interest. The resolving power decreases as 1/e (courtesy of [97]). (Five gratings can be fitted in a standard BESSY grating tank.) This means that for the SGM design the used gratings could be exchanged; each according to the energy range of interest in the different possible particular cases.***

A layout for an SGM is shown in Figure 115; the parameters are listed in Table 14.

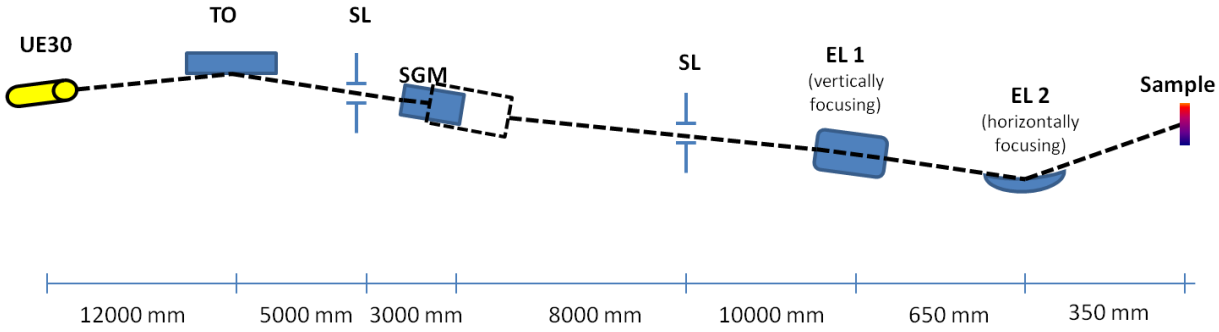

Figure 115: ***spherical grating monochromator beamline as a possible monochromator considered for RIXS experiments (top view).***

Table 14: ***beamline parameters of the SGM-design***

TO	SGM	EL1 (KB-mirror 1)	EL2 (KB-mirror 2)
toroidal mirror	**spherical grating mono**	**ellipsoidal mirror 1**	**ellipsoidal mirror 2**
grazing angle 2°	Entrance length 3000 mm	grazing angle 2°	grazing angle 2°
sagg. Entrance length 12000 mm	Exit length 8000 mm	entrance length 10000mm	entrance length 18650mm
sagg. Exit length 5000 mm	1st order of diffraction	exit length 1000mm	exit length 350mm
mer. Entrance 12000 mm	Grating radius 100000 mm		
mer. Exit 8000 mm	normal incidence α 88.96		
	normal incidence β -85.03		
	2250 lines/mm		

From ray tracing simulation we obtain an energy resolution of about 40,000 (applying slit sizes of 8 µm entrance and exit slit, respectively) from that SGM beamline and a distribution in the focal plane of the following form:

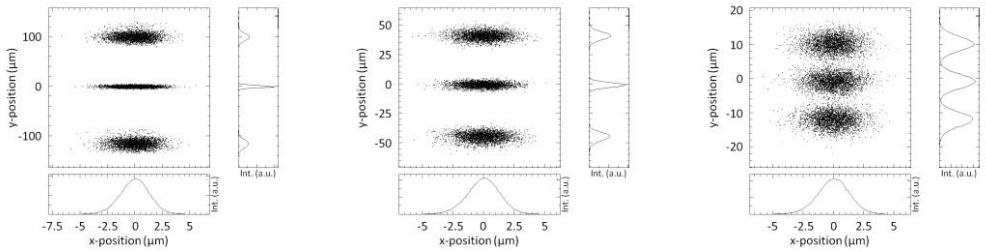

Figure 116: ***Distribution in the sample plane of the beamline at 776eV ±2.5eV (left), ±1eV (middle), ±260meV (right). (Note the different scale, focal spot of 776eV – which is in each case in the middle – is of the same size. The slit is fully open for simulation and display of these distributions.)***

RZP-RIXS-beamline

After simulation of this "classical" solution for a monochromator, one can make considerations on how to apply the knowledge about RZPs onto this concept. But, one needs to keep clearly in mind, that this SGM-beamline is build especially for the purpose to obtain really monochromatized light of one specific energy. The RZP approach, which is now presented, is of course totally different from that. The idea is to have a certain range of energy transferred into the sample but with a specific, well known distribution within this plane. This demand can be met with application of a RZP, as it has this required distribution intrinsically by its property of dispersion and focusing.

A novel conceptual design for an especially dedicated beamline for RIXS is proposed. The optical scheme of the beamline consists of only one mirror and two reflection zone plate arrays (RZPA), instead of nine optical elements in a previously reported "standard" design [96], providing imaging and dispersion actions in two orthogonal planes. With the application of RZP-arrays one could cover as well the entire energy range of interest by either changing each time to the specifically designed RZP-monochromator and its appropriate RZP-spectrometer; or keep them all right in place already from the beginning. Due to the reduction of the number of optical elements the proposed conceptual beamline is expected to have several times higher transmission at the energy of 776 eV (CoL_{α}). Figure 117 shows the setup for this kind of solution. The first RZPA is used as dispersive monochromator focusing the desired energy range onto the sample plane; the second one operates as spectrometer, using the scattered light from the sample. The two RZPAs are arranged orthogonal to each other – so the dispersion directions of those are orthogonal, too.

Lately, two new optical systems were developed based on total external Reflection Zone Plates (RZP). The first system, an RZPA monochromator, was successfully used at the BESSY II femtosecond slicing beamline [100]. The photon flux of this monochromator is on the order of 20 times higher compared to conventional optical systems with the same energy resolution. The second system is an RZPA spectrometer prototype successfully tested at the BESSY II beamline UE52 [28]. It is designed for parallel registration of fluorescence spectra in the energy range of 100-500 eV.

Hence, by use of combination of these two systems, we could get very promising results from our simulations for the optical scheme of a RIXS spectrometer. Figure 117 shows the sketch of the proposed RZP-beamline:

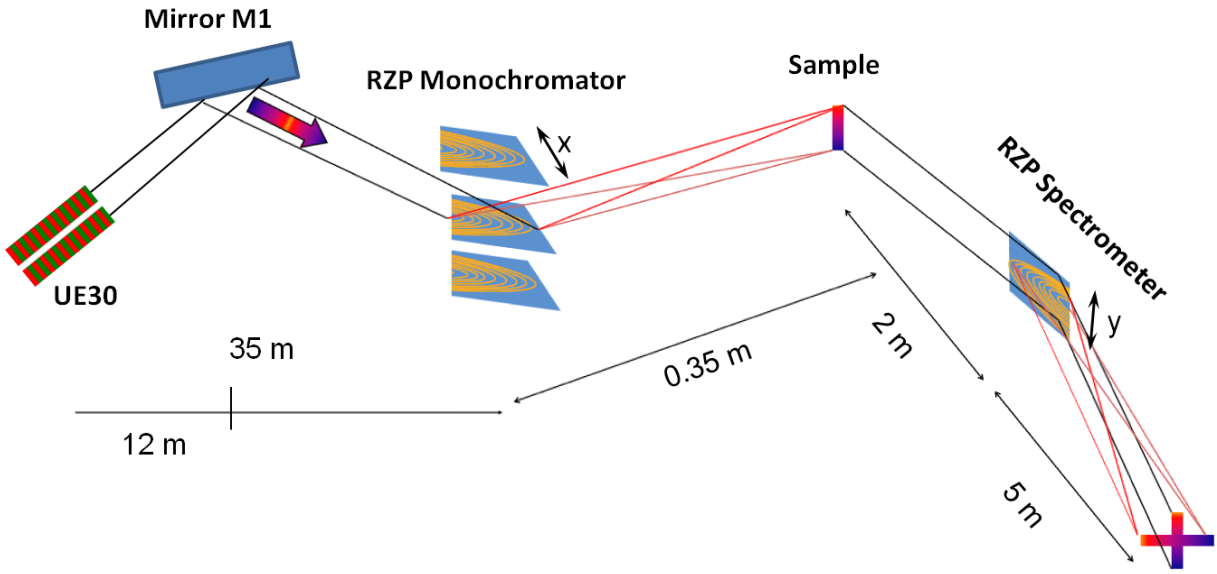

Figure 117: ***sketch of the cross-dispersive spectrometer setup. At the location of the "monochromator"-side it is indicated that different RZPs could be placed and replaced easily (RZP-arrays; RZPA) – in order to cover different energy ranges and obtain for each the desired high energy resolution. Same could be applied on the spectrometer side.***

The monochromator side of the (entire) beamline consists of a single mirror (M1) and a RZP as dispersive and focusing element. M1 is part of the switching-mirror unit, which will be installed anyway at L06. It distributes the beam into two planned beamline branches (RIXS beamline and a scheduled microscope-beamline, respectively). Here, exemplarily the properties for the energy of 776 eV (CoL_{α}) will be presented, as the different other energies of interest will be addressed each by particularly designed zone plates for those. The input parameters for design of the RZP must be optimized as it is described above already in chapters 2.3.2.2 and 3.3 and published in [101]. The actual zone plate parameters for the RZP-Monochromator are listed in Table 15.

Table 15: RZPMono parameters of the structure, using only pure Silicon

entrance arm length [m]	exit arm length [m]	position on RZP [mm]	α [°]	β [°]	line density [l/mm]	depth of profile [nm]	expected efficiency [%]
35	**0,35**	**-50**	**2,003**	**2,809**	**370**	12,5	6,117
		-40	2,002	2,881	409	12,5	7,007
		-30	2,002	2,957	451	12,5	6,807
		-20	2,001	3,037	497	12,5	6,517
		-10	2,001	3,121	547	12,5	6,181
		0	**2**	**3,21**	**601**	**12,5**	**5,844**
		10	1,999	3,305	660	12,5	5,499
		20	1,999	3,405	724	12,5	5,148
		30	1,998	3,511	794	12,5	4,804
		40	1,998	3,624	871	12,5	4,453
		50	**1,997**	**3,745**	**956**	12,5	4,108

From these parameters we learn, if we have a closer look into the last column – which represents the theoretically expected efficiency – that we have an optical element of just very low efficiency (integrated efficiency is about 5%). Similar considerations as in the precedent chapter lead to the idea to have this element covered with some coating, which could raise efficiency at this specific design energy (applying the corresponding grating parameters). So the coating of Nickel was taken into simulations in that way that as Substrate bulk Ni is used with a monolayer of NiO of 3nm thickness on top of it. All applying a roughness of 0.2 nm rms, which was an experimentally obtained value (see chapter 3.3). The influence of choosing the appropriate depth of profile was as well simulated, as so far assumed to be the same over the entire optical element. So the optimal values regarding perfect depth of profile and coating each at the specific position at the RZP is shown in Figure 118 and Table 16:

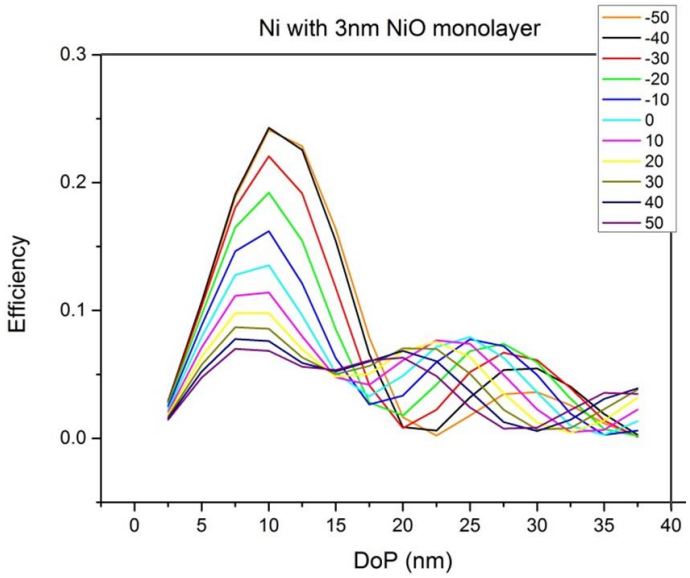

Figure 118: ***result of simulation to obtain the perfect depth of profile for the structure; already Ni-coating is taken into consideration (courtesy of [87]).***

With the choice of the appropriate depth of profile and adding the Nickel coating, one obtains the integrated efficiency of the entire zone plate structure (see Figure 119 and Table 16).

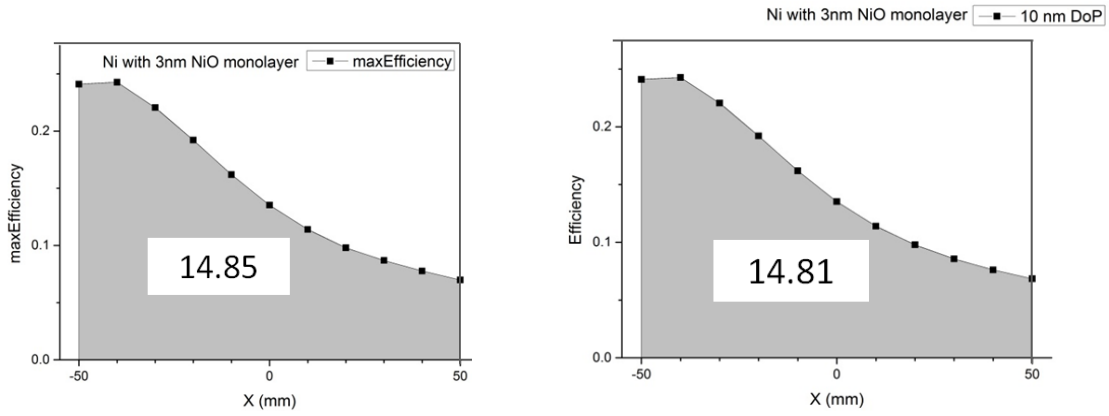

Figure 119: ***simulation of the integrated efficiency over the entire optical element; left: different depths of profile (as in the Table 16); right: constant depth of profile (10nm) (courtesy of [87]).***

Table 16: ***RZPMono parameters of the structure applying a coating of NiO monolayer on top of Ni bulk substrate.***

entrance arm length [m]	exit arm length [m]	position on RZP [mm]	α [°]	β [°]	line density [l/mm]	depth of profile [nm]	expected efficiency [%]
35	0,35	**-50**	**2,003**	**2,809**	**370**	10	**24,107**
		-40	2,002	2,881	409	10	24,277
		-30	2,002	2,957	451	10	22,055
		-20	2,001	3,037	497	10	19,213
		-10	2,001	3,121	547	10	16,195
		0	**2**	**3,21**	**601**	**10**	**13,529**
		10	1,999	3,305	660	10	11,399
		20	1,999	3,405	724	7,5	9,789
		30	1,998	3,511	794	7,5	8,568
		40	1,998	3,624	871	7,5	7,614
		50	**1,997**	**3,745**	**956**	**7,5**	**6,846**

Thus, one obtains a theoretical value of integrated efficiency for this specific optical element which is optimized (depth of profile, entrance angle, proper coating) for this specific design energy of 776eV. The integrated efficiency after all optimization steps will be around 15% in theory (3 times as high as in case of pure Si). For other energies, which should be covered, the same considerations should be made each for the different desired high resolved energy range. In this case, the integral efficiency of the element does not differ so much for the cases of having different profile depths and of having it constant. This relieves the possible actual fabrication.

As a result of the simulations, Figure 120 shows the energy distribution in the sample plane (after the RZP Monochromator) for 776 eV and two energies around this central energy. The energy interval (776 eV ± 26 meV, ±260 meV, ± 1 eV, ± 2.5 eV) is depicted at the left; which (approximately) corresponds to the width of the undulator harmonic. The entire size of the dispersion within this energy range onto the sample plane is around 50 µm. The simulation shows that the energy resolution will be very high (around the corresponding design energy of the RZP), as small energy differences like 26 meV can be well distinguished (see Figure 120, right) – this equates an energy resolution of E/ΔE ≈ 30,000. Accordingly, spots that originate from the sample serve as new source points for the following RZP spectrometer. For the spectrometer, a rotated horizontal dispersion direction is projected with the RZP positioned at 2m away from the sample.

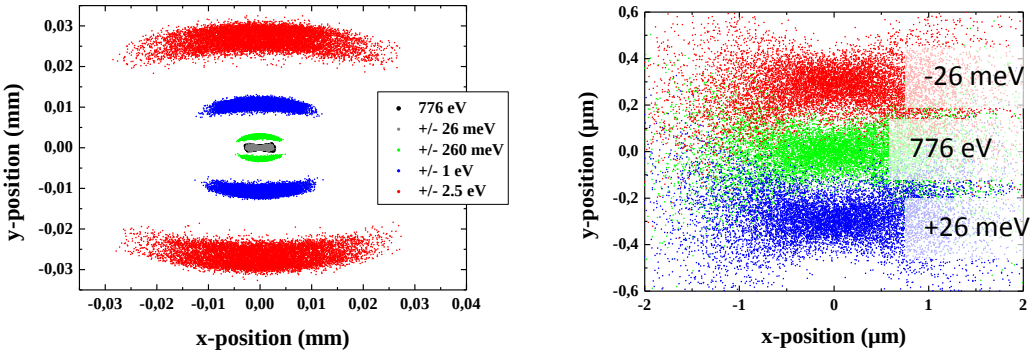

Figure 120: ***left: Distribution at the sample plane of the RZP monochromator at 776eV ± 2.5eV, ± 1 eV, ± 260 meV and ± 26 meV. Right: zoom in at the sample plane at energies very close to the design energy of interest (Note that these 2 pictures have different scales. The spot in the middle is always of the same size.) (The***

broadening of the energies "far away" is an optical effect of high focusing/diminution (imaging) of 100:1; seen as well for the SGM design in dispersive direction.)

As mentioned before, the source size in dispersive direction of the RZP matters significantly in the sense of bigger size means worse energy resolution. So it is obvious that the change of size of the resulting image of the RZP-monochromator at greater energy distances could influence the energy resolution capability of the RZP-spectrometer in a negative manner.

The above described properties are only applicable for narrow energy ranges around the central energy; as a consequence of the achromaticity of a RZP. Energies further away from that design energy are spread wider in the horizontal direction in the sample plane, which serves as new source point for the RZP-spectrometer. As easily comprehensible, having a look at Figure 77 in chapter 4.1, the optimal focusing plane would be tilted (around the "x-axis" of the image of the RZP-monochromator) whereas, however, the sample plane is necessarily vertical to allow a variable momentum transfer. Generally, in order to keep the source for the RZP-spectrometer still small as necessary, the sample could for example be structured in a way that its horizontal extension is small enough – e.g. by using a jet or any sample of just 2 µm or by inserting a 2 µm wide slit right in front of the sample. However, in both solutions the flux into the sample decreases with the distance (spatially as well as energetically) to the central energy. The resulting transmission through a slit of 2 µm is shown in Figure 121. Thus, one loses orders of magnitude of intensity if broader energy ranges are examined with the same RZP of this very high energy resolution. In order to overcome this problem, mirror M1 could be a toroidal mirror to focus those spots small enough to obtain good source points for the RZP spectrometer.

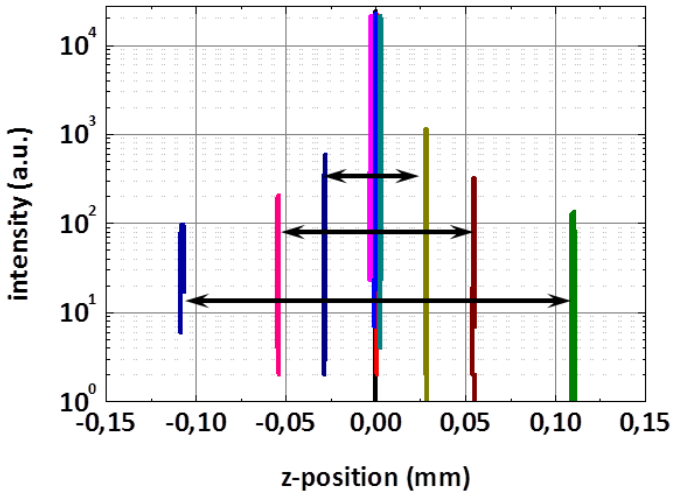

Figure 121: ***intensity/total flux through a slit of 2 µm size (horizontally) in the sample plane without additional horizontal focusing. (The 3 arrows indicate the energy distances of ±2.5eV (top), ±5eV (middle), ±10eV (bottom).)***

For the next simulation of the spectrometer, we took a source point with the dimensions of the focused energies in the sample plane (0.2 µm x 2 µm; horizontally x vertically) and apply different energies around this central energy of 776 eV again. The result of ray tracing simulation of the RZP-spectrometer side is shown in Figure 122:

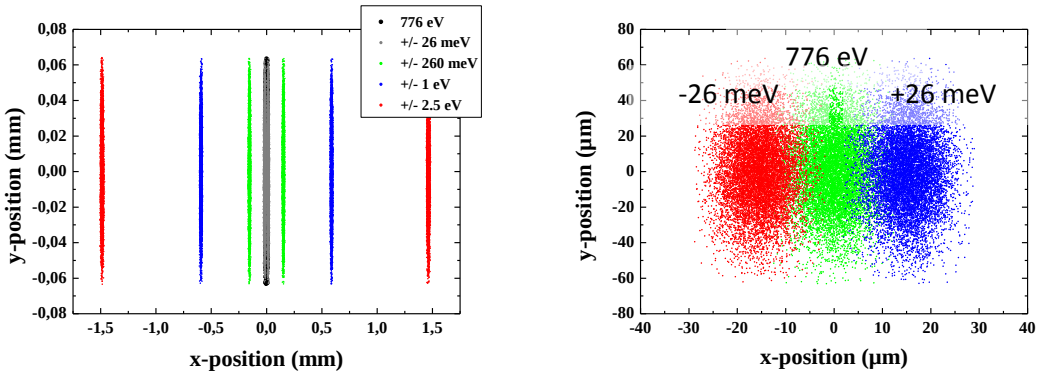

Figure 122: ***left: distribution at the sample plane of the RZP spectrometer at 776eV ± 2.5 eV, ± 1 eV, ± 260 meV and ± 26 meV. Right: zoom into the focal plane of the RZP spectrometer. (Note that these 2 pictures are of different scale.)***

Figure 122 shows the distribution of simply the spectral properties of the RZP-spectrometer. The source point is in case of simulation for Figure 122 all the time the perfectly focused spot in the middle of the RZP-Mono sample plane. Still at energy distances of ± 26 meV the spots corresponding to these three energies (centering and differing energies) could be very well separated. The parameters for this simulation are summarized in Table 17:

Table 17: ***design parameters for the RZP-spectrometer***

entrance angle α	exit angle β	entrance arm R_1'	exit arm R_2'	average line density
5°	2°	2 m	5 m	0.5 µm

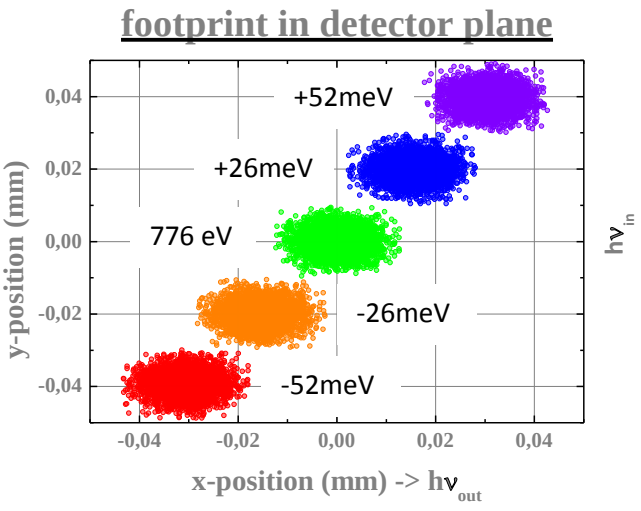

Figure 123: ***distribution in the detector plane (focal plane of the RZP spectrometer), containing information about both incoming and outgoing energies.***

Using the spots (distribution and size) coming from the RZP-Mono and the sample, respectively, at an energy range of around 100 meV around 776 eV in the following simulations, leads to a certain distribution in the sample plane of the spectrometer. In this case we assume the different positions of the different energies after being focused from the RZP-Mono. So we get in the end the photon-in – photon-out information in the detector plane of the RZP-spectrometer. Figure 123 shows the ray tracing simulation results of the different energies through the entire beamline (RZP - monochromator and RZP-spectrometer, respectively). The energies are distributed along the diagonal line of the detector. An energy difference of 26 meV translates into a spatial offset of 18 µm

horizontally and 20 µm vertically, which can be well resolved with existing detectors. From these simulation results, we obtain a total resolving power in the order of 30,000.

The above described seems so far to be quite reasonable, with a remarkably high energy resolution.

But, if one has a deeper look into the parameter to manufacture this kind of RZP-structures, one gets easily an idea of difficulties regarding the actual parameters. So the question about the RZP-spectrometer leads to unfortunate results so far. Further simulation regarding the device's parameters showed that with the given parameters, the RZP-spectrometer yields only very low efficiency (see Figure 124 and Table 18):

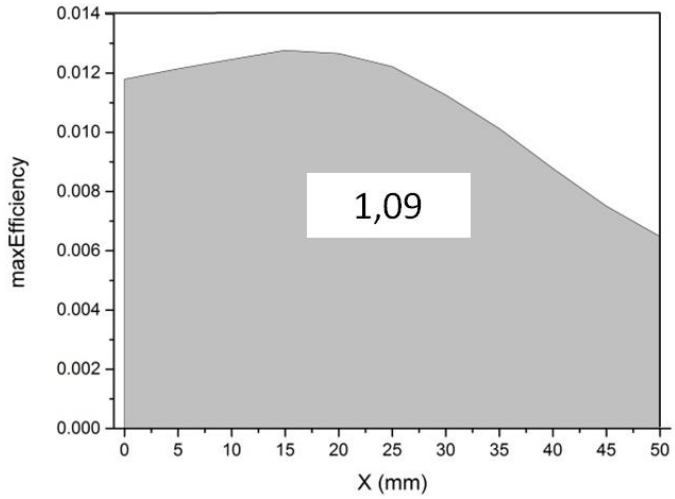

Figure 124: ***efficiency curve over the entire optical element of the RZP-spectrometer; this device obviously results only the very low efficiency of 1.1 % (courtesy of [87]).***

Table 18: ***RZP-spectrometer parameters; minus first order of diffraction, energy of 776 eV, NiO monolayer on Ni-bulk-substrate used for simulation.***

entrance arm length [m]	exit arm length [m]	position on RZP [mm]	α [°]	β [°]	line density [l/mm]	depth of profile [nm]	expected efficiency [%]
2	5	**-25**	**5,063**	**4,338**	**649**	35	1.18
		-20	5,05	4,342	634	35	1.22
		-15	5,038	4,346	618	35	1.25
		-10	5,025	4,351	602	35	1.28
		-5	5,013	4,355	586	35	1.27
		0	**5**	**4,359**	**571**	35	1.22
		5	4,988	4,364	555	35	1.12
		10	4,975	4,368	540	35	1.01
		15	4,963	4,373	525	35	0.88
		20	4,951	4,377	510	35	0.75
		25	**4,938**	**4,381**	**494**	35	0.65

This comes of course from the fact that at these angles of incidence and exit, combined with this energy of interest, the reflectivity tends to zero (see Figure 125).

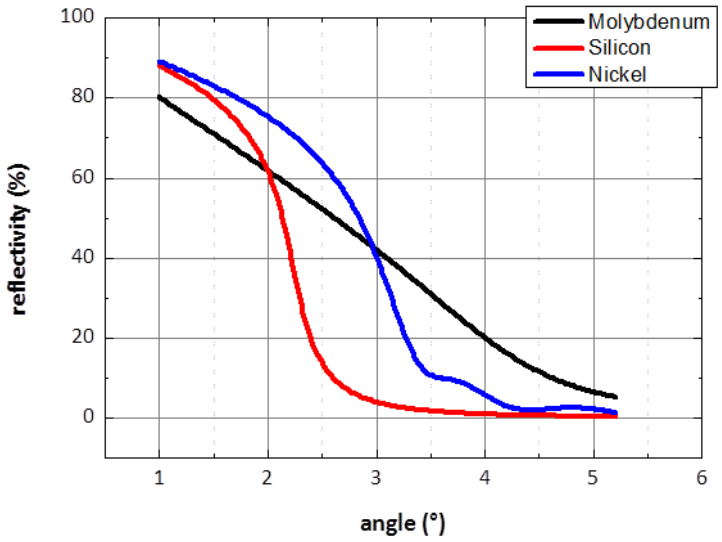

Figure 125: ***reflectivity of a (mirror) surface at 776 eV for Silicon (red line), Ni (blue line) and Molybdenum (black curve) (data generated using [102]); in all cases layers of 30 nm on top of bulk Si-substrate, with an roughness of 0.3 nm (rms) are represented.***

So, of course, the idea came up to change the parameters. The distances should be kept the same, in order not to shift the optical element even further away from the source (as described in chapter 3.3 already, the intensity decreases exponentially with the distance). But, the angle of incidence is changed to 2°. A change of parameters lead to the following better integrated efficiency (see Figure 126 and Table 19), but, having a look specifically at the line density in the table, one gets to mind the rough thumb-rule about potential energy resolution of a grating: "you need to illuminate at least this number of lines, which you aspire for energy resolution" (see chapter 2.3.2.1). Simply following this rule, this device would not be capable at all to result an energy resolution even close to the expected 30,000.

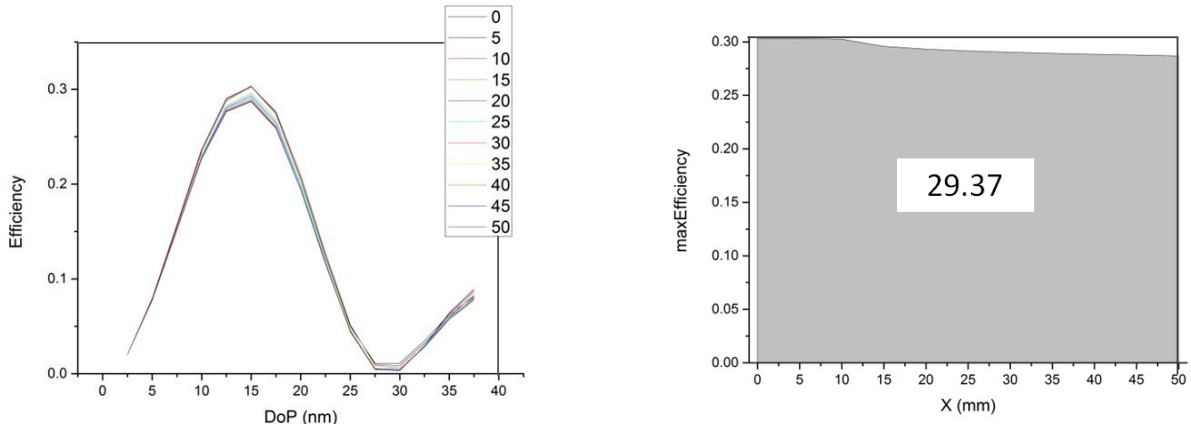

Figure 126: ***angle of incidence in the center changed to 2° (higher reflectivity); left: simulation to obtain the optimum profile depth (most efficient at 15 nm for the entire length); right: integral efficiency, over the entire device, of approximately 30 % (courtesy of [87]).***

Table 19: ***RZP-parameters at 2° as angle of incidence at the center of the device; higher expected efficiency, but improbable to obtain the desired very high energy resolution.***

entrance arm length [m]	exit arm length [m]	position on RZP [mm]	α [°]	β [°]	line density [l/mm]	depth of profile [nm]	expected efficiency [%]
2	5	**-25**	**2.025**	**1.420**	**199**	15	30.30
		-20	2.020	1.422	196	15	30.32
		-15	2.015	1.423	194	15	30.26
		-10	2.010	1.424	12	15	29.57
		-5	2.005	1.426	190	15	29.32
		0	**2**	**1.427**	**187**	15	29.16
		5	1.995	1.429	185	15	29.04
		10	1.990	1.430	183	15	28.94
		15	1.985	1.432	180	15	28.85
		20	1.980.	1.433	178	15	28.77
		25	**1.975**	**1.434**	**176**	15	28.70

As another idea, in order to keep the RZP in principle the same (line density of 571 l/mm in the center of the device) as for the first case at an incidence angle of 5°, the two parameters depth of profile and angle of incidence were varied. This result the following parameters (see Table 20):

Table 20: ***in order to obtain a reasonable combination of line-density and length of the device, the angle is set again to 5° (resulting most probably almost zero efficiency); the entrance and exit arms change as well)***

entrance arm length [m]	exit arm length [m]	position on RZP [mm]	α [°]	β [°]	line density [l/mm]	depth of profile [nm]
4.38	**2.62**	**-25**	**5.031**	**3.951**	**924**	10
		-20	5.025	3.957	913	10
		-15	5.019	3.964	902	10
		-10	5.013	3.970	891	10
		-5	5.006	3.977	881	10
		0	**5**	**3.984**	**870**	10
		5	4.994	3.990	859	10
		10	4.988	3.997	848	10
		15	4.981	4.004	837	10
		20	4.975	4.010	826	10
		25	**4.969**	**4.017**	**815**	10

Now, checking the line densities, at least in principle this device could result an appropriate energy resolution. Further development needs still to be done, in order to yield finally the realistic parameters for setting up a beamline at BESSY II and probably the European XFEL, capable to deliver the very high energy resolution in order to meet all the demands of the RIXS-user community in future. Unfortunately, in this case the distance from the source of X-rays is amplified; again the additional disadvantage comes into play that the intensity of light will be vanishing.

As a last possible option for coating, which comes to mind from looking at figure, would be Molybdenum. By keeping the grating parameters the same as in the first case, but applying Molybdenum as coating, resulted that the optimum depth of profile would be 25 nm. The simulation of the entire device finally showed some enhancement of the integral efficiency by a factor of 3.5. The result is shown in Figure 127, with the respective parameters as in Table 21:

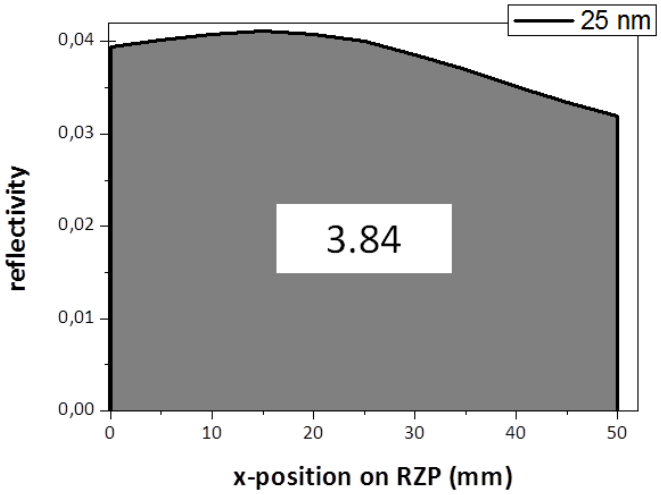

Figure 127: ***efficiency curve over the entire optical element of the RZP-spectrometer applying Mo as coating at a constant profile depth of 25 nm; this device obviously results at least a gain of integral intensity by the factor of 3.5 (integral efficiency ≈ 3.9%) (courtesy of [87]).***

Table 21: ***RZP-spectrometer parameters; minus first order of diffraction, energy of 776 eV, Mo coating is used for simulation (courtesy of [87]).***

entrance arm length [m]	exit arm length [m]	position on RZP [mm]	α [°]	β [°]	line density [l/mm]	depth of profile [nm]	expected efficiency [%]
2	5	**-25**	**5,063**	**4,338**	**649**	25	0.039
		-20	5,05	4,342	634	25	0.04
		-15	5,038	4,346	618	25	0.041
		-10	5,025	4,351	602	25	0.041
		-5	5,013	4,355	586	25	0.041
		0	**5**	**4,359**	**571**	25	0.04
		5	4,988	4,364	555	25	0.039
		10	4,975	4,368	540	25	0.037
		15	4,963	4,373	525	25	0.035
		20	4,951	4,377	510	25	0.033
		25	**4,938**	**4,381**	**494**	25	0.032

As described in the beginning, the energy resolution and beamline efficiency (in the sense of photon transmission) are mostly important for RIXS experiments. By using only just two elements, the transferred amount of energy is expected to be as high as possible. For an installation at the European XFEL, which is currently under construction in Hamburg, Germany, we assume an exceedingly high beam quality, as the source size and divergence will be by a few orders of magnitude smaller. From that we can expect at least the same possible resolutions and, what is even more significant, a lot more intensity. Most notably the beam will have the properties of a laser. A brilliant, coherent source such as the European XFEL will be conserved very well by using only a very small amount of optical elements in the beamlines. Of course, extensive tests of the auspicious properties have to be prepared and carried out now under real conditions.

Conclusion:

An innovative application of RZPs as singular optical elements was presented; considerations and simulations were done. For the first time, an all-RZP solution for cross-dispersive RIXS measurements was proposed. This system is capable of determining not only the energy loss but also the

momentum transfer within the sample. It was shown that the RZP-monochromator as well as the RZP-spectrometer were both capable of yielding an energy resolution in the range of $E/\Delta E \approx 30{,}000$. This means that here, it was possible to resolve the energy around 776 eV (Co 2p->3d resonance) with a precision of 26 meV. For the RZP monochromator side, an integral efficiency of around 14-15% could be expected after coating with Nickel. The advantage of using just this single optical element is to transmit a very high photon flux onto the sample. It is a small disadvantage that energies, away from the designed energy, broaden. This is due to the geometry of the RZP. This effect could possibly be compensated by an additional use of a focusing mirror prior to the RZP. For the RZP-spectrometer side, so far an integral efficiency of roughly 4% was calculated, applying a molybdenum coating to the optical element. This was proposed, because Silicon as well as Nickel have a reflectivity of almost 0% around the desired angles of incidence and exit. Further developments need to be done to increase the efficiency towards its maximum. This could probably be done by changing the geometry of the RZP. Here, the line density is a limiting factor; it strongly depends on the geometric parameters (angles and distances).

The use of an RZP and RZP arrays is a very good approach to obtain very high energy resolutions. On the other hand the same structure quickly leads to a larger broadening of the diffraction spots at greater ranges of energy. These two effects need to be balanced in order to optimize the RZP and compare them with conventional optics for specific cases of use. The SGM-beamline shows rather strong broadening in dispersive direction, but not so much in the perpendicular direction. The disadvantage of conventional optics is that they cannot focus the energies as well as an RZP-monochromator, which means that the illuminated spot in a sample would be larger (in the range of 5 µm (FWHM) compared to roughly 2 µm (FWHM) using an RZP). This spot serves as a new source for the RZP-spectrometer and would mean a worse energy resolution, as the source size in dispersive direction is a crucial parameter for RZP's energy resolution.

So far this is a case study. However, the idea was already accepted in the Scientific Advisory Committee at BESSY II and taken into consideration to be implemented at BESSY II, and probably at the European XFEL GmbH as well.

Parts of the project results are published in:

[Patent]: „DE 10 2012 013 530 B3" – *"Vorrichtung zur Messung resonanter inelastischer Röntgenstreuung einer Probe"*, application date: June 5th 2012, patent granted: August 29th 2013 – international application pending

[Rehanek_SRI]: J. Rehanek, F. Schäfers, H. Löchel, A. Firsov, J. Grünert, W. Freund, C. Ozkan, S. Molodtsov, A. Erko, *"A case study of novel X-ray Optics for FEL sources"*, Journal of Physics: Conference Series, Volume 425, 052013, pages 1-4 (2013)

[Rehanek_manu]: J. Rehanek, J. Schlappa, M. Scheer, F. Schäfers, C. Schüßler-Langeheine, A. Föhlisch, A. Erko, *„Conceptual design of a specialized beamline for cross-dispersive RIXS measurements"*, <in manuscript> (2014)

5. Conclusions – Outlook

Within the scope of a collaboration project with the European XFEL GmbH in Hamburg and with LBNL/LCLS in California, different kinds of spectrometers for X-ray Free-electron sources were conceptualized, designed and partially tested – especially for very high brilliance state-of-the-art facilities, namely X-ray Free Electron Lasers. In this work, two different fields of research have been covered: theoretical modeling and experimental testing of different optical schemes.

The overview of existing and future X-ray light sources – from synchrotron radiation (SR) to free electron lasers (FELs) – and their properties, led to the conclusion that conventional methods and optics used for SR have very limited use at the new FEL generation. New challenges and opportunities arise for the optical elements with these sources due to the extremely high intensities (peak brilliance in the order of 10^{34} photons/s/mrad^2/mm^2/0.1%bandwidth are expectable). It is very important to preserve as many photons as possible and to prohibit surface damage at the optical elements as good as possible. Additionally, energy resolutions ($E/\Delta E$) in the range of a few tens of thousands are inevitable (see below). Furthermore, the opportunity of ultra-fast measurements (as e.g. planned at the European XFEL repetition rates of 27 kHz; pulse durations in the order of 100 fs) gave rise to new requirements concerning the time resolution of these optical elements. New ideas need to be developed.

The theoretical analysis of existing X-ray optics in chapter 2 indicates a great potential of 2D and 3D variable line spacing (VLS) gratings (meaning focusing in a line and focusing in a single spot) for the soft energy range.

Commissioning – K-Monochromator Spectrometer (K-Mono):

The challenging commissioning of a SASE FEL, using a double-crystal or four-crystal monochromator, was described. Thus, two different methods of aligning the undulator segments of the entire FEL undulator were proposed. An experimental proof of principle of the two methods was shown. Simulating the K-Monochromator using the Si (111) channel-cut crystal an energy difference in the order of $\Delta E/E \approx 10^{-4}$ could be resolved, which agrees with the experimental K-parameter determination ($\Delta K/K$) in the range of 2.5×10^{-4} to 5×10^{-4}. This meets the demand which was initially made – it should be determinable in the order of 10^{-4}, as restriction from our partners from European XFEL. In other simulations using (333)- or (444)-reflex, $\Delta E/E$ could be resolved even in the range of 10^{-6}, which means that the K-parameter will be determinable at an even higher precision than required. These new methods will be applied at the commissioning of the European XFEL.

High-Resolution Single-Shot Spectrometer (HR-SSS):

Two diagnostic systems for measurements of the shot-to-shot spectral intensity distribution of SASE X-FELs were compared. For the first time a single-shot spectrometer on the basis of a Reflection Zone Plate was suggested and simulated. The comparison with a conventional answer to the problem showed that both systems are capable of resolving the XFEL spectrum sufficiently (10 meV at 10

keV). The first scheme consists of the combination of a focusing mirror and a crystal, which is used at a high index of lattice reflection plane to yield a high energy resolution. It is an offline-device. The second one – a spectrometer, consisting of only one single Reflection Zone Plate – melts focusing and dispersion into one step, thus, the number of optical elements is reduced. It is capable of both offline- and online-application. The high energy resolution is attainable with the presented schemes, as the huge distances and small source size (of 17µm x 17µm (fwhm)) at European XFEL help to focus individual energies; thus, achieving a very good separation.

High-transmission partial fluorescence yield XAS (Spectrometer):

For the first time, a new optical system has been conceptualized and realized for partial fluorescence yield XAS measurement at the L_3 absorption edge of Manganese in a highly dilute solution. So the main demand was high a throughput at simultaneous separation of the energy of the Mn-L-edge (above 638 eV) from the O-K-edge (around 525 eV). The problem was to get a signal out of a 10^{-3} molar concentrated solution. By focusing the energy of interest (Mn) with a dispersive RZP the signal could be separated from the energy of Oxygen. In addition, it was amplified sufficiently (to a small area) so that it could be measured at all, as above the noise-threshold. The RZP was used at a low energy resolution of $E/\Delta E = 100$, as consequently the line-density of the grating is comparatively low, resulting in a higher integral efficiency. The parameters of this spectrometer were designed and its properties regarding misalignments were simulated. It was tested at first at BESSY II and then used at the FEL facility LCLS in Stanford. The outcome of these first measurements posed the question if the overall efficiency of the device could be improved furthermore. The process of improving the overall efficiency of the spectrometer by simulation and experimental testing is described in detail. The influence of the depth of profile and the coating on the integral efficiency was simulated and tested at BESSY II, using different measurement opportunities (AFM, Reflectometer). Additionally, a pre-alignment technique of the optical element was developed. Structural modifications of different types of VLS-gratings are summarized. Finally, the improvement led to a significantly higher efficiency. For the first time, measurements of a highly dilute solution within the experimental enhancements of PS II measurements could be carried out. This will help to understand the function of PS II within the process of photosynthesis.

High-resolution energy- and momentum transfer measurement (RIXS):

A fundamental new optical system has been proposed and simulated for the first time. It comprises basically of two RZPs oriented perpendicular to each other. The first one acts as a monochromator. Its direction of dispersion is vertical, so that a certain energy distribution is delivered into a sample. The second one serves as a spectrometer, it catches the emitted light from the sample. Its direction of dispersion is horizontal. The purpose of this setup is to have a 2-dimensional scheme on a detector for the incident/absorbed and fluorescent energy for RIXS experiments at Synchrotron Radiation and Free Electron Laser sources as well. Additionally, the spectrometer arm will be swivel-mounted. With this setup, not only the energy change, but also the momentum transfer can be studied experimentally at very high resolutions. Such an apparatus will be able to provide the users with an energy resolution of $E/\Delta E \approx 30{,}000$ (26 meV at 776 eV). Additionally, by the reduction of the number

of optical elements – compared to other state-of-the-art conventional methods – the throughput is expected to be higher.

In summary, within this work, the potential and the limitations of applications of Reflection Zone Plates were explored. It is a very powerful approach to reduce the number of optical elements by melting the intrinsic properties of focusing and dispersion into one step. Used as a single element spectrometer for measurements of very low signals (as applied in the XAS project at LCLS), such an optical element can provide a sufficient spectrum out of an initially very low (fluorescence) signal. This is done by separating the energy of interest very well from other present energies and simultaneous by focusing and therewith intensification. Regarding very high energy resolutions (as presented in the European XFEL project HR-SSS) these elements are very promising. Nevertheless, due to the geometry and a-chromaticity of an RZP, energies away from the design energy will be broadened (as shown in case of the RZP-monochromator) significantly, if very high energy resolutions are demanded. In case of the RIXS RZP-spectrometer there are still a few developments necessary, which will be depleted in near future.

6. Publications, Patent

First author:

[Rehanek_SPIE]: J. Rehanek, F. Schäfers, A. Erko, M. Scheer, W. Freund, J. Grünert, C. Ozkan, S. Molodtsov, *"Simulations of diagnostic spectrometers for the European XFEL using the ray-trace tool RAY"*, Proceedings of the SPIE, Vol. 8141, 814109, pages 1-15 (2011)

[Rehanek_pDR]: J. Rehanek, F. Schäfers, A. Erko, "preliminary design report: Design considerations and simulation on the K-Monochromator", technical reports XFEL (2012)

[Rehanek_SRI]: J. Rehanek, F. Schäfers, H. Löchel, A. Firsov, J. Grünert, W. Freund, C. Ozkan, S. Molodtsov, A. Erko, „A case study of novel X-ray Optics for FEL sources", Journal of Physics: Conference Series, Volume 425, 052013, pages 1-4 (2013)

[Rehanek_manu]: J. Rehanek, J. Schlappa, M. Scheer, F. Schäfers, C. Schüßler-Langeheine, A. Föhlisch, A. Erko, *„Conceptual design of a specialized beamline for cross-dispersive RIXS measurements"*, <in manuscript>

Co-author:

[Ozkan_SPIE]: C. Ozkan, W. Freund, J. Rehanek, J. Buck, I. Zizak, J. Grünert, F. Schäfers, A. Erko, S. Molodtsov, *"Initial evaluation of the European XFEL undulator commissioning spectrometer with a single channel-cut crystal"*, Proceedings of the SPIE, Volume 85040, pages 1-7 (2012)

[77]: H. Löchel, M. Brzhezinskaya, A.Firsov, J. Rehanek, A. Erko, *"Reflection zone plates for 2D focusing and spectroscopy of hard X-rays"*, Journal of Physics: Conference Series, Volume 425, 052025, pages 1-4 (2013)

[29]: A. Firsov, A. Erko, F. Senf, J. Rehanek, M. Brzhezinskaya, R. Mitzner, Ph. Wernet, A. Föhlisch, *"Novel wavelength-dispersive X-ray fluorescence spectrometer"*, Journal of Physics: Conference Series, Volume 425, 152013, pages 1-5 (2013)

[86]: R. Mitzner, et al., *"L-edge X-ray absorption spectroscopy of dilute systems relevant to metalloproteins using an X-ray free-electron laser"*, The Journal of Physical Chemistry Letters, Volume *4*(21), pages 3641-3647. (2013) doi: 10.1021/jz401837f

[Kern]: J. Kern, J. Hattne, R. Tran, R. Alonso-Mori, H. Laksmono, S. Gul, R. Sierra, J. Rehanek, A. Erko, R. Mitzner, P. Wernet, U. Bergmann, N.K. Sauter, V. Yachandra, J. Yano, *"Methods development for diffraction and spectroscopy studies of metalloenzymes at XFELs"*, Philosophical Transactions of The Royal Society B, Vol. 369 no.1647 20130590 (2014)

[Braig]: C. Braig, H. Löchel, R. Mitzner, W. Quevedo, P. Loukas, M. Kubin, C. Weniger, A. Firsov, J. Rehanek, M. Brzhenzinskaya, P. Wernet, A. Föhlisch, A. Erko, *"Design and optimization of a parallel spectrometer for ultra-fast X-ray science"*, Optics Express, Vol. 22, Issue 10 pp. 12583-12602 (2014)

Talks:

(DPG Frühjahrstagung des AMOP, *"Interferometrische Untersuchung zur Systementwicklung"*, Düsseldorf, Germany, March 2007)

IONS Germany, *"Simulations for Euro-XFEL"*, Erlangen, Germany, May 20th – 22nd 2011

Kick-off meeting HZB-European XFEL, *"Raytracing for XFEL – K-Mono"*, Berlin, Germany, June 24th 2011

Kick-off meeting HZB-European XFEL, *"raytracing for XFEL – single shot spectrometer"*, Berlin, Germany, June 24th 2011

SPIE 2011 Optics and Photonics, Conference 8141: Advances in Computational Methods for X-Ray Optics II, *"Simulation of diagnostic spectrometers for the European XFEL using the raytrace tool RAY"*, (invited), San Diego, California, USA, August 2011

IONS-11, Rehanek, J; Schaefers, F; Erko, A; Scheer, M; Gruenert, J; Freund, W; Ozkan, C; Molodtsov, S: *"Simulations of X-ray Optics for the photon diagnostics at the European XFEL"*, International OSA Network of Students Paris, France, February 22nd - 25th 2012

Swedish-German Workshop on X-ray Optics, *"Raytracing x-ray optical devices for photon diagnostics at XFEL"*, Ahusstrand, Sweden, March 13th – 15th 2012

European XFEL Users' meeting 2012: Satellite Workshop on Photon Beam Diagnostics, *"Conceptual raytracing for the X-FEL diagnostics monochromators-spectrometers"*, Hamburg, Germany, January 26th 2012

European XFEL Users' meeting 2013: Satellite Workshop on Photon Beam Diagnostics, *"K-monochromator for photon diagnostics: simulation and first test results"*, Hamburg, Germany, January 24th 2013

INT-Seminar, Rehanek, J; Mitzner, R; Erko, A: *"Raytracing/first results of a RZP-spectrometer for a fluorescence experiment at LCLS"*, February 13th 2013

International conference on dynamic pathways in multidimensional landscapes, *"Reflection zone plates for RIXS and partial fluorescence yield XAS"*, Berlin, Germany, September 19th 2013

Posters:

Rehanek, J; Schaefers, F; Scheer, M; Gruenert, J; Freund, W; Ozkan, C; Molodtsov, S; Erko, A: *"Simulation of X-Ray Optics for Photon Diagnostics at the European XFEL"*, HZB Users' meeting 2011, December 1st 2011

Rehanek, J; Schaefers, F; Erko, A; Scheer, M; Gruenert, J; Freund, W; Ozkan, C; Molodtsov, S: *"Simulations of X-ray Optics for the photon diagnostics at the European XFEL"*, New Science Opportunities at FLASH, workshop at DESY, Hamburg, Germany, October 12th – 14th 2011

Freund, W; Ozkan, C; Buck, J; Gruenert, J; Rehanek, J; Schäfers, F; Erko, A: *"Initial Evaluation of the European XFEL Undulator Commissioning Spectrometer with a Single Channel-Cut Crystal"* 11th International Conference on Synchrotron Radiation Instrumentation SRI-12 Lyon, France, 09.07.2012 - 13.07.2012 (2012)

Rehanek, J; Schäfers, F; Firsov, A; Grünert, J; Freund, W; Ozkan, C; Molodtsov, S; Erko, A: "*A case study of novel X-ray Optics for European XFEL"*, 11th International Conference on Synchrotron Radiation Instrumentation SRI-12 Lyon, France, 09.07.2012 - 13.07.2012 (2012)

Rehanek, J; Schäfers, F; Firsov, A; Grünert, J; Freund, W; Ozkan, C; Molodtsov, S; Erko, A: *"A case study of novel X-ray Optics for RIXS experiments at the European XFEL"*, DESY/XFEL Users' meeting Hamburg, Germany, 25.01.2012 - 27.01.2012 (2012)

Löchel, H; Firsov, A; Brzhezinskaya, M; Rehanek, J; Erko, A: *"Reflection zone plates for 2D-focusing and spectroscopy of hard X-rays"* 11th International Conference on Synchrotron Radiation Instrumentation- SRI 2012 Lyon, France, 09.07.2012 - 13.07.2012 (2012)

Loechel, H; Brzhezinskaya, M; Firsov, A; Rehanek, J; Erko, A: *"Reflection Zone Plates for hard X-Ray spectroscopy"*, HZB User Meeting Berlin, Germany, 12.12.2012 - 14.12.2012 (2012)

Rehanek, J; Löchel, H: *"Reflection zone plates for X-ray monochromators and spectroscopy"* Workshop PNI in-house research NANO & MICRO Science and Technology, HZB, Berlin, Germany, 22.03.2012 - 23.03.2012 (2012)

Rehanek, J; Löchel, H; Schäfers, F; Brzhezinskaya, M; Zizak, I; Firsov, A; Erko, A: *"Reflection Zone Plates for X-Ray Monochromators and Spectroscopy"*, X-Ray Free Electron Laser school Annecy, France, 04.06.2012 - 08.06.2012 (2012)

Rehanek, J; Schäfers, F; Firsov, A; Föhlisch, A; Grünert, J; Molodtsov, S; Erko, A: *"A case study of novel Optics applied as a spectrometer for X-ray Free Electron Laser sources"*, IONS-NA 4 – International OSA Network of Students-North America, New York, USA , 10.10.2012 - 12.10.2012 (2012)

Rehanek, J; Mitzner, R; Yano, J; Kern, J; Weniger, C; Firsov, A; Senf, F; Quevedo, W; Alonso-Mori, R; Schröder, H; Schlotter, W; Wernet, P; Föhlisch, A; Bergmann, U; Brzhezinskaya, M; Yachandra, V; Erko, A: "Design of a Reflection Zone Plate Spectrometer with Ray Tracing and First Results for Fluorescence Experiments at LCLS", European XFEL Users' Meeting, Hamburg, Germany, January 23rd – 25th 2013

Patent:

[Patent]: „DE 10 2012 013 530 B3" – „Vorrichtung zur Messung resonanter inelastischer Röntgenstreuung einer Probe"; application date: June 5th 2012, patent **granted: August 29th 2013** – <international application pending>

7. Acknowledgements

First of all, I wish to express my immense gratitude to my PhD supervisor, Prof. Dr. Alexei Erko for providing me the opportunity to do my PhD work in his research group. I thank you very much for believing in me, even if I did not work (before 2011) in the field of synchrotron sources, Free-Electron Lasers or X-ray optics in general, trusting my ability to adapt to this very interesting new field. I appreciate that you included me in your research and development in this cutting-edge technology. Thank you for inspiring me, to awaken my interest for X-ray technology.

Прежде всего, хотел бы выразить свою искреннюю признательность моему научному руководителю, профессору доктору физ-мат наук Алексею Ерко, за уникальную возможность стать частью его исследовательской группы. Моя огромная благодарность за Ваше доверие – прежде у меня не было опыта работы с источниками синхротронного излучения, лазерами на свободных электронах и в целом рентгенооптики , и веру в мою способность проявить себя в этой интереснейшей новой сфере научного знания. Я высоко ценю тот факт, что мне удалось принять участие в руководимом Вами процессе научно-технологических исследований, и особенно – Вашу поддержку, и пробуждение во мне интереса к технологиям рентгеновских лучей.

I thank Prof. Dr. Holger Dau for his willingness to co-assess this thesis and supporting my intentions to finish my PhD and taking over the supervision. Thank you for the inspiration in the field of photosynthesis, especially Photosystem II, which is especially nowadays of very high interest and real important cutting-edge research.

I owe my deepest gratitude to my Mentor Dr. Franz Schäfers. He was and is a mentor for me in this academia (e.g. telling me something like: “I very much like to correct your writings – one can eliminate half of the words, without cutting out the meaning at all…” or your citation: “good day ladies and gentlemen, good morning dear students”…; I remember your sentence, describing yourself: “Wir Westfalen sagen immer die Wahrheit – und das auch immer zum falschen Zeitpunkt”) and was supporting me all the time as well by providing advices on how to deal with other people’s lack of ego and sensitiveness and the resulting behaviour. I thank you very much for introducing me very patiently to the field of X-ray optics, make use of your ray tracing code RAY and design of optical setups for application at synchrotrons and FELs. Thank you for introducing me to the “veterans” of Synchrotron optics, which made it very convenient for me to get into conversation and thus as well access to all the necessary and important knowledge as fast as possible, kind of “while passing by”.

I thank my colleague Heike Löchel very much! I thank you for all the good conversations and support during my years at HZB. I very much appreciate your help during all my writings, by constantly improving them, and problems which I faced, not only during work but also in my private life. I really enjoy sharing the office with you, having fruitful conversations about challenges in physics, life, politics, philosophy…actually everything! Thank you for being a friend. ☺

Thank you very much, Dr. Bernd Löchel, for constantly helping me to improve my thesis, for all the good conversations and useful hints, for supporting me with good advices (not only “keep your ears stiff”…).

I would like to express my high appreciation to Panagiotis Loukas. It was a pleasure to work with you, thank you very much for supporting me so extensively with the ray tracings, since you started working here, everything went way faster! Ευχαριστώ πολύ! ☺

I thank Dr. Michael Krumrey (PTB) for introducing me to the comprehensive field of crystal optics.

I thank Dr. Ivo Zizak for helping me to understand crystal optics and supporting me during beamtimes in Berlin and Hamburg with our colleagues from European XFEL. Thank you for introducing me to experiments at the µ-spot beamline, KMC-2, BAM and different experiments including crystals and SAXS with our colleagues Prof. Dr. Laifa Boufendi and Ibrahim Chiboub from Orleans.

Dr. Andreas Gaupp, Dr. Johannes Bahrdt and Dr. Michael Scheer I would like to thank for having introduced me to the huge field of undulator physics.

I would like to thank Dr. Friedmar Senf for making me familiar not only with experiments at the Reflectometer, but also for his immense support in beamline-design (once, he gave me a one-day crash course in designing an entire SGM beamline in a single day…) and also for being receptive for my thoughts and opinions regarding the challenges in working in the world of science.

I thank Dr. Rolf Mitzner for including me in the exciting project of investigation of photosynthesis. It was a very helpful and instructive work, we spent together. I learned a lot about the "real challenges" during design, setup and actual experiment at top-level research facilities. And I thank you for the good times after successful days in Stanford spending the evenings with our colleagues having a properly chilled Longboard Lager beer.

Dr. Wilson Quevedo, amigo! Gracias para todo lo que has hecho para mi. Todos los conversaciónes, la inspiración y el tiempo divertido. Splendid times we spent in the US…"Obama Schnitzel!" – and we will spend more! ☺

I thank Christian Weniger for your great support and help introducing me to vacuum technology, the good and funny conversations and great work together at LCLS and Feierabendbierchen…

I would like to express my gratitude to Ivo Rudolph for all the inspiring and fruitful conversations, from him I learned about feasibility and ideas on technological challenges of different kinds. Thank you for encouraging me and supporting me with the help of Adrian Polok to examine different ideas of coatings, which resulted in a big step forward within my understanding of different parameters and influences on optical elements – and of course for sharing good music and funny stuff… Mahlzeit!

I would like to thank Petra Eisert, most of my time at INT the heart and driving force behind all the administrative stuff, for supporting me very much during writing of a project report and paper drafts, I missed her and her help very much during the entire development process of this thesis…several times I broke together, as everything was under all pig… ☺

I would like to thank Dr. Peter Baumgärtel for all his support with the raytracing software as well and all the fruitful discussions he involved me regarding challenges and ideas on his implementations into the user-friendly handling of ray tracing, which finally led to the great development of the user interface compiled by him and the group of Prof. Dr. Hartmut Schirmacher from the Beuth-Hochschule Berlin.

I want to thank Johannes Wolf and Christoph Waberski for their big support with the AFM-measurements, and of course for the cookies and chocolate in their office…was great so far…yes, I know, I need to bring some myself…and I thank Oliver Kutz very much for fabricating the very useful boxes to transport the precious RZP-substrates properly. Thank you, Dr. Stephanie Lemke for the nice conversation and encouragement during stressful times (I still like the postcard "Wir essen jetzt Opa – Satzzeichen retten Leben")! Tino Seliger: Konichiwa! And thank you, Harald Köhrich for good neighbourhood in the office the last years. Thank you, Dr. Andrey Sokolov for introducing me to the use of the Reflectometer and for showing me, how to interpret the experimental data!

I thank my friend and colleague Dr. Çiğdem Özkan (now PSI, former European XFEL) for the great beamtimes and support during all the time, personally as well as work related. Ci vediamo prestissimo qua a Berlino…o altrove su questo mundo bellissimo, certo!

I am very grateful for the good conversations, fruitful discussions related to all areas of life and introduction to the technological part of fabrication of optical elements with my fellow PhD-students Jürgen Probst and Max Schöngen. Thank you for the crash course in fabrication of RZPs, Jürgen. Additionally, I thank for all the funny and nice discussions during lunchtime with Christoph Hülsen see you next time at Ostkreuz…

I thank Carsten Kuhn for all the funny and interesting conversations at the very close coffee kitchen and at "Feierabendbierchen".

I thank my colleagues from European XFEL, Dr. Jens Buck (really enjoyed the "important support" of on-the-fly evaluation at beamtimes! ☺), Wolfgang Freund and Dr. Jan Grünert, for supporting me within the collaboration project we did and are doing currently.

I thank Dr. Maria Brzhezinskaya and Dr. Alexander Firsov for the fabrication of the RZP-structures for the LCLS-project.

I thank Maha Dürr and Jennifer Bierbaum for encouraging me with funny conversations and stuff – Lieblingsjennifer: war jannz jroß, "unsere Orga" der Langen Nacht der Wissenschaft! Thank to all my colleagues from the Institute of Nanometre-Optics and Technology for building such a great atmosphere during my time here at HZB.

I cannot express my deep gratitude which I feel for my friends and family, who supported me all the time mentally, sympathetic and with their encouragement when I wanted to quit everything. Thank you very much for loving me, I love you!

And I really want to thank Marianna Levtov, the Love of my Life. Thank you for stepping into my life, still love the train, which brought us together, two travelers. There are so many things I want to let you know! Words are simply not enough! אותך אוהב אני

8. References

[1]: E.O. Lawrence, M.S. Livingston, "*The production of high speed light ions without the use of high voltages*", Physical Review, volume 40, pages 19-35 (1932)

[2]: M.O. Oliphant, *"The acceleration of particles to very high energies"*, Classified memo submitted to DSIR, United Kingdom, in September 1943, now in University of Birmingham Archive

[3]: J. Schwinger, *"Electron Radiation in High Energy Accelerators"*, Physical Review, Volume 70, pages 798-799 (1946)

[4]: J. Schwinger, *"On the Classical Radiation of Accelerated Electrons"*, Physical Review, Volume 75, pages 1912-1925 (1949)

[5]: V. I. Veksler, "A new method of accelerating relativistic particles", Comptes Rendus (Dokaldy) de l'Academie Sciences de l'URSS, Volume 43, 8, pages 329-331 (1944)

[6]: E. M. McMillan, *"The synchrotron – a proposed high energy accelerator"*, Physical Review, Volume 68, 143 (1945).

[7]: F. K. Goward and D. E. Barnes, Nature, Volume 158, page 413 ff. (1946)

[8]: F.R. Elder, A.M. Gurewitsch, R.V. Langmuir, H.C. Pollock, H. C., *"Radiation from Electrons in a Synchrotron"*, *Physical Review*, volume 71, Issue 11, pages 829-830 (1947)

[9]: SPEAR History at http://www-ssrl.slac.stanford.edu/content/spear3/spear-history (as at January 12, 2014)

[10]: John Madey, *"Stimulated Emission of Bremsstrahlung in a Periodic Magnetic Field"*, Journal of Applied Physics, Volume 42, pages 1906-1913 (1971)

[11]: J.R. Schneider, "FLASH – from accelerator test facility to the first single-pass soft X-ray free-electron laser", Journal of Physics B – Atomic, Molecular and Optical Physics, Volume 43, 194001 (9pp) (2010)

[12]: W. Ackermann et al., "Operation of a free-electron laser from the extreme ultraviolet to the water window" Nature Photonics 1, pages 336 - 342 (2007)

[13]: S. Schreiber, *"First Lasing in the Water Window with 4.1nm at FLASH",* proceedings of FEL'11, Shanghai, 2011

[14]: T. Åberg *et al.*, *"A VUV Free Electron Laser at the TESLA Test Facility at DESY"*, Conceptual Design Report TESLA FEL Report 1995-03, DESY (1995)

[15]: J. Feldhaus, "FLASH – the first soft X-ray free electron laser (FEL) user facility", Journal of Physics B – Atomic, Molecular and Optical Physics, Volume 43, 194002 (8pp) (2010)

[16]: H.H. Braun, *"The future of X-ray FELs"*, Proceedings of IPAC2012, New Orleans, Louisiana, USA, pages 4180-4184 (2012)

[17]: P.Emma et al., *"First Lasing and Operation of an Ångstrom-Wavelength Free-Electron Laser"*, Nature Photonics 4, 641 - 647 (2010)

[18]: J.Stöhr, *"The Scientific Revolution Enabled by X-ray Free Electron Lasers"*, Proceedings of IPAC2012, New Orleans, Louisiana, USA (2012)

[19]: H.Tanaka, *"The SPring-8 Angstrom Compact Free Electron Laser (SACLA)"*, Proceedings of IPAC2012, New Orleans, Louisiana, USA (2012)

[20]: O. Fuchs et al., Review of Scientific Instruments, Volume 80, 063103 (2009)

[21]: V.V. Aristov, S.V. Gaponov, V.M. Genkin, Yu.A. Gorbatov, A.I. Erko, V.V. Martynov, L.A. Matveeva, N.N. Salashenko, A.A. Fraerman, *"Focusing Properties of Shaped Multilayer Mirrors"*, JETP Letters, Volume 44, 265 (1986)

[22]: A.I. Erko, *"Synthesized Multilayer Fresnel X-ray Optics"*, Review of Scientific Instruments, Volume 60, pages 2502-2505 (1989)

[23]: T. Wilhein, D. Hambach, B. Niemann, M. Berglund, L. Rymell, H.M. Hertz, Applied Physical Letters, Volume 71, 190 (1997)

[24]: German Patent DE 195 42 679 A1, 16.11. (1995)

[25]: A. Erko, A. Firsov, K. Holldack, AIP Conference Proceedings, Volume 1234, pages 177-180 (2010)

[26]: C. Stamm, N. Pontius, T. Kachel, M. Wietstruck, H.A. Dürr, *"Femtosecond x-ray absorption spectroscopy of spin and orbital angular momentum in photo-excited Ni films during ultrafast demagnetization"*, Physical Review, B81, 104425 (2010)

[27]: I. Radu, K. Vahaplar, C. Stamm, T. Kachel, N. Pontius, H. A. Dürr, T. A. Ostler J. Barker, R. F. L. Evans, R. W. Chantrell, A. Tsukamoto, A. Itoh, A. Kirilyuk, Th. Rasing, A. V. Kimel, *"Transient ferromagnetic-like state mediating ultrafast reversal of antiferromagnetically coupled spins"*, Nature, Volume 472, pages 205–208 (2011)

[28]: A. Erko, A. Firsov, F. Senf, "*Novel Parallel VUV/X-Ray Fluorescence Spectrometer",* Spectrochimica Acta part b-Atomic Spectroscopy, Volume 67 , pages 57-63 (2013)

[29]: A. Firsov, A. Erko, F. Senf, J. Rehanek, M. Brzhezinskaya, R. Mitzner, Ph. Wernet, A. Föhlisch, *"Novel wavelength-dispersive X-ray fluorescence spectrometer"*, Journal of Physics: Conference Series, Volume 425, 152013, pages 1-5 (2013)

[30]: F. Schaefers, "*The BESSY Raytrace Program RAY"*, Modern Developments in X-Ray and Neutron Optics, Springer Series in Optical Sciences, Volume 137, pages 9-41, 2008

[31]: J.C. Maxwell, *"A dynamical theory of the electromagnetic field"*, Philosophical Transactions of the Royal Society London, 155:459 (1865)

[32]: A.G. Michette, C.J Buckley, editors, *"X-Ray Science and Technology"*, Institute of Physics Publishing, Bristol and Philadelphia, ISBN 0-7503-0233-X (1993)

[33]: H. Wiedemann, *"Synchrotron Radiation"*, Springer-Verlag, Berlin Heidelberg New York, ISBN 3-540-43392-9 (2003)

[34]: H. Onuki and P. Elleaume, editors, *"Undulators, Wigglers and their Applications"*, Taylor and Francis, London, ISBN 0–415–28040–0 (2003)

[35]: J. A. Clarke, *"The Science and Technology of Undulators and Wigglers"*, Oxford University Press, New York, ISBN 0-19-850855-7 (2004)

[36]: R. Walker, *"Insertion devices: undulators and wigglers"*, Proceedings of CERN Accelerator School, Synchrotron Radiation and Free Electron Lasers, Grenoble, France, CERN 98-04, editor S. Turner (1996)

[37]: P. Elleaume, *"Insertion devices"*, Proceedings of CERN Accelerator School, Synchrotron Radiation and Free Electron Lasers, Brunnen, Switzerland, CERN-2005-012, editor D. Brandt (2003)

[38]: J. Bahrdt, *"Insertion Devices"*, Proceedings of CERN Accelerator School, Intermediate Accelerator Physics, DESY Zeuthen, Germany, CERN-2006-002, editor D. Brandt (2003)

[39]: J. Bahrdt, *"Permanent magnets including undulators and wigglers"*, Proceedings of CERN Accelerator School, Magnets, Bruges, Belgium, CERN-2010-004, editor D. Brandt (2009)

[40]: J. Bahrdt, Y. Ivanyushenkov, *"Short Period Undulators for Storage Rings and Free Electron Lasers"*, Journal of Physics: Conference Series 425 (2013) 032001

[41]: http://home.web.cern.ch/about/engineering/radiofrequency-cavities

[42]: www.physik.uni-wuerzburg.de

[43]: P. Schmüser, M. Dohlus, J. Rossbach: "*Ultraviolet and Soft X-Ray Free-Electron-Lasers: Introduction to Physical Principles, Experimental Results, Technological Challenges"*, STMP 229 (Springer Berlin Heidelberg 2008), DOI 10.1007/978-3-540-79572-8

[44]: X-ray Data Booklet, edited by A.C. Thompson (2009)

[45]: D.T. Attwood *"Soft x-rays and extreme ultraviolet radiation: principles and applications"*, Cambridge University Press (2000)

[46]: www.psi.ch

[47]: http://photon-science.desy.de

[48]: http://sbfel3.ucsb.edu/www/ as on 16th of October 2013

[49]: http://www.nature.com/nphoton/journal/v4/n12/full/nphoton.2010.239.html

[50]: http://www.weltderphysik.de/gebiete/atome/synchrotronstrahlung/freie-elektronen-laser/

[51]: M. Martins et al., *"Single shot spectral characterization of a SASE free electron laser"*, application note, LOT-Oriel Group Europe. www.lot-oriel.com/ccd

[52]: R. Follath, *"The second generation of soft x-ray free-electron lasers"*, SPIE Newsroom, doi: 10.1117/2.1200708.0840

[53]: M. Born, E. Wolf et al., *"Principles of Optics: Electromagnetic Theory of Propagation, Interference and Diffraction of Light"*, Cambridge University Press, ISBN 0-521-64222-1 (2002)

[54]: T. Matsushita, H. Hashizume, *"X-ray monochromators"* in Handbook on Synchrotron Radiation volume 1, edited by E.E. Koch, North-Holland Publishing Co., Amsterdam pp.261 (1983)

[55]: J.M. Cowley, *"Diffraction Physics"*, Elsevier Science B.V., ISBN 0-444-82218-6 (1995)

[56]: W.B. Peatman, *"Gratings, Mirrors and Slits: beamline design for soft X-ray synchrotron radiation sources"*, Overseas Publishers Association Amsterdam B.V., ISBN 90-5699-028-4 (1997)

[57]: http://physics.nist.gov/cgi-bin/Xcom/

[58]: www.x-ray-optics.de

[59]: www.wikipedia.org

[60]: C.G. Darwin, *"The Theory of X-ray Reflection"*, Philosophical Magazine, Volume 27, pages 315-333 (1914)

[61]: C.G. Darwin, *"The Theory of X-ray Reflection: Part II"*, Philosophical Magazine, Volume 27, pages 675-690 (1914)

[62]: J.W.M. DuMond, *"Theory of the Use of More Than Two Successive X-Ray Crystal Reflections to Obtain Increased Resolving Power"*, Physical Review, Volume 52, pages 872-883 (1937)

[63]: lp.uni-goettingen.de

[64]: W.R. McKinney, *"Design of Grazing Incidence Monochromators Involving Unconventional Gratings"*, Proceedings of the SPIE 1055 (1989)

[65]: T. Harada, T. Kita, *"Mechanically Ruled Aberration-Corrected Concave Gratings"*, Applied optics, Volume 19, 3987 (1980)

[66]: F.M. Gerasimov, E.A. Yaskovlev, I.V. Peisakhson, B.V. Koshelev, *"Concave Diffraction Gratings with Variable Spacing"*, Opt. Spektrosk. Volume 28, 423 (1970)

[67]: M.C. Hettrick, *"Varied line space gratings: past present and future"*, SPIE Proceedings, Volume 560, 96 (1985)

[68]: H. Noda, T. Namioka, M. Seya, *"Geometric Theory of the Grating"*, Journal of the Optical Society of America, Volume 64, 1031 (1974)

[69]: A. Erko, A. Firsov, "Investigation of the properties of Bragg-Fresnel gratings", Proceedings of the SPIE, Volume 5539, pp 148-159 (2004)

[70]: M. Scheer, *"WAVE – A Computer Code for the Tracking of Electrons through Magnetic Fields and the Calculation of Spontaneous Synchrotron Radiation"*, Proceedings of ICAP, Warnemünde, Germany, TUACC2 (2012)

[71]: G. Geloni, J. Grünert, *"Announcement of Simulation Code Benchmark"*, available online on http://www.xfel.eu/project/organization/work_packages/wp_74/documents (2010)

[72]: Freund W., *"Conceptual Design Description - K-Mono"*, EDMS-No. EDMS Nr.: D00000001940181, (2011).

[73]: R. Dejus, I. Vasserman, S. Sasaki, and E. Moog, "Undulator A magnetic properties and spectral performance", Tech. Rep. ANL/APS/TB-45, Argonne National Laboratory, May, 2009.

[74]: C. Ozkan, W. Freund, J. Rehanek, J. Buck, I. Zizak, J. Grünert, F. Schäfers, A. Erko, S. Molodtsov, *"Initial evaluation of the European XFEL undulator commissioning spectrometer with a single channel-cut crystal"*, Proceedings of the SPIE, Volume 85040, pages 1-7 (2012)

[75]: M. Yabashi et al., "*Single-Shot Spectrometry for X-Ray Free-Electron Lasers"*, Phys.Rev.Lett. 97, 084802, 2006

[76]: Frank Siewert, personal communication 2011

[77]: H. Löchel, M. Brzhezinskaya, A.Firsov, J. Rehanek, A. Erko, *"Reflection zone plates for 2D focusing and spectroscopy of hard X-rays"*, Journal of Physics: Conference Series, Volume 425, 052025, pages 1-4 (2013)

[78]: J. Rehanek, F. Schaefers, H. Loechel, A. Firsov, J. Gruenert, W. Freund, C. Ozkan, S. Molodtsov, A. Erko, *„A case study of novel X-Ray Optics for FEL sources"*, Journal of Physics: Conference Series 425 (2013) 052013

[79]: D. Zhu, M. Cammarata, JM. Feldkamp, DM. Fritz, JB. Hastings, S. Lee, HT Lemke, A. Robert, JL. Turner, Y. Feng, *"A single-shot transmissive spectrometer for hard x-ray free electron lasers"*, Applied Physics Letters, Volume 101, 034103 (2012)

[80]: http://www.lbl.gov/vkyachan/research.html (as on 26th of December 2013)

[81]: P. Joliot, A. Joliot, *"A polarograhic method for detection of Oxygen production and reduction of Hill reagent by isolated chloroplasts"*, Biochimica et Biophysica Acta, Volume 153, pages 625-634 (1968)

[82]: P. Joliot, G. Barbieri, R. Chabaud, *"Un nouveau modele des centres photochimiques du systeme II"*, Photochemistry and Photobiology, Pergamon Press, Volume 10, pages 309-329 (1969)

[83]: B. Kok, B. Forbush, M. McGloin, "*Cooperation of charges in photosynthetic O2 evolution-I. A linear four step mechanism"*, Photochemistry and Photobiology, Pergamon Press, Volume 11, pages 457-475 (1970)

[84]: S. Brück, S. Treiber et al., *"The temperature-dependent magnetization profile across an epitaxial bilayer of ferromagnetic $La_{2/3}Ca_{1/3}MnO_3$ and superconducting $YBa_2Cu_3O_{7-\delta}$"*, ARXIV.org, Cornell University Library, (2010)

[85]: Alexander Avramenko developed in 2012 the code LOOPER, an extension of RAY/REFLEC for creation of huge data files from ray-tracing simulation varying several parameters

[86]: R. Mitzner, et al., *"L-edge X-ray absorption spectroscopy of dilute systems relevant to metalloproteins using an X-ray free-electron laser"*, The Journal of Physical Chemistry Letters, Volume *4*(21), pages 3641-3647. (2013) doi: 10.1021/jz401837f.

[87]: Panagiotis Loukas, personal communication 2013

[88]: Heike Löchel, personal communication 2013

[89]: Friedmar Senf, personal communication 2013

[90]: M. Moretti Sala, et al., *"Energy and symmetry of dd excitations in undoped layered cuprates measured by Cu L-3 resonant inelastic x-ray scattering"*, New Journal of Physics, Volume 13, 043026 (2011).

[91]: J. Schlappa, et al., *„Spin-orbital separation in the quasi-one-dimensional Mitt insulator Sr_2CuO_3"*, Nature 485, 82 (2012)

[92]: A. Kotani, S. Shin, *"Resonant inelastic x-ray scattering spectra for electrons in solids"*, Reviews of modern physics, Volume 73, pages 203-246 (2001)

[93]: L. J. P. Ament, M. van Veenendaal, T. P. Devereaux, J. P. Hill, and J. van den Brink, *"Resonant inelastic x-ray scattering studies of elementary excitations"*, Review of Modern Physics, Volume 83, 705 (2011).

[94]: A. Pietzsch, et al., *"Spatial Quantum Beats in Vibrational Resonant Inelastic Soft X-Ray Scattering at Dissociating States in Oxygen"*, Physical Review Letters, Volume 106, 153004 (2011)

[95]: *"Heisenberg RIXS, The European User Consortium for Momentum-time resolved resonant inelastic x-ray scattering at XFEL.EU"* A. Föhlisch, A. Erko, G. Ghiringhelli, L. Braicovic, et al.

[96]: V.N. Strocov, "*Concept of a spectrometer for resonant inelastic X-ray scattering with parallel detection in incoming and outgoing photon energies"*, Journal of Synchrotron Radiation 17, pages 103-106 (2010)

[97]: Christian Schüßler-Langeheine, personal communication 2013

[98]: Michael Scheer, personal communication 2012

[99]: F. Senf et al., *"Performance of the first undulator beamline U49-1-SGM at BESSY II"*, Nuclear Instruments and Methods in Physics Research A 467-468, pages 474-478 (2001)

[100]: A. Erko, A. Firsov, K. Holldack, *"New Developments in Femtosecond Soft X-ray Spectroscopy"*, AIP Conference Proceedings, Volume 1234, pages 177-180 (2010)

[101]: M. Brzhezinskaya, A. Firsov, K. Holldack, T. Kachel, R. Mitzner, N. Pontius, J.-S. Schmidt, M.Sperling, C. Stamm, A. Föhlisch, A. Erko, "*A novel monochromator for experiments with ultrashort X-ray pulses",* Journal of Synchrotron Radiation, Volume 20, pages 522-530 (2013)

[102]: http://henke.lbl.gov/optical_constants/layer2.html - CRXO-webpage

[103]: G. Wiederrecht, *Handbook of Nanofabrication*, Elsevier, ISBN 978-0-12-375176-8, pages 121-148 (2010)

[104]: M. Köhler, *Ätzverfahren für die Mikrotechnik*, Wiley-VCH, ISBN 3-527-28869-4 (1998)

[105]: M.J. Madou, *Fundamentals of Microfabrication*, 2nd ed., CRC Press, ISBN 0-8493-0826-7 (2002)

9. Annex - EBL – Electron Beam Lithography

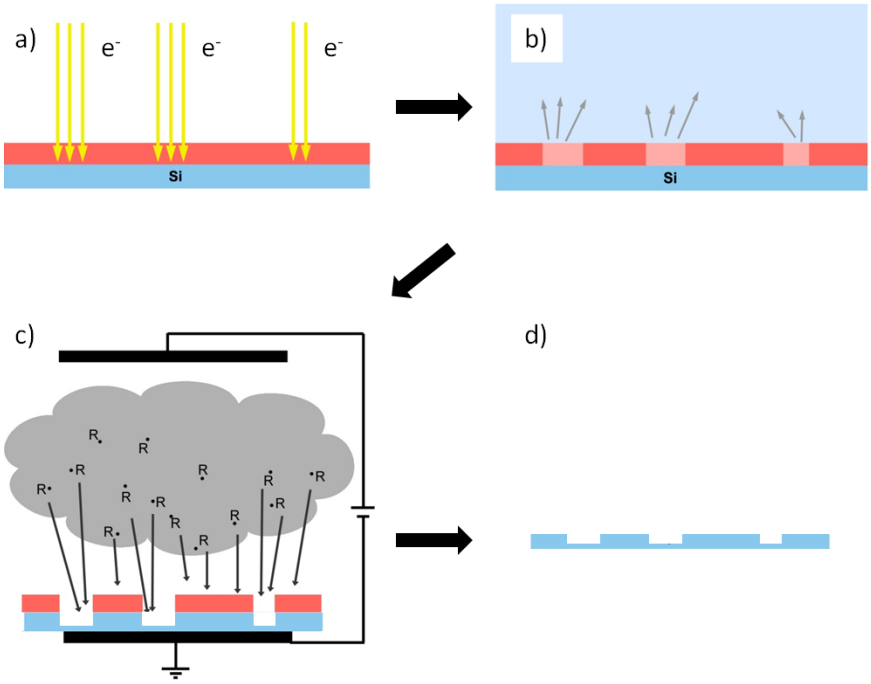

Figure 128: ***flow chart of the fabrication process for grating structures (e.g. RZPs) in principle (courtesy of H. Löchel and adapted in parts from [77]) (descriptions in text).***

The fabrication process for Reflection Zone Plates is depicted in Figure 128. In **step a)** some preparatory steps are summarized: a **silicon wafer** serves as substrate (blue layer in all steps). A liquid photo resist, in this case the **positive resist** Poly(methyl methacrylate) 950k (PMMA, red layer) is spin-coated onto the silicon substrate. The polymer PMMA comes in a solvent. The solution possesses a certain value of viscosity, regulated by the included amount of PMMA in the solvent. Depending on this viscosity and the rotation velocity used during spin coating, the desired resist layer thickness and homogeneity is adjusted.

After coating, the wafer gets baked on a hotplate, in order to vaporize the remaining solvent. In the next step the **e-beam writer** (VISTEC EBPG 5000+, running at an accelerating voltage of 100 kV) is used to literally write the designed structure, by deflecting an electron beam according to a CAD file. In this process, the primary electrons from the machine (which are too fast to directly interact efficiently) generate secondary electrons of lower energy inside silicon and resist, which then crack the long carbon-chains within the resist polymer efficiently. A correction of proximity effects can be done before e-beam writing with the structure calculation software (Nanomaker, Interface Ltd.). Proximity effects are resulting from back-scattered electrons exposing a wide area around a written feature, decreasing the exposure dose needed for subsequently written feature inside this area.

Step b) shows the process of the resist **development**. As mentioned above, PMMA is a positive resist. This means, the long and stable carbon-chains are destroyed (cracked) during the interaction with radiation. (Negative resists, which are also available for e-beam writing, apply the process vice versa, meaning that the initially shorter oligomers are merged to more stable long polymer chains.) The cracking process of the polymer produces molecules with lower molecular weight in comparison with

unexposed resist. In a bath of developer (AR600-56) mainly the resist parts of less molecular weight get dissolved. The optimal duration of development depends on resist thickness, developer concentration and temperature and is specified in the data sheet of the supplier, but needs to be adjusted with the exposure dose in preparation of writing.

Step c) illustrates the process of **reactive ion-etching (RIE)**. It is best described as a combination of both physical and chemical etching. The written and developed sample is transferred to a vacuum chamber at the electrical grounding plate of a capacitor. The chamber is subsequently filled with a Fluor-based gas at low pressure; usually for Si etching SF_6, C_4F_8, CHF_3 or a combination of these. The capacitor generates a radio-frequency field which produces plasma. Very reactive fluoride radicals and ions are formed in this plasma. These are accelerated towards the silicon surface. They etch the silicon in the resist grooves while the resist covered areas are protected against the attack. A high acceleration voltage between the two electrodes increases the anisotropy of the Si etching process; i.e. very straight and vertical side walls can be generated.

At **step d)**, after Fluor-etching, the remaining resist gets incinerated, removed by **application of an oxygen-plasma**. A clean silicon surface remains, structured with lines and spaces as designed. (As a side note: oxygen-plasma is sometimes used for a few seconds already before Fluor-etching, in case that some residual of the low-molecular-weighted resist should appear still after development.)

(After step b), the sample can also be coated with a thin metal layer instead of etching. If the sample is placed in Acetone, the resist will dissolve, leading to the metal layer on top of the resist lifting off, hence the name of the process “Lift-Off”. Only the parts of the metal layer in direct contact with the substrate, which is in the areas that have been written and removed during development, will stay.)

Depending on application, the resulting surface can be coated, in order to improve the reflectivity, hence efficiency, of the optical element (see LCLS-project, chapter 4.1, and RIXS-project, chapter 4.2). To deposit coating layers, two different processes are available at the INT laboratories: the deposition by evaporation of the coating-material (steaming), or transferring the coating material by ion bombardment of a target (sputtering, the atomized material condenses on the sample). The advantage of the latter is that the material is packed denser and stays more stable on the surface. Sputtered layers have higher adhesion to the substrate.

Sophisticated processes to produce RZPs with different depths of profile are currently under development at the INT laboratories. All presented processes are described in detail at [103], [104] and [105].

Eidesstattliche Erklärung

Hiermit versichere ich an Eides statt, dass ich die vorliegende Dissertation mit dem Titel “Beam Diagnostics and Spectroscopy at X-ray Free Electron Lasers” ohne fremde Hilfe angefertigt und keine anderen als die angegebenen Quellen und Hilfsmittel benutzt habe. Alle Teile, die wörtlich oder sinngemäß einer Veröffentlichung entstammen, sind als solche kenntlich gemacht. Diese Dissertation wurde noch nicht veröffentlicht und keiner anderen Fakultät oder Universität zur Prüfung vorgelegt.

Berlin, den 06.März 2014 _____

(Jens K. Rehanek)